The Dissertation Committee for Kyle Franklin Kaplan certifies that this is the approved version of the following dissertation:

Probing Conditions at Ionized/Molecular Gas Interfaces With High Resolution Near-Infrared Spectroscopy

Committee:

Harriet L. Dinerstein, Supervisor

Daniel T. Jaffe, Co-Supervisor

Neal J. Evans

Gary J. Ferland

John H. Lacy

Probing Conditions at Ionized/Molecular Gas Interfaces With High Resolution Near-Infrared Spectroscopy

by

Kyle Franklin Kaplan

Dissertation
Presented to the Faculty of the Graduate School of
The University of Texas at Austin
in Partial Fulfillment
of the Requirements
for the degree of
Doctor of Philosophy

The University of Texas at Austin
August, 2017

I dedicate this dissertation to those who encouraged my interest in astronomy as a child, including my parents, grandparents, and elementary school teachers. Without those who inspired me when I was young, I probably would not be following this path today.

Acknowledgements

I would like to express my thanks to everyone who helped make this dissertation possible. First I would like to thank my co-advisors Harriet Dinerstein and Dan Jaffe. They gave me the chance to switch to a new scientific topic part way through my graduate school career and provided the financial support I needed to finish this dissertation. Harriet has been invaluable in providing useful feedback on my writing and scientific ideas. Her expertise and knowledge of planetary nebulae and the vast literature that spans what we know about the interstellar medium is unmatched. Dan's ideas served as the basis for the science in this dissertation. He also has led the creation of the wonderful instrument IGRINS which I have used for all of this work. His experience and knowledge of infrared astronomy is unrivaled. Dan provided me with the opportunity to participate in the commissioning of IGRINS and observe for many nights with it.

I would like to thank my Ph.D. committee members Neal Evans, Gary Ferland, and John Lacy. Neal Evans was always there in the office across the hall willing to answer any question I might have. I have made extensive use of Gary Ferland's Cloudy code, and would like to thank Gary for all the helpful discussions we had on the Cloudy modeling. John Lacy was always happy to discuss the finer points of molecular physics in the ISM.

The instrument IGRINS has provided invaluable data upon which this dissertation, and my work would not be possible if not for the IGRINS Team that has designed, constructed, wrote the operating software, and helped commission this instrument. I have worked closely with the graduate students, post-docs, and research scientists that make up the IGRINS Team at UT Austin. Some have come and gone over my time here. I would like to acknowledge Mike Pavel, Hwihyun Kim, Gregory Mace, Kimberly Sokal, Ben Kidder, Jessica Luna, and Jacob McLane for all the discussions, help, and motivation they have given me. I would also like to acknowledge the members of the IGRINS Team in Korea. A special thank you to Jae-Joon Lee who wrote the IGRINS Pipeline Package (PLP) that I have used to reduce all my data and who worked hard to improve the pipeline based on feedback that I and

others have provided. I would also like to acknowledge Heeyoung Oh and Le Nguyen Huynh Anh who I have collaborated with on several projects.

A special thanks to all those who I have helped or who have helped me observe while at McDonald Observatory. I would especially like to extend my thanks to Nick Sterling who I, along with Harriet, have worked closely with on planetary nebulae. Nick spent many nights with me at McDonald, along with the undergraduates he brought along, to help observe planetary nebulae with IGRINS.

I would like to thank the many locations that have stayed open late at night where I could go and write this dissertation including the UT Perry-Castañeda Library, UT Life Sciences Library, UT Student Union Building, Strange Brew Austin Coffee (sadly now closed), Monkey Nest Coffee, Tea Haus, Epoch Coffee, and Bennu Coffee.

I would like to thank the grants that funded my work on this dissertation and the facilities where I took the data. This dissertation includes data taken at The McDonald Observatory of The University of Texas at Austin. This work used the Immersion Grating INfrared Spectrometer (IGRINS) that was developed under a collaboration between the University of Texas at Austin and the Korea Astronomy and Space Science Institute (KASI) with the financial support of the US National Science Foundation under grant AST-1229522 to the University of Texas at Austin, and of the Korean GMT Project of KASI. I also acknowledge support from the NSF grant AST-0708245 and JPL RSA 1427884.

I would like to acknowledge the Cambridge Astronomical Survey Unit and WFCAM Science Archive for making available data that were used for the finder charts in Figure 2.1. I would also like to thank Evelyne Roueff for pointing out the theoretical H_2 ground electronic state rovibrational energy levels in Komasa et al. (2011) from which we derive improved line wavelengths for the rovibrational transitions.

Probing Conditions at Ionized/Molecular Gas Interfaces With High Resolution Near-Infrared Spectroscopy

Kyle Franklin Kaplan, Ph.D.
The University of Texas at Austin, 2017

Supervisor: Harriet L. Dinerstein
Co-Supervisor: Daniel T. Jaffe

Regions of star formation and star death in our Galaxy trace the cycle of gas and dust in the interstellar medium (ISM). Gas in dense molecular clouds collapses to form stars, and stars at the end of their lives return the gas that made up their outer layers back out into the Galaxy. Hot stars generate copious amounts of ultraviolet photons which interact with the surrounding medium and dominate the energetics, ionization state, and chemistry of the gas. The interface where molecular gas is being dissociated into neutral atomic gas by far-UV photons from a nearby hot source is called a photodissociation or photon-dominated region (PDR). PDRs are found primarily in star forming regions where O and B stars serve as the source of UV photons, and in planetary nebulae where the hot core of the dying star acts as the UV source.

The main target of this dissertation is molecular hydrogen (H_2), the most abundant molecule in the Universe, made from hydrogen formed during the Big Bang. H_2 makes up the overwhelming majority of molecules found in the ISM and in PDRs. Far-UV radiation absorbed by H_2 will excite an electron in the molecule. The molecule then either dissociates ($\sim 10\%$ of the time; Field et al. 1966) or decays into excited rotational and vibrational ("rovibrational") levels of the electronic ground state. These excited rovibrational levels then decay via a radiative cascade to the ground rovibrational state ($v = 0$, $J = 0$), giving rise to a large number of transitions observable in emission from the mid-IR to the optical (Black & van Dishoeck, 1987). These transitions provide an excellent probe of the excitation and conditions within the gas. These transitions are also observed in warm H_2, such as in shocks, where collisions excite H_2 to higher rovibrational levels.

High resolution near-infrared spectroscopy, with its ability to see through dust,

and avoid telluric absorption and emission, serves as an effective tool to detect emission from ions, atoms, and molecules within PDRs. The Immersion Grating INfrared Spectrometer (IGRINS), with a high spectral resolution of $\sim$ 45,000 and simultaneous wavelength coverage of the near infrared H and K bands (1.45–2.45 μm) has proven to be an excellent instrument for such studies. Over 200 H_2 rovibrational transitions are observable within the wavelength coverage of IGRINS. In this dissertation, we use IGRINS on the 2.7m telescope at McDonald Observatory, to observe a variety of PDRs in the ISM and use the rovibrationally excited H_2 to probe the physical conditions within them. We fit our data with grids of Cloudy models (Ferland et al., 2013), which reproduce the observed H_2 rovibrational level populations, to determine the physical parameters in the gas such as temperature, density, and UV field intensity.

This dissertation is split into five chapters. In the first chapter, we introduce our science questions and explain our observations, data processing, and how to analyze H_2 emission. In the second chapter, we present a deep near-infrared spectrum of the Orion Bar PDR. In the third chapter, we analyze several other PDRs in star forming regions in a similar fashion to the Orion Bar, finding significant differences in their H_2 excitation and conditions. In the fourth chapter, we use the high spectral resolution of IGRINS to reveal kinematically and energetically distinct components of H_2 emission in three planetary nebulae (M 1-11, Vy 2-2, and Hen 2-459) consisting of UV-excited (PDR) H_2 and red- and blue-shifted thermal H_2 "bullets" that likely represent shocked molecular gas that is distinct from the UV-excited PDR components. In the fifth chapter, we summarize this dissertation, discuss the broader implications of this work, and suggest future directions for near-IR ISM research.

Contents

List of Tables

List of Figures

Chapter One: Introduction

1.1 PDRs

Ultraviolet (UV) radiation regulates the process of star formation and the energetics, ionization state, and chemistry of the interstellar medium (ISM). Photodissociation or Photon-dominated Regions (PDRs) are regions in the ISM at the interfaces between hot ionized gas and cool molecular gas that are energetically dominated by non-ionizing UV photons (Tielens & Hollenbach, 1985; Hollenbach & Tielens, 1997, 1999). PDRs arise in regions of massive star formation where the gas is ionized by newly formed hot OB stars, and make up the bulk of the neutral ISM in star forming galaxies such as the Milky Way. They also arise in planetary nebulae where the stripped central core of a former low-to-intermediate mass star is hot enough to generate UV photons which ionize the atoms and dissociate the molecules that make up the circumstellar material previously ejected by the star. PDRs reprocess much of the ultraviolet light emitted into the ISM, and reemit it in the infrared. In star forming regions, the absorbed UV radiation significantly affects the conditions within the gas, and these effects become incorporated into subsequent star formation. In the most extreme cases, starburst galaxies can have much of their starlight reprocessed and reradiated by PDRs. In planetary nebulae, PDRs signal the transition of ejected molecular gas to atomic and then ionized gas before being dispelled back into the ISM.

The standard one-dimensional model for a PDR, with the canonical model presented by Tielens & Hollenbach (1985), is a plane-parallel slab of gas illuminated on one side by stellar UV radiation. The interaction between UV photons and the gas sets up a differentiated structure that can be characterized by the phases of hydrogen, which transition from predominantly ionized (H II), to neutral atomic (H I), and then to molecular (H_2).

Figure 1.1 shows a schematic of a PDR from Hollenbach & Tielens (1997) depicting the changing gas conditions with distance from the UV source. The H II/H I and H I/H_2 interfaces are called the "ionization" and "dissociation" fronts respectively. Extreme-UV (EUV) photons with energies above the H I ionization potential

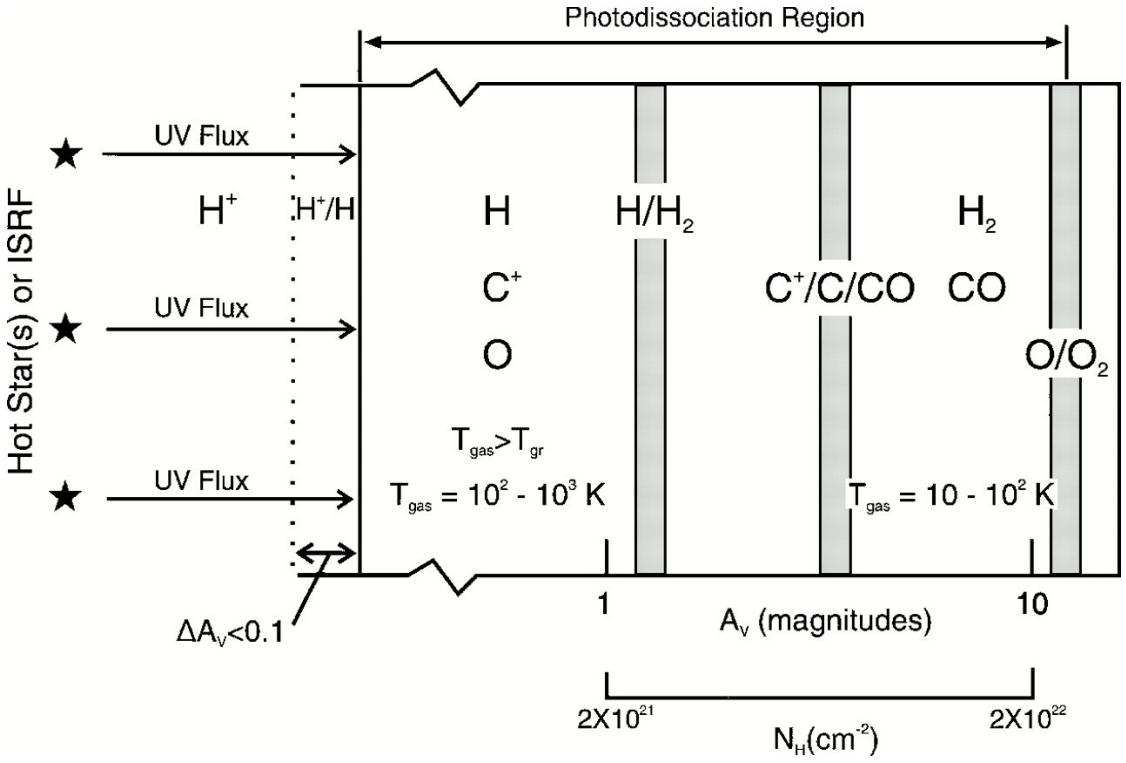

Figure 1.1: Schematic of a plane-parallel steady-state PDR from Hollenbach & Tielens (1997).

(> 13.6 eV, $\lambda < 912$ Å) pass through the H II zone and are absorbed by H I at the ionization front. Far-UV (FUV) photons with energies just below the Lyman continuum (11.2–13.6 eV, $912 < \lambda < 1110$ Å) pass through the H I zone but are absorbed by dust, elements with lower ionization potentials, and the Lyman and Werner bands of H_2. Beyond the dissociation front, the remaining FUV photons are rapidly attenuated as the cloud transitions to cold molecular gas.

H_2 makes up the bulk of the mass in dense shielded regions, and an overwhelming majority of all the molecules in the universe. It forms primarily on dust grain surfaces (Gould & Salpeter, 1963; Hollenbach & Salpeter, 1971), and plays a significant role as a coolant in the ISM (e.g. see Galli & Palla 1998; Shull & Beckwith 1982 and references therein). Figure 1.2 shows the basic properties of the transitions that give rise to the H_2 spectrum. H_2 is a diatomic molecule that can exist in excited electronic states as well as excited quantum rotational and vibrational levels of the ground electronic state, which are identified by the J and v quantum numbers respectively.

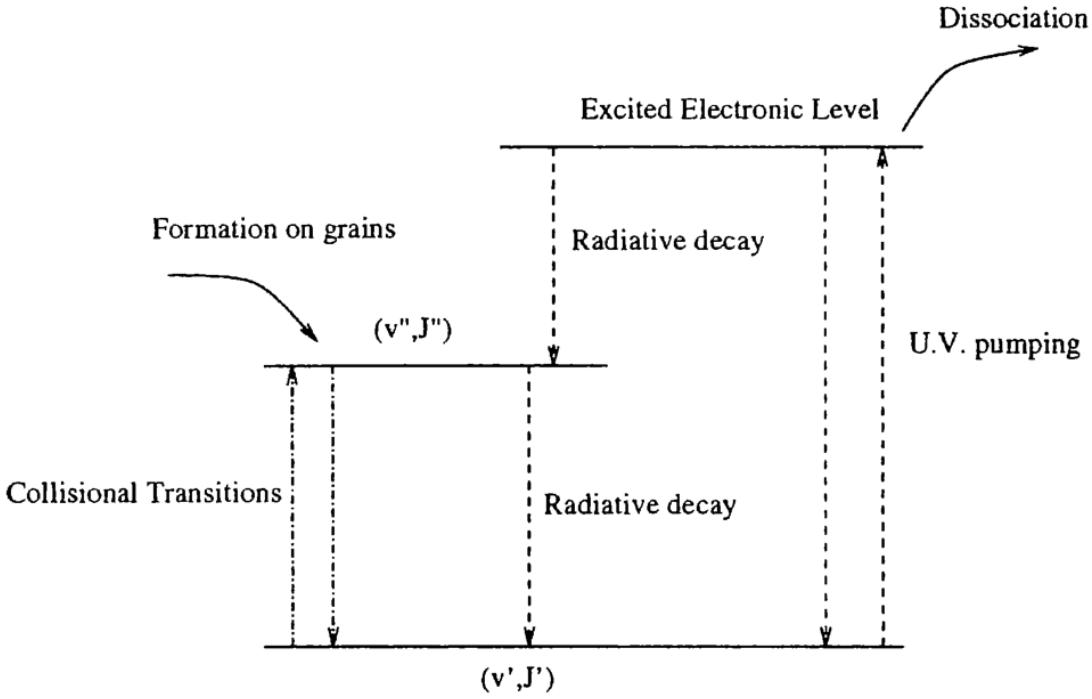

Figure 1.2: Diagram from Le Bourlot (2000) depicting the different energy levels, excitation processes, de-excitation processes, and dissociation of H_2.

Taking rotation and vibration together, we refer to these as "rovibrational" levels. H_2 can be excited above the ground rovibrational level ($J = 0$, $v = 0$) by two main processes: radiative UV excitation (fluorescence) and collisional (thermal) excitation. UV excitation occurs when FUV photons absorbed by H_2 excite the molecules to excited electronic states (through the Lyman and Werner bands), from which $\sim 10\%$ of the molecules will dissociate (Field et al., 1966), and the rest decay into bound excited rovibrational levels (Black & Dalgarno, 1976; Black & van Dishoeck, 1987). Collisional excitation occurs via inelastic collisions with other particles in the gas that leave the molecules in excited rovibrational states. Other minor processes such as "formation pumping," where H_2 forms on dust grains in excited rovibrational states, can also contribute.

These rovibrationally excited molecules decay via either collisions or a radiative cascade of rovibrational transitions, which have wavelengths ranging from the mid-infrared to the optical. H_2 is a homonuclear diatomic molecule lacking a perma-

nent electronic dipole moment, so the rovibrational transitions occur only as electric quadrupole transitions ($\Delta\ J = \ 0, \ \pm 2$), which are optically thin under most conditions. Since the line flux from each transition is proportional to the number of molecules in an upper level, observing many lines allows us to calculate the detailed H_2 rovibrational level populations. These emission lines have significant diagnostic power to reveal physical conditions within PDRs at the H I/H_2 dissociation front where most of the emission arises.

The UV and collisional excitation and de-excitation processes give rise to two limiting cases for the rovibrational level populations: the thermal limit and the case of "pure" unmodified radiative UV excitation. In dense and/or hot gas (such as in shocks), the rovibrational levels are excited and de-excited by frequent collisions and the level populations approach a thermal distribution. In low-density cool gas exposed to UV radiation, the level populations take on a distinctive non-thermal distribution that does not decline monotonically with increasing excitation energy. Observations of the rovibrational line flux ratios readily distinguish between these two limiting cases. However, in practice, many sources show level populations intermediate between UV-excited and thermal H_2. Two possible reasons are the superposition of spatially unresolved components, or collisional modification of UV-excited H_2. Sternberg & Dalgarno (1989) and Burton et al. (1990b) show that dense PDRs can exhibit level populations that are modified from the UV-excited case by collisions. For H_2 rovibrational states with low energies above ground, their excitation is easily dominated by collisions, bringing these states into thermal equilibrium with the gas. States at higher energies are primarily UV-excited, but collisional de-excitation modifies their populations from the UV-excited case. This collisional modification of the level populations in UV-excited H_2 can mimic the spectrum from an unresolved combination of UV-excited and thermal components.

1.2 IGRINS

The Immersion GRating INfrared Spectrometer (IGRINS) is a sensitive near-infrared (near-IR) cross-dispersed echelle spectrometer that uses a silicon immersion grating to achieve a high spectral resolution of $R = \lambda/\Delta\lambda \approx 45000$ or ≈ 6.7 km s^{-1} in two separate H and K band channels that are observed simultaneously to give a full

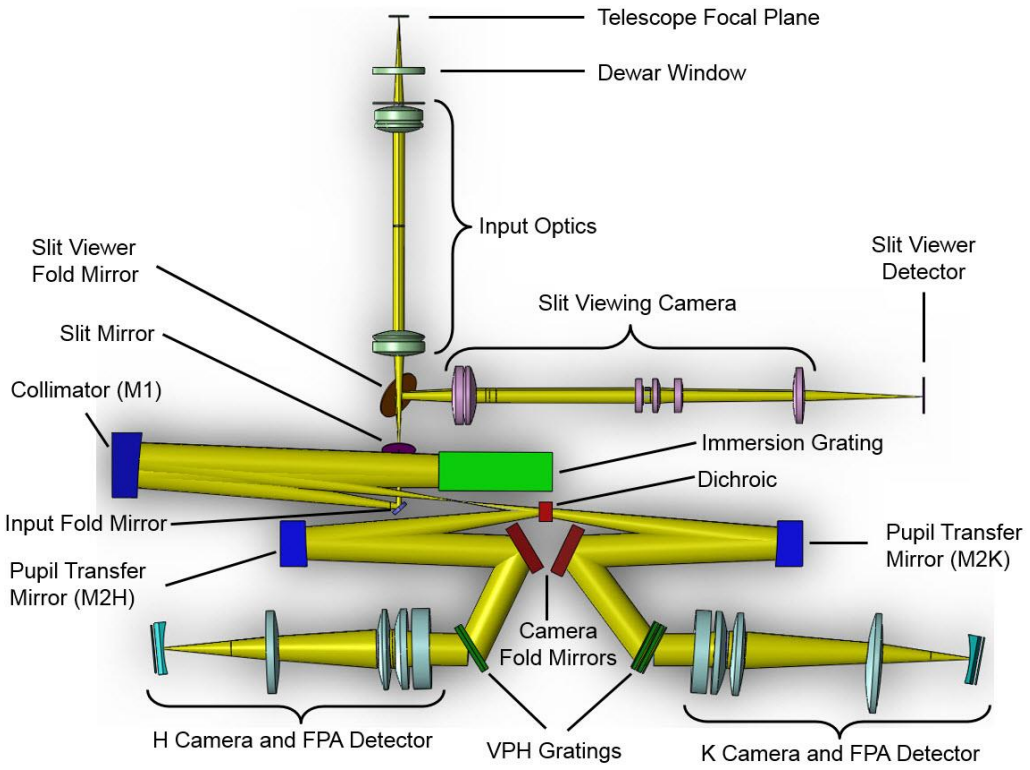

Figure 1.3: Schematic of the optics and detectors inside IGRINS, from Park et al. (2014).

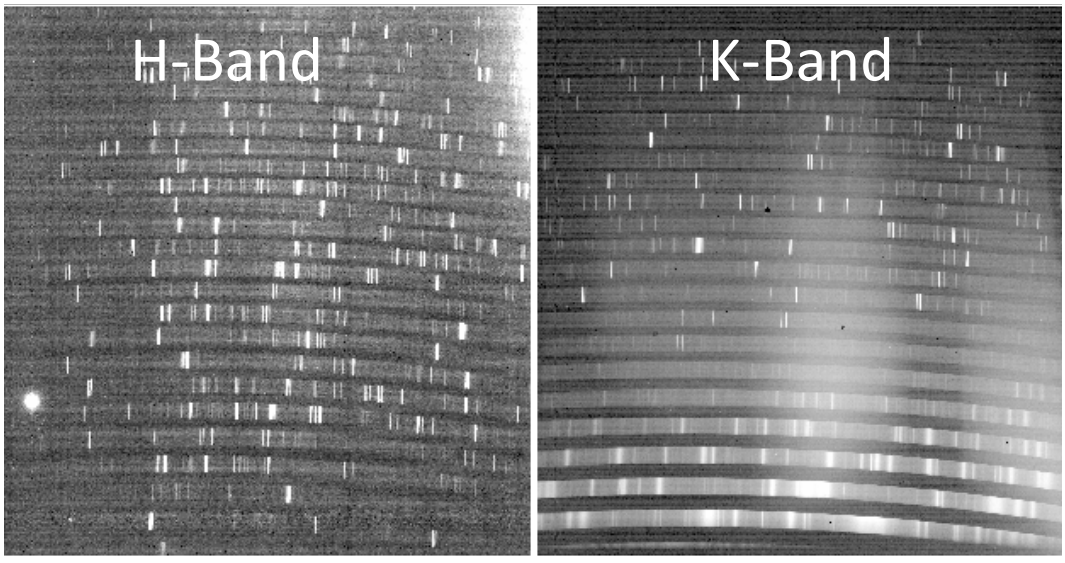

Figure 1.4: Example of the IGRINS H and K band echellograms. In this example, we show a spectrum of the Orion Bar.

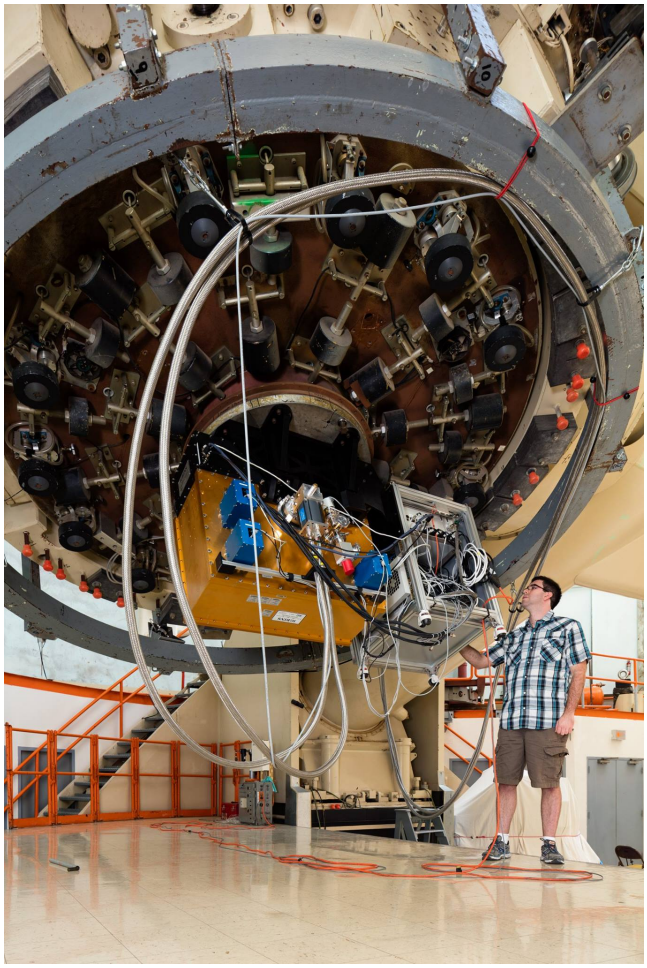

Figure 1.5: Photograph of IGRINS mounted at the Cassegrain focus of the 2.7 meter Harlan J. Smith Telescope at McDonald Observatory.

wavelength coverage of 1.45–2.45 μm (Yuk et al., 2010; Park et al., 2014). Figure 1.3 shows the internal layout of the instrument and Figure 1.4 shows example H and K band echellograms from an observation of the Orion Bar. IGRINS was developed as an international collaboration between The University of Texas at Austin and the Korea Astronomy and Space Science Institute (KASI). It was successfully commissioned in early 2014 and has enjoyed over three years of successful science observations while mounted on the 2.7 meter Harlan J. Smith Telescope at McDonald Observatory (see Figure 1.5) and Lowell Observatory's 4.3 meter Discovery Channel Telescope (DCT) (Mace et al., 2016). IGRINS has a fixed slit that covers $1'' \times 15''$ at McDonald Observatory and $0.63'' \times 9.3''$ at the Discovery Channel Telescope. The instrument

can be rotated on the telescope to place the slit at any desired position angle (PA) on the sky. It is scheduled to soon be deployed on Gemini Observatory's southern 8.1 meter telescope. IGRINS has served as a testbed and precursor to GMTNIRS that is planned to go on the GMT (Jaffe et al., 2006; Lee et al., 2010; Mace et al., 2016). All our observations presented in this dissertation were taken with IGRINS.

The superb spectral resolution of IGRINS provides many advantages, such as allowing us to resolve closely spaced lines, reducing sky background to achieve high signal-to-noise for unresolved lines, and study the kinematics within gas. If the near-IR spectrum shows hot gas with collisional line flux ratios, detailed kinematic information can help us differentiate whether the gas is heated by shocks or by another heating mechanism. Multiple pointings can be combined into slit-scan maps which then provide superb spatially resolved spectra.

1.3 Data Reduction and Calibrations

The IGRINS data is contaminated with cosmic rays and hot pixels, especially over the several hours used for most of our science observations. Before running the data reduction pipeline, cosmic rays and hot pixels are identified and masked from the raw science frames using Version 0.4 of the Python implementation of LA-Cosmic[1].

We reduce all our IGRINS data using the IGRINS Pipeline Package[2] (PLP) written by Jae-Joon Lee (Lee, 2015). The PLP finds and subtracts the vertical and horizontal medians of the inter-order pixels to remove the readout pattern from each raw frame. Flat frames are combined to create a master flat, which is used to correct pixel-to-pixel variations on the detector and to trace the aperture for each order in the echellograms. An A0V standard star spectrum is optimally extracted with a weighted sum along the positive and negative traces of the star, which are then collapsed into a single one-dimensional spectrum. For spatially extended targets that fill the slit, the sky and background emission are removed by subtracting sky frames taken at an offset position, from the science frames. For compact targets, such as some planetary nebulae, the target is nodded along the slit and one position is subtracted from the other to remove the sky background while still gathering photons from the target

[1]Python implementation of LA-Cosmic (van Dokkum, 2001) by Malte Tewes: `https://obswww.unige.ch/~tewes/cosmics_dot_py/`

[2]IGRINS Pipeline Package (PLP): `https://github.com/igrins/plp`

to make the most efficient use of observing time. We use telluric OH emission lines to construct an initial estimate of the wavelength solution by fitting 2D Chebyshev polynomials to the H and K band echellograms. The polynomial solution is refined by cross-correlating the telluric absorption lines in the A0V standard star spectrum with predictions from an atmospheric model generated with the Telfit[3] code by Gullikson et al. (2014). The final wavelength solution has sub-pixel accuracy with a typical uncertainty of ± 0.5 km s^{-1} or $< 6 \times 10^{-6}$ μm at any given point in the spectrum. We confirm the final wavelength solution by checking for differences between it and solutions derived using a ThAr arc lamp or the OH sky emission lines. Each order is extracted using the master flat frame to trace the order boundaries on the H and K band echellograms, and curvature of the slit image across each order is fit and corrected for using OH sky emission lines. The final data products from the PLP for 2D spectra are the extracted individual orders and their estimated variance (for propagating measurement uncertainties).

1.4 Data Calibration and Line Flux Extraction

1.4.1 Data Calibration

All subsequent data calibration and analysis is carried out with our publicly available "plotspec"[4] python code designed for analyzing the reduced 2D IGRINS spectra of emission line nebulae.

The science we want to do, including calculation of relative column densities of H_2 rovibrational states, requires reliable flux ratios for all observed lines across the large wavelength range covered by IGRINS. To obtain a reliable relative spectrophotometric flux calibration, we need to correct for atmospheric (telluric) absorption lines, atmospheric transmission, instrumental throughput, and detector response. A0V stars have a well-known continuum shape, broad H I absorption lines, and weak metal lines, making them preferred standards for telluric correction and relative flux calibration in the near-IR. For each of our science targets, we observed an A0V standard star at a similar airmass and adopt a technique similar to that used for telluric correction and

[3]Telfit: `http://www.as.utexas.edu/~kgulliks/projects.html`.
[4]Plotspec: `https://github.com/kfkaplan/plotspec`.

relative flux calibration in the SpeX data reduction package *Spextool*[5] (Vacca et al., 2003). We start by assuming that every A0V star has a continuum shape similar to that of Vega, and modify the model spectrum of Vega *vegallpr25.50000resam5* by R. Kurucz[6] to match the spectrum of the observed A0V standard star. First, the H I absorption lines in the model Vega spectrum are masked and a cubic spline is fit to the regions between the absorption lines to define the continuum. Next, the continuum is artificially reddened to match the A0V standard observed for each science target using the near-IR extinction law from Rieke & Lebofsky (1985), with $E(B-V)$ calculated from the standard star's B and V magnitudes. The H I absorption lines in the spectrum of the standard star are fit by scaling and Gaussian smoothing the H I lines in the model Vega spectrum and adding them to the artificially reddened continuum to create a synthetic spectrum of the standard star. This synthetic spectrum represents an estimate of the intrinsic spectrum of the standard star. Finally, we divide the IGRINS spectrum of the A0V standard by the synthetic spectrum to derive the counts-to-flux ratio at each wavelength, and simultaneously apply the telluric correction and relative flux calibration by dividing the science spectrum by this ratio.

The continuum in PDRs can arise from a combination of scattered starlight, thermal emission from dust grains, along with free-free and bound-free emission from the ionized gas. The central star can also contribute to the continuum if the target is compact enough that the star falls within the IGRINS slit, as is the case for some of the planetary nebulae we observed. Occasionally background stars fall on the slit, contributing continuum to the spectrum. Continuum is subtracted from each order with a running median filter that is 500 pixels wide in wavelength space. This technique usually fits the continuum well, while ignoring narrow features in the spectrum such as emission and absorption lines, bad pixels, or regions with a large amount of telluric absorption. After the continuum subtraction is done, all the orders are spliced together into a single 2D spectrum on a single wavelength grid.

Ideally, subtracting sky frames should remove all the OH sky emission, but since telluric OH emission lines vary in flux over time, OH line residuals are a possible source of contamination and could in some cases be misidentified as other lines. To minimize the effect of OH residuals in our observations of spatially extended targets,

[5]Spextool: `http://irtfweb.ifa.hawaii.edu/~spex/`.

[6]R. Kurucz synthetic stellar spectra: `http://kurucz.harvard.edu/stars.html`.

we apply a first order correction to OH line residuals by finding the difference between the first and last sky frames and varying the flux and flexure in the sky difference to best match the OH residuals, which are then subtracted to remove most of the OH residual flux.

All atomic and ionic lines are identified using wavelengths from Peter van Hoof's Atomic Line List v2.04[7]. The H_2 lines are identified using wavelengths calculated from the theoretical ground electronic state rovibrational level energies in Komasa et al. (2011), providing much improved agreement between the observed and theoretical line wavelengths over previously published values (observed and theoretically derived). For example, wavelengths determined from the commonly cited rovibrational energy levels in Dabrowski (1984) differ from the observed line centroids by up to 10^{-4} μm, well in excess of the precision of the IGRINS wavelength calibration. These differences are factors of 5-10 times larger than the residuals for the wavelengths based on Komasa et al. (2011).

1.4.2 Line Flux Extraction

Each emission line in a science target is linearly interpolated from 2D position-wavelength space onto a common position-velocity (PV) map of $\pm$100 km s^{-1} for PDRs in star forming regions with relatively narrow lines, and $\pm$150 km s^{-1} for planetary nebulae which typically exibit larger velocities. The flux per pixel is conserved during this interpolation. Figure 1.6 shows an example of a PV map. Lines that have been misidentified or contaminated by other nearby lines or noise sources are removed from consideration at this stage.

Line fluxes are extracted two different ways, depending on the nature of the target. The simplest way is by performing what is essentially aperture photometry in PV space. This is done for the atomic, ionic, and H_2 lines in planetary nebulae that are well extended in PV space. We start by drawing apertures around the lines in PV space using DS9[8] regions. The background is calculated from the median flux of all the pixels outside the aperture. The background is subtracted from each pixel and then the flux values for all the pixels inside the aperture are summed to calculate the

[7]Peter van Hoof's Atomic Line List: `http://www.pa.uky.edu/~peter/atomic/`
[8]DS9: `http://ds9.si.edu/site/Home.html`

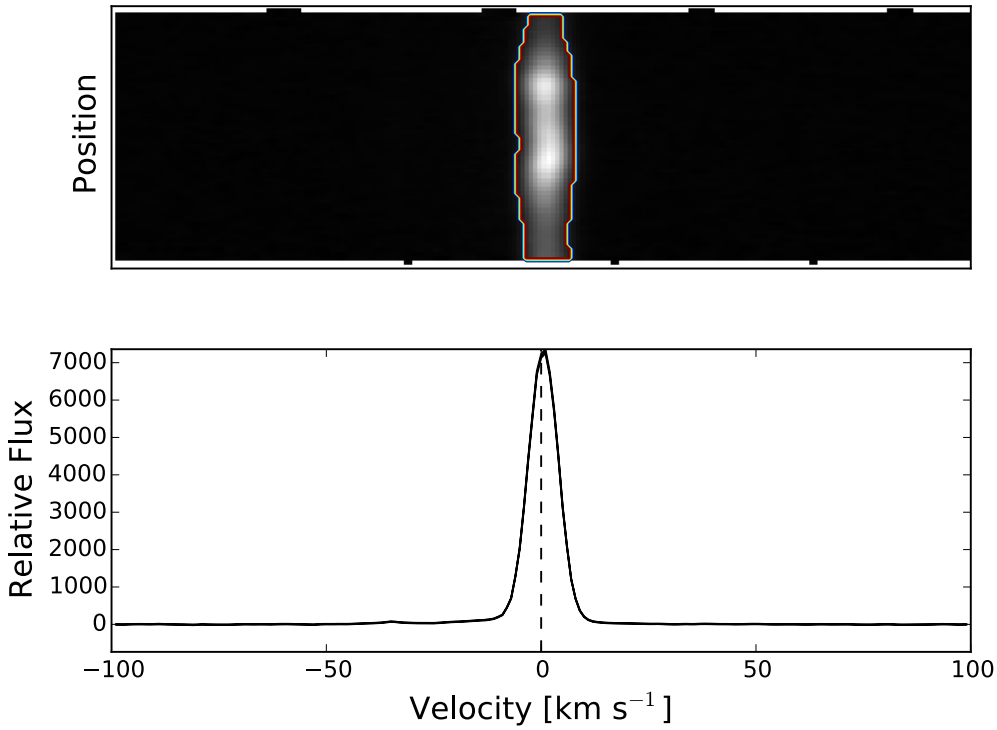

Figure 1.6: Example 2D PV map (top) and collapsed 1D diagram (bottom) of the 1-0 S(1) line observed in the Orion Bar.

flux for each emission line. This procedure is repeated to determine the variance to realistically propagate measurement uncertainties.

For PDRs in star forming regions, where the H_2 lines all have similarly narrow line profiles (e.g., Figure 1.6), we have adopted a robust optimal extraction scheme designed to scale with S/N across each line profile. We use the bright 1-0 S(1) line as the basis for our weighting scheme, and calculate the weights $w_{x,v}$ by squaring the flux $F_{x,v}^{\text{1-0 S(1)}}$ found in each pixel in position (x) and velocity (v) space for the 1-0 S(1) line:

$$w_{x,v} = (F_{x,v}^{\text{1-0 S(1)}})^2. \tag{1.1}$$

The weights are then normalized as follows:

$$w_{x,v} = w_{x,v} / \sum_x \sum_v w_{x,v}. \tag{1.2}$$

The background B per pixel is determined from the median value of all pixels in the PV diagram that are less than or equal to a small percentage (chosen for each science

target) of the brightest pixel flux in order to ensure that no line flux ends up in the background determination. We subtract the background from the flux in each pixel $F_{x,v}$, multiply by the weights $w_{x,v}$, and then sum the result to get the extracted line flux F:

$$F = \sum_{x} \sum_{v} (w_{x,v}(F_{x,v} - B)). \tag{1.3}$$

Each line extraction is visually inspected to ensure that it is a real feature. Lines that appear to be contaminated by blends, misidentifications such as OH residuals, or noise spikes are rejected. For propagation of the statistical uncertainties, the interpolation and extraction process is repeated for the variance reported by the PLP. We remove all lines with a signal-to-noise ratio < 3.

1.5 H_2 Level Populations as a Probe of the Excitation Mechanisms and Physical Conditions in PDRs

H_2 emission is a useful probe of the excitation and physical conditions of the gas in PDRs, especially when we are able to observe a large number of lines arising from levels with a wide range of excitation energies. The large wavelength coverage, sensitivity, and high spectral resolution has made IGRINS an extremely successful instrument for observing H_2 in many astrophysical objects (e.g., Oh et al. 2016a,b; Herczeg et al. 2016; Le et al. 2016; Kaplan et al. 2017). Much of the H_2 in the ISM resides in cold unexcited gas, where its near-IR emission is weak and hard to detect for two reasons. The first reason is that the rovibrational transitions are low probability electric-quadrupole transitions. The second reason is that even the lowest few excited pure rotational levels have fairly large energies above the ground state (even compared to all other diatomic molecules) due to the low molecular mass of H_2. For example, to excite the lowest energy pure rotational transition, $J = 2 \rightarrow 0$, requires an energy equivalent to a temperature of 510 K. PDRs exist on the boundaries between ionized and molecular gas, so are subjected to high levels of non-thermal excitation, making the normally weak emission lines from H_2 brighter and easier to detect in PDRs.

1.5.1 Excitation Diagrams

Most diagnostics employed to determine the excitation of H_2 rely on using ratios of rovibrational transition lines fluxes (or absorption profiles) to infer the populations of the rovibrational levels. Since the near-IR H_2 lines are optically thin, the line fluxes are linearly proportional to the column densities of molecules in the upper states of the transitions. We calculate the column density of H_2 in the upper state N_u of a given transition using the following equation,

$$N_u = \frac{F_{ul}}{\Delta E_{ul} hc A_{ul}}, \tag{1.4}$$

where F_{ul} is the flux of the transition from upper (u) to lower (l) rovibrational states, ΔE_{ul} is the difference in energy between the states in units of inverse cm (cm^{-1}), A_{ul} is the transition probability (s^{-1}) (we use the values from Wolniewicz et al. 1998, which are used in Cloudy), h is Planck's constant, and c is the speed of light. These values are normalized to the population of a selected reference level r, which has column density N_r and statistical weight g_r. In many cases, it is possible to observe multiple transitions arising from the same upper level, e.g. 1-0 S(1) and 1-0 Q(3), providing independent measurements of N_u for those upper states.

An excitation diagram is a plot of the logarithmic column density of a transition's upper state N_u divided by its quantum degeneracy g_u vs. the excitation energy above the ground state ($v = 0, J = 0$), and is a convenient diagnostic tool for determining excitation mechanisms. The large number of lines we observe with IGRINS makes excitation diagrams an ideal diagnostic tool to use.

The spin of the two protons in H_2 can be either aligned or anti-aligned, forming two distinct spin isomers called ortho-H_2 (spins aligned) and para-H_2 (spins anti-aligned). Since protons are fermions, the wave function of ortho-H_2 can have only odd values of J, while para-H_2 can only have even values of J. In collisional equilibrium at T >> 510 K, the statistical weights $g_{\rm nuc}$ for nuclear spin $s_{\rm nuc}$ give an ortho-to-para ratio of three because the vector-sum of $s_{\rm nuc}$ for both protons is either 0 or 1 and $g_{\rm nuc} = 2s_{\rm nuc} + 1$. The value of g_u depends on the upper rotational state J_u and whether the H_2 is ortho or para:

$$g_u^{\rm ortho} = 3(2J_u + 1), \quad g_u^{\rm para} = 2J_u + 1. \tag{1.5}$$

H_2 that is primarily excited and de-excited by collisions has thermal rovibrational level populations (e.g. such as in shock heated gas). In an isothermal gas, the

rovibrational level populations follow the Boltzmann distribution:

$$\left(\frac{N_u}{g_u}\Big/\frac{N_r}{g_r}\right) \propto \exp\left(-\frac{E_u}{kT}\right), \quad \ln\left(\frac{N_u}{g_u}\Big/\frac{N_r}{g_r}\right) = -\frac{E_u}{kT}, \tag{1.6}$$

where E_u is the energy above the ground rovibrational state, k is the Boltzmann constant, and T is the kinetic temperature of the gas; in other words, the level populations follow a linear trend on an excitation diagram with a slope inversely proportional to T. If multiple temperature components are present, or there is a temperature gradient, the slope becomes shallower at higher excitation energies (e.g., Rosenthal et al. 2000). This occurs because hotter gas dominates the excitation of states at the highest energies above ground, while cooler gas dominates the excitation of states at lower energies.

UV excitation of H_2 is a non-thermal process that leads to populations that do not show a monotonically decreasing trend for all the data-points on an excitation diagram, but instead follow a characteristic "sawtooth" pattern. Figure 1.7 shows an example of an excitation diagram of H_2 lines in the planetary nebula BD+30 3639 from Hora et al. (1999). The observed sawtooth pattern is indicative of UV excitation of the H_2.

One can fit straight lines to a series of rovibrational states of constant v to derive a "rotational temperature" or across states of constant J to derive a "vibrational temperature," but these are not necessarily equal to the kinetic temperature, unless the excitation is collisionally dominated. Instead, they are a shorthand way of characterizing the relative level populations. For UV-excited H_2, the level populations have high vibrational temperatures and lower rotational temperatures. While linear fits to these ladders (trends in constant v or J) have been used in past studies of UV-excited H_2, they are not an ideal description for our information-rich data sets where we probe up to high J for many rotational ladders, where the trends deviate from linear.

1.5.2 Effects of Collisions

The distinctive sawtooth pattern in UV-excited H_2 rovibrational level populations seen on an excitation diagram, as depicted in panel (a) of Figure 1.8, can be modified by collisions with other particles. Since the rate of collisions and the energy of each collision depends on both the temperature and density of the gas in a PDR, the subtle

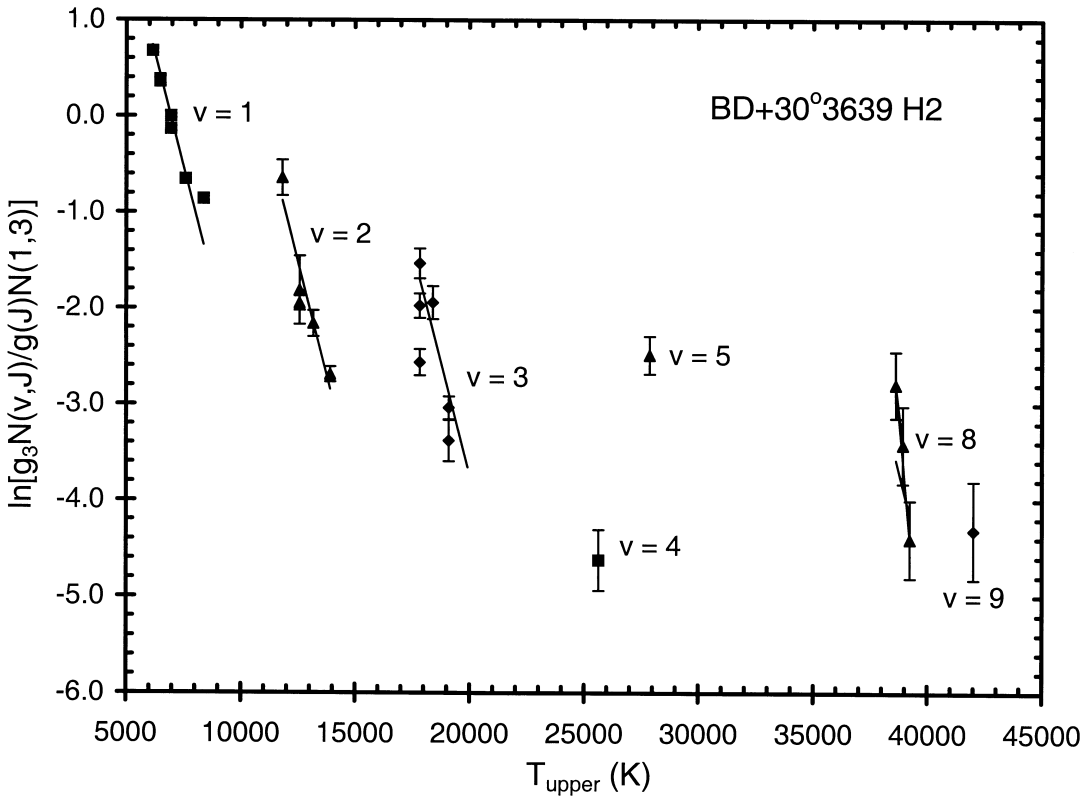

Figure 1.7: Example of an excitation diagram from Hora et al. (1999), showing the rovibrational level populations in H_2 for the planetary nebula BD+30 3639. Here you can clearly see the the "sawtooth" pattern exhibited by H_2 when the levels are populated by UV excitation. If the H_2 levels were primarily populated by collisions in a thermal gas, the points would follow a single monotonically decreasing trend on the excitation level diagram.

modifications to UV-excited H_2 rovibrational levels by collisions can be exploited to probe the physical conditions within a PDR.

The critical density of a given rovibrational level is the gas density where collisions start to dominate the level's excitation and de-excitation more than the processes of UV excitation and radiative decay. At densities above a level's critical density, the H_2 population for that level is primarily set by collisions, bringing that level's population into thermal equilibrium with the gas. Levels of low excitation energy, mainly the lowest few pure rotational states ($v = 0$), where the majority of the H_2 in a PDR lies, have low critical densities so their populations are in thermal equilibrium with the gas. The kinetic temperature of the gas sets the kinetic energy of the collisions,

so increasing the temperature raises the populations of the higher J states. For an isothermal gas, the Boltzmann distribution (Equation 1.6) describes these level populations. If the gas is warm enough, collisions can excite some of the molecules to $v = 1$ and maybe 2. The populations of levels with high critical densities, typically those with high excitation energies at $v \geqslant 1$, primarily depend on UV excitation and the subsequent radiative cascade set by the transition probabilities (A_{ul}) and other physical constants that are mostly invariant to external variables such as the UV radiation field intensity (Black & van Dishoeck, 1987; Sternberg, 1988; Sternberg & Dalgarno, 1989). During UV excitation and the subsequent radiative cascade, quantum selection rules allow transitions with all values of Δv but restrict the value of ΔJ to 0 or ± 2. In this sense, UV excitation crudely transposes the distribution of level populations for J at $v = 0$ set by the gas kinetic temperature to higher v. Making the gas warmer increases the relative column density of molecules at high J for all v and compresses each rotational ladder vertically on the excitation diagram while preserving the relative trend of a given rotational ladder (e.g., making the gas warmer vertically compresses the "bent knee" shape of the $v = 1$ rotational ladder). Panel (b) in Figure 1.8 depicts this effect.

Increasing the gas density increases the rates of collisional excitation for levels with critical densities near or below the gas density, and increases the rates of collisional de-excitation for levels with critical densities above the gas density. Increasing the temperature also tends to increase the rates of collisional de-excitation. This has differential effects on the populations of the lower energy $v = 0$ and 1 levels which have low critical densities vs. the higher energy $v > 1$ levels which have high critical densities. For the level populations in $v > 1$, their populations become increasingly depressed by collisional de-excitation as the gas density and/or temperature increases, while collisional excitation increases the populations of the $v = 0$ and 1 levels. Panel (c) in Figure 1.8 depicts this effect.

Increasing the temperature and/or density of the gas increases the fraction of H_2 where the rovibrational level populations are set or modified by collisions, which modifies the overall radiative cascade. Collisionally induced transitions do not follow the same route to the ground level as the radiative cascade. Radiative transitions favor low-J and are limited by quantum selection rules ($\Delta J = 0$ or ± 2), while collisionally induced transitions favor high-J and are not constrained by the same quantum rules. This raises the population of the high-J levels in a given rotational ladder

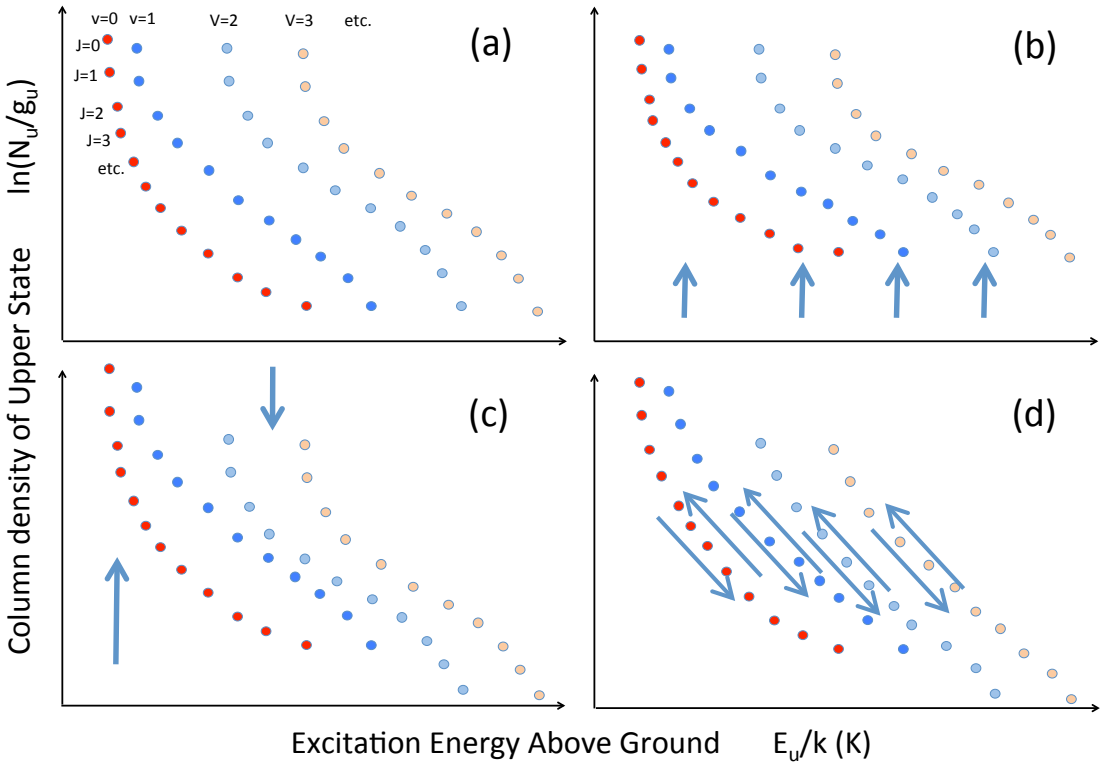

Figure 1.8: Set of four excitation diagram representations depicting the H_2 rovibrational level populations for UV excited H_2. Panel (a) depicts the characteristic sawtooth pattern of unmodified UV excitation. The other three panels depict how collisions modify these level populations from the unmodified UV excited case. Panel (b) shows how increasing the temperature of the gas raises the level populations at higher J in $v = 0$ which are then redistributed to higher v by UV excitation. Panel (c) shows the collisional excitation of $v = 0$ and $v = 1$ coupled with the collisional de-excitation of the higher v rotation ladders. Panel (d) illustrates how collisionally induced transitions modify the radiative cascade leading to smoother rotation ladder shapes.

and "straightens" the shape of the rotational and vibrational ladders as seen on the excitation diagram. Panel (d) in Figure 1.8 illustrates this the effect. This effect occurs simultaneously with, and at high density overwhelms, the compression of the rotational ladders caused by the redistribution of the collisionally excited $v = 0$ levels to higher v by UV excitation (e.g., the non-linear bends at high J in the rotational ladders get straightened into monotonically decreasing trends).

1.5.3 Ortho-to-Para Ratio

In thermal equilibrium, the statistical weights for nuclear spin give an ortho/para ratio of 3. The ratio is set or modified only during the formation of H_2, collisions between H_2 molecules and other species such as H or H^+, or selective dissociation of either ortho- or para-H_2. The numerous rovibrational transitions we observe in the near-IR come from both ortho and para-H_2, and radiative transitions cannot change ortho-H_2 into para-H_2 or vice-versa. If the rovibrational levels are populated primarily by UV pumping, Sternberg & Neufeld (1999) point out that the observed ortho/para ratio is modified by optical depth effects for the UV photons exciting the H_2. If lines are optically thick, the equivalent widths for the Lyman and Werner lines vary as the square root of the abundance of H_2, because we are on the "strong line" region of the curve of growth, so the observed ratio of UV-excited ortho/para H_2 becomes $\sqrt{\text{ortho/para}}$. If the *intrinsic* ortho/para ratio = 3, the *observed* ortho/para ratio from the rovibrational transitions in optically thick UV-excited H_2 becomes $\sqrt{\text{ortho/para}} = \sqrt{3} \approx 1.7$. Since this effect only applies for H_2 excited by UV pumping, collisionally excited H_2 will give the thermal ortho/para ratio. Consequently, the observed ortho/para ratio can be used as a probe of the dominant excitation mechanism of the gas. The PDR models we use to fit the data take these effects into account when predicting the rovibrational transition line fluxes.

1.6 Simulating H_2 Emission with Cloudy

For all of our modeling, we use version 13.03c of Cloudy[9] (Ferland et al., 2013), a one-dimensional plasma simulation code that solves for the physical conditions of a slab (or sphere) of gas irradiated by a photoionization source. It predicts the physical

[9]Cloudy: `http://nublado.org`.

conditions of the gas and the emergent spectrum and includes detailed physics for radiative transfer through the gas and the states of the constituent ions, atoms, molecules, and dust. This version of Cloudy includes a fully self-consistent treatment of H_2 including the excited electronic and rovibrational states, radiative and collisional excitation, photodissociation, and reformation on dust grains (Shaw et al., 2005).

Collisions in dense gas, such as the Orion Bar, can modify the H_2 rovibrational level populations in UV excited H_2 (Sternberg & Dalgarno, 1989; Burton et al., 1990b). For the Cloudy models, we have replaced the H_2–H^0 collision rate coefficients from Wrathmall et al. (2007) used by default in Cloudy 13.03c with updated values from Lique (2015). We use the default rates in Cloudy for H_2–H_2, H_2–H^+, and H_2–He collisions. For collision rate coefficients that have no data (typically high v and J), the "g-bar approximation" is used to estimate collision rate coefficients. The g-bar approximation assumes that the rate coefficient for a collisionally induced transition is a function of that transition's change in energy and assumes a particular functional form for this dependence (van Regemorter, 1962; Shaw et al., 2005).

To compare Cloudy models to some of our results, we have created grids of Cloudy models varying one or two parameters (e.g. temperature and density) to find the best fit to the observed H_2 rovibrational level populations. This has proven to be a useful technique to use the H_2 emission to constrain the physical conditions within PDRs.

Chapter Two: The Orion Bar PDR

Note: This chapter is based on the paper Kaplan et al. (2017) published in ApJ. Kyle F. Kaplan was the lead author in the paper and was in charge of the data acquisition, wrote the code to conduct the data analysis, and constructing and fitting models to the data to determine the properties of the observed gas.

We present a deep near-infrared spectrum of the Orion Bar Photodissociation Region (PDR) taken with the Immersion Grating INfrared Spectrometer (IGRINS) on the 2.7 m telescope at the McDonald Observatory. IGRINS has high spectral resolution ($R \sim 45000$) and instantaneous broad wavelength coverage (1.45–2.45 μm), enabling us to detect 87 emission lines from rovibrationally excited molecular hydrogen (H_2) that arise from transitions out of 69 upper rovibration levels of the electronic ground state. These levels cover a large range of rotational and vibrational quantum numbers and excitation energies, making them excellent probes of the excitation mechanisms of H_2 and physical conditions within the PDR. The Orion Bar PDR is thought to consist of cooler high density clumps or filaments (T = 50 to 250 K, $n_H = 10^5$ to 10^7 cm^{-3}) embedded in a warmer lower density medium (T = 250 to 1000 K, $n_H = 10^4$ to 10^5 cm^{-3}). We fit a grid of constant temperature and density Cloudy models, which recreate the observed H_2 level populations well, to constrain the temperature to a range of 600 to 650 K and the density to $n_H = 2.5 \times 10^3$ to 10^4 cm^{-3}. The best-fit model gives T = 625 K and $n_H = 5 \times 10^3$ cm^{-3}. This well-constrained warm temperature is consistent with kinetic temperatures found by other studies for the Orion Bar's lower density medium. However, the range of densities well fit by the model grid is marginally lower than those reported by other studies. We could be observing lower density gas than the surrounding medium, or perhaps a density-sensitive parameter in our models is not properly estimated.

2.1 Introduction

Interstellar PDRs are often found in star forming regions where molecular clouds are exposed to UV radiation from newly formed hot massive stars. At a distance

of $\sim 400 - 500$ pc (Schlafly et al., 2014), the Orion Nebula is the nearest example of high-mass star formation, and it serves as an archetype for more distant star forming regions found elsewhere in the Milky Way and in starburst galaxies. The optically visible part of the Orion Nebula is an H II region where the massive OB stars that make up the θ^1 or Trapezium cluster have ionized the adjacent gas and carved out a blister or cavity shaped region on the surface of the Orion Molecular Cloud (Zuckerman, 1973; Genzel & Stutzki, 1989; O'Dell, 2001; O'Dell et al., 2009). The UV radiation field generated by the Trapezium cluster is fairly well constrained (Ferland et al., 2012), with the O7V star θ^1 Ori C contributing most of the UV photons.

The southeastern edge of the blister is a dense PDR called the "Orion Bar," viewed nearly edge on (Tielens et al., 1993; Walmsley et al., 2000; Pellegrini et al., 2009). The H_2 emission from its dissociation front is bright and has been well studied. The first observations of the H_2 emission (e.g., Hayashi et al. 1985; Gatley & Kaifu 1987) found intermediate rovibrational level populations that they interpreted as a combination of UV and shock excitation in the H_2. Later studies by Hippelein & Müench (1989), Burton et al. (1990a) and Parmar et al. (1991) found that the H_2 line widths in the bar are narrow, with Local Standard of Rest (LSR) radial velocities matching the ambient molecular cloud, and therefore inconsistent with shocks, which typically exhibit significant lateral motion (e.g.. such as observed in Orion KL by Oh et al. 2016b). Hippelein & Müench (1989), Burton et al. (1990a), Parmar et al. (1991), and Luhman et al. (1998) suggested instead that the emission arises from collisionally modified UV-excited H_2.

The large spatial scale of the Orion Bar of ~ 0.5 pc long suggests that it is supported in a state of quasi-hydrostatic equilibrium by magnetic pressure that counteracts the winds and radiation pressure from the Trapezium stars (Pellegrini et al., 2009; Shaw et al., 2009). Others, such as Parmar et al. (1991), Goicoechea et al. (2016), and Salgado et al. (2016), argue that the Orion Bar is not in hydrostatic equilibrium but instead represents a slow moving (< 4 km s^{-1}) magnetohydrodynamic shock front of swept-up molecular material supported by a strong compressed magnetic field. Observations of the Orion Bar find complex molecules in the far-IR, sub-millimeter, and radio (Danby et al., 1988; Simon et al., 1997; Young Owl et al., 2000; Batrla & Wilson, 2003; Lis & Schilke, 2003; Parise et al., 2009; Goicoechea et al., 2011, 2016) that are tracers of relatively cool dense gas ($T = 50$ to 250 K, $n_H = 10^5$

to 10^7 cm^{-3}). Observations of the collisionally excited pure rotational ($v = 0$) lines of H_2 (Parmar et al., 1991; Allers et al., 2005; Shaw et al., 2009), ions such as C^+ (Tielens et al., 1993; Tauber et al., 1994; Wyrowski et al., 1997), and excited molecules that only form in the presence of rovibrationally excited H_2 (Nagy et al., 2013) trace warmer lower density gas (T = 250 to 1000 K, $n_H = 10^4$ to 10^5 cm^{-3}). The general consensus is that the Orion Bar PDR does not consist of a single homogenous slab of gas, but instead is composed of cooler dense molecular clumps or filaments embedded in a warmer lower density medium (Burton et al., 1990b; Parmar et al., 1991; Meixner & Tielens, 1993; Andree-Labsch et al., 2017). However, some have argued against the presence of dense clumps near the dissociation front where the H_2 emission is strongest (Marconi et al., 1998; Allers et al., 2005). These observations find that the Orion Bar gas is warmer than models predict, suggesting that an extra heating mechanism, not yet identified, is present. Several candidate heating mechanisms have been proposed including an enhanced flux of cosmic rays trapped by a strong magnetic field (Pellegrini et al., 2007, 2009; Shaw et al., 2009), a larger than expected number of photoelectrons from grains (Allers et al., 2005), X-rays emitted by young stars in the Orion Nebula (Shaw et al., 2009), or collisional de-excitation of formation pumped H_2 (Le Bourlot et al., 2012).

In this chapter, we use H_2 to probe the physical conditions and processes in the zone of the Orion Bar dissociation front. Chapter 2.2 describes our deep near-IR spectrum of the Orion Bar, taken at the location of the peak H_2 surface brightness, with IGRINS. Our spectrum contains a larger number of H_2 rovibrational transition emission lines observed at higher spectral resolution than all previous near-IR studies of the Orion Bar. All the lines are observed simultaneously through the same slit and cover a wide range of H_2 upper vibrational states from v = 1 to 11 with level energies up to 50,000 K above the ground state ($v = 0,\ J = 0$). This gives us an excellent handle on the excitation mechanisms of the H_2. In Chapter 2.4, we compare the observed H_2 rovibrational level populations to those predicted by Cloudy models (Shaw et al., 2005; Ferland et al., 2013), to check whether we can match the observed level populations in the Orion Bar, determine which models provide the best match, and discuss the implications of the temperature and density of the H_2 emitting gas derived from the model fits. We present our summary and conclusions in Chapter 2.5.

2.2 Observations

The data were taken with IGRINS on the 2.7 m Harlan J. Smith Telescope at the McDonald Observatory on the night of 2014 October 24 UT. Dark and flat calibration frames were taken with the internal IGRINS calibration unit at the beginning of the night. IGRINS was rotated at the Cassegrain focus to set the slit position angle (PA) on the sky to 135° counterclockwise from north, perpendicular to the dissociation front. Pointing and tracking were performed with the IGRINS slit-viewing camera, which images a $\sim 2' \times 3'$ field surrounding the slit in the K band every 10 s. We used the nearby star V1501 Ori at $05^h35^m15\overset{s}{.}55$, -05°24′14″.0 (J2000) for offslit guiding. The center of the slit was positioned at $05^h35^m19\overset{s}{.}73$, -05°25′26″.7 (J2000), within the maps from Allers et al. (2005). Figure 2.1 shows the finder chart and the IGRINS slit position and angle superposed on the Orion Bar. We took three 10 minute exposures on the target and three 10 minute exposures on the sky (30′ south and 30′ west of the target). The sky exposures were used to subtract various backgrounds such as telluric OH emission, H_2O emission, thermal emission, bias signal, and dark current. For telluric correction and relative flux calibration, we observed the A0V star HD 34317 with four exposures of 60 s each, nodding the star between two positions along the slit, around the same airmass and time we observed the Orion Bar. We subtracted one nod position from the other to remove sky and background while preserving the signal at each position.

The data are reduced, calibrated, and line fluxes extracted as described in Chapters 1.3 and 1.4. The H_2 rovibrational level populations are calculated as described in Chapter 1.5.1. Figure 2.2 shows example 1D and 2D PV maps for a selection of H_2 rovibrational transitions observed in the Orion Bar. Table 2.1 gives the fluxes for all lines with S/N > 3.

2.2.1 Effects of Dust Extinction

The dense molecular gas of the Orion Bar co-exists with copious amounts of dust. If there is enough dust in the foreground of the observed H_2 emission, the differential extinction across the H and K bands could be significant enough to affect the line ratios we use to derive the rovibrational level populations. An effective way to measure extinction is to compare the observed to theoretical line flux ratios from pairs

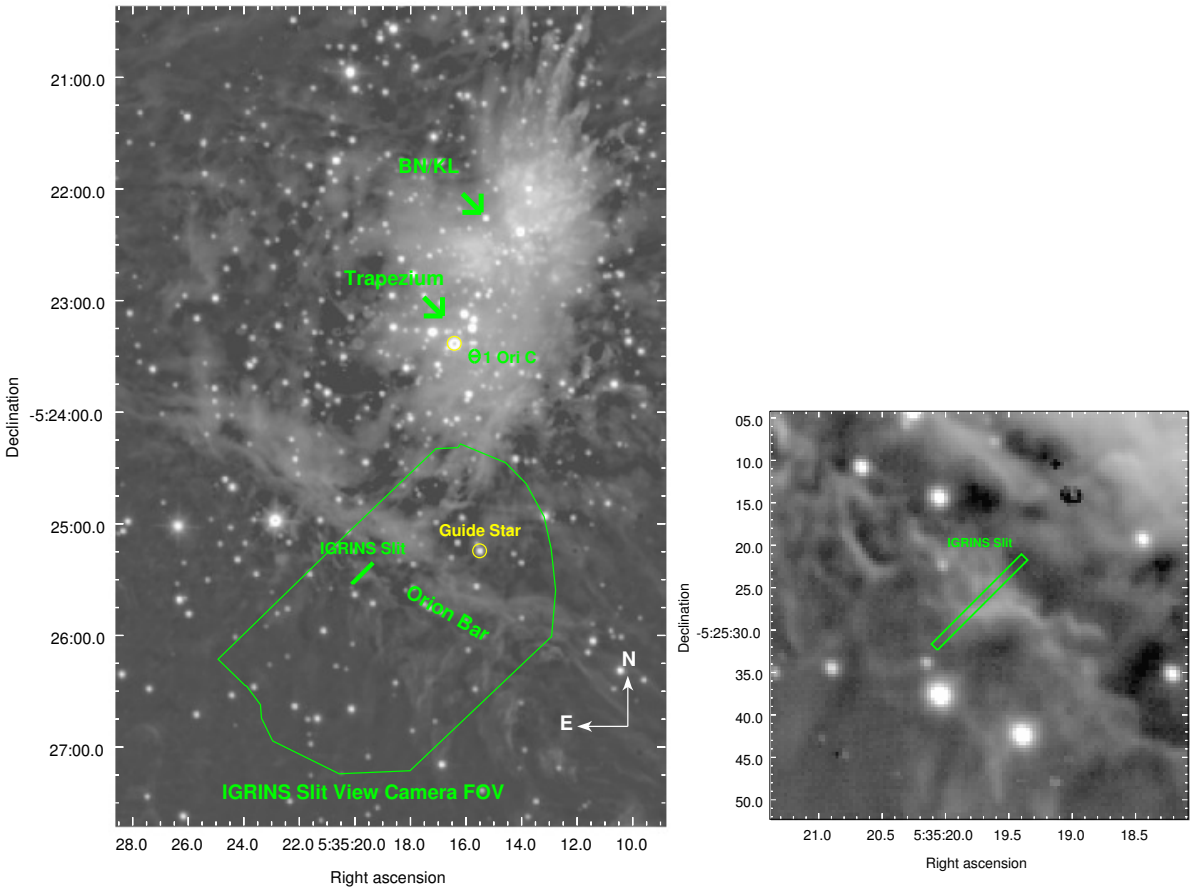

Figure 2.1: Left: finder chart showing the location of our pointing on the Orion Bar (slit to scale centered on $05^h35^m19\overset{s}{.}73$, -05°25′26″.7, J2000), the guide star V1501 Ori ($5^h35^m15\overset{s}{.}55$, -05°24′14″.0, J2000), the FOV of the IGRINS slit-viewing camera, and various features of the Orion Nebula including the Orion Bar, the Trapezium Cluster, Orion BN/KL, and the O-star θ^1 C, which is the primary source of UV photons interacting with the Orion Bar. IGRINS was rotated to slit PA 135° counterclockwise from the north. This narrow-band image of the H_2 1-0 S(1) line at 2.12183 μm used for the finder chart is from the Database of Near-IR Narrow-band WFCAM Images for Star Formation hosted by the JAC: `http://www.ukirt.hawaii.edu/TAP/singles.html`. The image was taken with WFCAM on UKIRT by Davis et al. (2009). This narrow-band H_2 image is not continuum subtracted, and thus it includes scattered starlight and other possible continuum sources such as bound-free emission. Right: zoomed-in view of the slit position.

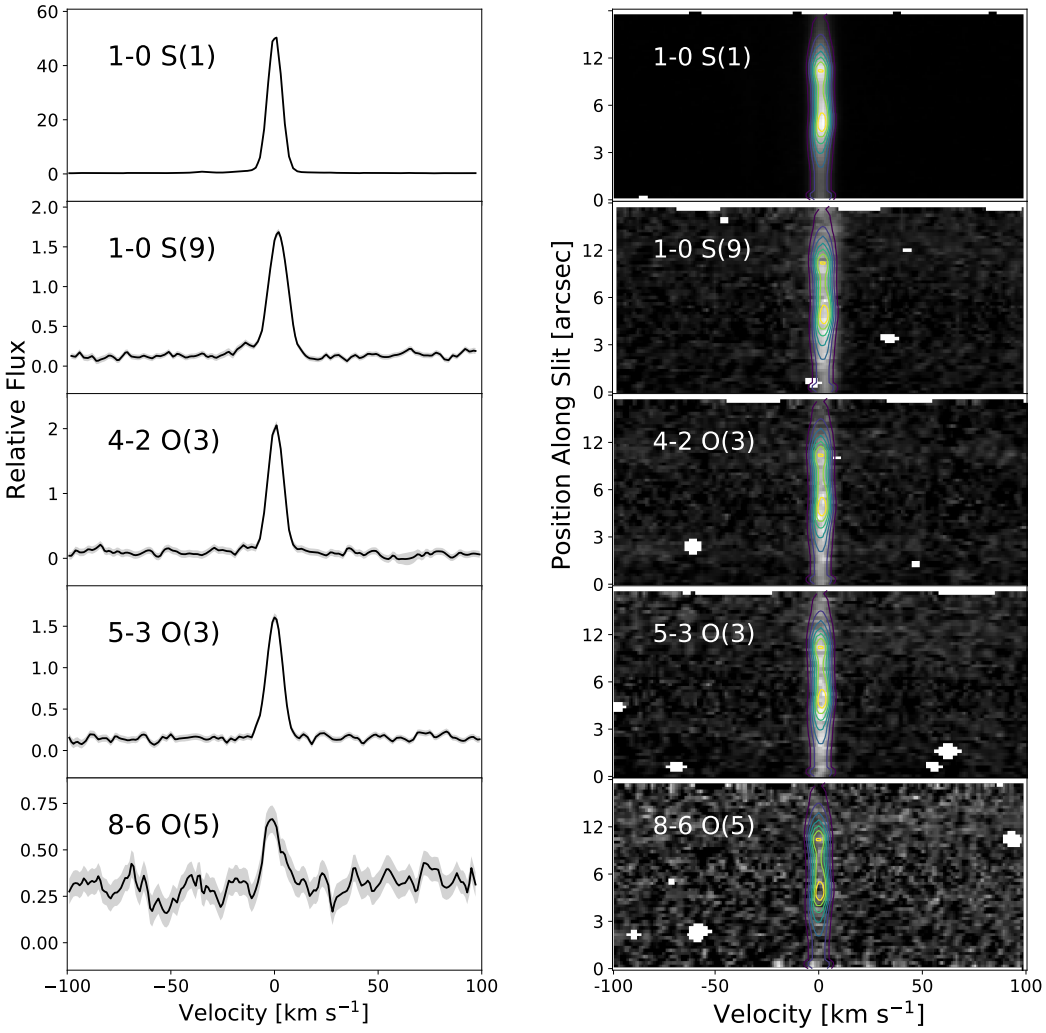

Figure 2.2: One-dimensional H_2 rovibrational line profiles (left) and two-dimensional PV diagrams (right) from the Orion Bar for the 1-0 S(1), 1-0 S(9), 4-2 O(3), 5-3 O(3), and 8-6 O(5) transitions, which arise from a range of upper v and J states. The dotted lines and light gray shading in the 1D line profiles shows the 1σ statistical uncertainty. The 2D color contours show the weights used to extract the flux for each line, as defined in Equations 1.1 and 1.2. The white spots on the 2D PV diagrams are masked cosmic rays.

Table 2.1: H_2 lines observed in the Orion Bar

$\lambda_{\rm vacuum}$ (μm) (1)	$\Delta\lambda$ (10^{-6} μm) (2)	H_2 line ID (3)	$\log_{10}(F_i/F_r)$ (4)	S/N (5)	v_u (6)	J_u (7)	E_u/k (K) (8)	$\log_{10}(A_{ul})$ [$\log_{10}(s^{-1})$] (9)	$\ln\left(\frac{N_u}{g_u}/\frac{N_r}{g_r}\right)$ (10)	N_u/N_m (11)
2.406592	0.95	1-0 Q(1)	$1.273^{+0.001}_{-0.001}$	817.4	1	1	6149	-6.37	$3.982^{+0.001}_{-0.001}$	0.60
2.413439	1.67	1-0 Q(2)	$0.762^{+0.001}_{-0.001}$	399.7	1	2	6471	-6.52	$3.743^{+0.002}_{-0.003}$	0.81
2.223290	0.72	1-0 S(0)	$0.731^{+0.001}_{-0.001}$	580.0	1	2	6471	-6.60	$3.771^{+0.002}_{-0.002}$	0.83
2.423730	5.72	1-0 Q(3)	$1.022^{+0.001}_{-0.001}$	488.6	1	3	6951	-6.56	$2.996^{+0.002}_{-0.002}$	0.86
2.121834	0.00	1-0 S(1)	$1.193^{+0.000}_{-0.000}$	1031.9	1	3	6951	-6.46	$3.035^{+0.001}_{-0.001}$	0.90
2.437489	0.00	1-0 Q(4)	$0.417^{+0.002}_{-0.002}$	225.6	1	4	7584	-6.58	$2.504^{+0.004}_{-0.004}$	1.36
2.033758	-0.72	1-0 S(2)	$0.643^{+0.001}_{-0.001}$	422.1	1	4	7584	-6.40	$2.436^{+0.002}_{-0.002}$	1.27
1.957559	-2.62	1-0 S(3)	$0.959^{+0.001}_{-0.001}$	339.8	1	5	8365	-6.38	$1.772^{+0.003}_{-0.003}$	1.73
1.788050	-21.46	1-0 S(6)	$-0.091^{+0.005}_{-0.006}$	78.8	1	8	11521	-6.45	$0.099^{+0.013}_{-0.013}$	0.60
1.747955	-2.86	1-0 S(7)	$0.285^{+0.003}_{-0.003}$	132.7	1	9	12817	-6.53	$-0.096^{+0.008}_{-0.008}$	0.67
1.714738	-2.26	1-0 S(8)	$-0.435^{+0.015}_{-0.015}$	29.2	1	10	14220	-6.63	$-0.532^{+0.034}_{-0.035}$	0.40
1.687761	-3.93	1-0 S(9)	$-0.202^{+0.005}_{-0.005}$	89.3	1	11	15721	-6.78	$-0.869^{+0.011}_{-0.011}$	0.43
1.666475	-1.67	1-0 S(10)	$-1.029^{+0.031}_{-0.034}$	13.4	1	12	17311	-6.98	$-1.306^{+0.072}_{-0.078}$	0.32
1.650413	0.60	1-0 S(11)	$-1.021^{+0.027}_{-0.029}$	15.4	1	13	18979	-7.27	$-1.789^{+0.063}_{-0.067}$	0.30
2.355605	-2.38	2-1 S(0)	$0.000^{+0.004}_{-0.004}$	97.8	2	2	12095	-6.43	$1.769^{+0.010}_{-0.010}$	1.92
2.247716	1.67	2-1 S(1)	$0.465^{+0.001}_{-0.001}$	376.5	2	3	12550	-6.30	$1.057^{+0.003}_{-0.003}$	1.71
2.154216	-1.43	2-1 S(2)	$-0.012^{+0.003}_{-0.003}$	159.3	2	4	13150	-6.25	$0.645^{+0.006}_{-0.006}$	1.30
2.073482	0.00	2-1 S(3)	$0.408^{+0.001}_{-0.001}$	323.5	2	5	13890	-6.24	$0.244^{+0.003}_{-0.003}$	1.73
1.679641	9.66	2-0 O(9)	$-1.421^{+0.060}_{-0.069}$	6.8	2	7	15763	-7.89	$-0.692^{+0.137}_{-0.159}$	1.18
1.522033	-0.60	3-1 O(5)	$-0.235^{+0.009}_{-0.009}$	46.6	3	3	17818	-6.70	$-0.025^{+0.021}_{-0.022}$	1.18
2.386471	-3.10	3-2 S(1)	$-0.006^{+0.006}_{-0.006}$	68.0	3	3	17818	-6.29	$-0.004^{+0.015}_{-0.015}$	1.21
1.581171	1.55	3-1 O(6)	$-0.837^{+0.027}_{-0.029}$	15.6	3	4	18386	-6.86	$-0.163^{+0.062}_{-0.066}$	1.18
2.287045	0.72	3-2 S(2)	$-0.392^{+0.006}_{-0.006}$	72.9	3	4	18386	-6.25	$-0.181^{+0.014}_{-0.014}$	1.16

Continued on next page...

Table 2.1 continued: H_2 lines observed in the Orion Bar

$\lambda_{\rm vacuum}$ (μm) (1)	$\Delta\lambda$ (10^{-6} μm) (2)	H_2 line ID (3)	$\log_{10}(F_i/F_r)$ (4)	S/N (5)	v_u (6)	J_u (7)	E_u/k (K) (8)	$\log_{10}(A_{ul})$ [$\log_{10}(s^{-1})$] (9)	$\ln\left(\frac{N_u}{g_u}/\frac{N_r}{g_r}\right)$ (10)	N_u/N_m (11)
2.201399	0.72	3-2 S(3)	$-0.013^{+0.003}_{-0.003}$	150.1	3	5	19086	-6.25	$-0.645^{+0.007}_{-0.007}$	1.55
2.128015	1.43	3-2 S(4)	$-0.508^{+0.006}_{-0.006}$	69.3	3	6	19911	-6.28	$-0.813^{+0.014}_{-0.015}$	1.49
2.065584	1.43	3-2 S(5)	$-0.181^{+0.004}_{-0.004}$	100.1	3	7	20856	-6.34	$-1.182^{+0.010}_{-0.010}$	1.95
1.509865	0.00	4-2 O(3)	$0.000^{+0.006}_{-0.006}$	70.1	4	1	22079	-6.11	$0.000^{+0.014}_{-0.014}$	1.00
1.563515	1.07	4-2 O(4)	$-0.489^{+0.010}_{-0.010}$	43.8	4	2	22352	-6.29	$-0.107^{+0.023}_{-0.023}$	1.00
1.622299	-2.74	4-2 O(5)	$-0.328^{+0.009}_{-0.009}$	47.4	4	3	22759	-6.44	$-0.791^{+0.021}_{-0.021}$	0.92
1.686462	2.26	4-2 O(6)	$-1.045^{+0.033}_{-0.036}$	12.7	4	4	23295	-6.58	$-1.224^{+0.076}_{-0.082}$	0.71
1.756281	0.00	4-2 O(7)	$-0.754^{+0.014}_{-0.014}$	30.6	4	5	23955	-6.73	$-1.475^{+0.032}_{-0.033}$	1.20
2.266764	2.15	4-3 S(4)	$-1.007^{+0.040}_{-0.044}$	10.5	4	6	24733	-6.39	$-1.637^{+0.091}_{-0.100}$	1.07
2.200974	0.72	4-3 S(5)	$-0.690^{+0.012}_{-0.012}$	35.7	4	7	25623	-6.49	$-1.957^{+0.028}_{-0.028}$	1.59
2.145873	-0.72	4-3 S(6)	$-1.322^{+0.042}_{-0.047}$	9.8	4	8	26616	-6.64	$-2.124^{+0.097}_{-0.108}$	1.03
2.099586	5.48	4-2 O(11)	$-1.647^{+0.084}_{-0.104}$	4.7	4	9	27706	-7.36	$-2.449^{+0.193}_{-0.239}$	1.45
2.100426	4.29	4-3 S(7)	$-1.192^{+0.030}_{-0.033}$	13.8	4	9	27706	-6.86	$-2.542^{+0.070}_{-0.075}$	1.33
1.549455	-2.62	4-2 Q(11)	$-0.819^{+0.022}_{-0.023}$	19.6	4	11	30139	-6.34	$-3.372^{+0.050}_{-0.052}$	0.72
1.560736	-1.55	5-3 O(2)	$-0.509^{+0.012}_{-0.012}$	35.8	5	0	26606	-5.65	$-0.020^{+0.028}_{-0.028}$	1.30
1.613520	1.55	5-3 O(3)	$-0.211^{+0.007}_{-0.007}$	64.9	5	1	26735	-5.95	$-0.787^{+0.015}_{-0.016}$	0.76
1.671814	8.94	5-3 O(4)	$-0.671^{+0.016}_{-0.016}$	27.3	5	2	26992	-6.12	$-0.846^{+0.036}_{-0.037}$	0.77
1.515792	-5.01	5-3 Q(4)	$-0.614^{+0.021}_{-0.022}$	20.1	5	4	27878	-6.13	$-1.367^{+0.049}_{-0.051}$	0.98
1.528648	1.07	5-3 Q(5)	$-0.320^{+0.013}_{-0.013}$	34.1	5	5	28498	-6.14	$-1.954^{+0.029}_{-0.030}$	1.30
2.057127	-4.77	5-3 O(9)	$-1.313^{+0.055}_{-0.063}$	7.4	5	7	30063	-6.81	$-2.727^{+0.127}_{-0.146}$	1.27
1.562635	-2.03	5-3 Q(7)	$-0.552^{+0.012}_{-0.012}$	36.9	5	7	30063	-6.17	$-2.728^{+0.027}_{-0.027}$	1.27
1.608398	-5.36	5-3 Q(9)	$-0.628^{+0.015}_{-0.015}$	29.3	5	9	32014	-6.19	$-3.053^{+0.034}_{-0.035}$	1.46
1.675032	1.55	6-4 O(2)	$-0.747^{+0.014}_{-0.015}$	29.6	6	0	30942	-5.55	$-0.709^{+0.033}_{-0.034}$	1.04

Continued on next page...

Table 2.1 continued: H_2 lines observed in the Orion Bar

$\lambda_{\rm vacuum}$ (μm) (1)	$\Delta\lambda$ (10^{-6} μm) (2)	H_2 line ID (3)	$\log_{10}(F_i/F_r)$ (4)	S/N (5)	v_u (6)	J_u (7)	E_u/k (K) (8)	$\log_{10}(A_{ul})$ [$\log_{10}(s^{-1})$] (9)	$\ln\left(\frac{N_u}{g_u}/\frac{N_r}{g_r}\right)$ (10)	N_u/N_m (11)
1.601534	-4.29	6-4 Q(1)	$-0.348^{+0.009}_{-0.009}$	49.0	6	1	31063	-5.85	$-1.339^{+0.020}_{-0.021}$	0.74
1.732641	-0.60	6-4 O(3)	$-0.388^{+0.012}_{-0.012}$	37.0	6	1	31063	-5.85	$-1.354^{+0.027}_{-0.027}$	0.73
1.536891	0.60	6-4 S(0)	$-0.706^{+0.018}_{-0.019}$	23.4	6	2	31303	-6.08	$-1.091^{+0.042}_{-0.044}$	0.90
1.607390	-1.67	6-4 Q(2)	$-0.665^{+0.014}_{-0.015}$	29.6	6	2	31303	-6.00	$-1.134^{+0.033}_{-0.034}$	0.86
1.796524	0.60	6-4 O(4)	$-0.734^{+0.023}_{-0.025}$	18.2	6	2	31303	-6.01	$-1.169^{+0.054}_{-0.057}$	0.83
1.501560	2.03	6-4 S(1)	$-0.270^{+0.010}_{-0.011}$	41.3	6	3	31661	-5.94	$-1.872^{+0.024}_{-0.024}$	0.95
1.616224	-1.67	6-4 Q(3)	$-0.468^{+0.008}_{-0.009}$	50.7	6	3	31661	-6.04	$-2.031^{+0.020}_{-0.020}$	0.81
1.628094	-0.60	6-4 Q(4)	$-0.929^{+0.025}_{-0.026}$	17.1	6	4	32132	-6.06	$-2.197^{+0.057}_{-0.060}$	0.73
2.029684	-3.34	6-4 O(7)	$-0.998^{+0.022}_{-0.023}$	19.4	6	5	32711	-6.39	$-2.659^{+0.050}_{-0.053}$	1.02
1.661304	4.41	6-4 Q(6)	$-1.105^{+0.029}_{-0.031}$	14.3	6	6	33394	-6.08	$-2.889^{+0.067}_{-0.072}$	0.85
1.708041	4.53	6-4 Q(8)	$-1.244^{+0.040}_{-0.044}$	10.4	6	8	35040	-6.11	$-3.383^{+0.091}_{-0.101}$	0.87
1.728799	0.00	7-5 Q(1)	$-0.506^{+0.013}_{-0.013}$	33.6	7	1	35057	-5.82	$-1.702^{+0.029}_{-0.030}$	0.78
1.735762	4.17	7-5 Q(2)	$-1.032^{+0.030}_{-0.032}$	14.1	7	2	35281	-5.97	$-1.975^{+0.069}_{-0.074}$	0.51
1.746280	-1.79	7-5 Q(3)	$-0.670^{+0.020}_{-0.021}$	21.7	7	3	35613	-6.01	$-2.488^{+0.045}_{-0.047}$	0.77
1.620548	1.55	7-5 S(1)	$-0.539^{+0.010}_{-0.010}$	44.8	7	3	35613	-5.93	$-2.438^{+0.022}_{-0.023}$	0.81
1.760446	-4.05	7-5 Q(4)	$-1.097^{+0.034}_{-0.037}$	12.3	7	4	36051	-6.03	$-2.571^{+0.078}_{-0.085}$	0.82
2.204989	-0.72	7-5 O(7)	$-1.182^{+0.033}_{-0.036}$	12.7	7	5	36588	-6.31	$-3.188^{+0.076}_{-0.082}$	0.87
1.561510	-1.55	7-5 S(3)	$-0.607^{+0.014}_{-0.014}$	30.8	7	5	36588	-5.86	$-3.250^{+0.032}_{-0.033}$	0.82
1.540006	-6.68	7-5 S(4)	$-1.069^{+0.043}_{-0.048}$	9.6	7	6	37220	-5.87	$-3.382^{+0.100}_{-0.111}$	0.72
1.523623	-0.95	7-5 S(5)	$-0.717^{+0.023}_{-0.024}$	18.7	7	7	37941	-5.89	$-3.758^{+0.052}_{-0.055}$	1.05
1.512240	2.50	7-5 S(6)	$-1.251^{+0.073}_{-0.088}$	5.4	7	8	38743	-5.95	$-3.902^{+0.169}_{-0.203}$	0.74
1.979270	-1.31	7-5 Q(11)	$-1.361^{+0.058}_{-0.066}$	7.0	7	11	41558	-6.18	$-4.739^{+0.133}_{-0.153}$	0.92
2.092904	7.63	7-5 Q(13)	$-1.576^{+0.059}_{-0.068}$	6.9	7	13	43693	-6.26	$-5.154^{+0.136}_{-0.157}$	0.85

Continued on next page...

Table 2.1 continued: H_2 lines observed in the Orion Bar

$\lambda_{\rm vacuum}$ (μm) (1)	$\Delta\lambda$ (10^{-6} μm) (2)	H_2 line ID (3)	$\log_{10}(F_i/F_r)$ (4)	S/N (5)	v_u (6)	J_u (7)	E_u/k (K) (8)	$\log_{10}(A_{ul})$ [$\log_{10}(s^{-1})$] (9)	$\ln\left(\frac{N_u}{g_u}/\frac{N_r}{g_r}\right)$ (10)	N_u/N_m (11)
2.041830	2.62	8-6 O(3)	$-0.684^{+0.012}_{-0.012}$	35.3	8	1	38708	-5.80	$-2.005^{+0.028}_{-0.029}$	0.83
2.210763	2.15	8-6 O(5)	$-0.993^{+0.034}_{-0.037}$	12.1	8	3	39219	-6.05	$-2.888^{+0.079}_{-0.086}$	0.56
1.763952	-4.05	8-6 S(1)	$-0.864^{+0.040}_{-0.044}$	10.4	8	3	39219	-5.97	$-3.003^{+0.092}_{-0.101}$	0.50
2.310167	1.67	8-6 O(6)	$-1.529^{+0.091}_{-0.116}$	4.3	8	4	39622	-6.17	$-2.971^{+0.210}_{-0.266}$	0.54
1.701803	-6.79	8-6 S(3)	$-1.014^{+0.031}_{-0.033}$	13.5	8	5	40116	-5.93	$-3.935^{+0.072}_{-0.077}$	0.52
1.664584	2.15	8-6 S(5)	$-1.169^{+0.035}_{-0.038}$	11.9	8	7	41355	-6.01	$-4.441^{+0.081}_{-0.088}$	0.76
2.172715	-1.43	9-7 O(2)	$-1.280^{+0.042}_{-0.046}$	9.9	9	0	41903	-5.57	$-1.645^{+0.096}_{-0.106}$	0.82
2.073187	-1.43	9-7 Q(1)	$-1.088^{+0.036}_{-0.039}$	11.6	9	1	41997	-5.91	$-2.661^{+0.082}_{-0.090}$	0.93
2.253724	1.67	9-7 O(3)	$-0.969^{+0.027}_{-0.029}$	15.4	9	1	41997	-5.85	$-2.451^{+0.063}_{-0.067}$	1.15
2.345581	-8.58	9-7 O(4)	$-1.406^{+0.069}_{-0.082}$	5.8	9	2	42185	-5.98	$-2.518^{+0.159}_{-0.188}$	0.51
1.987350	-4.05	9-7 S(0)	$-1.401^{+0.052}_{-0.059}$	7.9	9	2	42185	-6.18	$-2.204^{+0.119}_{-0.135}$	0.70
2.084098	9.06	9-7 Q(2)	$-1.258^{+0.065}_{-0.076}$	6.2	9	2	42185	-6.06	$-2.103^{+0.149}_{-0.175}$	0.77
2.100664	3.58	9-7 Q(3)	$-1.237^{+0.031}_{-0.033}$	13.7	9	3	42462	-6.11	$-3.385^{+0.071}_{-0.076}$	0.60
2.151876	3.58	9-7 Q(5)	$-1.362^{+0.038}_{-0.042}$	10.8	9	5	43274	-6.16	$-3.971^{+0.088}_{-0.097}$	0.69
2.230268	-4.53	9-7 Q(7)	$-1.558^{+0.073}_{-0.088}$	5.5	9	7	44392	-6.23	$-4.545^{+0.168}_{-0.203}$	0.90
1.548849	0.60	10-7 O(3)	$-1.054^{+0.050}_{-0.056}$	8.2	10	1	44903	-5.98	$-2.722^{+0.115}_{-0.130}$	0.79
2.176855	1.67	10-8 S(1)	$-1.388^{+0.042}_{-0.046}$	9.9	10	3	45317	-6.27	$-3.314^{+0.096}_{-0.106}$	0.93
1.648305	-1.67	10-7 O(5)	$-1.273^{+0.044}_{-0.049}$	9.3	10	3	45317	-6.29	$-3.282^{+0.102}_{-0.114}$	0.97

Continued on next page...

Table 2.1 continued: H_2 lines observed in the Orion Bar

$\lambda_{\rm vacuum}$ (μm)	$\Delta\lambda$ (10^{-6} μm)	H_2 line ID	$\log_{10}(F_i/F_r)$	S/N	v_u	J_u	E_u/k (K)	$\log_{10}(A_{ul})$ [$\log_{10}(s^{-1})$]	$\ln\left(\frac{N_u}{g_u}/\frac{N_r}{g_r}\right)$	N_u/N_m
(1)	(2)	(3)	(4)	(5)	(6)	(7)	(8)	(9)	(10)	(11)

Columns are as follows. (1) The H_2 line vacuum wavelength in μm calculated from the ground electronic state rovibrational energy levels in Komasa et al. (2011). (2) The observed line centroid wavelength (in the Orion Bar rest frame) minus the expected theoretical line wavelength calculated from the level energies in Komasa et al. (2011) in units of $10^{-6}\mu$m. (3) H_2 line rovibrational identifications in spectroscopic notation in the format "W-X Y(Z)." W and X denote the transition's upper and lower v states. Y denotes the change in J, where S is $\Delta J = -2$, Q is $\Delta J = 0$, and O is $\Delta J = +2$. Z denotes the upper J state. (4) The base 10 logarithm of the line flux F_i normalized to the 4-2 O(3) reference line flux F_r. The uncertainty quoted is the statistical noise. (5) The signal-to-noise ratio for the line flux. (6) The transition's upper vibrational state. (7) The transition's upper rotational state. (8) The energy of the upper state E_u above the ground ($v = 0$, $J = 0$) divided by the Boltzmann constant k to convert the energies into temperature units. (9) The base 10 logarithm of the rovibrational radiative transition probability A_{ul} from Wolniewicz et al. (1998), in units of s^{-1} . (10) The natural logarithm of the column density in a transition's upper state N_u divided by the quantum degeneracy g_u, normalized to N_r/g_r for the reference line 4-2 O(3). This is the value plotted in the excitation diagram shown in Figure 2.3. The uncertainty quoted is based on the statistical noise. (11) The ratio of the observed column density of the transition's upper state N_u to the column density predicted by our best-fit model N_m, as shown in the bottom of Figure 2.3.

of lines arising from the same upper level that are widely separated in wavelength. Two such line pairs in our data with sufficient S/N and wide separation in wavelength are the 3-1 O(5)/3-2 S(1) transitions spanning $\lambda = 1.55220 - 2.238645$ μm and the 3-1 O(6)/3-2 S(2) transitions spanning $\lambda = 1.58115 - 2.28703$ μm. Assuming the near-IR extinction law from Rieke & Lebofsky (1985), the observed 3-1 O(5)/3-2 S(1) and 3-1 O(6)/3-2 S(2) line ratios give extinctions of $A_V = 8.50$ and 8.00 mag respectively (or $A_K = 0.99$ and 0.93 mag). We therefore apply an extinction correction of $A_V = 8.25$ or $A_K = 0.96$ to our spectrum before extracting line fluxes. This value of the extinction is consistent with the foreground extinction of $A_V \sim 1.3$ mag or $A_K \sim 0.15$ mag towards the ionized gas (Weilbacher et al., 2015), allowing for additional extinction between the ionized gas and the region of excited H_2. Our value for extinction in the Bar is lower than the values of $A_K = 2.3 \pm 0.8$ mag and 2.6 ± 0.7 mag for two regions in the Bar $\sim 22''$ NE of the slit measured by Luhman et al. (1998). However, it is possible that the extinction is variable depending on the chosen sightline, and that the bright H_2 emitting region we targeted is a sightline with lower extinction.

2.3 H_2 Level Populations

We calculate the H_2 rovibrational level populations using the techniques described in Chapter 1.5.1. In the Orion Bar, we measure relative fluxes and calculate level populations for 87 lines with S/N > 3, yielding the relative N_u values reported in Table 2.1 which arise from 69 independent rovibrational states with excitation energies up to $E_u/k = 50{,}000$ K above the ground ($v = 0,\ J = 0$) state. These values are normalized to the population of the $v = 4,\ J = 1$ level, which is taken to be the reference level r, giving N_r and g_r. We selected $v = 4,\ J = 1$ to be the reference level because it is primarily excited by UV photons and its population is derived from the bright 4-2 O(3) line. The top panel of Figure 2.3 shows the excitation diagram for the relative H_2 rovibrational level column densities (or level populations) we observe in the Orion Bar.

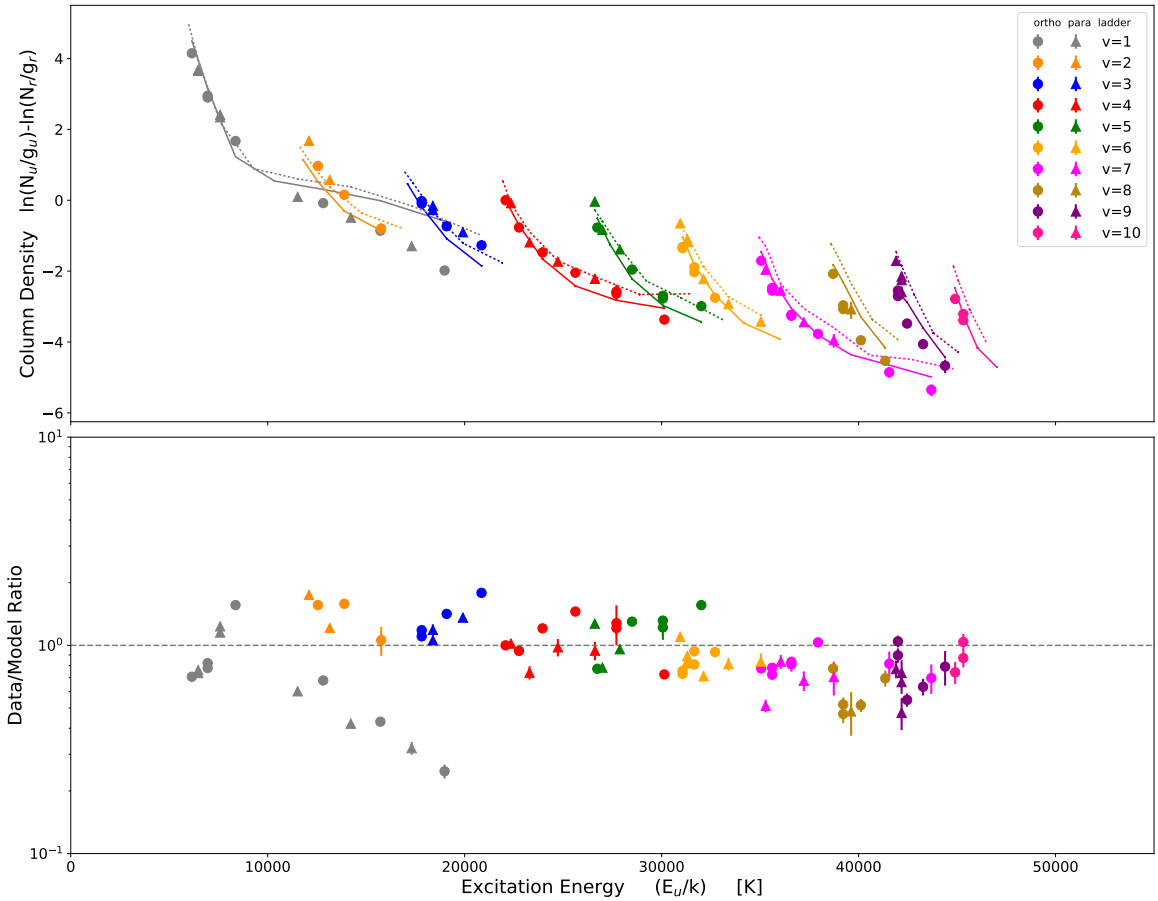

Figure 2.3: Top: excitation diagram showing observed H_2 rovibrational level populations in the Orion Bar as the data-points vs. energy above the ground rovibrational ($v = 0$, $J = 0$) state. Our best-fit constant density and temperature ($n_H = 5 \times 10^3$ cm^{-3} and $T = 625$ K) Cloudy model is shown by colored lines. The error bars represent the 1σ statistical uncertainty, and in most cases the symbols are larger than the error bars. The solid lines are the model fit for the ortho levels, and the dotted lines are for the para levels. Both data and model predictions are normalized to the reference 4-2 O(3) line arising from the $v = 4$, $J = 1$ state, identified by N_r and g_r for the column density and quantum degeneracy respectively. A purely isothermal gas would form a straight line on this diagram, while non-thermal mechanisms produce different patterns. The sawtooth pattern is characteristic of UV excitation. In warm and/or dense gas, as seen here for the Orion Bar, collisions modify the level populations from the UV-excited case. Bottom: the observed Orion Bar H_2 rovibrational level populations divided by the Cloudy model, showing how well the model fits the data. The dashed line denotes a ratio of unity for which the data and model would be in perfect agreement.

2.4 Modeling and Interpretation

Our large dataset allows us to test our understanding of the physics in the Orion Bar by comparing the observed H_2 rovibrational level populations to model predictions.

2.4.1 Constant Temperature and Density Cloudy Models

2.4.1.1 Description of the Model Grid

While constant temperature and density models do not properly capture the structure of the full Orion Bar PDR from the ionized zone to the cold molecular regions, such simple models do reproduce the H_2 rovibrational level populations within the narrow H_2 emitting region. It is possible that the temperature and density are nearly uniform across the narrow observed emitting region, explaining why these models provide good fits. To explore the parameter space, we ran a grid of models with constant temperatures ranging from $T = 200$ to 800 K and constant densities ranging from $n_H = 6.3 \times 10^2$ to 10^5 cm^{-3}. The gas turbulence and incident radiation field (from the O7V star θ^1 Ori C) used in these models are taken from the models in Pellegrini et al. (2009) and Shaw et al. (2009). This model grid allows us to explore the effects of different values of temperature and density on the H_2 rovibrational level populations.

2.4.1.2 Fitting the Model Grid

With our model grid, we fit our observations of the Orion Bar and pinpoint the gas temperature and density by leveraging the effects of collisions on UV-excited H_2 (see Chapter 1.5.2). The main effect of higher density is to increase the collision rates. Temperature affects both the collision rates and the thermal populations of the $v = 0$ ladder from which the relative level populations in J are transposed to higher v via UV excitation. Because of these dual effects of the temperature on the level populations, the model grid provides good leverage in fixing the gas temperature, while the density is less well-constrained.

We quantify the goodness of fit of the models to the data with a χ^2 parameter of the logarithm of the data-to-model ratios $\sum \left[\log_{10}(N_{\rm obs}/N_{\rm model})\right]^2$. This gives all the data points equal weight regardless of the large dynamic range in the level populations. Figure 2.4 shows a contour plot of $\sum \left[\log_{10}(N_{\rm obs}/N_{\rm model})\right]^2$ for the grid of constant density vs. constant temperature models, which are marked as dots. The

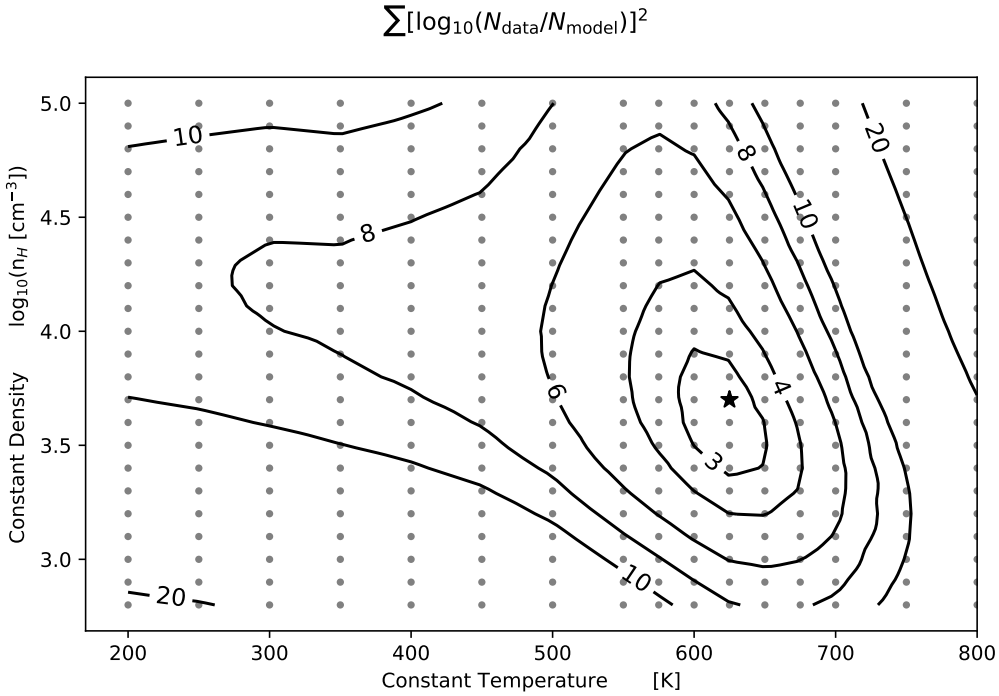

Figure 2.4: Contour plot of χ^2 of the logarithm of the data-to-model ratio $\sum\left[\log_{10}(N_{\rm obs}/N_{\rm model})\right]^2$ for determining how well a model fits the observed H_2 rovibrational level populations. The constant temperature and constant density models on the grid range from $T = 200$ to 800 K and $n_H = 6.3\times10^2$ to 10^5 cm^{-3}. Each model is represented by a grey point. The best-fit model ($T = 625$ K, $n_H = 5 \times 10^3$ cm^{-3}) is represented by the black star.

best-fit model, marked with a star in Figure 2.4, has $\sum\left[\log_{10}(N_{\rm obs}/N_{\rm model})\right]^2 = 2.48$ with parameters of $T = 625$ K and $n_H = 5 \times 10^3$ cm^{-3}. Table 2.2 shows all input parameters for the best-fit model. The other models in the grid have identical parameters except for temperature and/or density. Figure 2.3 shows the Orion Bar data with the best-fit model's predicted level populations, and column 11 in Table 2.1 gives the ratios of the data to the best-fit model. The level populations observed in the data and the best-fit model agree with each other within 0.5 dex.

As expected, we find that only a narrow range of temperatures, between 600 and 650 K, fits the data well. This temperature range is consistent with the warm gas discussed in Chapter 2.1.

The range of densities that fit the data is, again as expected, less well constrained than the temperature. We get good fits between $n_H = 2.5 \times 10^3$ to 10^4 cm^{-3}, which

Table 2.2: Best-fit Cloudy Model Parameters

Parameter	Value
Constant Temperature	625 K
Constant Density (n_H)	5×10^3 cm^{-3}
Turbulence	2 km s^{-1} [a]
Abundances	Orion[b]
Grains	Orion[b]
Cosmic Ray Flux	Galactic Background[b]
Incident Radiation Field (O7V star θ^1 Ori C)	Kurucz Stellar Atmosphere model, $T_{\rm eff} = 39700$ K[a]
No. of Ionizing Photons from θ^1 Ori C	$Q(\mathrm{H}) = 8.13 \times 10^{48}$ s^{-1}[a]
Cloud Face Distance from θ^1 Ori C	0.114 pc[a]
Stopping Condition	$A_V = 14$ mag
No. of Iterations	10

[a]Parameters from Cloudy models of Orion Bar by Pellegrini et al. (2009) and Shaw et al. (2009).
[b]Stored prescription in Cloudy.

are marginally consistent with the values of $n_H \geqslant 10^4$ cm^{-3} reported by nearly all other measurements and estimates from excited H_2 and other species in the literature. If we assume pressure equilibrium where $P/k \sim 10^8$ cm^{-3} K from Goicoechea et al. (2016) and T = 600 to 650 K from our model grid, we get a density of $n_H \sim 10^5$ cm^{-3}. This is at least an order of magnitude greater than the densities of $n_H = 2.5 \times 10^3$ to 10^4 cm^{-3} best fit by the model grid. It is unclear why the best model fits have lower than expected densities. One possibility is that the UV-excited H_2 emitting gas at our slit position actually has lower density than the majority of the gas in the Orion Bar, and previous studies of the Orion Bar were biased because they used species such as the pure rotational lines of H_2 that trace the higher density gas. If the Orion Bar really does consist of a two phase medium with cooler dense clumps embedded in a warmer low-density medium (e.g., Burton et al. 1990b; Parmar et al. 1991; Meixner & Tielens 1993; Andree-Labsch et al. 2017), the H_2 emission we observed arises from the warmer low-density gas. Perhaps we are viewing the lowest density part of the cloud face, where self shielding is lowest and the UV radiation field interacting with the H_2 is strongest. Another possibility is that some density-sensitive parameter(s) in the Cloudy models, such as the H_2 formation rate or the collisional rate coefficients, are overestimated or underestimated compared to their actual values.

The overall level populations across the different rotational ladders are well matched by the model, but the model overpredicts the populations for the high J levels in the $v = 1$ ladder. Le et al. (2016) found similar results when fitting models by Draine & Bertoldi (1996) to their IGRINS observations of rovibrationally excited H_2 in the NGC 7023 PDR. One possible explanation for this discrepancy is "formation pumping," where H_2 forms on dust grains in excited rovibrational states. The distribution of rovibrational level populations for newly formed H_2 assumed in the models might be overpredicting the observed level populations at high J. Cloudy assumes the prescription of Takahashi & Uehara (2001) for formation pumping. We ran a separate model grid with the formation pumping prescription of Draine & Bertoldi (1996) and another set of grids with the formation pumping prescription set to thermal (Boltzmann) distributions with temperatures of 1500, 5000, 10,000, and 17,329[1] K. We find that changing the formation pumping prescription in Cloudy does have a large effect on the predicted level populations at high J, but these alternate prescriptions do not provide better fits than the default Takahashi & Uehara (2001) prescription. The range of temperatures that best fit our data does not significantly change when we explore alternative formation pumping prescriptions, but the range of best-fit densities approaches $n_H = 5 \times 10^4$ cm^{-3} for the Boltzmann distribution prescriptions as the temperature is lowered from 17,329 to 1500 K. Since the high J lines are sensitive to the adopted formation pumping prescription, using new formation pumping prescriptions or fine tuning existing prescriptions to fit the high J levels might be an avenue for exploring formation pumping in future studies.

2.4.2 Hydrostatic Models

We ran a suite of hydrostatic Cloudy models of the Orion Bar, based on the models from Pellegrini et al. (2009) and Shaw et al. (2009). These models were designed to simulate the full structure of the Orion Bar PDR and the H_2 emission. We ran models with varying cosmic-ray fluxes, grain types, magnetic field strengths, temperature floors, and treatments for H_2 collisions. While our best-fit constant density and constant temperature model fits the data well at $\sum \left[\log_{10}(N_{\rm obs}/N_{\rm model})\right]^2 = 2.48$, all the hydrostatic models provided poorer fits of $\sum \left[\log_{10}(N_{\rm obs}/N_{\rm model})\right]^2 > 10$.

[1]The default thermal formation pumping prescription in Cloudy has a temperature of 17,329 K, corresponding to 1.5 eV or one-third of the energy released during the formation of an H_2 molecule, as described in Le Bourlot (1991).

The main complication we find is that leaving the g-bar approximation on (as defined in Chapter 1.6) yields unphysical rovibrational level populations, making it necessary to disable this feature. Disabling the g-bar approximation means omitting some of the H_2 physics (Shaw et al., 2005). This could introduce artificial effects between levels with well-known collision rate coefficients (mainly levels with $v \leqslant 3$) and those without, and it is unclear whether the predicted H_2 level populations for these models are physically meaningful. Turning the g-bar approximation off has a negligible effect on our constant temperature and density model grid fits. Clearly, there exists an interdependence between the collisional processes for H_2 and how the structure of the PDR is calculated in these hydrostatic models, that is less significant for the simpler constant temperature and density models. The hydrostatic model predictions for H_2 rovibrational level populations would greatly benefit from well-known collisional rate coefficients for transitions between high v and J states. New and improved collisional data for H_2 will ultimately give us a better understanding of PDR physics.

2.5 Summary and Conclusions

We observed the Orion Bar PDR in a deep pointed observation with IGRINS at the 2.7 m telescope at the McDonald Observatory. The instrument's high spectral resolution of $R \sim 45{,}000$ and broad wavelength coverage of the near-IR H and K bands (1.45-2.45 μm) enables us to detect 87 H_2 rovibrational transition emission lines with S/N > 3. We extract the flux of each line with a robust weighting scheme and calculate the column density of H_2 for a total of 69 different rovibrational states, which have excitation energies up to $E_u/k = 50{,}000$ K above the ground state ($v = 0$, $J = 0$). The large range in rotational (J) levels, vibrational (v) levels, and excitation energy covered by the observed transitions allow us to perform a detailed study of the excitation of H_2 within the Orion Bar PDR. We compare the observed rovibrational level populations to predictions from one-dimensional Cloudy 13.03c (Ferland et al., 2013) models.

As a result of our analysis, we find the following.

1. The line-of-sight extinction towards the H_2 emitting region is $A_V = 8.25$ or $A_K = 0.96$, as measured from line pairs arising from common upper states.

2. Constant temperature and density Cloudy models provide a better fit to the IGRINS H_2 data than the hydrostatic models of Shaw et al. (2009) and Pellegrini et al. (2009), which explicitly solve for the structure throughout the PDR and have nearly constant pressure. This could be due to the fact that the $v \geqslant 1$ transitions we observe in the Orion Bar with the $1'' \times 15''$ slit arise from a relatively narrow zone of the overall PDR structure. Another possible explanation for the poorer fit of the hydrostatic models is that this results from disabling the g-bar approximation for the collisional rate coefficients of the high-v levels (van Regemorter, 1962; Shaw et al., 2005), which may omit physical effects important in determining the level populations.

3. The model grid, combined with the large number of rovibrational levels we probe, constrains the temperature for the observed H_2 emitting region to 600–650 K, consistent with earlier findings. The best-fit model gives a temperature of 625 K.

4. The model grid constrains the density to $n_H = 2.5 \times 10^3$ to 10^4 cm^{-3}, with the best-fit model giving $n_H = 5 \times 10^3$ cm^{-3}, which is marginally lower than most values in the literature. The reason may be either that this emission arises predominantly in the lower density inter-clump region of a two-component clumpy medium (with which our density is marginally consistent), or that one or more of the assumed parameters in the Cloudy models are sensitive to density and their values are over- or underestimated.

Chapter Three: Survey of Star Forming Region PDRs

3.1 Introduction

PDRs arise in a wide variety of ISM environments. They are found at the edges of large scale regions of massive star formation, at the edges of compact H II regions, as reflection nebulae around newly formed B stars, and in planetary nebulae where UV light emitted from stripped post-AGB stars interacts with previously ejected gas. In fact, most of the molecular gas in the ISM lies outside of dense dark molecular cores, and therefore is exposed to FUV photons from the interstellar radiation, which satisfies the conditions for a PDR (see review by Hollenbach & Tielens 1999). From our vantage point within the Galactic disk, we can observe many nearby star forming regions such as Orion, Taurus, and Ophiuchus.

PDRs in star forming regions arise where molecular clouds that have not fully collapsed or dispersed. Consequently, the newly formed O and B stars, massive enough to generate plentiful FUV photons, can excite and dissociate the surrounding molecular cloud. On large scales and when the UV radiation field is steady with time, PDRs exist in a state of semi-equilibrium with a differentiated structure set up by different species absorbing UV radiation at different energies (see Figure 1.1 and the discussion in Chapter 1.1). In a differentiated PDR, EUV photons are absorbed by H I, but FUV photons can pass through the H I to excite H_2 at the interface between the neutral gas and the molecular gas. H_2 dissociation from absorption of UV photons is balanced by H_2 reformation on dust grains.

Since the EUV photons are all absorbed by H I, the FUV photons that excite H_2 fall within a narrow range of energies from 11.2–13.6 eV ($912 < \lambda < 1110$ Å). The spectral slope of an O or B star's stellar radiation field varies little over this energy range, so the star's temperature has little effect on the H_2 level populations (Draine & Bertoldi, 1996). The gas temperature is set by the balance between gas heating and cooling. In a PDR, the source of energy is the FUV photons being absorbed by H_2 or dust grains. The gas is heated either from collisions with photo-electrons kicked

off of dust grains by UV photons, or from collisional de-excitation of UV-excited H_2. The cooling occurs mainly via radiation from atomic and ionic species. For molecular gas with low densities and temperatures, the emergent spectrum from UV-excited H_2 is fairly invariant to the properties of the gas and the UV source (Black & van Dishoeck, 1987; Sternberg, 1988; Sternberg & Dalgarno, 1989; Draine & Bertoldi, 1996). At higher temperatures and/or densities, collisions between H_2 and other particles modify the H_2 rovibrational level populations and the emergent spectrum (as discussed in Chapter 1.5.2). Thus, we can utilize the effects of collisions on the rovibrational level populations of UV-excited H_2 to probe the gas temperature, gas density, and FUV intensity in a PDR.

IGRINS has proven to be a useful tool for studying PDRs. In Chapter 2, we performed a detailed analysis of a single deep IGRINS observation of the H_2 rovibrational transition emission in the warm Orion Bar PDR. We have shown that a sensitive high resolution near-IR spectrometer that covers a large wavelength range, such as IGRINS, is an excellent instrument for observing emission from the many different H_2 rovibrational transitions. The fluxes of these transitions allow us to measure the H_2 rovibrational level populations and to use the populations as a probe of the physical conditions within the PDR. However, the Orion Bar is just one PDR at the edge of a region of high-mass star formation. The true power of this sort of analysis can be realized when it is applied to several different PDRs that cover a range of UV field intensities, gas densities, and gas temperatures. In this chapter, we apply a similar analysis as that performed on the Orion Bar to several additional PDRs found in star forming regions, and examine the similarities and differences between them.

3.2 Star Forming Region PDR Survey

We selected the following four PDRs for this survey: the Horsehead Nebula, S 140, IC 63, and NGC 2023, based on their observability, previous detections of UV-excited H_2, and to ensure a set of targets with a variety of differing properties (UV field, density, temperature, etc.). We compare them to our previous results for the Orion Bar (see Chapter 2 and Kaplan et al. 2017).

Table 3.1: Star Forming Region PDR Survey, PDR Properties, and Observing Details

PDR	Orion bar	Horsehead Nebula	S 140	IC 63	NGC 2023
Type	H II Region Edge	Dark Nebula Edge	H II Region Edge	Reflection Nebula	Reflection Nebula
Distance (pc)	450 ± 50^{a}	344 ± 25^{b}	764 ± 27^{c}	188 ± 28^{d}	704 ± 108^{e}
Illuminating Star	θ^1 Ori C	σ Ori	HD 211880	γ Cas	HD 37903
Spec. Type$_\star$	O7V^{f}	O9.5V^{i}	B0.5V^{l}	B0.5IVpe^{m}	B1.5V^{p}
$T_{\star,\mathrm{eff}}$ (K)	$39{,}000^{f}$	$33{,}000^{j}$	$29{,}000^{l}$	$25{,}000^{n}$	$23{,}700^{p}$
χ	3×10^{4} ^{g}	100^{k}	400^{l}	650^{o}	550^{q}
n_H (cm $^{-3}$)	5×10^{3} ^{h}	2×10^{4} ^{k}	10^{4} ^{l}	5×10^{4} ^{o}	10^{4}–10^{5} ^{q}
χ/n_H (cm^{-3})	6.0	5.0×10^{-3}	4.0×10^{-2}	1.3×10^{-2}	1.1×10^{-2}
R.A. (J2000)	$05^{\mathrm{h}}35^{\mathrm{m}}19\overset{\mathrm{s}}{.}73$	$05^{\mathrm{h}}40^{\mathrm{m}}53\overset{\mathrm{s}}{.}60$	$22^{\mathrm{h}}19^{\mathrm{m}}13\overset{\mathrm{s}}{.}40$	$00^{\mathrm{h}}59^{\mathrm{m}}02\overset{\mathrm{s}}{.}74$	$05^{\mathrm{h}}41^{\mathrm{m}}37\overset{\mathrm{s}}{.}71$
Dec. (J2000)	$-05°25'26\overset{''}{.}7$	$-02°28'00\overset{''}{.}0$	$+63°17'53\overset{''}{.}9$	$+60°53'06\overset{''}{.}7$	$-02°16'50\overset{''}{.}0$
Date Obs. (UT)	2014 Oct 24	2015 Nov 01	2015 Nov 02	2015 Nov 03	2015 Nov 03
Exp. Time (s)	600	300	600	600	600
No. of Exp.	3	11	10	8	7
PA (°)	135	76	45	45	15
Obs. Mode	Nod-Off-Slit	Nod-Off-Slit	Nod-Off-Slit	Nod-Off-Slit	Nod-Off-Slit
Std. Star	HD 34317	HR 1482	HR 8422	HR 598	HR 1724
A_K	0.63	0.54	0.54	0.29	0.46
1-0 S(1)/2-1 S(1)	5.35	2.79	2.42	2.91	3.09

References: [a]Schlafly et al. (2014), [b]Caballero (2008), [c]Hirota et al. (2008), [d]Perryman et al. (1997), [e]van Leeuwen (2007), [f]Ferland et al. (2012), [g]Allers et al. (2005), [h]Kaplan et al. (2017), [i]Warren & Hesser (1977), [j]Panagia (1973), [k]Abergel et al. (2003) [l]Timmermann et al. (1996) [m]Shenavrin et al. (2011) [n]Sigut & Jones (2007) [o]Thi et al. (2009) [p]Compiègne et al. (2008) [q]Habart et al. (2011)

3.2.1 Horsehead Nebula

The Horsehead Nebula, named for its iconic shape, is a dark portion of the L630 molecular cloud blocking out the light from emission and stars behind it. The PDR arises where UV light from the O9.5V star σ Ori (Warren & Hesser, 1977) falls upon the western facing edge of the "head." Since the star is relatively distant from Horsehead ($\approx$ 3.5 pc, Abergel et al. 2003) compared to the geometry of the other PDRs in this study, its UV field intensity is the lowest of the sample ($\chi \sim 100$, Abergel et al. 2003). Like the Orion Bar, the Horsehead PDR is viewed nearly edge on. The H_2 1-0 S(1) line emission has been mapped by Habart et al. (2005) and the pure rotational lines were mapped by Habart et al. (2011). We have selected the location of brightest H_2 1-0 S(1) line emission at $05^h40^m53\overset{s}{.}60$ $-02°28'00\overset{''}{.}0$ (J2000) to place the IGRINS slit, with PA = 76°, which is perpendicular to the dissociation front.

3.2.2 S 140

Sharpless 140 (S 140) is an H II region surrounding a cluster of several B stars with some reflection nebulosity in the background. The brightest UV source is the B0.5V star HD 211880 (Timmermann et al., 1996). H_2 emission has been observed with ISO by Timmermann et al. (1996) and Habart et al. (2004) and they derive parameters for the PDR that could be considered "typical" for the PDRs in our survey. S 140 somewhat resembles the Orion Bar in that the PDR lies at the edge of an H II region, but with a less intense FUV radiation field. We decided to place the IGRINS slit at $22^h19^m13\overset{s}{.}40$ $+63°17'53\overset{''}{.}9$, which is on the edge of the bright near-IR filament in S 140 tracing the PDR with the slit rotated to a PA of 45°, perpendicular to the dissociation front.

3.2.3 IC 63

IC 63 is a nearby (188 ± 28 pc, Perryman et al. 1997) reflection nebula near the B0.5IVpe star γ Cas (Shenavrin et al., 2011). The H_2 emission has been the subject of numerous studies including those by Witt et al. (1989), Sternberg & Dalgarno (1989), Luhman et al. (1997), Hurwitz (1998), Habart et al. (2004), France et al. (2005), Thi et al. (2009), and Fleming et al. (2010). In K band images, the PDR

forms a "V" shaped cloud with the tip of the V pointing southwest towards γ Cas. We positioned the IGRINS slit at $00^{h}59^{m}02\overset{s}{.}74$ $+60°53'06\overset{''}{.}7$, the brightest part of the tip of the nebula nearest to γ Cas, with the slit at a PA of 45°, perpendicular to the dissociation front.

3.2.4 NGC 2023

NGC 2023 is a reflection nebula surrounding the B1.5V star HD 37903 (Compiègne et al., 2008). It is located near the Horsehead Nebula and is one of the brightest and best studied star forming region PDRs. The studies of its UV-excited H_2 emission are extensive: Sellgren (1986), Hasegawa et al. (1987), Takayanagi et al. (1987), Gatley et al. (1987), Sternberg (1988), Sternberg (1989), Tanaka et al. (1989), Hippelein & Müench (1989), Howe et al. (1990), Burton et al. (1990a), Burton (1992), Field et al. (1994), Field et al. (1998), Burton et al. (1998), Martini et al. (1999), Takami et al. (2000), Habart et al. (2004), Fleming et al. (2010), Habart et al. (2011), and Sheffer et al. (2011). We placed the IGRINS slit at $05^{h}41^{m}37\overset{s}{.}71$ $-02°16'50\overset{''}{.}0$ with a PA of 135° to be perpendicular to the bright southern ridge.

3.3 Observations

All targets were observed with IGRINS on the 2.7 m Harlan J. Smith telescope at McDonald Observatory (Chapter 1.2) using the nod-off-slit mode with equal amounts of time spent on target and sky. An A0V standard star was observed at a similar airmass as each target for telluric absorption line correction and relative spectrophotometric flux calibration. Table 3.1 lists the coordinates of the IGRINS slit positions, UT of observations, PAs, integration times, and A0V standard stars used for all our observations.

3.4 Data Reduction, Calibrations, Line Flux Extractions, and Extinction Corrections

Our data reduction, calibration, and line flux extraction procedures follow those used for the Orion Bar study described in Chapter 2. Data reduction is carried out using

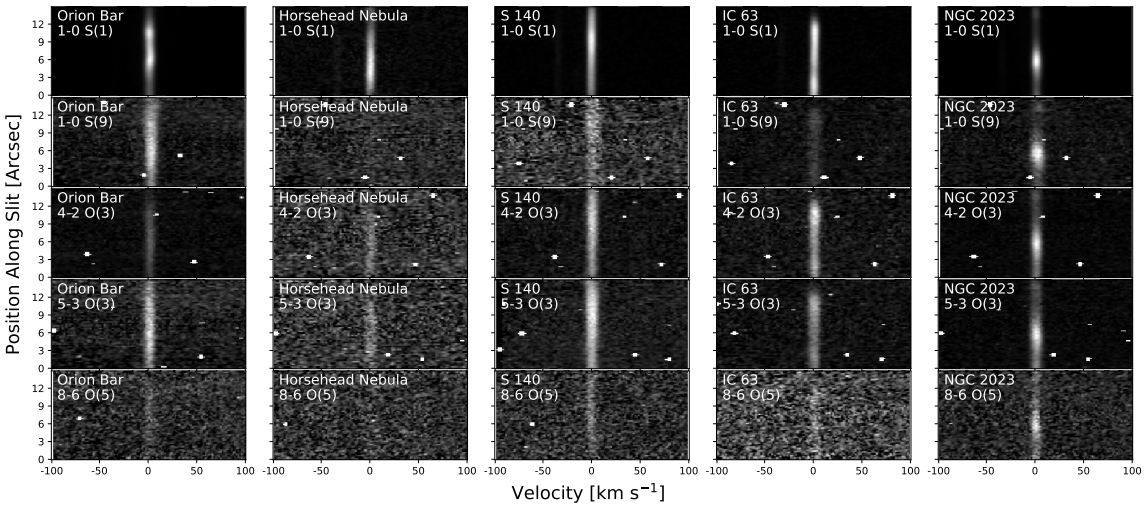

Figure 3.1: PV diagram thumbnails of a representative set of H_2 emission lines seen in all the PDRs in our survey. These transitions arise from upper states with a wide range of excitation energies. White dots indicate masked cosmic rays.

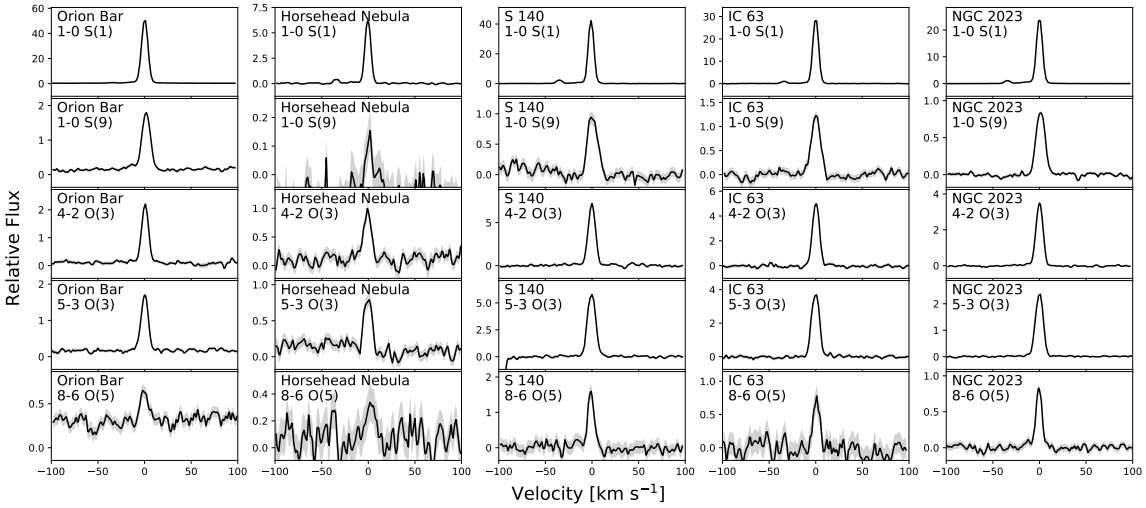

Figure 3.2: 1D thumbnails of a representative set of H_2 emission lines seen in all the PDRs in our survey. The 1D spectra are created by summing all the pixels along the slit in position space. These transitions arise from upper states with a wide range of excitation energies. The grey shaded region represents the $\pm 1\sigma$ uncertainty.

the public IGRINS Pipeline Package (Lee, 2015)[1] after removing cosmic rays from the raw frames (see Chapter 1.3). The 2D orders from the echellograms are combined into one long 2D spectrum. The A0V standard stars are used for telluric absorption line correction and relative spectrophotometric flux calibration (see Chapter 1.4.1). The 2D line profiles are linearly interpolated into PV space and the fluxes extracted using a weighted optimal extraction routine with the profile of the 1-0 S(1) line serving as the weights. The line extraction procedure is described in more detail in Chapter 1.4.2. We add a 15% systematic uncertainty to all the extracted line fluxes to account for unforeseen uncertainty in the relative flux calibration, telluric correction, and extinction correction. Figures 3.1 and 3.2 show 2D and 1D thumbnails from a representative set of H_2 lines observed in each PDR. The lines all appear quite narrow, indicating gas velocities of only a few km s^{-1}. The low velocity widths imply that the the H_2 is UV-excited and not shocked, since we would expect to see larger velocities along the line of sight in shocks unless there is an unfavorable alignment. Table 3.2 lists the extracted flux of each H_2 line for all the PDRs, with the fluxes normalized to the 4-2 O(3) line in each source.

To correct for dust extinction, we assume the extinction law is a power law of the form $A_\lambda \propto \lambda^{-\alpha}$, and we set $\alpha = 1.8$ from Martin & Whittet (1990). We then vary A_K to find the best value that gives the between the observed flux ratios of every pair of H_2 emission lines that arise from the same upper v and J state. We report the best-fit A_K for each PDR in Table 3.1.

3.5 H_2 Level Populations

The observed H_2 rovibrational transition emission lines are optically thin, so their fluxes are proportional to the number of molecules in the upper level of each transition. We calculate the H_2 rovibrational level populations from the emission line fluxes following the procedures detailed in Chapter 1.5.1. Table A.1 lists the physical constants that were used to calculate the level populations. We normalize all the column densities to the population of the $v = 4$, $J = 1$ level derived from the 4-2 O(3) transition, which is a fairly bright and easy to measure line uncontaminated by nearby telluric absorption or OH emission lines. Table 3.3 gives the derived H_2 level

[1]IGRINS Pipeline Package (PLP): `https://github.com/igrins/plp`

Table 3.2: H_2 line fluxes for the star forming region PDR survey (normalized to the 4-2 O(3) line).

Line ID	λ (μm)	v_u	J_u	Orion Bar	Horsehead Nebula	S 140	IC 63	NGC 2023
1-0 Q(1)	2.406592	1	1	$2.556 \pm 0.242 \times 10^1$	6.168 ± 0.623	4.286 ± 0.433	5.297 ± 0.643	7.807 ± 0.836
1-0 Q(2)	2.413439	1	2	6.081 ± 0.576	3.529 ± 0.358	2.380 ± 0.241	2.294 ± 0.279	2.575 ± 0.276
1-0 S(0)	2.223290	1	2	5.652 ± 0.498	3.503 ± 0.333	2.145 ± 0.204	2.126 ± 0.250	2.340 ± 0.238
1-0 Q(3)	2.423730	1	3	$1.103 \pm 0.105 \times 10^1$	3.345 ± 0.341	2.342 ± 0.238	2.865 ± 0.349	3.364 ± 0.362
1-0 S(1)	2.121834	1	3	$1.636 \pm 0.138 \times 10^1$	4.623 ± 0.422	3.680 ± 0.336	4.366 ± 0.502	5.336 ± 0.524
1-0 Q(4)	2.437489	1	4	2.748 ± 0.263	1.601 ± 0.165	1.091 ± 0.111	1.101 ± 0.134	1.192 ± 0.129
1-0 S(2)	2.033758	1	4	4.531 ± 0.364	2.640 ± 0.232	1.902 ± 0.167	1.985 ± 0.223	2.108 ± 0.200
1-0 S(3)	1.957559	1	5	9.209 ± 0.707	2.944 ± 0.251	2.393 ± 0.202	3.265 ± 0.360	4.122 ± 0.379
1-0 Q(6)	2.475559	1	6	–	–	0.381 ± 0.040	0.466 ± 0.059	0.462 ± 0.051
1-0 S(6)	1.788050	1	8	0.873 ± 0.060	–	0.201 ± 0.016	-	–
1-0 S(7)	1.747955	1	9	2.092 ± 0.138	0.335 ± 0.037	0.362 ± 0.027	0.632 ± 0.066	0.773 ± 0.064
1-0 S(8)	1.714738	1	10	0.405 ± 0.027	–	$9.441 \pm 0.858 \times 10^{-2}$	0.149 ± 0.018	0.172 ± 0.014
1-0 S(9)	1.687761	1	11	0.667 ± 0.042	0.177 ± 0.018	0.119 ± 0.009	0.228 ± 0.023	0.266 ± 0.021
1-0 S(10)	1.666475	1	12	$9.843 \pm 0.669 \times 10^{-2}$	–	$2.553 \pm 0.298 \times 10^{-2}$	$3.947 \pm 0.606 \times 10^{-2}$	$5.726 \pm 0.474 \times 10^{-2}$
1-0 S(11)	1.650413	1	13	$8.172 \pm 0.555 \times 10^{-2}$	–	-	$4.942 \pm 0.635 \times 10^{-2}$	$4.567 \pm 0.377 \times 10^{-2}$
2-1 S(0)	2.355605	2	2	1.047 ± 0.097	1.396 ± 0.142	0.897 ± 0.089	0.812 ± 0.098	0.771 ± 0.082
2-1 S(1)	2.247716	2	3	3.057 ± 0.272	1.656 ± 0.160	1.519 ± 0.146	1.500 ± 0.177	1.728 ± 0.177
2-1 S(2)	2.154216	2	4	1.035 ± 0.088	1.076 ± 0.101	0.843 ± 0.078	0.762 ± 0.088	0.794 ± 0.079
2-0 O(6)	1.486989	2	4	–	–	0.131 ± 0.009	$7.990 \pm 1.022 \times 10^{-2}$	$8.583 \pm 0.681 \times 10^{-2}$
2-0 O(7)	1.546377	2	5	–	–	$6.324 \pm 0.490 \times 10^{-2}$	$8.783 \pm 0.992 \times 10^{-2}$	$9.029 \pm 0.667 \times 10^{-2}$
2-1 S(3)	2.073482	2	5	2.661 ± 0.218	1.027 ± 0.093	1.051 ± 0.094	-	1.427 ± 0.138
2-1 S(4)	2.004109	2	6	–	–	-	-	0.456 ± 0.043
2-0 O(8)	1.610517	2	6	–	–	$3.300 \pm 0.458 \times 10^{-2}$	-	–
2-0 O(9)	1.679641	2	7	$3.717 \pm 0.330 \times 10^{-2}$	–	-	-	$1.775 \pm 0.184 \times 10^{-2}$

Continued on next page...

Table 3.2 continued: H_2 line fluxes for the star forming region PDR survey (normalized to the 4-2 O(3) line).

Line ID	λ (μm)	v_u	J_u	Orion Bar	Horsehead Nebula	S 140	IC 63	NGC 2023
2-1 S(9)	1.790479	2	11	–	–	-	-	$8.307 \pm 0.726 \times 10^{-2}$
2-1 S(10)	1.768836	2	12	–	–	-	-	$1.590 \pm 0.228 \times 10^{-2}$
2-1 S(15)	1.738801	2	17	–	–	-	-	$1.316 \pm 0.165 \times 10^{-2}$
2-1 S(17)	1.758762	2	19	–	–	-	-	$2.373 \pm 0.237 \times 10^{-2}$
3-1 O(4)	1.467714	3	2	–	–	0.584 ± 0.034	0.623 ± 0.057	0.509 ± 0.035
3-1 O(5)	1.522033	3	3	0.584 ± 0.031	–	0.392 ± 0.024	0.437 ± 0.041	0.455 ± 0.032
3-2 S(1)	2.386471	3	3	1.035 ± 0.098	0.845 ± 0.093	0.756 ± 0.076	0.810 ± 0.099	0.708 ± 0.076
3-1 O(6)	1.581171	3	4	0.150 ± 0.009	–	0.162 ± 0.011	0.124 ± 0.013	0.132 ± 0.010
3-2 S(2)	2.287045	3	4	0.424 ± 0.038	0.520 ± 0.053	0.409 ± 0.040	0.343 ± 0.041	0.372 ± 0.039
3-1 O(7)	1.645348	3	5	–	–	$8.056 \pm 0.586 \times 10^{-2}$	$9.630 \pm 1.008 \times 10^{-2}$	0.127 ± 0.010
3-2 S(3)	2.201399	3	5	1.015 ± 0.089	0.423 ± 0.042	0.459 ± 0.043	0.512 ± 0.060	0.618 ± 0.062
3-2 S(4)	2.128015	3	6	0.323 ± 0.027	0.182 ± 0.020	0.158 ± 0.015	0.188 ± 0.022	0.215 ± 0.021
3-2 S(5)	2.065584	3	7	0.687 ± 0.056	–	0.199 ± 0.018	0.267 ± 0.031	0.362 ± 0.035
3-1 O(9)	1.789869	3	7	–	–	$2.024 \pm 0.274 \times 10^{-2}$	-	$3.838 \pm 0.356 \times 10^{-2}$
3-2 S(7)	1.969231	3	9	–	–	$6.964 \pm 0.678 \times 10^{-2}$	0.116 ± 0.014	0.127 ± 0.013
3-1 Q(13)	1.502463	3	13	–	–	$4.503 \pm 0.417 \times 10^{-2}$	$5.038 \pm 0.760 \times 10^{-2}$	$8.245 \pm 0.625 \times 10^{-2}$
3-1 Q(14)	1.533983	3	14	–	–	-	-	$2.769 \pm 0.267 \times 10^{-2}$
3-1 Q(15)	1.568584	3	15	–	–	-	-	$4.206 \pm 0.380 \times 10^{-2}$
3-1 Q(16)	1.606526	3	16	–	–	-	-	$1.531 \pm 0.188 \times 10^{-2}$
4-2 O(2)	1.461133	4	0	–	–	0.906 ± 0.052	0.786 ± 0.072	0.715 ± 0.048
4-2 O(3)	1.509865	4	1	1.000 ± 0.052	1.000 ± 0.063	1.000 ± 0.060	1.000 ± 0.092	1.000 ± 0.069
4-2 O(4)	1.563515	4	2	0.339 ± 0.019	0.690 ± 0.046	0.533 ± 0.034	0.498 ± 0.047	0.440 ± 0.032
4-2 O(5)	1.622299	4	3	0.499 ± 0.030	0.533 ± 0.042	0.437 ± 0.029	0.442 ± 0.043	0.465 ± 0.035
4-2 O(6)	1.686462	4	4	$9.867 \pm 0.685 \times 10^{-2}$	0.218 ± 0.022	-	0.103 ± 0.011	0.104 ± 0.008
4-2 O(7)	1.756281	4	5	0.189 ± 0.013	–	$7.152 \pm 0.570 \times 10^{-2}$	$9.382 \pm 1.044 \times 10^{-2}$	0.115 ± 0.010

Continued on next page...

Table 3.2 continued: H_2 line fluxes for the star forming region PDR survey (normalized to the 4-2 O(3) line).

Line ID	λ (μm)	v_u	J_u	Orion Bar	Horsehead Nebula	S 140	IC 63	NGC 2023
4-3 S(3)	2.344453	4	5	–	0.167 ± 0.024	0.204 ± 0.020	0.241 ± 0.030	0.273 ± 0.029
4-3 S(4)	2.266764	4	6	0.102 ± 0.011	–	$6.974 \pm 0.834 \times 10^{-2}$	$7.670 \pm 1.298 \times 10^{-2}$	$8.935 \pm 0.966 \times 10^{-2}$
4-2 Q(7)	1.459195	4	7	–	–	-	0.305 ± 0.037	0.375 ± 0.026
4-3 S(5)	2.200974	4	7	0.215 ± 0.019	–	$7.664 \pm 0.767 \times 10^{-2}$	0.109 ± 0.014	0.133 ± 0.014
4-2 Q(8)	1.477736	4	8	–	–	$8.049 \pm 0.695 \times 10^{-2}$	-	–
4-3 S(6)	2.145873	4	8	$4.987 \pm 0.511 \times 10^{-2}$	–	$1.763 \pm 0.276 \times 10^{-2}$	$2.169 \pm 0.490 \times 10^{-2}$	$3.209 \pm 0.353 \times 10^{-2}$
4-2 Q(9)	1.498876	4	9	–	–	0.100 ± 0.007	0.115 ± 0.012	0.199 ± 0.014
4-2 O(11)	2.099586	4	9	$2.241 \pm 0.330 \times 10^{-2}$	–	-	-	$1.664 \pm 0.219 \times 10^{-2}$
4-3 S(7)	2.100426	4	9	$6.658 \pm 0.614 \times 10^{-2}$	–	-	$3.220 \pm 0.564 \times 10^{-2}$	$3.770 \pm 0.393 \times 10^{-2}$
4-2 Q(11)	1.549455	4	11	0.154 ± 0.009	–	$5.165 \pm 0.391 \times 10^{-2}$	-	0.107 ± 0.008
4-2 Q(12)	1.579217	4	12	–	–	-	-	$3.050 \pm 0.262 \times 10^{-2}$
4-2 Q(13)	1.612237	4	13	–	–	-	-	$5.893 \pm 0.474 \times 10^{-2}$
4-2 Q(14)	1.648782	4	14	–	–	-	-	$1.025 \pm 0.144 \times 10^{-2}$
4-2 Q(15)	1.689178	4	15	–	–	-	-	$2.093 \pm 0.197 \times 10^{-2}$
4-3 S(17)	2.047446	4	19	–	–	-	-	$1.740 \pm 0.216 \times 10^{-2}$
4-3 S(19)	2.116170	4	21	–	–	-	-	$9.839 \pm 1.697 \times 10^{-3}$
5-3 O(2)	1.560736	5	0	0.308 ± 0.017	0.798 ± 0.053	0.575 ± 0.036	0.569 ± 0.054	0.461 ± 0.033
5-3 Q(1)	1.492933	5	1	–	–	-	-	0.994 ± 0.067
5-3 O(3)	1.613520	5	1	0.647 ± 0.038	0.743 ± 0.052	0.760 ± 0.051	0.725 ± 0.070	0.622 ± 0.047
5-3 Q(2)	1.497982	5	2	–	0.874 ± 0.062	0.546 ± 0.032	0.551 ± 0.051	0.466 ± 0.032
5-3 O(4)	1.671814	5	2	0.226 ± 0.014	0.596 ± 0.045	0.386 ± 0.027	0.331 ± 0.033	0.324 ± 0.025
5-3 Q(3)	1.505588	5	3	–	1.121 ± 0.083	-	-	0.713 ± 0.049
5-3 O(5)	1.735889	5	3	–	0.559 ± 0.059	0.268 ± 0.020	0.260 ± 0.027	0.266 ± 0.022
5-3 Q(4)	1.515792	5	4	0.239 ± 0.013	–	0.276 ± 0.017	0.262 ± 0.025	0.250 ± 0.017
5-3 Q(5)	1.528648	5	5	0.480 ± 0.026	–	0.258 ± 0.016	0.385 ± 0.036	0.376 ± 0.026

Continued on next page...

Table 3.2 continued: H_2 line fluxes for the star forming region PDR survey (normalized to the 4-2 O(3) line).

Line ID	λ (μm)	v_u	J_u	Orion Bar	Horsehead Nebula	S 140	IC 63	NGC 2023
5-3 O(8)	1.966206	5	6	–	–	-	-	$2.798 \pm 0.309 \times 10^{-2}$
5-3 Q(6)	1.544232	5	6	–	–	$6.950 \pm 0.621 \times 10^{-2}$	0.128 ± 0.015	0.142 ± 0.010
5-4 S(4)	2.424758	5	6	–	–	-	-	$2.882 \pm 0.432 \times 10^{-2}$
5-3 O(9)	2.057127	5	7	$5.221 \pm 0.562 \times 10^{-2}$	–	$3.233 \pm 0.395 \times 10^{-2}$	$4.111 \pm 0.689 \times 10^{-2}$	$3.867 \pm 0.431 \times 10^{-2}$
5-3 Q(7)	1.562635	5	7	0.296 ± 0.016	–	0.131 ± 0.009	0.185 ± 0.018	0.228 ± 0.016
5-4 S(6)	2.297937	5	8	–	–	-	-	$2.407 \pm 0.386 \times 10^{-2}$
5-3 O(10)	2.156073	5	8	–	–	-	-	$1.224 \pm 0.243 \times 10^{-2}$
5-3 Q(8)	1.583975	5	8	–	–	-	-	$7.357 \pm 0.589 \times 10^{-2}$
5-3 Q(9)	1.608398	5	9	0.257 ± 0.015	–	$9.285 \pm 0.664 \times 10^{-2}$	0.120 ± 0.013	0.131 ± 0.010
5-3 Q(10)	1.636082	5	10	–	–	-	-	$3.474 \pm 0.300 \times 10^{-2}$
5-3 Q(11)	1.667248	5	11	–	–	-	$5.608 \pm 0.768 \times 10^{-2}$	$6.768 \pm 0.562 \times 10^{-2}$
5-3 Q(12)	1.702170	5	12	–	–	$2.124 \pm 0.282 \times 10^{-2}$	-	–
5-4 S(11)	2.153924	5	13	–	–	-	-	$1.167 \pm 0.188 \times 10^{-2}$
5-4 S(13)	2.152833	5	15	–	–	-	-	$1.633 \pm 0.227 \times 10^{-2}$
5-4 S(15)	2.181794	5	17	–	–	-	-	$2.773 \pm 0.353 \times 10^{-2}$
6-4 O(2)	1.675032	6	0	0.200 ± 0.013	0.633 ± 0.046	0.416 ± 0.029	0.372 ± 0.037	0.328 ± 0.026
6-4 Q(1)	1.601534	6	1	0.473 ± 0.027	0.791 ± 0.055	0.658 ± 0.043	0.668 ± 0.065	0.670 ± 0.050
6-4 O(3)	1.732641	6	1	0.434 ± 0.029	–	0.522 ± 0.038	0.481 ± 0.050	0.488 ± 0.040
6-4 S(0)	1.536891	6	2	0.196 ± 0.011	0.634 ± 0.042	0.356 ± 0.022	0.330 ± 0.031	0.297 ± 0.021
6-4 Q(2)	1.607390	6	2	0.219 ± 0.013	0.628 ± 0.044	0.456 ± 0.030	0.367 ± 0.036	0.349 ± 0.026
6-4 O(4)	1.796524	6	2	0.195 ± 0.014	–	0.378 ± 0.029	0.351 ± 0.038	0.306 ± 0.026
6-4 S(1)	1.501560	6	3	0.525 ± 0.027	0.530 ± 0.038	0.582 ± 0.035	0.572 ± 0.053	0.575 ± 0.039
6-4 Q(3)	1.616224	6	3	0.352 ± 0.021	0.362 ± 0.027	-	0.354 ± 0.035	0.387 ± 0.029
6-4 S(2)	1.471213	6	4	–	–	0.252 ± 0.034	-	–
6-4 Q(4)	1.628094	6	4	0.119 ± 0.008	–	0.139 ± 0.010	0.161 ± 0.016	0.148 ± 0.011

Continued on next page...

Table 3.2 continued: H_2 line fluxes for the star forming region PDR survey (normalized to the 4-2 O(3) line).

Line ID	λ (μm)	v_u	J_u	Orion Bar	Horsehead Nebula	S 140	IC 63	NGC 2023
6-4 O(7)	2.029684	6	5	0.104 ± 0.009	–	$7.533 \pm 0.709 \times 10^{-2}$	$8.994 \pm 1.096 \times 10^{-2}$	$9.967 \pm 0.958 \times 10^{-2}$
6-4 Q(5)	1.643084	6	5	–	–	0.163 ± 0.011	-	0.204 ± 0.016
6-4 Q(6)	1.661304	6	6	$7.854 \pm 0.531 \times 10^{-2}$	–	-	$7.983 \pm 0.865 \times 10^{-2}$	$7.545 \pm 0.599 \times 10^{-2}$
6-4 O(9)	2.224960	6	7	–	–	-	-	$3.624 \pm 0.414 \times 10^{-2}$
6-4 Q(7)	1.682897	6	7	–	–	0.111 ± 0.009	0.152 ± 0.016	0.162 ± 0.013
6-4 Q(8)	1.708041	6	8	$5.809 \pm 0.438 \times 10^{-2}$	–	$2.958 \pm 0.289 \times 10^{-2}$	-	$3.703 \pm 0.323 \times 10^{-2}$
6-4 Q(9)	1.736958	6	9	–	–	$3.047 \pm 0.373 \times 10^{-2}$	$5.935 \pm 0.746 \times 10^{-2}$	$6.427 \pm 0.542 \times 10^{-2}$
6-3 Q(19)	1.478765	6	19	–	–	$3.680 \pm 0.449 \times 10^{-2}$	-	–
7-5 Q(1)	1.728799	7	1	0.330 ± 0.022	0.422 ± 0.042	0.469 ± 0.034	0.442 ± 0.046	0.427 ± 0.035
7-5 S(0)	1.658492	7	2	–	0.265 ± 0.023	0.189 ± 0.013	0.153 ± 0.016	0.151 ± 0.012
7-5 Q(2)	1.735762	7	2	0.101 ± 0.007	0.274 ± 0.025	0.207 ± 0.016	0.181 ± 0.019	0.174 ± 0.014
7-5 O(4)	1.943455	7	2	–	–	0.254 ± 0.022	0.223 ± 0.025	–
7-5 Q(3)	1.746280	7	3	0.215 ± 0.015	0.490 ± 0.046	0.290 ± 0.022	0.264 ± 0.028	0.269 ± 0.022
7-5 S(1)	1.620548	7	3	0.288 ± 0.017	0.253 ± 0.021	0.324 ± 0.022	0.304 ± 0.030	0.324 ± 0.025
7-5 O(5)	2.022053	7	3	–	–	0.212 ± 0.019	0.124 ± 0.017	–
7-5 S(2)	1.588294	7	4	–	0.222 ± 0.019	0.149 ± 0.010	0.143 ± 0.014	0.162 ± 0.012
7-5 Q(4)	1.760446	7	4	$8.754 \pm 0.655 \times 10^{-2}$	–	$9.776 \pm 0.775 \times 10^{-2}$	0.101 ± 0.011	$9.850 \pm 0.834 \times 10^{-2}$
7-5 O(6)	2.109001	7	4	–	–	$5.280 \pm 0.656 \times 10^{-2}$	$6.877 \pm 1.224 \times 10^{-2}$	$6.647 \pm 0.730 \times 10^{-2}$
7-5 O(7)	2.204989	7	5	$7.021 \pm 0.690 \times 10^{-2}$	–	$6.344 \pm 0.689 \times 10^{-2}$	$5.216 \pm 0.932 \times 10^{-2}$	$6.442 \pm 0.675 \times 10^{-2}$
7-5 Q(5)	1.778390	7	5	–	–	0.124 ± 0.010	$8.924 \pm 1.179 \times 10^{-2}$	0.155 ± 0.013
7-5 S(3)	1.561510	7	5	0.257 ± 0.014	0.271 ± 0.022	0.189 ± 0.012	0.214 ± 0.021	0.255 ± 0.018
7-5 O(8)	2.310862	7	6	–	–	-	-	$1.522 \pm 0.279 \times 10^{-2}$
7-5 S(4)	1.540006	7	6	$8.188 \pm 0.539 \times 10^{-2}$	–	$8.673 \pm 0.594 \times 10^{-2}$	0.105 ± 0.011	0.108 ± 0.008
7-5 O(9)	2.427661	7	7	–	–	-	-	$2.283 \pm 0.357 \times 10^{-2}$
7-5 S(5)	1.523623	7	7	0.191 ± 0.011	–	0.101 ± 0.007	0.158 ± 0.015	0.184 ± 0.013

Continued on next page...

Table 3.2 continued: H_2 line fluxes for the star forming region PDR survey (normalized to the 4-2 O(3) line).

Line ID	λ (μm)	v_u	J_u	Orion Bar	Horsehead Nebula	S 140	IC 63	NGC 2023
7-5 S(6)	1.512240	7	8	$5.411 \pm 0.441 \times 10^{-2}$	–	$2.446 \pm 0.305 \times 10^{-2}$	$5.306 \pm 0.724 \times 10^{-2}$	$6.159 \pm 0.459 \times 10^{-2}$
7-5 S(7)	1.505784	7	9	–	–	-	-	0.124 ± 0.010
7-5 S(8)	1.504232	7	10	–	–	-	-	$2.741 \pm 0.316 \times 10^{-2}$
7-5 Q(11)	1.979270	7	11	$4.380 \pm 0.471 \times 10^{-2}$	–	$2.075 \pm 0.282 \times 10^{-2}$	-	$2.754 \pm 0.309 \times 10^{-2}$
7-5 S(9)	1.507629	7	11	–	–	$3.776 \pm 0.508 \times 10^{-2}$	$7.425 \pm 1.106 \times 10^{-2}$	$3.284 \pm 0.359 \times 10^{-2}$
7-5 Q(12)	2.032316	7	12	–	–	-	-	$8.293 \pm 1.538 \times 10^{-3}$
7-5 Q(13)	2.092904	7	13	$2.492 \pm 0.304 \times 10^{-2}$	–	-	-	$1.345 \pm 0.184 \times 10^{-2}$
8-6 O(2)	1.970799	8	0	–	–	0.267 ± 0.023	0.191 ± 0.023	–
8-6 O(3)	2.041830	8	1	0.218 ± 0.018	0.435 ± 0.041	0.350 ± 0.031	0.280 ± 0.032	0.299 ± 0.029
8-6 S(0)	1.804886	8	2	–	–	$9.425 \pm 0.799 \times 10^{-2}$	$7.779 \pm 1.072 \times 10^{-2}$	$9.609 \pm 0.839 \times 10^{-2}$
8-6 O(4)	2.121592	8	2	–	0.261 ± 0.027	0.192 ± 0.018	0.140 ± 0.017	0.171 ± 0.017
8-6 O(5)	2.210763	8	3	0.108 ± 0.011	0.162 ± 0.030	0.140 ± 0.014	0.119 ± 0.016	0.146 ± 0.015
8-6 S(1)	1.763952	8	3	0.136 ± 0.011	–	$9.624 \pm 0.895 \times 10^{-2}$	0.144 ± 0.018	0.140 ± 0.012
8-6 S(2)	1.729672	8	4	–	–	$9.111 \pm 0.738 \times 10^{-2}$	$7.328 \pm 0.977 \times 10^{-2}$	$9.350 \pm 0.789 \times 10^{-2}$
8-6 O(6)	2.310167	8	4	$3.117 \pm 0.523 \times 10^{-2}$	–	$4.427 \pm 0.566 \times 10^{-2}$	$3.189 \pm 0.730 \times 10^{-2}$	$5.008 \pm 0.568 \times 10^{-2}$
8-6 S(3)	1.701803	8	5	0.101 ± 0.007	–	$7.645 \pm 0.601 \times 10^{-2}$	0.111 ± 0.012	0.121 ± 0.010
8-6 O(7)	2.420824	8	5	–	–	-	-	$3.953 \pm 0.549 \times 10^{-2}$
8-6 Q(5)	1.943225	8	5	–	–	$6.467 \pm 0.618 \times 10^{-2}$	$5.686 \pm 0.851 \times 10^{-2}$	$8.090 \pm 0.779 \times 10^{-2}$
8-6 Q(6)	1.970468	8	6	–	–	-	$3.495 \pm 0.811 \times 10^{-2}$	$2.825 \pm 0.365 \times 10^{-2}$
8-6 S(4)	1.680153	8	6	–	–	$3.934 \pm 0.336 \times 10^{-2}$	$4.123 \pm 0.568 \times 10^{-2}$	$4.177 \pm 0.354 \times 10^{-2}$
8-6 Q(7)	2.003105	8	7	–	–	-	-	$5.854 \pm 0.741 \times 10^{-2}$
8-6 S(5)	1.664584	8	7	$6.655 \pm 0.469 \times 10^{-2}$	–	$5.935 \pm 0.458 \times 10^{-2}$	$8.594 \pm 0.934 \times 10^{-2}$	$7.274 \pm 0.581 \times 10^{-2}$
8-6 Q(8)	2.041614	8	8	–	–	-	-	$1.553 \pm 0.240 \times 10^{-2}$
8-6 S(6)	1.655023	8	8	–	–	$3.359 \pm 0.371 \times 10^{-2}$	-	$3.711 \pm 0.338 \times 10^{-2}$
8-6 Q(9)	2.086607	8	9	–	–	$2.287 \pm 0.384 \times 10^{-2}$	-	$2.965 \pm 0.357 \times 10^{-2}$

Continued on next page...

Table 3.2 continued: H_2 line fluxes for the star forming region PDR survey (normalized to the 4-2 O(3) line).

Line ID	λ (μm)	v_u	J_u	Orion Bar	Horsehead Nebula	S 140	IC 63	NGC 2023
8-6 S(7)	1.651475	8	9	–	–	$2.405 \pm 0.285 \times 10^{-2}$	-	$4.238 \pm 0.359 \times 10^{-2}$
8-6 Q(11)	2.199456	8	11	–	–	-	-	$2.245 \pm 0.330 \times 10^{-2}$
8-6 S(9)	1.662916	8	11	–	–	-	-	$1.380 \pm 0.153 \times 10^{-2}$
8-5 Q(13)	1.477482	8	13	–	–	$4.379 \pm 0.482 \times 10^{-2}$	-	–
9-7 O(2)	2.172715	9	0	$5.680 \pm 0.582 \times 10^{-2}$	0.166 ± 0.020	0.135 ± 0.013	0.103 ± 0.013	0.101 ± 0.010
9-7 Q(1)	2.073187	9	1	$9.092 \pm 0.840 \times 10^{-2}$	–	-	0.129 ± 0.015	0.172 ± 0.017
9-7 O(3)	2.253724	9	1	0.111 ± 0.011	0.176 ± 0.024	0.186 ± 0.018	0.140 ± 0.018	0.168 ± 0.017
9-7 O(4)	2.345581	9	2	$4.174 \pm 0.594 \times 10^{-2}$	0.192 ± 0.026	0.107 ± 0.011	$8.573 \pm 1.209 \times 10^{-2}$	$9.434 \pm 1.022 \times 10^{-2}$
9-7 S(0)	1.987350	9	2	$4.268 \pm 0.428 \times 10^{-2}$	0.148 ± 0.017	$9.031 \pm 0.833 \times 10^{-2}$	$6.271 \pm 0.819 \times 10^{-2}$	$6.990 \pm 0.667 \times 10^{-2}$
9-7 Q(2)	2.084098	9	2	$5.939 \pm 0.698 \times 10^{-2}$	0.183 ± 0.029	0.115 ± 0.011	$6.777 \pm 1.055 \times 10^{-2}$	$8.568 \pm 0.891 \times 10^{-2}$
9-7 O(5)	2.449297	9	3	–	–	$8.045 \pm 1.179 \times 10^{-2}$	0.101 ± 0.020	$8.139 \pm 1.064 \times 10^{-2}$
9-7 Q(3)	2.100664	9	3	$6.036 \pm 0.558 \times 10^{-2}$	0.152 ± 0.018	$8.909 \pm 0.840 \times 10^{-2}$	$7.087 \pm 0.892 \times 10^{-2}$	$9.402 \pm 0.927 \times 10^{-2}$
9-6 O(5)	1.475519	9	3	–	–	$5.235 \pm 0.564 \times 10^{-2}$	-	$6.492 \pm 0.615 \times 10^{-2}$
9-7 S(1)	1.942958	9	3	–	–	$8.258 \pm 0.803 \times 10^{-2}$	-	0.104 ± 0.010
9-6 O(6)	1.525166	9	4	–	–	$3.385 \pm 0.324 \times 10^{-2}$	-	–
9-7 Q(4)	2.123137	9	4	–	–	$3.689 \pm 0.403 \times 10^{-2}$	-	–
9-7 Q(5)	2.151876	9	5	$4.577 \pm 0.457 \times 10^{-2}$	–	$3.955 \pm 0.429 \times 10^{-2}$	$3.433 \pm 0.555 \times 10^{-2}$	$5.088 \pm 0.524 \times 10^{-2}$
9-7 Q(7)	2.230268	9	7	$2.750 \pm 0.395 \times 10^{-2}$	–	$2.368 \pm 0.337 \times 10^{-2}$	-	$2.839 \pm 0.339 \times 10^{-2}$
9-7 Q(8)	2.281426	9	8	–	–	-	-	$1.553 \pm 0.276 \times 10^{-2}$
10-7 O(2)	1.508549	10	0	–	–	0.113 ± 0.008	-	0.105 ± 0.008
10-7 O(3)	1.548849	10	1	$8.338 \pm 0.583 \times 10^{-2}$	–	0.125 ± 0.008	0.101 ± 0.011	0.119 ± 0.009
10-7 Q(1)	1.461391	10	1	–	–	-	0.274 ± 0.034	0.168 ± 0.013
10-8 Q(1)	2.322474	10	1	–	–	$8.491 \pm 1.015 \times 10^{-2}$	$5.730 \pm 1.283 \times 10^{-2}$	$9.216 \pm 1.079 \times 10^{-2}$
10-7 O(4)	1.595267	10	2	–	–	$7.881 \pm 0.595 \times 10^{-2}$	$6.185 \pm 0.822 \times 10^{-2}$	$6.979 \pm 0.548 \times 10^{-2}$
10-8 Q(2)	2.337184	10	2	–	–	$3.990 \pm 0.475 \times 10^{-2}$	$4.535 \pm 0.762 \times 10^{-2}$	$4.909 \pm 0.551 \times 10^{-2}$

Continued on next page...

Table 3.2 continued: H_2 line fluxes for the star forming region PDR survey (normalized to the 4-2 O(3) line).

Line ID	λ (μm)	v_u	J_u	Orion Bar	Horsehead Nebula	S 140	IC 63	NGC 2023
10-8 S(0)	2.225259	10	2	–	–	$3.168 \pm 0.413 \times 10^{-2}$	-	$2.558 \pm 0.323 \times 10^{-2}$
10-8 Q(3)	2.359611	10	3	–	–	$4.626 \pm 0.574 \times 10^{-2}$	-	$3.996 \pm 0.484 \times 10^{-2}$
10-8 S(1)	2.176855	10	3	$4.352 \pm 0.450 \times 10^{-2}$	$9.020 \pm 1.423 \times 10^{-2}$	$3.917 \pm 0.419 \times 10^{-2}$	$4.340 \pm 0.641 \times 10^{-2}$	$4.900 \pm 0.511 \times 10^{-2}$
10-7 O(5)	1.648305	10	3	$6.046 \pm 0.430 \times 10^{-2}$	–	$4.852 \pm 0.405 \times 10^{-2}$	-	$5.448 \pm 0.437 \times 10^{-2}$
10-7 Q(3)	1.482704	10	3	–	–	0.138 ± 0.012	-	$8.115 \pm 0.707 \times 10^{-2}$
10-8 S(2)	2.138638	10	4	–	–	-	-	$1.773 \pm 0.238 \times 10^{-2}$
10-7 Q(4)	1.500204	10	4	–	–	$3.236 \pm 0.352 \times 10^{-2}$	-	$5.041 \pm 0.394 \times 10^{-2}$
10-7 O(6)	1.708625	10	4	–	–	-	-	$1.511 \pm 0.174 \times 10^{-2}$
10-8 Q(4)	2.390217	10	4	–	–	$2.924 \pm 0.534 \times 10^{-2}$	-	$2.664 \pm 0.401 \times 10^{-2}$
10-8 Q(5)	2.429671	10	5	–	–	$2.375 \pm 0.417 \times 10^{-2}$	-	$2.379 \pm 0.361 \times 10^{-2}$
10-8 S(3)	2.110354	10	5	–	–	-	-	$2.635 \pm 0.526 \times 10^{-2}$
10-7 Q(7)	1.584507	10	7	–	–	-	-	$3.408 \pm 0.327 \times 10^{-2}$
10-7 Q(9)	1.674084	10	9	–	–	-	-	$1.716 \pm 0.179 \times 10^{-2}$
10-8 S(8)	2.122900	10	10	–	–	$2.573 \pm 0.316 \times 10^{-2}$	-	–
11-8 O(2)	1.712094	11	0	–	–	0.100 ± 0.008	$8.072 \pm 0.948 \times 10^{-2}$	$6.747 \pm 0.570 \times 10^{-2}$
11-8 O(3)	1.760924	11	1	–	–	0.111 ± 0.009	$6.896 \pm 0.871 \times 10^{-2}$	0.101 ± 0.009
11-8 Q(1)	1.657102	11	1	–	–	$9.804 \pm 0.707 \times 10^{-2}$	-	0.104 ± 0.008
11-8 S(0)	1.611071	11	2	–	–	-	-	$3.961 \pm 0.368 \times 10^{-2}$
11-8 S(1)	1.591504	11	3	–	–	$6.301 \pm 0.452 \times 10^{-2}$	$6.974 \pm 0.808 \times 10^{-2}$	$7.662 \pm 0.579 \times 10^{-2}$
11-8 Q(3)	1.687032	11	3	–	–	$3.998 \pm 0.358 \times 10^{-2}$	-	$5.371 \pm 0.449 \times 10^{-2}$
11-8 Q(4)	1.711844	11	4	–	–	$2.418 \pm 0.282 \times 10^{-2}$	-	$1.855 \pm 0.208 \times 10^{-2}$
11-8 S(2)	1.578830	11	4	–	–	$3.085 \pm 0.294 \times 10^{-2}$	-	$3.742 \pm 0.310 \times 10^{-2}$
11-8 S(3)	1.573164	11	5	–	–	$2.857 \pm 0.314 \times 10^{-2}$	$4.716 \pm 0.673 \times 10^{-2}$	$4.722 \pm 0.374 \times 10^{-2}$
11-8 Q(5)	1.744026	11	5	–	–	$2.765 \pm 0.311 \times 10^{-2}$	-	$2.239 \pm 0.236 \times 10^{-2}$
11-8 S(4)	1.574790	11	6	–	–	$7.518 \pm 0.576 \times 10^{-2}$	$2.606 \pm 0.524 \times 10^{-2}$	$1.601 \pm 0.170 \times 10^{-2}$

Continued on next page...

Table 3.2 continued: H_2 line fluxes for the star forming region PDR survey (normalized to the 4-2 O(3) line).

Line ID	λ (μm)	v_u	J_u	Orion Bar	Horsehead Nebula	S 140	IC 63	NGC 2023
11-8 S(5)	1.584201	11	7	–	–	-	-	$1.833 \pm 0.257 \times 10^{-2}$
12-9 O(2)	2.007052	12	0	–	–	-	-	$3.879 \pm 0.435 \times 10^{-2}$
12-9 Q(1)	1.940134	12	1	–	–	-	-	$5.883 \pm 0.611 \times 10^{-2}$
12-9 O(3)	2.069971	12	1	–	–	$8.326 \pm 0.772 \times 10^{-2}$	$6.107 \pm 0.812 \times 10^{-2}$	$6.456 \pm 0.639 \times 10^{-2}$
12-9 O(4)	2.146015	12	2	–	–	$4.696 \pm 0.490 \times 10^{-2}$	$2.833 \pm 0.535 \times 10^{-2}$	$3.491 \pm 0.378 \times 10^{-2}$
12-9 Q(3)	1.986307	12	3	–	–	$3.437 \pm 0.362 \times 10^{-2}$	-	$3.228 \pm 0.334 \times 10^{-2}$
12-9 O(5)	2.237053	12	3	–	–	-	-	$2.625 \pm 0.425 \times 10^{-2}$
12-9 Q(5)	2.076394	12	5	–	–	-	-	$1.342 \pm 0.192 \times 10^{-2}$
13-9 O(2)	1.657943	13	0	–	–	$1.337 \pm 0.211 \times 10^{-2}$	-	$1.245 \pm 0.147 \times 10^{-2}$
13-9 Q(1)	1.614808	13	1	–	–	$2.190 \pm 0.245 \times 10^{-2}$	$3.216 \pm 0.488 \times 10^{-2}$	$2.665 \pm 0.234 \times 10^{-2}$
13-9 O(3)	1.703755	13	1	–	–	$2.377 \pm 0.258 \times 10^{-2}$	-	$2.340 \pm 0.224 \times 10^{-2}$
13-9 Q(2)	1.633121	13	2	–	–	$2.247 \pm 0.242 \times 10^{-2}$	-	$1.359 \pm 0.152 \times 10^{-2}$
13-9 S(1)	1.576873	13	3	–	–	$6.883 \pm 0.517 \times 10^{-2}$	-	$1.875 \pm 0.208 \times 10^{-2}$
13-9 Q(3)	1.661581	13	3	–	–	$3.159 \pm 0.281 \times 10^{-2}$	-	–
13-9 S(2)	1.581345	13	4	–	–	-	-	$1.308 \pm 0.205 \times 10^{-2}$
13-9 S(3)	1.596931	13	5	–	–	$4.337 \pm 0.496 \times 10^{-2}$	-	–
14-9 O(3)	1.543789	14	1	–	–	-	-	$3.167 \pm 0.385 \times 10^{-2}$
14-9 O(4)	1.598285	14	2	–	–	-	-	$1.787 \pm 0.226 \times 10^{-2}$

populations in each PDR relative to this reference level, and Figure 3.3 shows the level populations in excitation diagrams.

We detect a large number of lines in each PDR. The extremely high S/N spectrum we obtained of NGC 2023 is especially impressive with over 200 transitions observed. The $v = 4$ rotational ladder, as seen in the excitation diagram of Figure 3.4, shows many transitions up to 4-3 S(19) which arises from $v = 4$, $J = 21$ at an excitation energy of $E_u/k = 45202$ K.

3.6 Cloudy Model Fits

We fit each PDR in our sample with a single constant density Cloudy model (Ferland et al. 2013; see Chapter 1.6 for an in depth discussion of Cloudy) using the parameters for the density (n_H), illuminating star ($T_{\star,\mathrm{eff}}$), and UV field intensity (χ) given in Table 3.1. For the Orion Bar, we use our best-fit model from Chapter 2. To facilitate comparison with the data, the level populations from the models are normalized to the population of the $v = 4$, $J = 1$ state as derived from the flux of the 4-2 O(3) line. We show the Cloudy models overlaid on the excitation diagrams in Figure 3.5 and the ratios of the level populations in the data to the model predictions (N_{obs}/N_{model}) in Figure 3.6 and Table 3.3. These Cloudy models all recreate the observed level populations to within 1.0 dex, confirming the H_2 in the PDRs are primarily UV-excited and not shocked. A few interesting patterns emerge in nearly all the data-to-model ratios.

We utilized a grid of constant density and constant temperature models to find the best fit to the Orion Bar observations in Chapter 2.4.1.2. The best-fit model from the grid fit the Orion Bar level populations within 0.5 dex. For the other PDRs, we ran single constant density models assuming n_H reported in the literature (see Table 3.1) and we let the temperature vary as a free parameter. These single constant density models give fits to the observed level populations within 1.0 dex. For the other PDRs in our survey that are not the Orion Bar, we have not yet optimized our model fits with grids. The better fit for the Orion Bar model provided by the the model grid vs. the single constant density models fit to the other PDRs clearly demonstrates the utility of model grids. Future work with these IGRINS data will utilize model grids to find optimal fits and help constrain the temperatures and densities within these

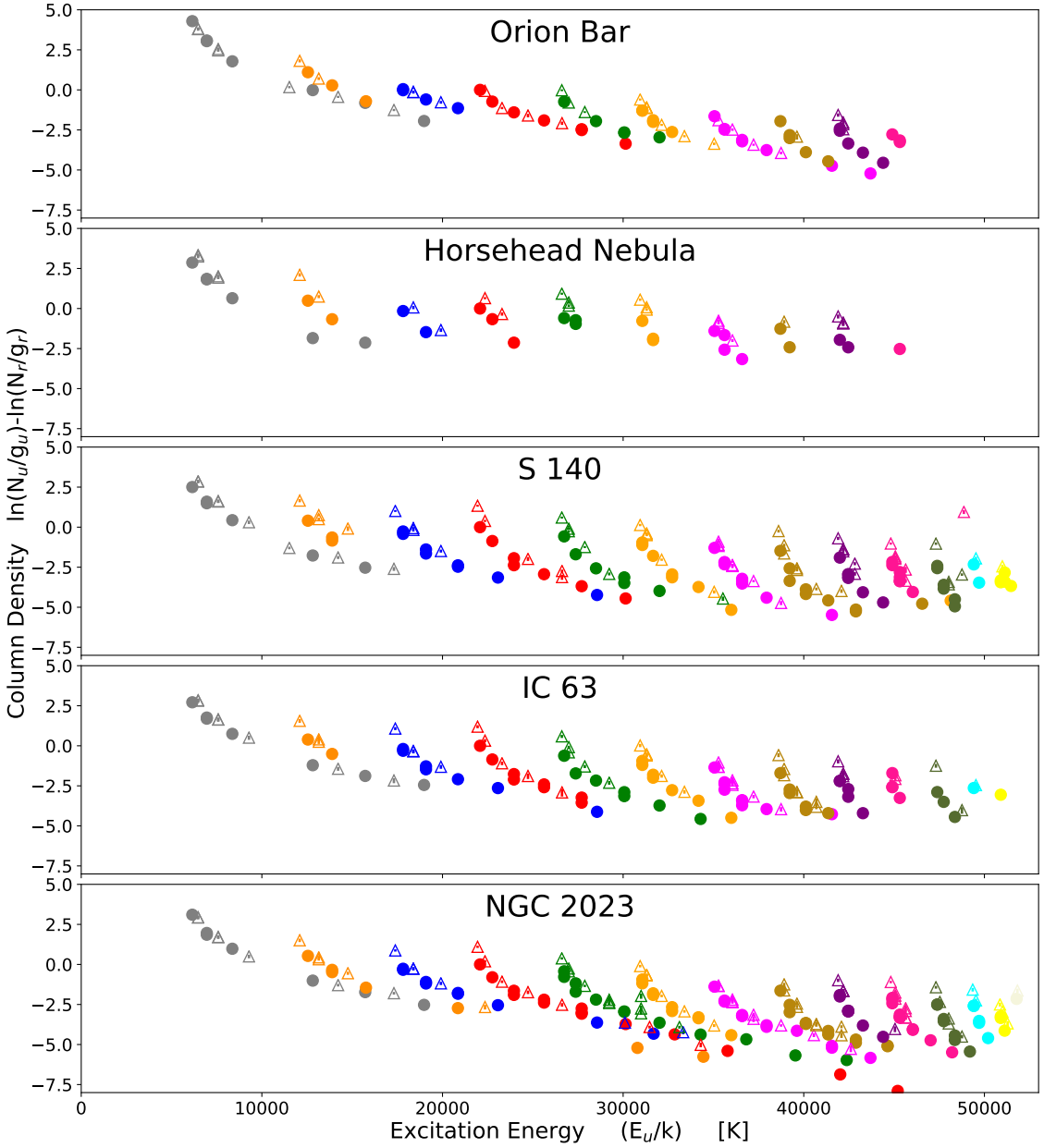

Figure 3.3: Excitation diagrams showing the H_2 rovibrational level populations derived from our IGRINS observations of H_2 emission lines in each of the star forming region PDRs in this survey. Note the similarities and slight differences among the PDRs. See Chapter 1.5.1 for a detailed explanation of excitation diagrams.

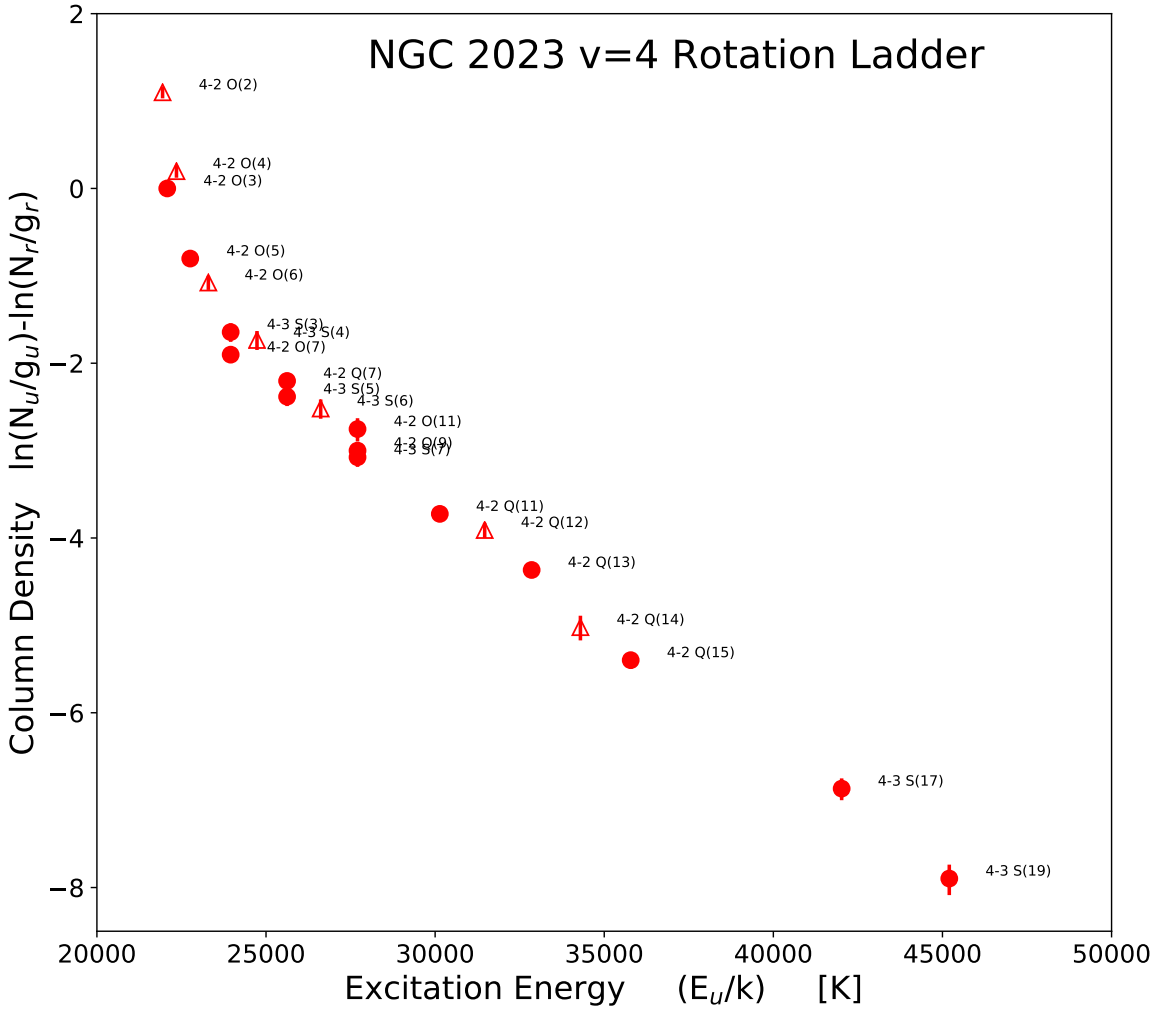

Figure 3.4: Excitation diagram showing the H_2 rovibrational level populations of the $v = 4$ rotational ladder in NGC 2023. The high S/N IGRINS spectrum of NGC 2023 gives impressive results, allowing us to see transitions up to 4-3 S(19) and to infer level populations in $v = 4$ across a large dynamic range in column density and a large range of J.

Table 3.3: H_2 column densities in star forming region PDRs and comparison to Cloudy Models

H_2 Line ID	λ (μm)	v_u	J_u	Orion Bar		Horsehead Nebula		S 140		IC 63		NGC 2023	
				$\ln\left(\frac{N_u}{g_u}/\frac{N_r}{g_r}\right)$	N_u/N_m	$\ln\left(\frac{N_u}{g_u}/\frac{N_r}{g_r}\right)$	N_u/N_m	$\ln\left(\frac{N_u}{g_u}/\frac{N_r}{g_r}\right)$	N_u/N_m	$\ln\left(\frac{N_u}{g_u}/\frac{N_r}{g_r}\right)$	N_u/N_m	$\ln\left(\frac{N_u}{g_u}/\frac{N_r}{g_r}\right)$	N_u/N_m
1-0 Q(1)	2.406592	1	1	$4.291^{+0.090}_{-0.099}$	0.82	$2.869^{+0.096}_{-0.107}$	2.94	$2.505^{+0.096}_{-0.106}$	2.13	$2.717^{+0.114}_{-0.129}$	2.55	$3.105^{+0.102}_{-0.113}$	4.24
1-0 Q(2)	2.413439	1	2	$3.793^{+0.091}_{-0.100}$	0.85	$3.249^{+0.097}_{-0.107}$	4.14	$2.855^{+0.096}_{-0.107}$	2.65	$2.818^{+0.115}_{-0.130}$	3.59	$2.933^{+0.102}_{-0.113}$	4.50
1-0 S(0)	2.223290	1	2	$3.819^{+0.084}_{-0.092}$	0.87	$3.341^{+0.091}_{-0.100}$	4.56	$2.851^{+0.091}_{-0.100}$	2.65	$2.841^{+0.111}_{-0.125}$	3.68	$2.938^{+0.097}_{-0.107}$	4.52
1-0 Q(3)	2.423730	1	3	$3.043^{+0.091}_{-0.100}$	0.90	$1.850^{+0.097}_{-0.107}$	1.74	$1.493^{+0.097}_{-0.107}$	1.45	$1.695^{+0.115}_{-0.130}$	1.47	$1.855^{+0.102}_{-0.114}$	2.00
1-0 S(1)	2.121834	1	3	$3.083^{+0.081}_{-0.088}$	0.94	$1.819^{+0.087}_{-0.096}$	1.69	$1.591^{+0.087}_{-0.096}$	1.60	$1.762^{+0.109}_{-0.122}$	1.57	$1.962^{+0.094}_{-0.103}$	2.23
1-0 Q(4)	2.437489	1	4	$2.554^{+0.091}_{-0.100}$	1.43	$2.014^{+0.098}_{-0.109}$	3.57	$1.631^{+0.097}_{-0.108}$	2.13	$1.639^{+0.115}_{-0.130}$	2.85	$1.719^{+0.102}_{-0.114}$	2.87
1-0 S(2)	2.033758	1	4	$2.466^{+0.077}_{-0.084}$	1.31	$1.926^{+0.084}_{-0.092}$	3.26	$1.598^{+0.084}_{-0.092}$	2.07	$1.641^{+0.107}_{-0.119}$	2.85	$1.701^{+0.091}_{-0.100}$	2.82
1-0 S(3)	1.957559	1	5	$1.783^{+0.074}_{-0.080}$	1.75	$0.643^{+0.082}_{-0.089}$	2.32	$0.436^{+0.081}_{-0.088}$	1.63	$0.746^{+0.105}_{-0.117}$	2.69	$0.979^{+0.088}_{-0.097}$	2.50
1-0 Q(6)	2.475559	1	6	–	–	–	–	$0.307^{+0.100}_{-0.111}$	1.32	$0.509^{+0.119}_{-0.135}$	1.38	$0.501^{+0.106}_{-0.118}$	1.38
1-0 S(6)	1.788050	1	8	$0.173^{+0.066}_{-0.071}$	0.65	–	–	$-1.297^{+0.075}_{-0.081}$	0.35	–	–	–	–
1-0 S(7)	1.747955	1	9	$-0.014^{+0.064}_{-0.068}$	0.73	$-1.847^{+0.104}_{-0.116}$	0.34	$-1.769^{+0.073}_{-0.078}$	0.33	$-1.212^{+0.099}_{-0.110}$	0.71	$-1.010^{+0.079}_{-0.086}$	0.64
1-0 S(8)	1.714738	1	10	$-0.435^{+0.063}_{-0.068}$	0.44	–	–	$-1.892^{+0.087}_{-0.095}$	0.29	$-1.434^{+0.111}_{-0.125}$	0.45	$-1.292^{+0.079}_{-0.086}$	0.45
1-0 S(9)	1.687761	1	11	$-0.808^{+0.061}_{-0.065}$	0.45	$-2.133^{+0.098}_{-0.108}$	0.28	$-2.531^{+0.071}_{-0.076}$	0.21	$-1.881^{+0.097}_{-0.108}$	0.31	$-1.729^{+0.076}_{-0.083}$	0.39
1-0 S(10)	1.666475	1	12	$-1.255^{+0.066}_{-0.070}$	0.33	–	–	$-2.604^{+0.110}_{-0.124}$	0.24	$-2.169^{+0.143}_{-0.167}$	0.33	$-1.797^{+0.080}_{-0.086}$	0.39
1-0 S(11)	1.650413	1	13	$-1.942^{+0.066}_{-0.070}$	0.26	–	–	–	–	$-2.445^{+0.121}_{-0.138}$	0.35	$-2.524^{+0.079}_{-0.086}$	0.30
2-1 S(0)	2.355605	2	2	$1.814^{+0.089}_{-0.098}$	2.00	$2.102^{+0.097}_{-0.107}$	4.05	$1.660^{+0.095}_{-0.105}$	2.05	$1.560^{+0.114}_{-0.129}$	3.64	$1.508^{+0.101}_{-0.112}$	2.94
2-1 S(1)	2.247716	2	3	$1.103^{+0.085}_{-0.093}$	1.79	$0.490^{+0.092}_{-0.101}$	1.41	$0.404^{+0.092}_{-0.101}$	1.30	$0.391^{+0.112}_{-0.126}$	1.24	$0.533^{+0.098}_{-0.108}$	1.48
2-1 S(2)	2.154216	2	4	$0.707^{+0.082}_{-0.089}$	1.39	$0.746^{+0.089}_{-0.098}$	2.41	$0.502^{+0.089}_{-0.097}$	1.67	$0.401^{+0.110}_{-0.123}$	1.84	$0.442^{+0.095}_{-0.105}$	1.69
2-0 O(6)	1.486989	2	4	–	–	–	–	$0.747^{+0.064}_{-0.068}$	2.13	$0.251^{+0.120}_{-0.137}$	1.59	$0.322^{+0.076}_{-0.083}$	1.50
2-0 O(7)	1.546377	2	5	–	–	–	–	$-0.837^{+0.075}_{-0.081}$	1.43	$-0.508^{+0.107}_{-0.120}$	3.66	$-0.481^{+0.071}_{-0.077}$	1.69
2-1 S(3)	2.073482	2	5	$0.283^{+0.079}_{-0.086}$	1.80	$-0.669^{+0.087}_{-0.095}$	2.37	$-0.646^{+0.086}_{-0.094}$	1.72	–	–	$-0.339^{+0.092}_{-0.102}$	1.95
2-1 S(4)	2.004109	2	6	–	–	–	–	–	–	–	–	$-0.548^{+0.090}_{-0.099}$	1.20
2-0 O(8)	1.610517	2	6	–	–	–	–	$-0.086^{+0.130}_{-0.150}$	2.59	–	–	–	–

Continued on next page...

Table 3.3 continued: H_2 line fluxes for the star forming region PDR survey (normalized to the 4-2 O(3) line).

H_2 Line ID	λ (μm)	v_u	J_u	Orion Bar		Horsehead Nebula		S 140		IC 63		NGC 2023	
				$\ln\left(\frac{N_u}{g_u}/\frac{N_r}{g_r}\right)$	N_u/N_m	$\ln\left(\frac{N_u}{g_u}/\frac{N_r}{g_r}\right)$	N_u/N_m	$\ln\left(\frac{N_u}{g_u}/\frac{N_r}{g_r}\right)$	N_u/N_m	$\ln\left(\frac{N_u}{g_u}/\frac{N_r}{g_r}\right)$	N_u/N_m	$\ln\left(\frac{N_u}{g_u}/\frac{N_r}{g_r}\right)$	N_u/N_m
2-0 O(9)	1.679641	2	7	$-0.711^{+0.085}_{-0.093}$	1.16	–	–	–	–	–	–	$-1.450^{+0.099}_{-0.110}$	0.80
2-1 S(9)	1.790479	2	11	–	–	–	–	–	–	–	–	$-2.727^{+0.084}_{-0.091}$	0.29
2-1 S(10)	1.768836	2	12	–	–	–	–	–	–	–	–	$-2.659^{+0.134}_{-0.155}$	0.47
2-1 S(15)	1.738801	2	17	–	–	–	–	–	–	–	–	$-5.210^{+0.118}_{-0.134}$	0.15
2-1 S(17)	1.758762	2	19	–	–	–	–	–	–	–	–	$-5.761^{+0.095}_{-0.105}$	0.28
3-1 O(4)	1.467714	3	2	–	–	–	–	$1.011^{+0.057}_{-0.060}$	1.80	$1.076^{+0.088}_{-0.096}$	3.31	$0.874^{+0.067}_{-0.072}$	2.37
3-1 O(5)	1.522033	3	3	$-0.021^{+0.051}_{-0.054}$	1.19	–	–	$-0.419^{+0.060}_{-0.063}$	1.12	$-0.310^{+0.089}_{-0.098}$	1.46	$-0.271^{+0.067}_{-0.072}$	1.36
3-2 S(1)	2.386471	3	3	$0.045^{+0.090}_{-0.099}$	1.27	$-0.158^{+0.104}_{-0.116}$	1.57	$-0.268^{+0.096}_{-0.107}$	1.30	$-0.200^{+0.116}_{-0.131}$	1.63	$-0.334^{+0.101}_{-0.113}$	1.28
3-1 O(6)	1.581171	3	4	$-0.132^{+0.059}_{-0.062}$	1.22	–	–	$-0.058^{+0.066}_{-0.070}$	1.82	$-0.325^{+0.100}_{-0.111}$	1.62	$-0.259^{+0.072}_{-0.077}$	1.55
3-2 S(2)	2.287045	3	4	$-0.136^{+0.087}_{-0.095}$	1.21	$0.068^{+0.096}_{-0.107}$	2.31	$-0.171^{+0.093}_{-0.103}$	1.62	$-0.348^{+0.113}_{-0.128}$	1.59	$-0.266^{+0.099}_{-0.110}$	1.54
3-1 O(7)	1.645348	3	5	–	–	–	–	$-1.646^{+0.070}_{-0.076}$	1.28	$-1.468^{+0.100}_{-0.111}$	2.47	$-1.190^{+0.075}_{-0.081}$	1.53
3-2 S(3)	2.201399	3	5	$-0.599^{+0.084}_{-0.091}$	1.62	$-1.475^{+0.096}_{-0.106}$	2.08	$-1.392^{+0.090}_{-0.099}$	1.65	$-1.284^{+0.111}_{-0.125}$	2.97	$-1.095^{+0.096}_{-0.106}$	1.69
3-2 S(4)	2.128015	3	6	$-0.773^{+0.081}_{-0.088}$	1.55	$-1.344^{+0.104}_{-0.117}$	1.92	$-1.490^{+0.088}_{-0.097}$	1.39	$-1.311^{+0.111}_{-0.125}$	1.78	$-1.181^{+0.094}_{-0.104}$	1.39
3-2 S(5)	2.065584	3	7	$-1.142^{+0.079}_{-0.085}$	2.03	–	–	$-2.383^{+0.086}_{-0.095}$	1.06	$-2.087^{+0.109}_{-0.123}$	1.58	$-1.782^{+0.092}_{-0.101}$	1.21
3-1 O(9)	1.789869	3	7	–	–	–	–	$-2.470^{+0.127}_{-0.145}$	0.98	–	–	$-1.830^{+0.089}_{-0.097}$	1.16
3-2 S(7)	1.969231	3	9	–	–	–	–	$-3.147^{+0.093}_{-0.102}$	0.60	$-2.640^{+0.116}_{-0.132}$	1.17	$-2.545^{+0.094}_{-0.104}$	0.63
3-1 Q(13)	1.502463	3	13	–	–	–	–	$-4.234^{+0.088}_{-0.097}$	0.45	$-4.121^{+0.141}_{-0.164}$	1.03	$-3.629^{+0.073}_{-0.079}$	0.70
3-1 Q(14)	1.533983	3	14	–	–	–	–	–	–	–	–	$-3.637^{+0.092}_{-0.102}$	0.42
3-1 Q(15)	1.568584	3	15	–	–	–	–	–	–	–	–	$-4.323^{+0.087}_{-0.095}$	0.40
3-1 Q(16)	1.606526	3	16	–	–	–	–	–	–	–	–	$-4.230^{+0.116}_{-0.131}$	0.40
4-2 O(2)	1.461133	4	0	–	–	–	–	$1.336^{+0.056}_{-0.059}$	1.79	$1.195^{+0.088}_{-0.096}$	1.78	$1.100^{+0.064}_{-0.069}$	1.75
4-2 O(3)	1.509865	4	1	$0.000^{+0.050}_{-0.053}$	1.00	$0.000^{+0.062}_{-0.066}$	1.00	$0.000^{+0.058}_{-0.062}$	1.00	$0.000^{+0.088}_{-0.096}$	1.00	$0.000^{+0.067}_{-0.071}$	1.00
4-2 O(4)	1.563515	4	2	$-0.064^{+0.054}_{-0.057}$	1.04	$0.648^{+0.064}_{-0.069}$	1.74	$0.390^{+0.062}_{-0.066}$	1.35	$0.322^{+0.091}_{-0.100}$	1.32	$0.197^{+0.070}_{-0.075}$	1.27

Continued on next page...

Table 3.3 continued: H_2 line fluxes for the star forming region PDR survey (normalized to the 4-2 O(3) line).

H_2 Line ID	λ (μm)	v_u	J_u	Orion Bar		Horsehead Nebula		S 140		IC 63		NGC 2023	
				$\ln\left(\frac{N_u}{g_u}/\frac{N_r}{g_r}\right)$	N_u/N_m	$\ln\left(\frac{N_u}{g_u}/\frac{N_r}{g_r}\right)$	N_u/N_m	$\ln\left(\frac{N_u}{g_u}/\frac{N_r}{g_r}\right)$	N_u/N_m	$\ln\left(\frac{N_u}{g_u}/\frac{N_r}{g_r}\right)$	N_u/N_m	$\ln\left(\frac{N_u}{g_u}/\frac{N_r}{g_r}\right)$	N_u/N_m
4-2 O(5)	1.622299	4	3	$-0.733^{+0.057}_{-0.061}$	0.97	$-0.665^{+0.075}_{-0.082}$	1.76	$-0.866^{+0.065}_{-0.070}$	1.26	$-0.854^{+0.094}_{-0.103}$	1.62	$-0.802^{+0.073}_{-0.079}$	1.25
4-2 O(6)	1.686462	4	4	$-1.133^{+0.067}_{-0.072}$	0.78	$-0.342^{+0.095}_{-0.105}$	2.58	–	–	$-1.091^{+0.104}_{-0.116}$	1.08	$-1.077^{+0.077}_{-0.084}$	0.92
4-2 O(7)	1.756281	4	5	$-1.403^{+0.066}_{-0.070}$	1.29	–	–	$-2.376^{+0.077}_{-0.083}$	1.06	$-2.104^{+0.106}_{-0.118}$	1.96	$-1.902^{+0.080}_{-0.087}$	1.15
4-3 S(3)	2.344453	4	5	–	–	$-2.133^{+0.136}_{-0.157}$	1.80	$-1.937^{+0.096}_{-0.106}$	1.64	$-1.766^{+0.116}_{-0.131}$	2.75	$-1.644^{+0.101}_{-0.112}$	1.49
4-3 S(4)	2.266764	4	6	$-1.598^{+0.101}_{-0.113}$	1.12	–	–	$-1.982^{+0.113}_{-0.127}$	1.55	$-1.887^{+0.156}_{-0.185}$	1.94	$-1.734^{+0.103}_{-0.114}$	1.23
4-2 Q(7)	1.459195	4	7	–	–	–	–	–	–	$-2.411^{+0.114}_{-0.129}$	2.42	$-2.203^{+0.067}_{-0.071}$	1.32
4-3 S(5)	2.200974	4	7	$-1.907^{+0.085}_{-0.093}$	1.67	–	–	$-2.936^{+0.095}_{-0.105}$	1.15	$-2.584^{+0.118}_{-0.133}$	2.03	$-2.383^{+0.097}_{-0.107}$	1.10
4-2 Q(8)	1.477736	4	8	–	–	–	–	$-2.735^{+0.083}_{-0.090}$	1.20	–	–	–	–
4-3 S(6)	2.145873	4	8	$-2.078^{+0.098}_{-0.108}$	1.08	–	–	$-3.118^{+0.146}_{-0.170}$	0.82	$-2.910^{+0.203}_{-0.256}$	0.89	$-2.519^{+0.104}_{-0.117}$	0.72
4-2 Q(9)	1.498876	4	9	–	–	–	–	$-3.686^{+0.065}_{-0.069}$	0.69	$-3.549^{+0.101}_{-0.113}$	0.82	$-3.000^{+0.067}_{-0.071}$	0.68
4-2 O(11)	2.099586	4	9	$-2.456^{+0.137}_{-0.159}$	1.44	–	–	–	–	–	–	$-2.753^{+0.124}_{-0.141}$	0.87
4-3 S(7)	2.100426	4	9	$-2.507^{+0.088}_{-0.097}$	1.37	–	–	–	–	$-3.234^{+0.161}_{-0.192}$	1.12	$-3.076^{+0.099}_{-0.110}$	0.63
4-2 Q(11)	1.549455	4	11	$-3.357^{+0.055}_{-0.059}$	0.73	–	–	$-4.451^{+0.073}_{-0.079}$	0.38	–	–	$-3.724^{+0.070}_{-0.075}$	0.40
4-2 Q(12)	1.579217	4	12	–	–	–	–	–	–	–	–	$-3.909^{+0.083}_{-0.090}$	0.41
4-2 Q(13)	1.612237	4	13	–	–	–	–	–	–	–	–	$-4.366^{+0.077}_{-0.084}$	0.38
4-2 Q(14)	1.648782	4	14	–	–	–	–	–	–	–	–	$-5.021^{+0.131}_{-0.151}$	0.13
4-2 Q(15)	1.689178	4	15	–	–	–	–	–	–	–	–	$-5.398^{+0.090}_{-0.099}$	0.15
4-3 S(17)	2.047446	4	19	–	–	–	–	–	–	–	–	$-6.868^{+0.117}_{-0.133}$	0.13
4-3 S(19)	2.116170	4	21	–	–	–	–	–	–	–	–	$-7.897^{+0.159}_{-0.189}$	0.04
5-3 O(2)	1.560736	5	0	$-0.023^{+0.054}_{-0.057}$	1.29	$0.927^{+0.064}_{-0.068}$	1.37	$0.600^{+0.061}_{-0.066}$	1.13	$0.590^{+0.091}_{-0.100}$	0.95	$0.379^{+0.070}_{-0.075}$	0.80
5-3 Q(1)	1.492933	5	1	–	–	–	–	–	–	–	–	$-0.428^{+0.066}_{-0.070}$	1.02
5-3 O(3)	1.613520	5	1	$-0.737^{+0.057}_{-0.060}$	0.80	$-0.597^{+0.068}_{-0.073}$	0.85	$-0.576^{+0.064}_{-0.069}$	0.85	$-0.622^{+0.093}_{-0.102}$	0.88	$-0.775^{+0.072}_{-0.078}$	0.72
5-3 Q(2)	1.497982	5	2	–	–	$0.375^{+0.068}_{-0.073}$	2.08	$-0.096^{+0.058}_{-0.061}$	1.30	$-0.085^{+0.088}_{-0.096}$	1.36	$-0.254^{+0.066}_{-0.071}$	1.03

Continued on next page...

Table 3.3 continued: H_2 line fluxes for the star forming region PDR survey (normalized to the 4-2 O(3) line).

H_2 Line ID	λ (μm)	v_u	J_u	Orion Bar		Horsehead Nebula		S 140		IC 63		NGC 2023	
				$\ln\left(\frac{N_u}{g_u}/\frac{N_r}{g_r}\right)$	N_u/N_m	$\ln\left(\frac{N_u}{g_u}/\frac{N_r}{g_r}\right)$	N_u/N_m	$\ln\left(\frac{N_u}{g_u}/\frac{N_r}{g_r}\right)$	N_u/N_m	$\ln\left(\frac{N_u}{g_u}/\frac{N_r}{g_r}\right)$	N_u/N_m	$\ln\left(\frac{N_u}{g_u}/\frac{N_r}{g_r}\right)$	N_u/N_m
5-3 O(4)	1.671814	5	2	$-0.788^{+0.061}_{-0.065}$	0.82	$0.182^{+0.073}_{-0.079}$	1.72	$-0.253^{+0.068}_{-0.073}$	1.11	$-0.408^{+0.096}_{-0.106}$	0.98	$-0.429^{+0.076}_{-0.082}$	0.87
5-3 Q(3)	1.505588	5	3	–	–	$-0.729^{+0.071}_{-0.077}$	3.09	–	–	–	–	$-1.181^{+0.067}_{-0.071}$	1.59
5-3 O(5)	1.735889	5	3	–	–	$-0.959^{+0.101}_{-0.112}$	2.46	$-1.693^{+0.071}_{-0.077}$	0.96	$-1.725^{+0.099}_{-0.110}$	1.41	$-1.703^{+0.079}_{-0.086}$	0.94
5-3 Q(4)	1.515792	5	4	$-1.385^{+0.053}_{-0.056}$	0.96	–	–	$-1.241^{+0.060}_{-0.063}$	1.72	$-1.290^{+0.091}_{-0.100}$	2.13	$-1.338^{+0.067}_{-0.072}$	1.30
5-3 Q(5)	1.528648	5	5	$-1.950^{+0.052}_{-0.055}$	1.31	–	–	$-2.571^{+0.061}_{-0.064}$	1.11	$-2.171^{+0.090}_{-0.099}$	1.23	$-2.196^{+0.068}_{-0.073}$	0.68
5-3 O(8)	1.966206	5	6	–	–	–	–	–	–	–	–	$-2.409^{+0.105}_{-0.117}$	1.00
5-3 Q(6)	1.544232	5	6	–	–	–	–	$-2.918^{+0.086}_{-0.094}$	1.04	$-2.305^{+0.109}_{-0.122}$	2.25	$-2.206^{+0.071}_{-0.077}$	1.23
5-4 S(4)	2.424758	5	6	–	–	–	–	–	–	–	–	$-2.350^{+0.140}_{-0.162}$	1.07
5-3 O(9)	2.057127	5	7	$-2.656^{+0.102}_{-0.114}$	1.37	–	–	$-3.135^{+0.115}_{-0.130}$	1.34	$-2.895^{+0.155}_{-0.184}$	1.11	$-2.956^{+0.106}_{-0.118}$	0.56
5-3 Q(7)	1.562635	5	7	$-2.674^{+0.054}_{-0.057}$	1.34	–	–	$-3.487^{+0.063}_{-0.068}$	0.94	$-3.141^{+0.093}_{-0.102}$	0.87	$-2.936^{+0.070}_{-0.075}$	0.57
5-4 S(6)	2.297937	5	8	–	–	–	–	–	–	–	–	$-1.968^{+0.149}_{-0.175}$	1.79
5-3 O(10)	2.156073	5	8	–	–	–	–	–	–	–	–	$-2.754^{+0.181}_{-0.221}$	0.81
5-3 Q(8)	1.583975	5	8	–	–	–	–	–	–	–	–	$-3.051^{+0.077}_{-0.083}$	0.60
5-3 Q(9)	1.608398	5	9	$-2.963^{+0.057}_{-0.061}$	1.60	–	–	$-3.983^{+0.069}_{-0.074}$	0.88	$-3.728^{+0.100}_{-0.111}$	1.17	$-3.641^{+0.073}_{-0.079}$	0.54
5-3 Q(10)	1.636082	5	10	–	–	–	–	–	–	–	–	$-3.915^{+0.083}_{-0.090}$	0.26
5-3 Q(11)	1.667248	5	11	–	–	–	–	–	–	$-4.567^{+0.128}_{-0.147}$	0.73	$-4.379^{+0.080}_{-0.087}$	0.36
5-3 Q(12)	1.702170	5	12	–	–	–	–	$-4.457^{+0.124}_{-0.142}$	0.54	–	–	–	–
5-4 S(11)	2.153924	5	13	–	–	–	–	–	–	–	–	$-4.674^{+0.150}_{-0.176}$	0.27
5-4 S(13)	2.152833	5	15	–	–	–	–	–	–	–	–	$-5.681^{+0.130}_{-0.149}$	0.11
5-4 S(15)	2.181794	5	17	–	–	–	–	–	–	–	–	$-5.968^{+0.120}_{-0.136}$	0.15
6-4 O(2)	1.675032	6	0	$-0.601^{+0.061}_{-0.065}$	1.16	$0.554^{+0.070}_{-0.076}$	1.74	$0.134^{+0.068}_{-0.073}$	1.38	$0.021^{+0.096}_{-0.106}$	0.93	$-0.104^{+0.076}_{-0.082}$	0.81
6-4 Q(1)	1.601534	6	1	$-1.288^{+0.056}_{-0.060}$	0.78	$-0.773^{+0.067}_{-0.071}$	1.21	$-0.957^{+0.064}_{-0.068}$	0.99	$-0.941^{+0.092}_{-0.102}$	1.16	$-0.939^{+0.072}_{-0.077}$	1.05
6-4 O(3)	1.732641	6	1	$-1.295^{+0.064}_{-0.068}$	0.77	–	–	$-1.112^{+0.071}_{-0.077}$	0.85	$-1.193^{+0.098}_{-0.109}$	0.90	$-1.180^{+0.079}_{-0.085}$	0.82

Continued on next page...

Table 3.3 continued: H_2 line fluxes for the star forming region PDR survey (normalized to the 4-2 O(3) line).

H_2 Line ID	λ (μm)	v_u	J_u	Orion Bar		Horsehead Nebula		S 140		IC 63		NGC 2023	
				$\ln\left(\frac{N_u}{g_u}/\frac{N_r}{g_r}\right)$	N_u/N_m	$\ln\left(\frac{N_u}{g_u}/\frac{N_r}{g_r}\right)$	N_u/N_m	$\ln\left(\frac{N_u}{g_u}/\frac{N_r}{g_r}\right)$	N_u/N_m	$\ln\left(\frac{N_u}{g_u}/\frac{N_r}{g_r}\right)$	N_u/N_m	$\ln\left(\frac{N_u}{g_u}/\frac{N_r}{g_r}\right)$	N_u/N_m
6-4 S(0)	1.536891	6	2	$-1.098^{+0.054}_{-0.057}$	0.89	$0.078^{+0.064}_{-0.068}$	2.48	$-0.498^{+0.060}_{-0.064}$	1.40	$-0.576^{+0.090}_{-0.099}$	1.37	$-0.680^{+0.068}_{-0.073}$	1.06
6-4 Q(2)	1.607390	6	2	$-1.124^{+0.057}_{-0.061}$	0.87	$-0.068^{+0.068}_{-0.073}$	2.14	$-0.389^{+0.064}_{-0.069}$	1.56	$-0.607^{+0.094}_{-0.103}$	1.33	$-0.657^{+0.072}_{-0.078}$	1.09
6-4 O(4)	1.796524	6	2	$-1.117^{+0.071}_{-0.076}$	0.87	–	–	$-0.451^{+0.075}_{-0.081}$	1.47	$-0.526^{+0.102}_{-0.113}$	1.44	$-0.665^{+0.082}_{-0.089}$	1.08
6-4 S(1)	1.501560	6	3	$-1.893^{+0.050}_{-0.053}$	0.93	$-1.885^{+0.069}_{-0.074}$	1.05	$-1.792^{+0.058}_{-0.062}$	1.11	$-1.808^{+0.088}_{-0.096}$	1.00	$-1.804^{+0.066}_{-0.071}$	0.70
6-4 Q(3)	1.616224	6	3	$-1.998^{+0.057}_{-0.061}$	0.84	$-1.971^{+0.072}_{-0.077}$	0.97	–	–	$-1.992^{+0.093}_{-0.103}$	0.84	$-1.904^{+0.073}_{-0.078}$	0.64
6-4 S(2)	1.471213	6	4	–	–	–	–	$-1.951^{+0.127}_{-0.146}$	1.28	–	–	–	–
6-4 Q(4)	1.628094	6	4	$-2.185^{+0.061}_{-0.065}$	0.74	–	–	$-2.031^{+0.068}_{-0.073}$	1.18	$-1.882^{+0.096}_{-0.106}$	1.65	$-1.966^{+0.074}_{-0.080}$	0.91
6-4 O(7)	2.029684	6	5	$-2.629^{+0.081}_{-0.088}$	1.05	–	–	$-2.948^{+0.090}_{-0.099}$	1.20	$-2.771^{+0.115}_{-0.130}$	1.15	$-2.668^{+0.092}_{-0.101}$	0.63
6-4 Q(5)	1.643084	6	5	–	–	–	–	$-3.131^{+0.067}_{-0.072}$	1.00	–	–	$-2.909^{+0.074}_{-0.080}$	0.50
6-4 Q(6)	1.661304	6	6	$-2.889^{+0.065}_{-0.070}$	0.85	–	–	–	–	$-2.873^{+0.103}_{-0.115}$	2.40	$-2.929^{+0.076}_{-0.083}$	0.94
6-4 O(9)	2.224960	6	7	–	–	–	–	–	–	–	–	$-3.300^{+0.108}_{-0.121}$	0.92
6-4 Q(7)	1.682897	6	7	–	–	–	–	$-3.737^{+0.074}_{-0.080}$	1.39	$-3.429^{+0.103}_{-0.115}$	2.17	$-3.359^{+0.077}_{-0.083}$	0.87
6-4 Q(8)	1.708041	6	8	$-3.364^{+0.073}_{-0.078}$	0.89	–	–	$-4.039^{+0.093}_{-0.103}$	0.77	–	–	$-3.814^{+0.084}_{-0.091}$	0.36
6-4 Q(9)	1.736958	6	9	–	–	–	–	$-5.162^{+0.115}_{-0.130}$	0.40	$-4.495^{+0.118}_{-0.134}$	0.85	$-4.416^{+0.081}_{-0.088}$	0.33
6-3 Q(19)	1.478765	6	19	–	–	–	–	$-4.587^{+0.115}_{-0.130}$	6.21	–	–	–	–
7-5 Q(1)	1.728799	7	1	$-1.645^{+0.064}_{-0.068}$	0.82	$-1.400^{+0.095}_{-0.105}$	1.03	$-1.293^{+0.071}_{-0.076}$	1.02	$-1.352^{+0.098}_{-0.109}$	1.40	$-1.387^{+0.078}_{-0.085}$	1.13
7-5 S(0)	1.658492	7	2	–	–	$-0.764^{+0.084}_{-0.092}$	1.74	$-1.101^{+0.068}_{-0.072}$	1.17	$-1.311^{+0.097}_{-0.107}$	1.11	$-1.327^{+0.075}_{-0.081}$	0.88
7-5 Q(2)	1.735762	7	2	$-1.892^{+0.069}_{-0.074}$	0.55	$-0.894^{+0.087}_{-0.095}$	1.53	$-1.173^{+0.072}_{-0.078}$	1.08	$-1.309^{+0.100}_{-0.111}$	1.12	$-1.349^{+0.079}_{-0.086}$	0.86
7-5 O(4)	1.943455	7	2	–	–	–	–	$-0.908^{+0.082}_{-0.089}$	1.41	$-1.040^{+0.108}_{-0.121}$	1.46	–	–
7-5 Q(3)	1.746280	7	3	$-2.481^{+0.067}_{-0.072}$	0.77	$-1.658^{+0.089}_{-0.098}$	2.24	$-2.182^{+0.072}_{-0.078}$	1.20	$-2.279^{+0.101}_{-0.112}$	1.08	$-2.257^{+0.080}_{-0.086}$	0.69
7-5 S(1)	1.620548	7	3	$-2.441^{+0.057}_{-0.061}$	0.81	$-2.570^{+0.082}_{-0.089}$	0.90	$-2.321^{+0.065}_{-0.070}$	1.05	$-2.388^{+0.094}_{-0.103}$	0.97	$-2.321^{+0.073}_{-0.079}$	0.64
7-5 O(5)	2.022053	7	3	–	–	–	–	$-2.202^{+0.084}_{-0.092}$	1.18	$-2.739^{+0.126}_{-0.144}$	0.68	–	–
7-5 S(2)	1.588294	7	4	–	–	$-1.997^{+0.082}_{-0.089}$	1.98	$-2.400^{+0.064}_{-0.069}$	1.16	$-2.438^{+0.096}_{-0.106}$	0.92	$-2.312^{+0.071}_{-0.077}$	0.65

Continued on next page...

Table 3.3 continued: H_2 line fluxes for the star forming region PDR survey (normalized to the 4-2 O(3) line).

H_2 Line ID	λ (μm)	v_u	J_u	Orion Bar		Horsehead Nebula		S 140		IC 63		NGC 2023	
				$\ln\left(\frac{N_u}{g_u}/\frac{N_r}{g_r}\right)$	N_u/N_m	$\ln\left(\frac{N_u}{g_u}/\frac{N_r}{g_r}\right)$	N_u/N_m	$\ln\left(\frac{N_u}{g_u}/\frac{N_r}{g_r}\right)$	N_u/N_m	$\ln\left(\frac{N_u}{g_u}/\frac{N_r}{g_r}\right)$	N_u/N_m	$\ln\left(\frac{N_u}{g_u}/\frac{N_r}{g_r}\right)$	N_u/N_m
7-5 Q(4)	1.760446	7	4	$-2.479^{+0.072}_{-0.078}$	0.90	–	–	$-2.369^{+0.076}_{-0.083}$	1.19	$-2.335^{+0.108}_{-0.121}$	1.02	$-2.361^{+0.081}_{-0.088}$	0.62
7-5 O(6)	2.109001	7	4	–	–	–	–	$-2.428^{+0.117}_{-0.133}$	1.12	$-2.164^{+0.164}_{-0.196}$	1.21	$-2.198^{+0.104}_{-0.116}$	0.73
7-5 O(7)	2.204989	7	5	$-3.123^{+0.094}_{-0.103}$	0.93	–	–	$-3.225^{+0.103}_{-0.115}$	1.54	$-3.421^{+0.164}_{-0.197}$	1.13	$-3.209^{+0.100}_{-0.111}$	0.60
7-5 Q(5)	1.778390	7	5	–	–	–	–	$-3.380^{+0.077}_{-0.084}$	1.31	$-3.711^{+0.124}_{-0.142}$	0.84	$-3.157^{+0.082}_{-0.090}$	0.64
7-5 S(3)	1.561510	7	5	$-3.212^{+0.054}_{-0.058}$	0.85	$-3.158^{+0.078}_{-0.084}$	2.01	$-3.520^{+0.063}_{-0.067}$	1.14	$-3.396^{+0.092}_{-0.101}$	1.16	$-3.220^{+0.070}_{-0.075}$	0.60
7-5 O(8)	2.310862	7	6	–	–	–	–	–	–	–	–	$-3.394^{+0.169}_{-0.203}$	0.55
7-5 S(4)	1.540006	7	6	$-3.423^{+0.064}_{-0.068}$	0.69	–	–	$-3.365^{+0.066}_{-0.071}$	1.33	$-3.170^{+0.099}_{-0.110}$	1.59	$-3.143^{+0.070}_{-0.075}$	0.70
7-5 O(9)	2.427661	7	7	–	–	–	–	–	–	–	–	$-3.895^{+0.145}_{-0.170}$	0.34
7-5 S(5)	1.523623	7	7	$-3.761^{+0.054}_{-0.057}$	1.04	–	–	$-4.403^{+0.064}_{-0.068}$	0.83	$-3.953^{+0.093}_{-0.103}$	0.62	$-3.797^{+0.068}_{-0.073}$	0.38
7-5 S(6)	1.512240	7	8	$-3.938^{+0.078}_{-0.085}$	0.71	–	–	$-4.732^{+0.117}_{-0.133}$	0.54	$-3.957^{+0.128}_{-0.147}$	0.85	$-3.808^{+0.072}_{-0.077}$	0.48
7-5 S(7)	1.505784	7	9	–	–	–	–	–	–	–	–	$-4.144^{+0.077}_{-0.084}$	0.64
7-5 S(8)	1.504232	7	10	–	–	–	–	–	–	–	–	$-4.412^{+0.109}_{-0.122}$	0.52
7-5 Q(11)	1.979270	7	11	$-4.734^{+0.102}_{-0.114}$	0.92	–	–	$-5.481^{+0.127}_{-0.146}$	0.38	–	–	$-5.198^{+0.106}_{-0.119}$	0.16
7-5 S(9)	1.507629	7	11	–	–	–	–	$-4.946^{+0.126}_{-0.145}$	0.65	$-4.270^{+0.139}_{-0.161}$	0.91	$-5.085^{+0.104}_{-0.116}$	0.18
7-5 Q(12)	2.032316	7	12	–	–	–	–	–	–	–	–	$-5.271^{+0.170}_{-0.205}$	0.17
7-5 Q(13)	2.092904	7	13	$-5.218^{+0.115}_{-0.130}$	0.80	–	–	–	–	–	–	$-5.834^{+0.128}_{-0.147}$	0.16
8-6 O(2)	1.970799	8	0	–	–	–	–	$-0.246^{+0.083}_{-0.091}$	1.61	$-0.580^{+0.113}_{-0.128}$	1.06	–	–
8-6 O(3)	2.041830	8	1	$-1.954^{+0.079}_{-0.086}$	0.87	$-1.263^{+0.091}_{-0.100}$	1.41	$-1.480^{+0.085}_{-0.093}$	1.07	$-1.703^{+0.108}_{-0.121}$	0.99	$-1.638^{+0.091}_{-0.100}$	0.85
8-6 S(0)	1.804886	8	2	–	–	–	–	$-1.642^{+0.081}_{-0.089}$	0.95	$-1.834^{+0.129}_{-0.148}$	0.96	$-1.623^{+0.084}_{-0.091}$	0.91
8-6 O(4)	2.121592	8	2	–	–	$-0.823^{+0.099}_{-0.109}$	2.41	$-1.128^{+0.088}_{-0.097}$	1.59	$-1.445^{+0.112}_{-0.127}$	1.42	$-1.244^{+0.094}_{-0.104}$	1.33
8-6 O(5)	2.210763	8	3	$-2.825^{+0.095}_{-0.105}$	0.60	$-2.420^{+0.167}_{-0.201}$	1.52	$-2.572^{+0.096}_{-0.106}$	1.12	$-2.729^{+0.128}_{-0.147}$	1.06	$-2.524^{+0.098}_{-0.109}$	0.81
8-6 S(1)	1.763952	8	3	$-3.008^{+0.077}_{-0.083}$	0.50	–	–	$-3.355^{+0.089}_{-0.098}$	0.51	$-2.949^{+0.117}_{-0.133}$	0.85	$-2.981^{+0.083}_{-0.090}$	0.52
8-6 S(2)	1.729672	8	4	–	–	–	–	$-2.675^{+0.078}_{-0.084}$	1.28	$-2.892^{+0.125}_{-0.143}$	1.19	$-2.649^{+0.081}_{-0.088}$	0.81

Continued on next page...

Table 3.3 continued: H_2 line fluxes for the star forming region PDR survey (normalized to the 4-2 O(3) line).

H_2 Line ID	λ (μm)	v_u	J_u	Orion Bar		Horsehead Nebula		S 140		IC 63		NGC 2023	
				$\ln\left(\frac{N_u}{g_u}/\frac{N_r}{g_r}\right)$	N_u/N_m	$\ln\left(\frac{N_u}{g_u}/\frac{N_r}{g_r}\right)$	N_u/N_m	$\ln\left(\frac{N_u}{g_u}/\frac{N_r}{g_r}\right)$	N_u/N_m	$\ln\left(\frac{N_u}{g_u}/\frac{N_r}{g_r}\right)$	N_u/N_m	$\ln\left(\frac{N_u}{g_u}/\frac{N_r}{g_r}\right)$	N_u/N_m
8-6 O(6)	2.310167	8	4	$-2.919^{+0.155}_{-0.184}$	0.56	–	–	$-2.569^{+0.120}_{-0.137}$	1.43	$-2.897^{+0.206}_{-0.260}$	1.18	$-2.445^{+0.107}_{-0.120}$	1.00
8-6 S(3)	1.701803	8	5	$-3.890^{+0.068}_{-0.073}$	0.55	–	–	$-4.172^{+0.076}_{-0.082}$	0.93	$-3.797^{+0.104}_{-0.116}$	1.33	$-3.715^{+0.078}_{-0.085}$	0.56
8-6 O(7)	2.420824	8	5	–	–	–	–	–	–	–	–	$-3.671^{+0.130}_{-0.149}$	0.58
8-6 Q(5)	1.943225	8	5	–	–	–	–	$-3.882^{+0.091}_{-0.100}$	1.24	$-4.011^{+0.140}_{-0.162}$	1.07	$-3.658^{+0.092}_{-0.101}$	0.59
8-6 Q(6)	1.970468	8	6	–	–	–	–	–	–	$-3.501^{+0.209}_{-0.264}$	2.40	$-3.714^{+0.122}_{-0.138}$	0.73
8-6 S(4)	1.680153	8	6	–	–	–	–	$-3.857^{+0.082}_{-0.089}$	1.34	$-3.810^{+0.129}_{-0.148}$	1.76	$-3.797^{+0.081}_{-0.089}$	0.67
8-6 Q(7)	2.003105	8	7	–	–	–	–	–	–	–	–	$-4.153^{+0.119}_{-0.135}$	0.46
8-6 S(5)	1.664584	8	7	$-4.460^{+0.068}_{-0.073}$	0.75	–	–	$-4.574^{+0.074}_{-0.080}$	1.13	$-4.204^{+0.103}_{-0.115}$	1.01	$-4.371^{+0.077}_{-0.083}$	0.37
8-6 Q(8)	2.041614	8	8	–	–	–	–	–	–	–	–	$-4.421^{+0.144}_{-0.168}$	0.35
8-6 S(6)	1.655023	8	8	–	–	–	–	$-3.985^{+0.105}_{-0.117}$	1.57	–	–	$-3.885^{+0.087}_{-0.095}$	0.59
8-6 Q(9)	2.086607	8	9	–	–	–	–	$-5.145^{+0.155}_{-0.184}$	0.74	–	–	$-4.886^{+0.114}_{-0.128}$	0.29
8-6 S(7)	1.651475	8	9	–	–	–	–	$-5.258^{+0.112}_{-0.126}$	0.66	–	–	$-4.692^{+0.081}_{-0.089}$	0.36
8-6 Q(11)	2.199456	8	11	–	–	–	–	–	–	–	–	$-5.105^{+0.137}_{-0.159}$	0.31
8-6 S(9)	1.662916	8	11	–	–	–	–	–	–	–	–	$-5.074^{+0.105}_{-0.118}$	0.32
8-5 Q(13)	1.477482	8	13	–	–	–	–	$-4.779^{+0.104}_{-0.117}$	3.38	–	–	–	–
9-7 O(2)	2.172715	9	0	$-1.567^{+0.098}_{-0.108}$	0.89	$-0.494^{+0.115}_{-0.130}$	1.87	$-0.698^{+0.091}_{-0.100}$	1.67	$-0.967^{+0.119}_{-0.135}$	1.29	$-0.986^{+0.097}_{-0.107}$	1.09
9-7 Q(1)	2.073187	9	1	$-2.553^{+0.088}_{-0.097}$	1.04	–	–	–	–	$-2.203^{+0.113}_{-0.127}$	1.20	$-1.913^{+0.093}_{-0.102}$	1.11
9-7 O(3)	2.253724	9	1	$-2.422^{+0.093}_{-0.102}$	1.19	$-1.955^{+0.129}_{-0.148}$	1.23	$-1.900^{+0.093}_{-0.103}$	1.14	$-2.186^{+0.121}_{-0.138}$	1.22	$-2.001^{+0.098}_{-0.109}$	1.02
9-7 O(4)	2.345581	9	2	$-2.457^{+0.133}_{-0.154}$	0.54	$-0.933^{+0.126}_{-0.144}$	2.87	$-1.511^{+0.100}_{-0.111}$	1.49	$-1.737^{+0.132}_{-0.152}$	1.49	$-1.642^{+0.103}_{-0.115}$	1.26
9-7 S(0)	1.987350	9	2	$-2.133^{+0.096}_{-0.106}$	0.75	$-0.886^{+0.111}_{-0.125}$	3.00	$-1.383^{+0.088}_{-0.097}$	1.69	$-1.748^{+0.123}_{-0.140}$	1.47	$-1.639^{+0.091}_{-0.100}$	1.27
9-7 Q(2)	2.084098	9	2	$-2.031^{+0.111}_{-0.125}$	0.83	$-0.907^{+0.149}_{-0.176}$	2.94	$-1.373^{+0.091}_{-0.100}$	1.71	$-1.898^{+0.145}_{-0.169}$	1.26	$-1.664^{+0.099}_{-0.110}$	1.24
9-7 O(5)	2.449297	9	3	–	–	–	–	$-2.934^{+0.137}_{-0.158}$	1.22	$-2.703^{+0.180}_{-0.220}$	2.39	$-2.922^{+0.123}_{-0.140}$	1.04
9-7 Q(3)	2.100664	9	3	$-3.344^{+0.088}_{-0.097}$	0.63	$-2.422^{+0.109}_{-0.123}$	2.63	$-2.955^{+0.090}_{-0.099}$	1.19	$-3.183^{+0.119}_{-0.134}$	1.48	$-2.901^{+0.094}_{-0.104}$	1.06

Continued on next page...

Table 3.3 continued: H_2 line fluxes for the star forming region PDR survey (normalized to the 4-2 O(3) line).

H_2 Line ID	λ (μm)	v_u	J_u	Orion Bar		Horsehead Nebula		S 140		IC 63		NGC 2023	
				$\ln\left(\frac{N_u}{g_u}/\frac{N_r}{g_r}\right)$	N_u/N_m	$\ln\left(\frac{N_u}{g_u}/\frac{N_r}{g_r}\right)$	N_u/N_m	$\ln\left(\frac{N_u}{g_u}/\frac{N_r}{g_r}\right)$	N_u/N_m	$\ln\left(\frac{N_u}{g_u}/\frac{N_r}{g_r}\right)$	N_u/N_m	$\ln\left(\frac{N_u}{g_u}/\frac{N_r}{g_r}\right)$	N_u/N_m
9-6 O(5)	1.475519	9	3	–	–	–	–	$-3.108^{+0.102}_{-0.114}$	1.02	–	–	$-2.892^{+0.091}_{-0.100}$	1.07
9-7 S(1)	1.942958	9	3	–	–	–	–	$-3.170^{+0.093}_{-0.102}$	0.96	–	–	$-2.937^{+0.090}_{-0.099}$	1.02
9-6 O(6)	1.525166	9	4	–	–	–	–	$-2.275^{+0.091}_{-0.101}$	2.91	–	–	–	–
9-7 Q(4)	2.123137	9	4	–	–	–	–	$-2.913^{+0.104}_{-0.116}$	1.54	–	–	–	–
9-7 Q(5)	2.151876	9	5	$-3.920^{+0.095}_{-0.105}$	0.73	–	–	$-4.066^{+0.103}_{-0.115}$	1.60	$-4.207^{+0.150}_{-0.176}$	1.62	$-3.814^{+0.098}_{-0.109}$	0.82
9-7 Q(7)	2.230268	9	7	$-4.551^{+0.134}_{-0.155}$	0.89	–	–	$-4.701^{+0.133}_{-0.154}$	1.48	–	–	$-4.520^{+0.113}_{-0.127}$	0.48
9-7 Q(8)	2.281426	9	8	–	–	–	–	–	–	–	–	$-4.030^{+0.163}_{-0.195}$	0.80
10-7 O(2)	1.508549	10	0	–	–	–	–	$-1.022^{+0.066}_{-0.071}$	1.88	–	–	$-1.098^{+0.071}_{-0.076}$	1.75
10-7 O(3)	1.548849	10	1	$-2.779^{+0.068}_{-0.073}$	0.74	–	–	$-2.372^{+0.063}_{-0.067}$	0.83	$-2.583^{+0.105}_{-0.117}$	0.65	$-2.424^{+0.070}_{-0.076}$	0.60
10-7 Q(1)	1.461391	10	1	–	–	–	–	–	–	$-1.705^{+0.118}_{-0.133}$	1.56	$-2.193^{+0.072}_{-0.077}$	0.76
10-8 Q(1)	2.322474	10	1	–	–	–	–	$-2.170^{+0.113}_{-0.127}$	1.02	$-2.564^{+0.202}_{-0.254}$	0.66	$-2.089^{+0.111}_{-0.124}$	0.84
10-7 O(4)	1.595267	10	2	–	–	–	–	$-1.827^{+0.073}_{-0.078}$	1.66	$-2.070^{+0.125}_{-0.143}$	1.84	$-1.949^{+0.076}_{-0.082}$	1.49
10-8 Q(2)	2.337184	10	2	–	–	–	–	$-1.967^{+0.112}_{-0.127}$	1.44	$-1.839^{+0.155}_{-0.184}$	2.31	$-1.760^{+0.106}_{-0.119}$	1.80
10-8 S(0)	2.225259	10	2	–	–	–	–	$-1.926^{+0.123}_{-0.140}$	1.50	–	–	$-2.140^{+0.119}_{-0.135}$	1.23
10-8 Q(3)	2.359611	10	3	–	–	–	–	$-3.133^{+0.117}_{-0.133}$	1.64	–	–	$-3.279^{+0.114}_{-0.129}$	1.16
10-8 S(1)	2.176855	10	3	$-3.254^{+0.098}_{-0.109}$	0.99	$-2.525^{+0.147}_{-0.172}$	4.28	$-3.359^{+0.102}_{-0.113}$	1.31	$-3.256^{+0.138}_{-0.160}$	2.50	$-3.135^{+0.099}_{-0.110}$	1.34
10-7 O(5)	1.648305	10	3	$-3.156^{+0.069}_{-0.074}$	1.10	–	–	$-3.376^{+0.080}_{-0.087}$	1.29	–	–	$-3.260^{+0.077}_{-0.084}$	1.18
10-7 Q(3)	1.482704	10	3	–	–	–	–	$-2.801^{+0.083}_{-0.091}$	2.29	–	–	$-3.331^{+0.084}_{-0.091}$	1.10
10-8 S(2)	2.138638	10	4	–	–	–	–	–	–	–	–	$-3.304^{+0.126}_{-0.144}$	1.11
10-7 Q(4)	1.500204	10	4	–	–	–	–	$-3.348^{+0.103}_{-0.115}$	1.66	–	–	$-2.905^{+0.075}_{-0.081}$	1.66
10-7 O(6)	1.708625	10	4	–	–	–	–	–	–	–	–	$-3.330^{+0.109}_{-0.122}$	1.09
10-8 Q(4)	2.390217	10	4	–	–	–	–	$-2.647^{+0.168}_{-0.202}$	3.33	–	–	$-2.740^{+0.140}_{-0.163}$	1.96
10-8 Q(5)	2.429671	10	5	–	–	–	–	$-4.048^{+0.162}_{-0.193}$	2.84	–	–	$-4.047^{+0.141}_{-0.164}$	1.09

Continued on next page...

Table 3.3 continued: H_2 line fluxes for the star forming region PDR survey (normalized to the 4-2 O(3) line).

H_2 Line ID	λ (μm)	v_u	J_u	Orion Bar		Horsehead Nebula		S 140		IC 63		NGC 2023	
				$\ln\left(\frac{N_u}{g_u}/\frac{N_r}{g_r}\right)$	N_u/N_m	$\ln\left(\frac{N_u}{g_u}/\frac{N_r}{g_r}\right)$	N_u/N_m	$\ln\left(\frac{N_u}{g_u}/\frac{N_r}{g_r}\right)$	N_u/N_m	$\ln\left(\frac{N_u}{g_u}/\frac{N_r}{g_r}\right)$	N_u/N_m	$\ln\left(\frac{N_u}{g_u}/\frac{N_r}{g_r}\right)$	N_u/N_m
10-8 S(3)	2.110354	10	5	–	–	–	–	–	–	–	–	$-4.085^{+0.182}_{-0.223}$	1.05
10-7 Q(7)	1.584507	10	7	–	–	–	–	–	–	–	–	$-4.736^{+0.092}_{-0.101}$	0.59
10-7 Q(9)	1.674084	10	9	–	–	–	–	–	–	–	–	$-5.487^{+0.099}_{-0.110}$	0.44
10-8 S(8)	2.122900	10	10	–	–	–	–	$0.951^{+0.116}_{-0.131}$	980.38	–	–	–	–
11-8 O(2)	1.712094	11	0	–	–	–	–	$-1.028^{+0.073}_{-0.079}$	1.83	$-1.245^{+0.111}_{-0.125}$	1.41	$-1.424^{+0.081}_{-0.088}$	0.93
11-8 O(3)	1.760924	11	1	–	–	–	–	$-2.418^{+0.076}_{-0.082}$	0.93	$-2.889^{+0.119}_{-0.135}$	0.65	$-2.507^{+0.082}_{-0.090}$	0.77
11-8 Q(1)	1.657102	11	1	–	–	–	–	$-2.559^{+0.070}_{-0.075}$	0.81	–	–	$-2.502^{+0.076}_{-0.082}$	0.78
11-8 S(0)	1.611071	11	2	–	–	–	–	–	–	–	–	$-2.337^{+0.089}_{-0.097}$	1.19
11-8 S(1)	1.591504	11	3	–	–	–	–	$-3.602^{+0.069}_{-0.074}$	1.05	$-3.501^{+0.110}_{-0.123}$	1.15	$-3.407^{+0.073}_{-0.079}$	0.74
11-8 Q(3)	1.687032	11	3	–	–	–	–	$-3.839^{+0.086}_{-0.094}$	0.83	–	–	$-3.544^{+0.080}_{-0.087}$	0.65
11-8 Q(4)	1.711844	11	4	–	–	–	–	$-3.418^{+0.110}_{-0.124}$	2.00	–	–	$-3.684^{+0.107}_{-0.119}$	0.83
11-8 S(2)	1.578830	11	4	–	–	–	–	$-3.568^{+0.091}_{-0.100}$	1.72	–	–	$-3.375^{+0.079}_{-0.086}$	1.14
11-8 S(3)	1.573164	11	5	–	–	–	–	$-4.942^{+0.104}_{-0.117}$	1.91	$-4.441^{+0.133}_{-0.154}$	4.92	$-4.440^{+0.076}_{-0.083}$	1.14
11-8 Q(5)	1.744026	11	5	–	–	–	–	$-4.505^{+0.107}_{-0.119}$	2.96	–	–	$-4.716^{+0.100}_{-0.112}$	0.87
11-8 S(4)	1.574790	11	6	–	–	–	–	$-2.958^{+0.074}_{-0.080}$	8.94	$-4.017^{+0.183}_{-0.225}$	2.86	$-4.505^{+0.101}_{-0.112}$	0.66
11-8 S(5)	1.584201	11	7	–	–	–	–	–	–	–	–	$-5.439^{+0.131}_{-0.151}$	0.48
12-9 O(2)	2.007052	12	0	–	–	–	–	–	–	–	–	$-1.572^{+0.106}_{-0.119}$	0.39
12-9 Q(1)	1.940134	12	1	–	–	–	–	–	–	–	–	$-2.595^{+0.099}_{-0.110}$	0.74
12-9 O(3)	2.069971	12	1	–	–	–	–	$-2.326^{+0.089}_{-0.097}$	0.94	$-2.636^{+0.125}_{-0.143}$	0.86	$-2.581^{+0.094}_{-0.104}$	0.75
12-9 O(4)	2.146015	12	2	–	–	–	–	$-1.949^{+0.099}_{-0.110}$	1.66	$-2.455^{+0.173}_{-0.209}$	1.70	$-2.246^{+0.103}_{-0.115}$	1.46
12-9 Q(3)	1.986307	12	3	–	–	–	–	$-3.465^{+0.100}_{-0.111}$	1.28	–	–	$-3.527^{+0.098}_{-0.109}$	0.95
12-9 O(5)	2.237053	12	3	–	–	–	–	–	–	–	–	$-3.644^{+0.150}_{-0.176}$	0.85
12-9 Q(5)	2.076394	12	5	–	–	–	–	–	–	–	–	$-4.599^{+0.134}_{-0.154}$	0.60

Continued on next page...

Table 3.3 continued: H_2 line fluxes for the star forming region PDR survey (normalized to the 4-2 O(3) line).

H_2 Line ID	λ (μm)	v_u	J_u	Orion Bar		Horsehead Nebula		S 140		IC 63		NGC 2023	
				$\ln\left(\frac{N_u}{g_u}/\frac{N_r}{g_r}\right)$	N_u/N_m	$\ln\left(\frac{N_u}{g_u}/\frac{N_r}{g_r}\right)$	N_u/N_m	$\ln\left(\frac{N_u}{g_u}/\frac{N_r}{g_r}\right)$	N_u/N_m	$\ln\left(\frac{N_u}{g_u}/\frac{N_r}{g_r}\right)$	N_u/N_m	$\ln\left(\frac{N_u}{g_u}/\frac{N_r}{g_r}\right)$	N_u/N_m
13-9 O(2)	1.657943	13	0	–	–	–	–	$-2.428^{+0.146}_{-0.171}$	0.32	–	–	$-2.500^{+0.112}_{-0.126}$	0.31
13-9 Q(1)	1.614808	13	1	–	–	–	–	$-3.440^{+0.106}_{-0.119}$	0.36	$-3.056^{+0.141}_{-0.165}$	0.92	$-3.244^{+0.084}_{-0.092}$	0.63
13-9 O(3)	1.703755	13	1	–	–	–	–	$-3.324^{+0.103}_{-0.115}$	0.40	–	–	$-3.340^{+0.091}_{-0.100}$	0.57
13-9 Q(2)	1.633121	13	2	–	–	–	–	$-2.446^{+0.102}_{-0.114}$	0.95	–	–	$-2.948^{+0.106}_{-0.118}$	0.94
13-9 S(1)	1.576873	13	3	–	–	–	–	$-2.835^{+0.072}_{-0.078}$	2.65	–	–	$-4.135^{+0.105}_{-0.117}$	0.80
13-9 Q(3)	1.661581	13	3	–	–	–	–	$-3.400^{+0.085}_{-0.093}$	1.51	–	–	–	–
13-9 S(2)	1.581345	13	4	–	–	–	–	–	–	–	–	$-3.680^{+0.145}_{-0.170}$	0.86
13-9 S(3)	1.596931	13	5	–	–	–	–	$-3.671^{+0.108}_{-0.122}$	4.92	–	–	–	–
14-9 O(3)	1.543789	14	1	–	–	–	–	–	–	–	–	$-2.150^{+0.115}_{-0.130}$	1.78
14-9 O(4)	1.598285	14	2	–	–	–	–	–	–	–	–	$-1.634^{+0.119}_{-0.135}$	9.69

PDRs.

The Cloudy models presented here do not properly reproduce transitions from high J levels in the $v = 1$ rotational ladder, with the models overpredicting their level populations for every PDR in our sample. This holds true for the model grid fit for the Orion Bar and the single model fits for the other PDRs. This also appears to be the case for the high J levels in other rotational ladders in NGC 2023, where our high signal-to-noise data probes to very high J (e.g. the $v = 4$ rotational ladder seen in Figure 3.4). As discussed in Chapter 2.4.1.2 and Le et al. (2016), this discrepancy might be due to "formation pumping" where H_2 forms in excited rovibrational states on dust grains. This mechanism might be the dominant mechanism populating the high J levels. Cloudy uses the formation pumping prescription of Takahashi & Uehara (2001), and other formation pumping prescriptions in Cloudy have been shown to significantly change the high J levels (as discussed in Chapter 2.4.1.2). Since the level populations at high J in every PDR are consistently overpredicted by the Cloudy models, this suggests that the same mechanism is active in all PDRs. If the mechanism responsible for the effect is indeed formation pumping, these observations may help refine our understanding.

3.7 PDR Comparison

3.7.1 Qualitative Comparison

Qualitatively, the level populations seen in Table 3.3 and Figure 1.5.1 appear similar across all the star forming region PDRs in our survey, showing the same sawtooth pattern indicative of UV excitation. This is expected since the spectrum of UV-excited H_2 depends mainly on known physical constants and is fairly invariant to the conditions within the gas (Black & van Dishoeck, 1987; Sternberg & Dalgarno, 1989; Shaw et al., 2005).

While the excitation diagrams of the PDRs generally look similar, the level populations in the Orion Bar show stronger collisional modification than the others. This is likely because the Orion Bar is warmer than the other PDRs considered here. The $v = 1$ rotational ladder for Orion has larger level populations and all the rotational ladders have shallower slopes (higher rotational temperatures) than the other PDRs. In Chapter 2, we found the gas temperature in the Orion Bar to be 625 K. Chap-

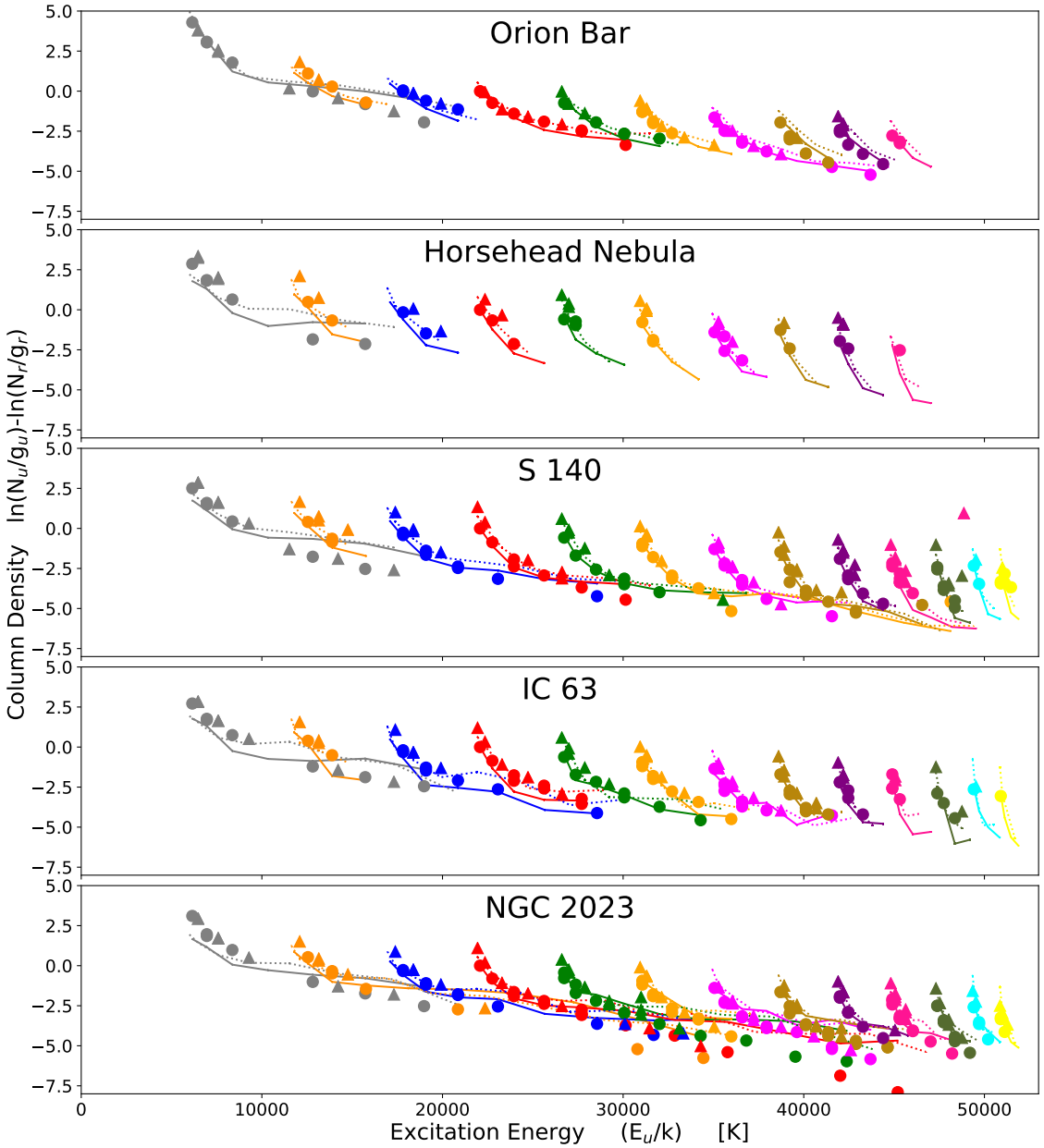

Figure 3.5: Excitation diagrams of all the observed PDRs, with the respective Cloudy model fits overlaid as solid lines for the ortho levels and and dashed lines for the para levels.

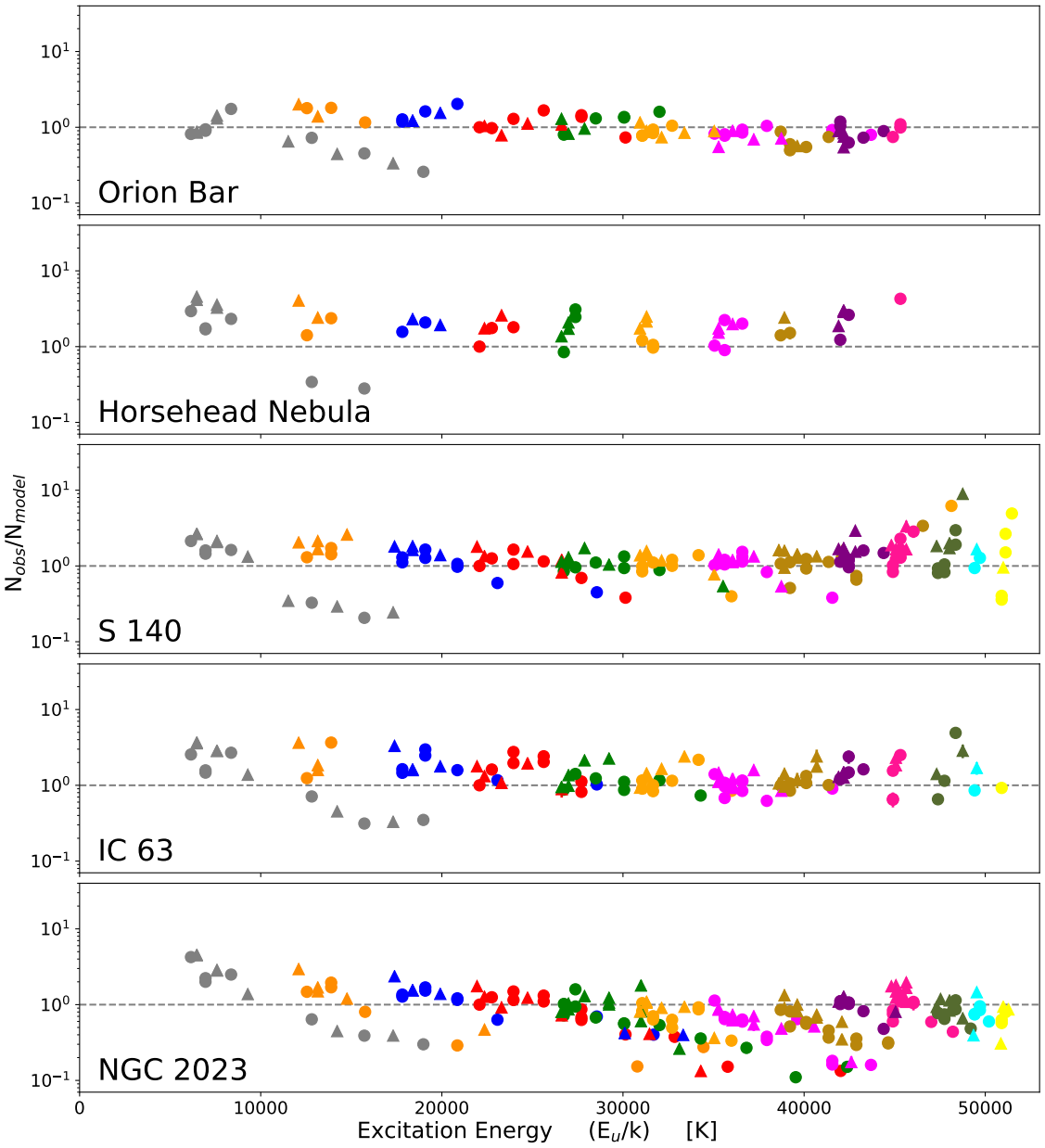

Figure 3.6: Semi-log plots of the ratios of the observed rovibrational level populations in our data (N_{obs}) to the model predictions (N_{model}) shown in Figure 3.5. The horizontal dashed line represents a ratio of unity where the data and model are in perfect agreement. Deviations from unity show where the level populations are not exactly matched by the model predictions.

ter 1.5.2 details how warmer temperatures increase collisional effects on the level populations of H_2 in a PDR. A higher temperature increases the rate of collisions, which increases the collisional excitation of the low excitation energy states (mainly $v = 1$) and increases the collisional de-excitation of the high excitation states (mainly $v > 1$). This leads to larger level populations in the $v = 1$ rotational ladder and lower level populations in the $v > 1$ rotational ladders. Higher temperatures also mean the collisions are more energetic so they more easily excite higher J levels of the pure rotational ($v = 0$) states, from which the underlying J level populations get transposed to higher v by UV excitation. The end result of this process are rotational ladders with shallower slopes. Both of these effects are apparent in the excitation diagram of the Orion Bar, while they are less apparent in the other, colder, PDRs.

3.7.2 The 1-0 S(1)/2-1 S(1) Line Ratio

The 1-0 S(1)/2-1 S(1) line flux ratio has historically been used to differentiate between shocked and UV-excited H_2 (e.g., Hayashi et al. 1985; Black & van Dishoeck 1987; Burton 1992). In H_2-emitting regions with thermal level populations such as shocks, the ratio can be high. For example, a 1,000 K gas would have 1-0 S(1)/2-1 S(1) $\sim$ 200. Here we repurpose it to be a proxy for collisional modification of the H_2 rovibrational level populations. For unmodified UV-excited H_2, this line ratio is $\sim$ 1.8 (Black & van Dishoeck, 1987). The value of this ratio increases with increasing degrees of collisional modification. Warmer and/or denser gas will populate via collisional excitation the low excitation energy $v = 1$, $J = 3$ level traced by the 1-0 S(1) line more than the higher excitation energy $v = 2$, $J = 3$ level traced by the 2-1 S(1) line.

We report 1-0 S(1)/2-1 S(1) ratio for each PDR in Table 3.1 and plot 1-0 S(1)/2-1 S(1) vs. χ/n_H in Figure 3.7. All the PDRs have ratios > 1.8, indicating some degree of collisional modification. S 140, the Horsehead Nebula, IC 63, and NGC 2023 have 1-0 S(1)/2-1 S(1) that range from 2.42 to 3.09 while the Orion Bar has a larger ratio of 5.35.

According to Draine & Bertoldi (1996), the value of χ/n_H determines where the dissociation front lies within the cloud. At low χ/n_H, the dissociation front lies at low optical depth near the ionization front where the temperature is hotter. In this case, the 1-0 S(1)/2-1 S(1) ratio is moderately sensitive to temperature, as appears to be the case for the Horsehead Nebula, IC 63, and NGC 2023. At higher χ/n_H, the

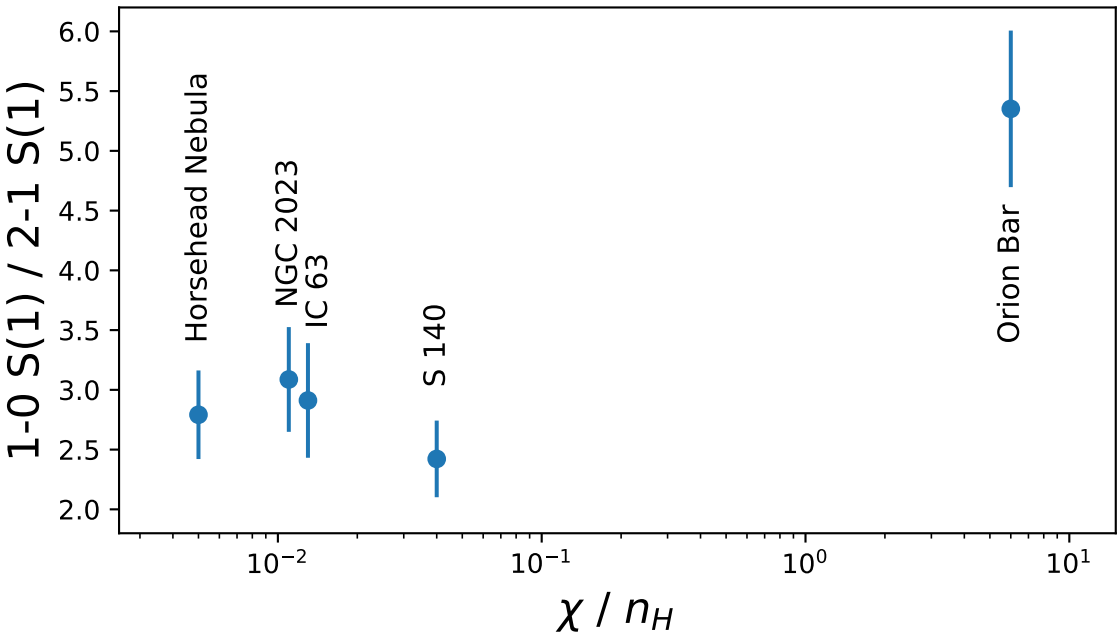

Figure 3.7: Semi-log plot of the UV field intensity divided by the gas density χ/n_H vs. the 1-0 S(1)/2-1 S(1) line ratio. Here we see behavior that mirrors the predictions by Draine & Bertoldi (1996). At low χ/n_H such as in the Horsehead Nebula, IC 63, and NGC 2023, the 1-0 S(1)/2-1 S(1) is temperature sensitive due to the effects of collisions. At higher χ/n_H where the effects of collisions are less pronounced, except at high temperatures, we can clearly see S 140 approach the value of 1-0 S(1)/2-1 S(1) for unmodified UV excitation and the Orion Bar, with its warmer gas (625 K), shows a high 1-0 S(1)/2-1 S(1) ratio.

dissociation front moves further into the cloud away from the ionization front where the optical depth is higher and the gas is cooler, reducing the effects of collisions. S 140 has a moderately high χ/n_H but the lowest 1-0 S(1)/2-1 S(1) of our sample at 2.42, closest to the unmodified UV-excited case, out of all the PDRs in our sample. Conversely, if the temperature is hot enough, collisional effects become important, even if χ/n_H is high. This appears to be the case for the Orion Bar PDR which has warm gas (625 K), high χ/n_H, and a high 1-0 S(1)/2-1 S(1) ratio. While our observations, and those of others, reveal the gas in the Orion Bar is warm (see Chapter 2.4.1.2), the source of this excess heating in the Orion Bar remains undetermined.

3.7.3 Comparison to a Quiescent UV-excited PDR Model

A more robust method to quantify the strength of collisional modification of the UV-excited H_2 rovibrational level populations in our PDR sample is to compare all the observed level populations to a Cloudy model of a quiescent low density PDR that predicts rovibrational level populations that are UV-excited and mostly unmodified by collisional effects. We run a Cloudy model with a constant density of 10^2 cm^{-3}, cosmic rays turned off, an illuminating star represented as a 27,000 K blackbody with a luminosity of $L/L_{\odot} = 10^4$, and the cloud face set to a distance of 5 pc from the illuminating star. We normalize the model to the $v = 4$, $J = 1$ column density determined from the 4-2 O(3) line as we have done for our PDR sample. Figure 3.8 shows the excitation diagrams for our PDRs with the quiescent UV-excited model overplotted, and Figure 3.9 shows the ratios of the observed level populations to the quiescent UV-excited model. This comparison expands upon the behavior seen in the 1-0 S(1)/2-1 S(1) ratio.

For rotational ladders of $v > 1$, the observed PDRs consistently have their level populations at high J underpredicted by the quiescent UV-excited model. This might not be the case for the Horsehead Nebula since we do not probe to high J due to its low surface brightness. Higher gas temperatures increase the energy of the collisions which increase the populations of the higher J pure rotational ($v = 0$) states before UV excitation transposes the relative populations in J at $v =$ to higher v states.

The low-J, $v = 1$ levels are also consistently higher in the observed data than in the model, with the exception of S 140. Like our results from the 1-0 S(1)/2-1 S(1) ratio, S 140 appears to have level populations that are the least collisionally modified of all the PDRs in our sample. The collisional excitation of the $v = 1$ and de-excitation of $v > 1$ levels in the Orion Bar is evident, with deviations up to an order of magnitude from the model for the $v = 1$ low-J states.

3.7.4 Comparison to S 140

Here we compare all the PDRs in the survey to S 140 directly. This avoids the assumptions and uncertainties about PDR physics that must be made in models, and directly compares the level populations between the different PDRs in our sample. For this comparison, we average all column densities derived for each v and J level in S 140 in cases where multiple transitions arising from the same upper level were

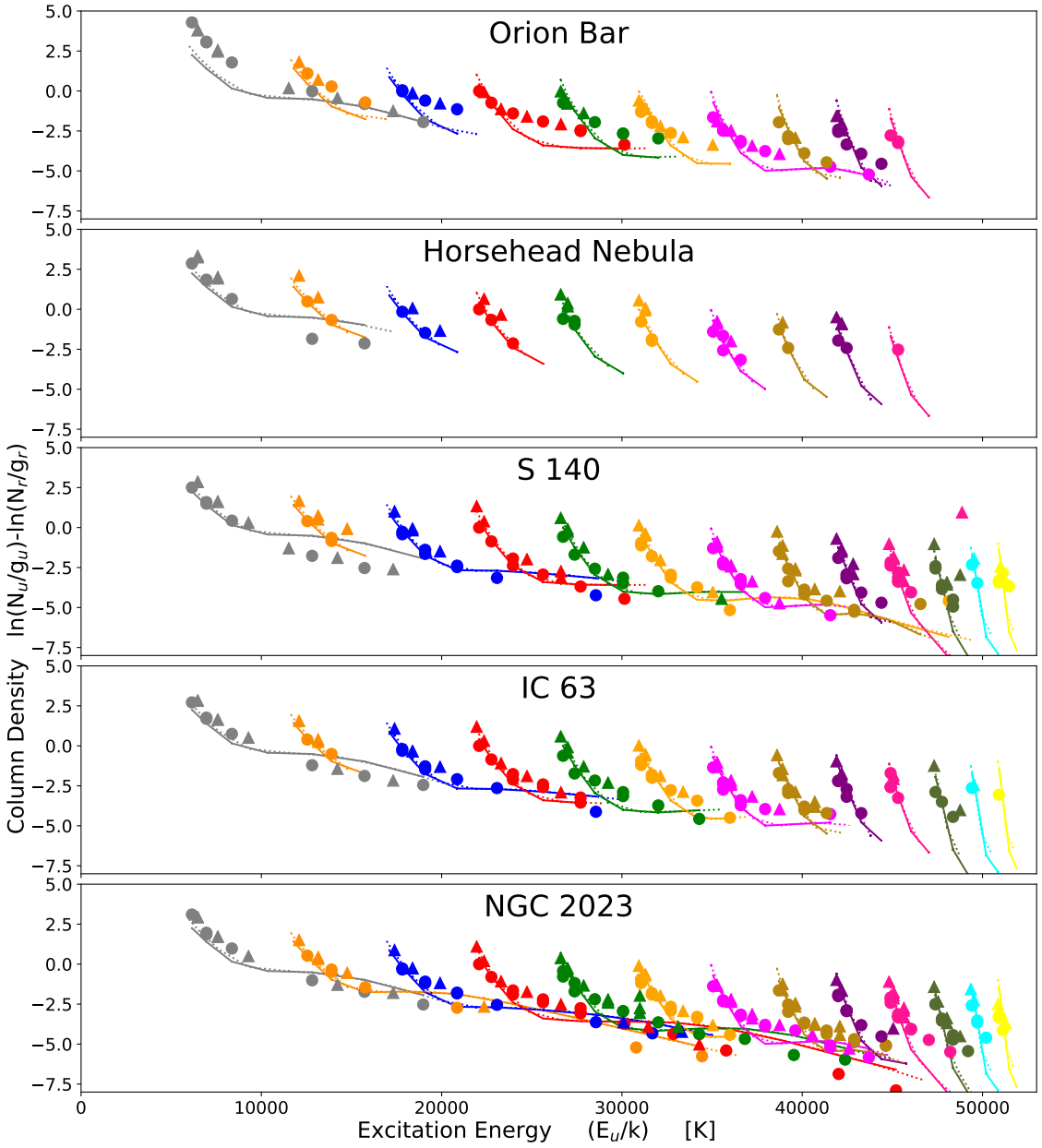

Figure 3.8: Excitation diagrams of all the PDRs with a quiescent UV-excited Cloudy model fits overlaid as solid lines for the ortho levels and and dashed lines for the para levels.

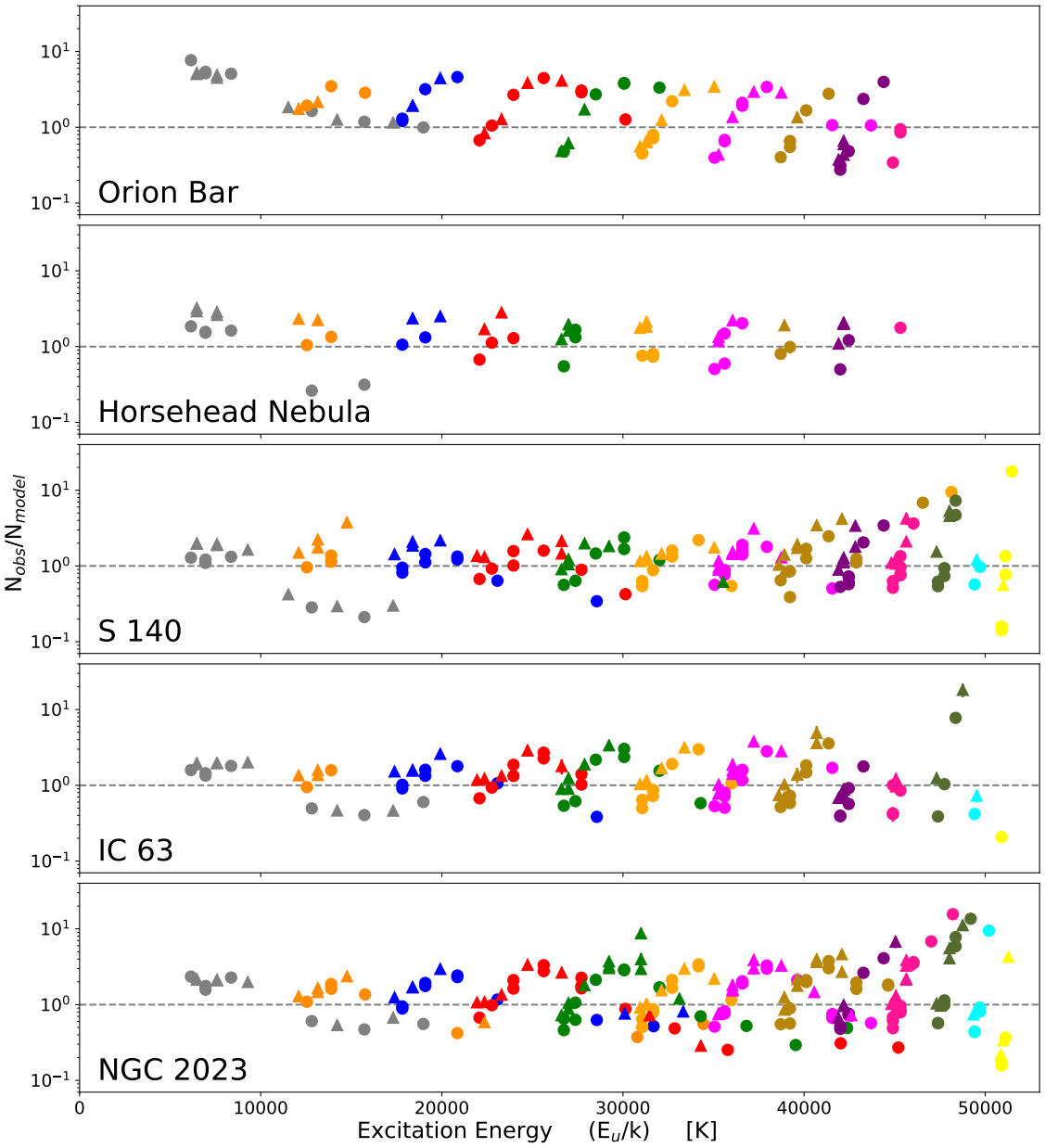

Figure 3.9: Semi-log plots of the ratios of the observed rovibrational level populations in our data (N_{obs}) to the quiescent UV-excited Cloudy model (N_{model}) shown in Figure 3.8. The horizontal dashed line represents a ratio of unity where the data and model are in perfect agreement. Deviations from unity show where the level populations are not exactly matched by the model predictions.

observed. We overplot S 140 on the excitation diagrams for all the PDRs in Figure 3.10 and the ratio of the observed level populations to S 140 in Figure 3.11.

The results are similar to the comparison to the quiescent PDR Cloudy model. We find that the PDRs all show some degree of collisional modification to their rovibrational level populations that is greater than the collisional modification found in S 140. Overall, the PDRs show higher populations in $v = 1$ than S 140. This arises from collisional excitation of the $v = 1$ rotational ladder and de-excitation of the $v > 1$ ladders. They all also show higher populations in high J levels than S 140, which is a sign of more energetic collisions in warmer gas populating the higher J pure rotational levels before UV excitation brings the molecules into high v (see Chapter 1.5.2 for a more in depth discussion). Besides S 140, IC 63 shows the second weakest amount of collisional modification to its UV-excited level populations out of the PDRs in our sample. The Horsehead Nebula and NGC 2023 both show stronger signs of collisional modification than IC 63. The Orion Bar shows the most dramatic difference, with collisional excitation raising the populations of the $v = 1$ levels while collisional de-excitation lowers the populations in the $v > 1$ levels.

3.8 Summary and Conclusions

We have expanded the analysis we have done for the Orion Bar PDR in Chapter 2 to a survey of four additional PDRs found in regions of high-mass star formation: the Horsehead Nebula, S 140, IC 63, and NGC 2023. We compare the results for these sources to those of the Orion Bar PDR. These PDRs were all observed with single deep IGRINS pointings to maximize the S/N. They span a range of densities, UV field intensities, and illuminating star temperatures. Each PDR displays low velocity UV-excited H_2, with many near-IR emission lines arising from the H_2 rovibrational transitions. From these line fluxes, we calculate the detailed H_2 rovibrational level populations in each PDR.

We have found the following:

1. All the PDRs show quiescent molecular gas traced by H_2 with motions of only a few km s^{-1} and rovibrational level populations that clearly show that the gas is excited by FUV photons as opposed to shock excitation.

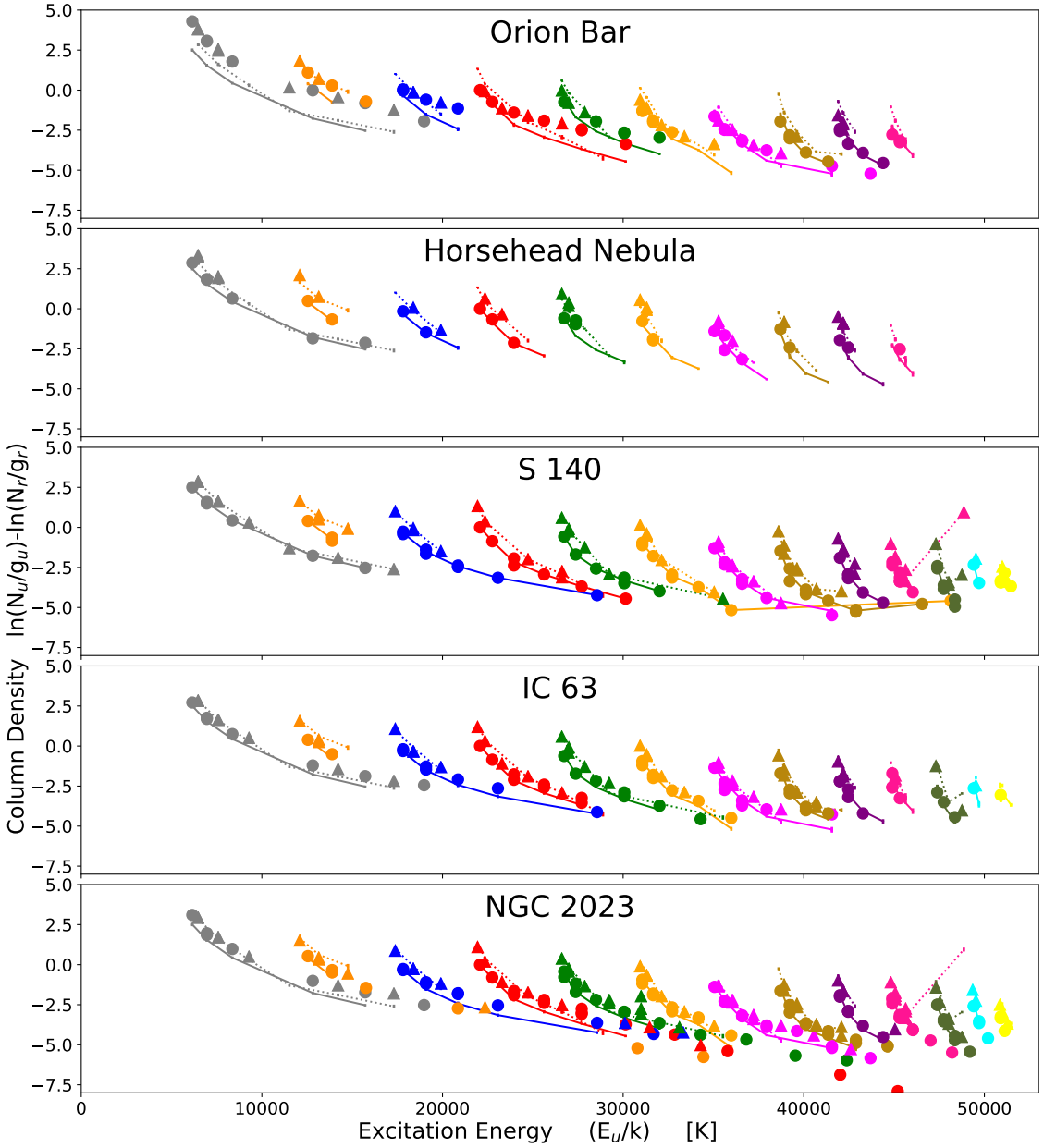

Figure 3.10: Excitation diagrams of all the PDRs with the mean observed population of each level in S 140 overlaid as solid lines for the ortho levels and and dashed lines for the para levels.

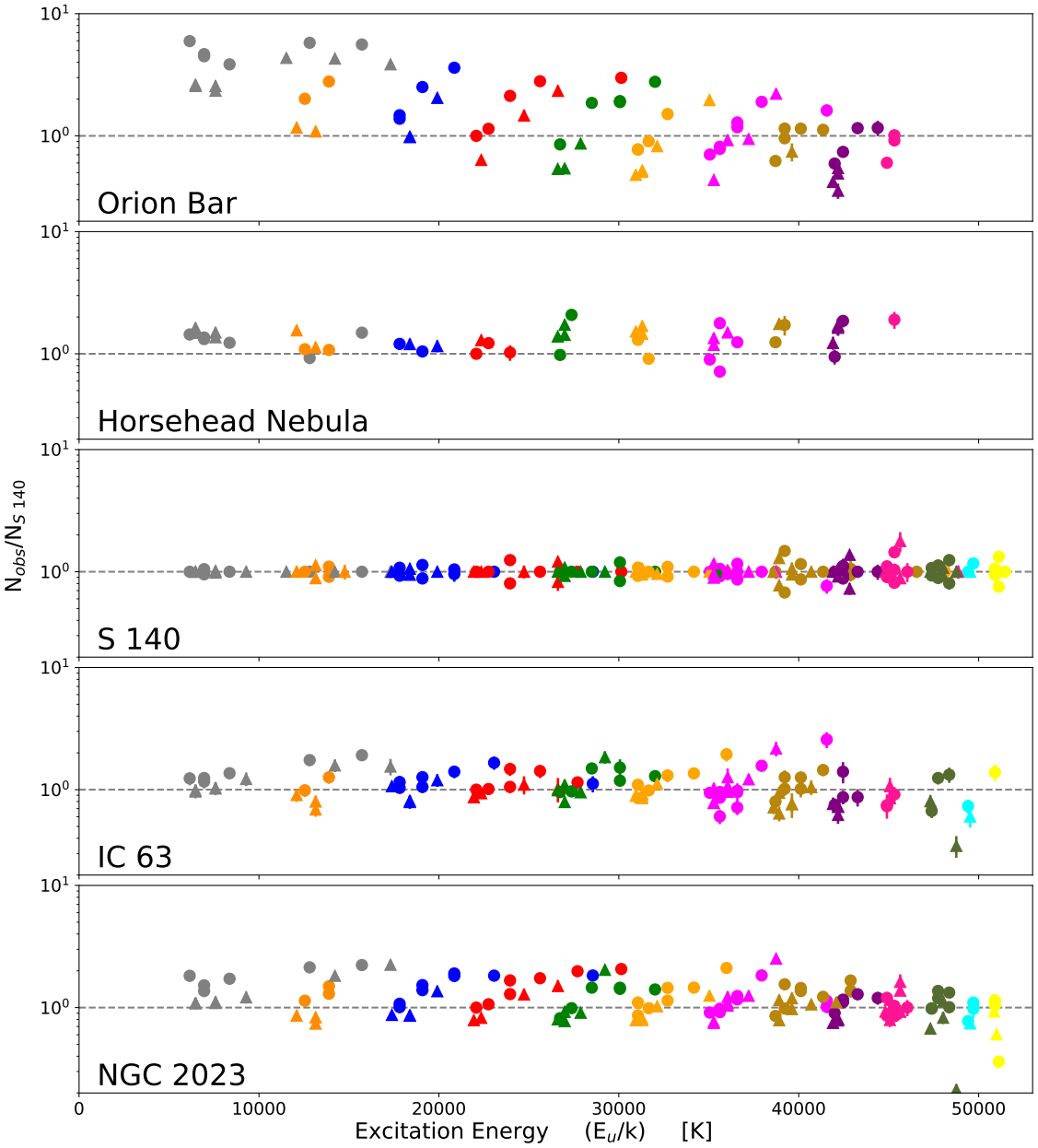

Figure 3.11: Semi-log plots of the ratios of the observed rovibrational level populations in our data (N_{obs}) to S 140 ($N_{S\ 140}$) shown in Figure 3.8. The horizontal dashed line represents a ratio of unity where the data and S 140 are in perfect agreement.

2. Our spectrum for NGC 2023 has particularly high S/N. Over 200 H_2 lines were observed, including transitions up to high J such as 4-3 S(19) which arises from the $v = 4$, $J = 21$ level at an excitation energy of $E_u/k = 45202$ K.

3. We confirm the UV-excited nature of the H_2 by fitting each PDR spectrum to a Cloudy model. The constant density and constant temperature model grid for the Orion Bar provides a better fit to the data than the single constant density models run for the other PDRs for which we adopted density values from the literature. This shows the utility of model grids to explore parameter space and provide the best model fits.

4. The Cloudy models consistently overpredict the level populations at high J for all our PDRs, suggesting we might want to revisit the prescription used for "formation pumping" in these models, which has a significant effect on the level populations at high J.

5. A comparison of all the PDRs to the 1-0 S(1)/2-1 S(1) line ratio and to a Cloudy model of a quiescent UV-excited PDR show that all of the observed PDRs have some degree of collisional modification to their level populations.

6. The observed PDR with level populations closest to the unmodified UV-excited case is S 140, while the one with the most collisionally modified level populations is the Orion Bar. The other PDRs show varying degrees of collisional modification. Both S 140 and the Orion Bar have the highest value of χ/n_H. According to Draine & Bertoldi (1996), when χ/n_H is high, the dissociation front lies deeper in the cloud at higher optical depth where the gas is cooler, explaining why S 140 is the most unmodified UV-excited case. Conversely the Orion Bar has the highest χ/n_H, but displays the largest deviations from the UV-excited case. This is caused by the warm temperature in the Bar, where the energy deposited into the PDR by UV photons is insufficient to account for the needed heating. The source of excess heating within the Bar remains an open question (as discussed in Chapter 2.4.1.2).

7. A direct comparison between S 140 and the other PDRs in the survey show that the other PDRs exhibit higher level populations at high J than S 140, sug-

gesting they have higher temperatures. The warm Orion Bar shows the largest deviation, along with clear signs of collisional excitation and de-excitation.

Chapter Four: Three Planetary Nebulae with Multiple Components of Kinematically Symmetric H_2 Emission

We report the near-IR detection of kinematically distinct structures with different states of excitation in H_2 in three planetary nebulae: M 1-11, Vy 2-2, and Hen 2-459. These nebulae each contain the following structures: a central ionized nebula, an expanding shell of UV-excited H_2, and two components of hot H_2 that are symmetric and equidistant from the nebular center in both position and velocity. These observations were made with IGRINS, a near-infrared spectrometer with high spectral resolution ($R \sim 45000$) over the full H and K bands (1.45 to 2.45 μm). The central photoionized zone is traced by H and He recombination lines, and collisionally excited [Kr III] and [Se IV] lines, and the surrounding slowly-expanding molecular gas is seen in UV-excited H_2 rovibrational emission lines. In Vy 2-2, we observe a bipolar flow traced by [Fe II] and [Fe III] emission through the ionized zone of the nebulae, as seen projected on the sky. The flow ends in bright, high velocity ($\sim$ 50 to 100 km s^{-1}) red-shifted and blue-shifted shocked "bullets" of collisionally excited (thermal) H_2 rovibrational emission with excitation temperatures of $T \sim 1500$ K. The H_2 "bullets" likely arise where the outflow is colliding with and shocking previously ejected molecular gas. M 1-11 hosts similar H_2 "bullets," but unlike Vy 2-2, the [Fe II] and [Fe III] lines do not appear to trace a bipolar outflow. Hen 2-459 shows a structure reminiscent of Vy 2-2 with high velocity H_2 bullets and [Fe II] and [Fe III] emission, but it is unclear whether this is a caused by a bipolar outflow.

4.1 Introduction

Planetary nebulae (PNe) form when low and intermediate-mass stars eject their outer layers into the interstellar medium (ISM) at the end of the asymptotic giant branch (AGB) phase of their evolution. General overviews of our understanding of PNe are given by Peimbert (1990), Kwok (2000), and Barlow & Méndez (2007). In the "pre-" or "proto-PN" phase, the central post-AGB star has not yet undergone enough mass-

loss to expose the hot core, so the ejected material consists of dusty molecular gas. As the planetary nebula (PN) evolves, progressive mass-loss reveals deeper hotter layers of the central star. UV radiation starts to dissociate the molecules and ionize the atoms in the central part of the nebula. PNe are a brief evolutionary stage in the life of a star, and the ejected gas in the nebula diffuses back into the ISM on the order of tens of thousands of years, leaving behind a slowly cooling white dwarf.

PNe exhibit wide variations in morphology, which is shaped by the nebula's age, binarity, progenitor mass, and the surrounding circumstellar material lost during the preceding stellar evolutionary stages. Up to 20% of PNe appear roughly spherically symmetric, while the rest show some kind of asymmetry (Manchado et al., 1996; Parker et al., 2006; Sahai et al., 2007, 2011). The causes of asymmetric morphology are widely discussed in the literature (e.g., Balick & Frank 2002; Kwok 2010), and have been the subject of a series of conferences entitled Asymmetric Planetary Nebulae (Harpaz & Soker, 1995; Kastner et al., 2000; Meixner et al., 2004; Corradi et al., 2007; Zijlstra et al., 2011; De Marco, 2014), but the issue remains unsettled. The original "interacting winds" model by Kwok et al. (1978) was based on the picture of recently ejected material colliding with and compressing previously ejected material to produce a dense gas shell. This was expanded upon by Frank et al. (1993), who explored the possible origin of asymmetric morphology when the earlier mass-loss was not spherically symmetric. Material could be ejected asymmetrically from the star due to rapid stellar rotation, surface instabilities, or a strong magnetic field interacting with the ejected material as suggested by García-Segura et al. (1999) and Sabin et al. (2007). Much of the recent literature has focused on the possibility that asymmetric structure is mainly caused by binary interactions (e.g, De Marco 2009; Jones & Boffin 2017). It is possible that multiple mechanisms play a role in creating asymmetric structures observed in PNe.

In this paper we will discuss structures we serendipitously found in three PNe: M 1-11, Vy 2-2, and Hen 2-459. These nebulae were observed with the Immersion Grating INfrared Spectrometer (IGRINS; see Chapter 1.2 for more details) which simultaneously observes the near-IR H and K bands (1.45–2.45 μm) at a high resolution of $R \sim 45,000$ (Park et al., 2014). The observations were taken as part of a survey of 61 PNe to study both emission from molecular hydrogen (H_2) and elements synthesized by slow neutron-capture processes within the progenitor star. The high spectral resolution of IGRINS allows us to resolve distinct spatio-kinematical

substructures in spatially compact nebulae.

The three nebulae discussed here share many characteristics. The extent of the central photoionized zone in position-velocity (PV) space is traced by H and He recombination lines along with collisionally excited [Kr III] and [Se IV] lines. The extent of these lines in PV space roughly depends on the ionization potential (IP) range of the species that gives rise to these lines. Ions of higher IP are more centrally concentrated (e.g. He I, [Kr III], and [Se IV]) than those of lower IP (e.g. H I).

Near-IR lines of [Fe II] and [Fe III] are observed in all three PNe. In at least two of the three PNe, the [Fe II] and [Fe III] lines appear to trace out a structure that is distinct from the rest of the photoionized gas.

All three PNe also exhibit H_2 emission. Near-IR H_2 emission arises from radiative decay out of excited rotational-vibrational (rovibrational) levels of the ground electronic state. These levels can be populated by two main mechanisms: UV excitation and collisions. Far-UV photons, with energies too low to ionize H I ($11.2 \rightarrow 13.6$ eV, $1110 \rightarrow 912$ Å), can excite H_2 to higher electronic states, which then radiatively decay into excited rovibrational states (e.g. Black & van Dishoeck 1987; Dinerstein et al. 1988). Collisions with other particles in the gas can also excite H_2 to higher rovibrational states. For example, shocks mechanically heat the gas and collisions from thermal motions in the heated gas result in level populations that obey Boltzmann statistics. Since shocks and UV excitation give rise to different emergent line intensity ratios, observed H_2 emission spectra can be used to discern the excitation mechanism (see Chapters 1 and 2 for further discussion). However, many PNe display line intensity ratios that are intermediate between these two processes (Davis et al., 2003a; Otsuka et al., 2013). This situation can arise when there is a superposition of shock and fluorescent components that are unresolved (e.g. Davis et al. 2003a), or when a relatively dense gas is illuminated by a strong FUV radiation field and collisional de-excitation modifies the level populations (e.g. Sternberg & Dalgarno 1989). In the case of the three PNe we observe, the integrated intermediate H_2 line intensities which might be attributed to collisional modification of UV-excited H_2 rovibrational level populations such as in the Orion Bar (Chapter 2) and to a lesser extent the other PDRs (Chapter 3), are actually due to the superposition of slowly-expanding UV-excited H_2 and a set of higher velocity red- and blue-shifted "bullets" of collisonally excited (likely shocked) H_2 emission.

4.2 Observations

The observations we present in this paper are part of a near-IR spectroscopic survey of 61 PNe. The two scientific goals of the PNe survey are to investigate the abundances of slow neutron-capture elements in PNe (e.g., Sterling et al. 2016) and to study the excitation and kinematics of H_2 in the PNe. All of the data were taken with the Immersion Grating INfrared Spectrometer (IGRINS, see Chapter 1.2). Most of the observations were obtained at the Cassegrain focus of the 2.7 m Harlan J. Smith telescope at McDonald Observatory (McD), and a few on Lowell Observatory's 4.3 m Discovery Channel Telescope (DCT). Targets that are large or had known H_2 emission were typically observed in a nod-off-slit mode where the slit position was alternated between the nebular center and sky. Targets that are compact and/or did not have known H_2 emission were observed in the nod-on-slit mode where the center of the nebula was alternated between two positions on the slit.

In this chapter, we report the results for our observations of three PNe from our survey: M 1-11, Vy 2-2, and Hen 2-459. Table 4.1 summarizes our observations. These nebulae were selected from our larger survey due to the similar characteristics they share in their IGRINS spectra. They have distances from the literature ranging from 2–4 kpc. Their central stars have effective temperatures ranging from $T^{\star}_{\rm eff}$ = 31,830 to 59,500 K and luminosities of $L^{\star}/L_{\odot}$ =4,710 to 23,440. M 1-11 and Vy 2-2 were observed at McD with the nod-off-slit mode. Hen 2-459 was observed both at McD and on the DCT with the nod-on-slit mode. Figure 4.1 shows the finder charts and apparent slit size for each of our observations. A standard A0V star was observed near the airmass of each nebula, and used for telluric absorption line correction and relative spectrophotometric flux calibration.

The data reduction and calibration procedures are described in Chapters 1.3 and 1.4.1. For our nod-on-slit observations of Hen 2-549, we combine the two slit positions in the 2D spectrum by matching the continuum position and summing them. The reduced data are linearly interpolated into PV space on a velocity grid of 1 km s^{-1} pixels with a velocity range of $\pm$150 km s^{-1}. Figures 4.2 and 4.3 show the PV diagrams for selected H I, He I, [Kr III], [Se IV], [Fe II], [Fe III], and H_2 lines.

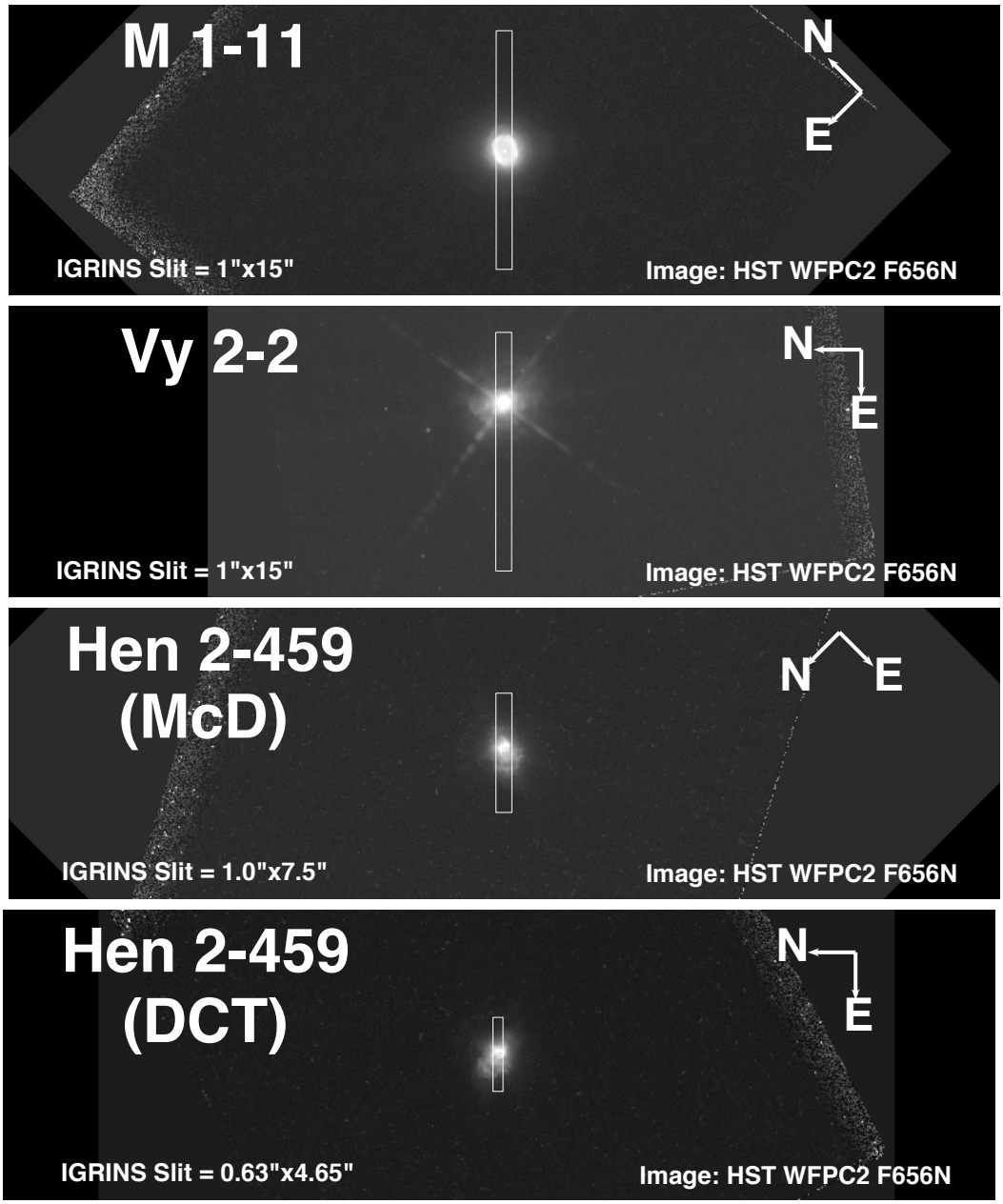

Figure 4.1: Finder charts for all our observations of the PNe M 1-11, Vy 2-2, and Hen 2-459 overlaid on archival HST WFPC2 F656N (Hα) images. These finder charts show the position and PA of each PN on the slit, and the apparent slit length to the PV diagrams. Since Hen 2-459 was observed by nodding between two positions on the slit, the apparent slit length shown here is smaller than the actual IGRINS slit.

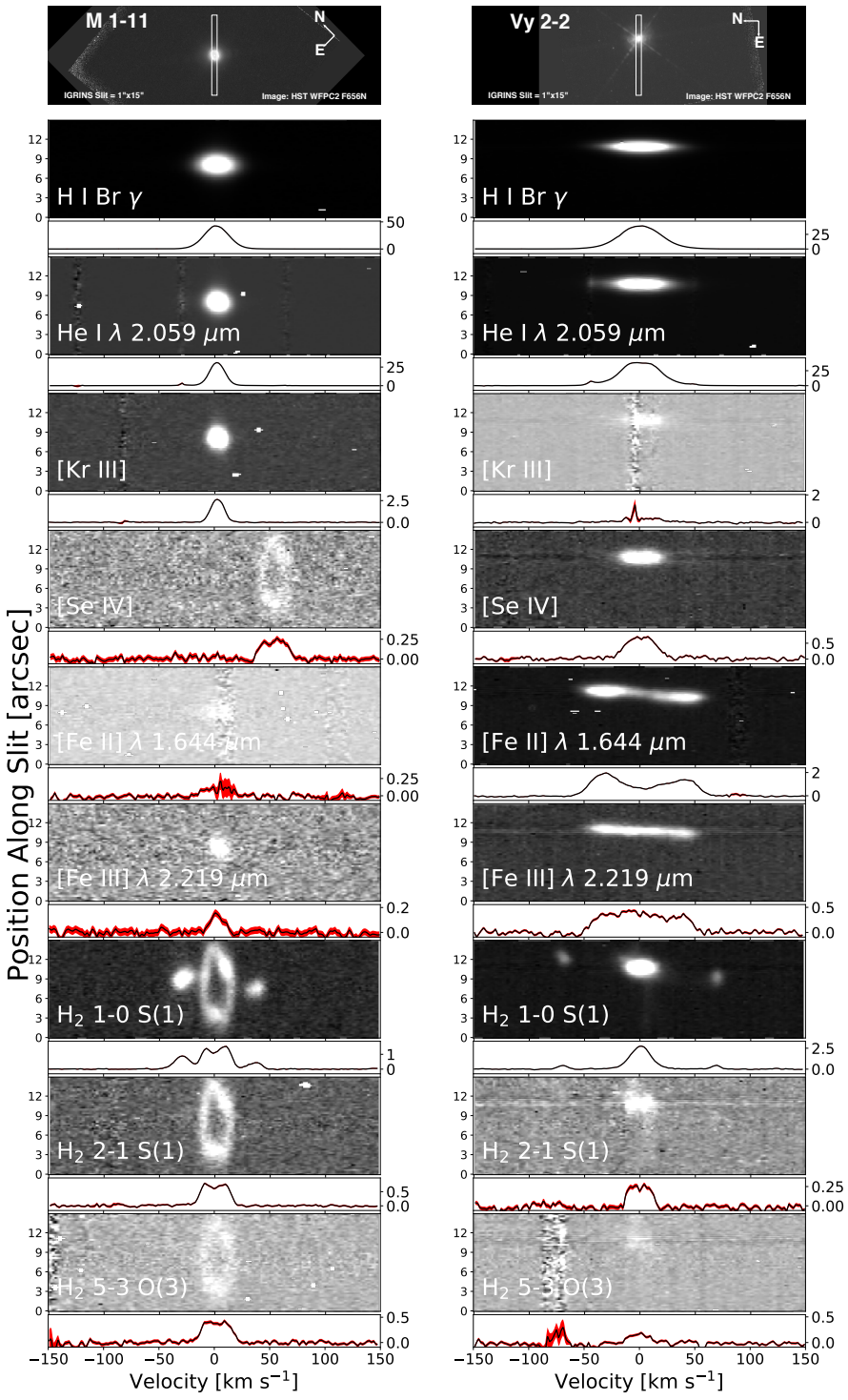

Figure 4.2: Top boxes show the finder charts from Figure 4.1 for the PNe M1-11 (left) and Vy 2-2 (right). Below these are PV diagrams of selected H I, He I, [Kr III], [Se IV], [Fe II], [Fe III], and H_2 lines. Note that the H_2 3-2 S(2) line is ~ 50 km s^{-1} redward of the position of the undetected [Se IV] line in the M 1-11 PV diagram.

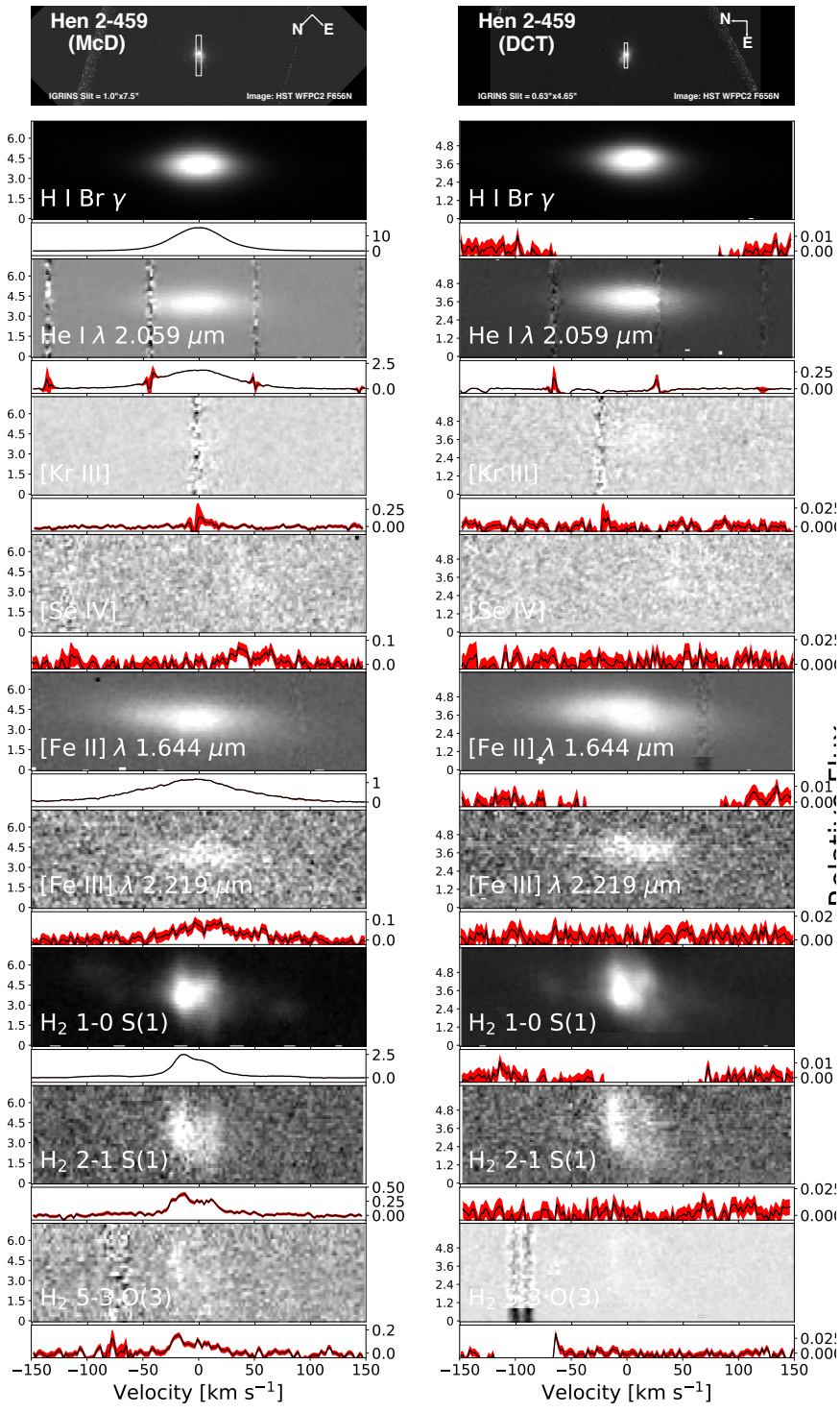

Figure 4.3: Top boxes show the finder charts from Figure 4.1 for the PN Hen 2-459 at McD (left) and at DCT (right). Below these are PV diagrams of selected H I, He I, [Kr III], [Se IV], [Fe II], [Fe III], and H_2 lines. Note that the H_2 3-2 S(2) line is ~ 50 km s^{-1} redward of the position of the undetected [Se IV] line in the Hen 2-459 PV diagrams.

Table 4.1: Summary of PN Observations and Parameters from Literature

PN	M 1-11	Vy 2-2	Hen 2-459	
PNG	232.8-04.7	045.4-02.7	068.3-02.7	
R.A.	$07^{\rm h}11^{\rm m}16\overset{\rm s}{.}69^a$	$19^{\rm h}24^{\rm m}22\overset{\rm s}{.}22^a$	$20^{\rm h}13^{\rm m}57\overset{\rm s}{.}89^a$	
Dec.	$-19°51'02\overset{''}{.}6^a$	$+09°53'56\overset{''}{.}3^a$	$+29°33'55\overset{''}{.}9^a$	
Peimbert Type	IIa[b]	III[b]	I[c]	
Morphology	Elongated, lobes closed[d]	Irregular[d]	Irregular[d]	
Distance (kpc)	2.10[e]	3.6 ± 0.4[g], 3.5 ± 1.2[h]	3.353[k]	
Spec. Type	[WC10-11][f]	-	[WC9][l]	
$T^\star_{\rm eff}$ (K)	31,830[e]	59,500[i]	77,000[m]	
$L^\star/L_\odot$	4,710[a]	6,000 ± 1,500[j]	23,440[m]	
$\log(g)^\star$ [cm s^{-2}]	3.5[e]	3.6[i]	-	
Telescope	McDonald 2.7m	McDonald 2.7m	McDonald 2.7m	Lowell DCT 4.3m
Date Obs. (UT)	2014 Dec 05	2014 Sep 24	2016 Jun 22	2016 Sep 27
Exp. Time	180 s	300 s	300 s	600 s
No. of Exp.	12	6	12	4
PA	135°	90°	45°	90°
Obs. Mode	Nod-Off-Slit	Nod-Off-Slit	Nod-On-Slit	Nod-On-Slit
Std. Star	18 Lep	HD 205314	HR 7098	HR 7734

References: [a]All positions reported are from 2MASS (Skrutskie et al., 2006), [b]Quireza et al. (2007), [c]Girard et al. (2007), [d]Sahai et al. (2011), [e]Otsuka et al. (2013), [f]Otsuka et al. (2014), [g]Christianto & Seaquist (1998), [h]Frew et al. (2016), [i]Cazetta & Maciel (2000), [j]Vickers et al. (2015) [k]Cahn et al. (1992), [l]Tylenda et al. (1993), [m]Leuenhagen & Hamann (1998).

4.3 Notes on the Individual PNe

4.3.1 M 1-11

M 1-11 is a well studied, low excitation PN ($T^\star_{\rm eff}$ = 31,830 K, Otsuka et al. 2013). It features a $\sim 5-6''$ halo of molecular gas traced by the emission of complex molecules (Otsuka et al., 2013) and dust (Phillips & Ramos-Larios, 2005). M 1-11 was part of a long term variability monitoring project by Kondratyeva (2005) who monitored the flux of spectral lines in several PNe from the early 1970s to early 2000s. They found that the ([O III]$\lambda\lambda 4959 + 5007$)/H$\beta$ and ([N II]$\lambda\lambda 6548 + 6383$)/H$\alpha$ line ratios increased steadily from 1988 along with a slight increase for He I, while the fluxes of Hα and Hβ remained relatively constant. A spectrum taken in 2013 by Hajduk et al. (2015) confirms that the ([O III]$\lambda\lambda 4959 + 5007$)/H$\beta$ ratio is continuing to increase with time. Increasing collisionally excited line flux ratios are sometimes interpreted as due to an increase in $T^\star_{\rm eff}$ as the central star evolves, but the timescales observed for M 1-11 are quite short so changing gas conditions in the nebula is more likely the

cause. Specifically, falling density means less collisional de-excitation.

Previous near-IR studies by Lumsden et al. (2001) and Otsuka et al. (2013) detected emission from H_2 with rovibrational level populations that appear to be primarily UV-excited, although Otsuka et al. (2013) found that the H_2 in the center of the nebula appeared more thermal than the outer regions, based on the variation of the 1-0 S(1)/2-1 S(1) flux ratio along their slit. With our high resolution near-IR spectra, we are able to kinematically separate the slowly expanding UV excited H_2 from the faster moving thermal H_2 as we will discuss later.

4.3.2 Vy 2-2

Vy 2-2 is a compact PN with a bipolar outflow. It hosts a central star with a $T^{\star}_{\rm eff}$ = 59,500 K and $L/L_{\odot}$ = 6,000 ± 1,500 (Cazetta & Maciel, 2000; Vickers et al., 2015). HST images show that the central ionized zone subtends only $\sim 0.5''$ on the sky, and reveals a bipolar structure with a larger extent and a major axis at PA of $\sim 135°$ (Sahai & Trauger, 1998). The PA for our IGRINS observations was 90°, which cuts through the bipolar structure at an angle of 45°. A high spectral resolution optical study of [N II] emission at multiple PAs by Miranda & Solf (1991) clearly shows a bipolar outflow. Previous studies of the H_2 emission by Hora et al. (1999) and Likkel et al. (2006) indicate that the H_2 emission from Vy 2-2 appears to be mainly UV-excited, but those data do not have high angular resolution.

4.3.3 Hen 2-459

Hen 2-459 is the most irregularly shaped of the three PNe in this study (Sahai et al., 2011), and hosts the hottest central star at $T^{\star}_{\rm eff}$ = 77,000 K and $L/L_{\odot}$ = 23,440 (Leuenhagen & Hamann, 1998). There is some speculation that its morphology is the result of binary (or even triple) star interactions (e.g., Soker 2016). Its H_2 emission has not been well studied in the literature.

4.4 Structure of the Ionized Gas in PV Space

The high spectral resolution of IGRINS allows us to study the detailed kinematics of the lines we observed, and to resolve distinct structures in PV space that are not

distinguishable at lower spectral resolution. To provide a precise quantitive measure of a line's location in PV space, we adopt the technique of spectroastrometry, by finding the running mean position of the centroid of a given line along the velocity axis (Bailey, 1998; Takami et al., 2004; Porter et al., 2005; Gnerucci et al., 2013; Blanco Cárdenas et al., 2014; Brittain et al., 2015). This method takes advantage of the fact that the centroid of a line can be determined to higher precision than the spatial resolution. When individual components of a nebula with different velocities fall on slightly different positions along the slit, these positions can be precisely measured given sufficient spectral resolution to separate different components in PV space. This technique is frequently used to search for and/or characterize accretion disks. Here we use it to determine whether emission lines of different species in the observed PNe are truly coming from the same components in PV space. First, we Gaussian smooth the signal-to-noise per pixel in PV space, and then mask out pixels where S/N < 2 so that only pixels with sufficient S/N are used in the calculation. We then calculate the first moment in position x (the mean $\overline{x}$) as a function of velocity v as follows:

$$\overline{x}(v) = \sum_{x} \left(F_{x,v}\ x\right) / \sum_{x} F_{x,v} \tag{4.1}$$

where $F_{x,v}$ is the flux in a pixel at a given position and velocity. Figure 4.4 shows the spectroastrometric positions for a selected set of lines for all our PNe observations (compare to the PV diagrams in Figures 4.2 and 4.3).

The H I and He I recombination and [Kr III] and [Se IV] collisionally excited lines trace the central ionized zones and appear roughly symmetric in PV space in all three PNe. In general, the ionization structure of the nebula approximately follows the IP of each species where more highly ionized species are confined to regions closer to the ionizing star. H I has an IP of 13.6 eV and appears the most extended in PV space. He I and [Kr III] appear less extended in PV space, because He I and Kr II have IPs of 24 eV. The region emitting in [Se IV] is the most compact, since Se III has an IP of 31 eV. For both M 1-11 and Vy 2-2, the H I, He I, and [Kr III] lines are symmetric in reflections across both position and velocity axes. For Hen 2-459, H I and He I show a slight asymmetry across the velocity axis, although this is less clear for the more compact [Kr III] line.

Unlike the other ionic lines, the [Fe II] and [Fe III] lines in Vy 2-2 and Hen 2-459 show a structure starting at the center of the nebula and diverging at higher red and blue shifted velocities in opposite directions in position along the slit. These

structures appear roughly equidistant from the center of the PN along both the position and velocity axes. The [Fe II] and [Fe III] lines in Vy 2-2 and Hen 2-459 appear to end at the edge of the ionized zone traced by the H I, suggesting they are tracing a component embedded within the ionized zone, although we cannot rule out that this could just be a projection effect. No such structure is apparent in M 1-11, where the [Fe II] and [Fe III] lines are symmetric when reflected across the position and velocity axes, like the H I and He I recombination lines.

To calculate the fluxes of the atomic emission lines, we draw single apertures around the lines in PV space using DS9 regions as described in Chapter 1.4. Since the lines vary in their extent for each nebula and species, we use different apertures for each PN and different apertures for the recombination lines and for the collisionally excited lines. We add a 15% systematic uncertainty to all the extracted line fluxes to account for systematic uncertainty in the relative flux calibration, telluric correction, and extinction correction. We report the line fluxes for most of the detected [Fe II], [Fe III], [Kr III], and [Se IV] lines and a selection of bright H I and He I lines in Table 4.2. All atomic and ionic line fluxes are normalized to the bright H I Br γ 2.1633 μm line.

4.5 Extinction Corrections

Foreground and internal dust extinction can affect observed line flux ratios. Extinction measured by Tylenda et al. (1992) in the optical for the PNe using the Balmer decrement gives $A_V = 3.20$, 4.59, and 5.79 mag for M 1-11, Vy 2-2, and Hen 2-459 respectively. These values for A_V correspond to $A_K = 0.37$, 0.54, and 0.68 mag. These give a differential extinction between the H and K bands of ~ 0.4, which is substantial enough to affect our observed line ratios. We apply extinction corrections for these values of A_V to all our PNe data.

We check the accuracy of these corrections by comparing the extinction corrected ratio of HI Br 14 to Br γ in our data to the theoretical value. PyNeb (Luridiana et al., 2015), using atomic data from Storey & Hummer (1995), gives an intrinsic ratio of Br 14/Br $\gamma \sim 0.12$ over a wide range of temperatures and densities. As seen in Table 4.2, our extinction corrected values for HI Br 14/Br γ are 0.122 ± 0.006, 0.132 ± 0.007, 0.117 ± 0.006, and 0.140 ± 0.007 for our M 1-11, Vy 2-2, Hen 2-459

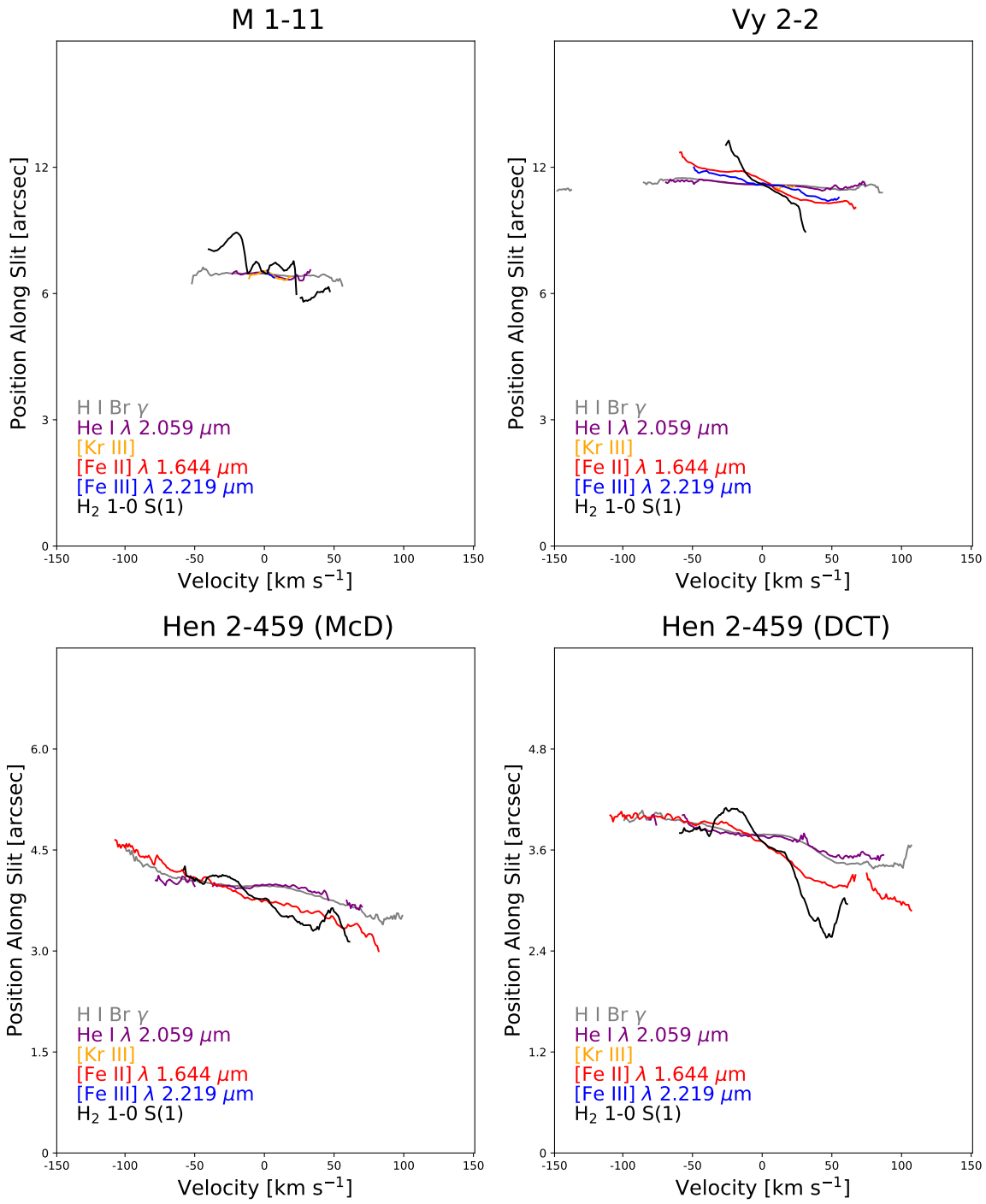

Figure 4.4: Running flux-weighted average spectroastrometric positions for selected lines. The H I and He I lines trace the central ionized zone of each PN and show little asymmetry in PV space.

Table 4.2: Atomic Line fluxes (Normalized to H I Br γ)

Line ID	λ (μm)	M 1-11	Vy 2-2	Hen 2-459 (McD)	Hen 2-459 (DCT)
H I Br γ	2.166120	1.000 ± 0.150	1.000 ± 0.150	1.000 ± 0.150	1.000 ± 0.150
H I Br 14	1.588488	0.122 ± 0.018	0.132 ± 0.020	0.117 ± 0.018	0.140 ± 0.021
He I	1.700704	$3.811 \pm 0.582 \times 10^{-2}$	0.144 ± 0.022	$4.148 \pm 1.042 \times 10^{-3}$	$7.896 \pm 1.396 \times 10^{-3}$
He I	2.058690	0.482 ± 0.072	1.027 ± 0.154	0.160 ± 0.024	0.177 ± 0.027
He I	2.112588	$1.107 \pm 0.167 \times 10^{-2}$	$5.594 \pm 0.839 \times 10^{-2}$	$2.456 \pm 0.596 \times 10^{-3}$	$2.818 \pm 0.499 \times 10^{-3}$
[Fe II]	1.533890	$6.839 \pm 1.648 \times 10^{-4}$	$2.306 \pm 0.346 \times 10^{-2}$	$2.257 \pm 0.350 \times 10^{-2}$	$3.240 \pm 0.487 \times 10^{-2}$
[Fe II]	1.599909	$5.466 \pm 1.325 \times 10^{-4}$	$1.493 \pm 0.224 \times 10^{-2}$	$1.729 \pm 0.264 \times 10^{-2}$	$2.349 \pm 0.353 \times 10^{-2}$
[Fe II]	1.643998	$3.397 \pm 0.582 \times 10^{-3}$	$8.621 \pm 1.293 \times 10^{-2}$	0.153 ± 0.023	0.164 ± 0.025
[Fe II]	1.664221	$2.409 \pm 0.879 \times 10^{-4}$	$7.091 \pm 1.068 \times 10^{-3}$	$1.063 \pm 0.165 \times 10^{-2}$	$1.270 \pm 0.191 \times 10^{-2}$
[Fe II]	1.677334	$6.365 \pm 1.264 \times 10^{-4}$	$1.482 \pm 0.223 \times 10^{-2}$	$1.803 \pm 0.273 \times 10^{-2}$	$2.513 \pm 0.377 \times 10^{-2}$
[Fe II]	1.711595	$< 9.254 \times 10^{-5}$	$3.117 \pm 0.479 \times 10^{-3}$	$2.661 \pm 0.602 \times 10^{-3}$	$5.556 \pm 0.854 \times 10^{-3}$
[Fe II]	1.748898	$< 1.300 \times 10^{-4}$	$< 1.444 \times 10^{-4}$	$< 8.403 \times 10^{-4}$	$< 2.973 \times 10^{-4}$
[Fe II]	2.223754	$< 7.623 \times 10^{-5}$	$5.770 \pm 0.869 \times 10^{-3}$	$2.542 \pm 0.383 \times 10^{-2}$	$1.243 \pm 0.187 \times 10^{-2}$
[Fe III]	2.145730	$6.534 \pm 1.192 \times 10^{-4}$	$6.887 \pm 1.035 \times 10^{-3}$	$2.025 \pm 0.417 \times 10^{-3}$	$2.164 \pm 0.350 \times 10^{-3}$
[Fe III]	2.218670	$1.875 \pm 0.291 \times 10^{-3}$	$1.737 \pm 0.261 \times 10^{-2}$	$2.990 \pm 0.583 \times 10^{-3}$	$5.266 \pm 0.811 \times 10^{-3}$
[Fe III]	2.242470	$8.353 \pm 1.589 \times 10^{-4}$	$7.752 \pm 1.168 \times 10^{-3}$	$2.029 \pm 0.609 \times 10^{-3}$	$1.684 \pm 0.357 \times 10^{-3}$
[Kr III]	2.198660	$3.239 \pm 0.486 \times 10^{-2}$	$6.068 \pm 0.956 \times 10^{-3}$	$1.363 \pm 0.699 \times 10^{-3}$	$1.424 \pm 0.291 \times 10^{-3}$
[Se IV]	2.286650	$< 1.115 \times 10^{-4}$	$1.176 \pm 0.176 \times 10^{-2}$	$< 1.599 \times 10^{-4}$	$1.971 \pm 1.399 \times 10^{-4}$

(McD), and Hen 2-459 (DCT) observations respectively, which are within 3σ of the theoretical value.

4.6 Fe Line Ratios as Density Diagnostics

Strong emission from [Fe II] and [Fe III] lines in shocked gas is commonly observed in the near-IR (Nisini et al., 2002; Pesenti et al., 2003; Takami et al., 2006; Pyo et al., 2002; Davis et al., 2003b; Koo et al., 2016). The [Fe II] and [Fe III] lines we observe with IGRINS have flux ratios that are mostly sensitive to density and insensitive to temperature; thus we exploit this fact to use them as density diagnostics. Despite sustained efforts to compute the relevant atomic data for Fe, the theoretical determination of density from the line ratios still has uncertainties up to 50% with even the most modern data (Bautista et al., 2015). We observe the [Fe II] 1.534, 1.600, 1.644, 1.664, and 1.677 μm lines from which we calculate densities using the prescriptions given by Koo et al. (2016). For the [Fe III] 2.146, 2.219, and 2.242 μm lines that we observe, we calculate densities using PyNeb (Luridiana et al., 2015), with atomic from Sugar & Corliss (1985), Quinet et al. (1996), Zhang (1996), and Johansson et al. (2000). Table 4.3 shows our derived densities and compares the results for different PNe, between [Fe II] and [Fe III], and for the different line ratios. Overall, we measure densities of $n_H = 5 \times 10^3$–10^5 cm^{-3}.

Even if the atomic constants are not well known, the line ratios can show us that there are variations in density. Figure 4.5 shows the resolved [Fe II] λ 1.677 μm/[Fe II] λ 1.644 μm ratio in PV space. The [Fe II] lines in M 1-11 have S/N too low to show spatial variations in the ratios. Vy 2-2 shows some variation along the velocity axis, with a higher ratio at low velocity, which decreases towards higher velocities (although the redshifted side appears to reverse the trend somewhat at ~ 50 km s^{-1}), indicating possibly higher density in the center. The line ratio in Hen 2-459 is flat, indicating that the density is mostly uniform for the gas from which the [Fe II] emission arises.

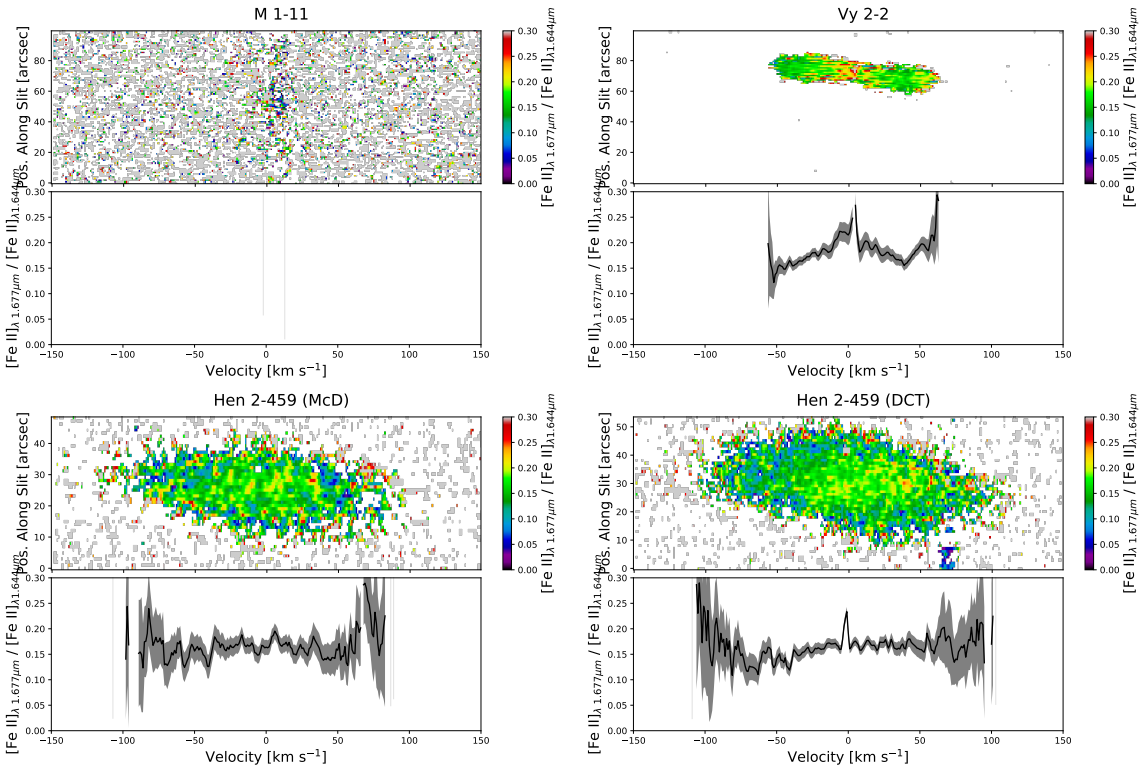

Figure 4.5: [Fe II] λ 1.677 μm/[Fe II] λ 1.644 μm line ratios, which can trace variations in density. The top panels show the line flux ratio in PV space, and the bottom panels show the ratio after summing the line fluxes along the slit. The gray shading on the bottom panels represents the $\pm 1\sigma$ uncertainty in the ratio.

4.7 H_2 Components and Excitation

The H_2 lines in each nebula show two types of spatio-kinematically distinct components. The first type appears as a ring surrounding the central ionized zone (along the position axis) in M 1-11, a nearly unresolved point source in Vy 2-2, and a more irregular structure in Hen 2-459. This H_2 component has low expansion velocities of ≤ 25 km s^{-1} and is seen in transitions with upper states that arise from a large range of excitation energies. Figures 4.2 and 4.3 show that this component appears in the 1-0 S(1), 2-1 S(1), and 5-3 O(3) lines. The second type of component consists of a pair of high velocity red- and blue-shifted "bullets" traveling at the same velocities but in opposite directions. They are traveling at ± 40 km s^{-1} in M 1-11 and ± 75 km s^{-1} in Vy 2-2 and Hen 2-459. The bullets are only seen in H_2 lines that arise from low excitation energies, e.g. 1-0 S(1). The positions of these bullets in PV space are

Table 4.3: Densities Determined from [Fe II] and [Fe III] Lines

Fe Ion	Ratio	Ref.	n_H (cm^{-3})			
			M 1-1	Vy 2-2	Hen 2-459 (McD)	Hen 2-459 (DCT)
[Fe II]	1.534 μm/1.644 μm	a	$1.343 \pm 0.201 \times 10^4$	$3.322 \pm 0.498 \times 10^4$	$6.415 \pm 0.962 \times 10^3$	$1.272 \pm 0.191 \times 10^4$
[Fe II]	1.600 μm/1.644 μm	a	$1.941 \pm 0.201 \times 10^4$	$2.366 \pm 0.498 \times 10^4$	$8.944 \pm 0.962 \times 10^3$	$1.455 \pm 0.191 \times 10^4$
[Fe II]	1.664 μm/1.644 μm	a	$1.293 \pm 0.194 \times 10^4$	$1.849 \pm 0.277 \times 10^4$	$1.235 \pm 0.185 \times 10^4$	$1.584 \pm 0.238 \times 10^4$
[Fe II]	1.677 μm/1.644 μm	a	$2.853 \pm 0.428 \times 10^4$	$2.134 \pm 0.320 \times 10^4$	$7.741 \pm 1.161 \times 10^3$	$1.499 \pm 0.225 \times 10^4$
[Fe III]	2.219 μm/2.146 μm	b	$< 4.883 \times 10^4$	$< 7.543 \times 10^4$	-	$< 1.074 \times 10^5$
[Fe III]	2.242 μm/2.146 μm	b	$< 3.529 \times 10^5$	$< 5.738 \times 10^5$	$2.449 \pm 2.117 \times 10^5$	$4.085 \pm 3.806 \times 10^6$
[Fe III]	2.219 μm/2.242 μm	b	$1.807 \pm 1.743 \times 10^4$	$1.826 \pm 1.729 \times 10^4$	-	-

References: (a) Bautista et al. (2015), (b)PyNeb (Luridiana et al., 2015) with the atomic data for Fe III taken from Sugar & Corliss (1985), Quinet et al. (1996). Zhang (1996), and Johansson et al. (2000).

coincident with the edge of the ionized zone traced by H I and (at least for Vy 2-2 and Hen 2-459) coincident with the ends of the structures traced by the [Fe II] and [Fe III] lines. This might imply that the velocity of the bullets represents the velocity of otherwise unseen molecular gas expanding away from the central star just outside the ionized zone of each nebulae.

The low velocity H_2 and the higher velocity bullets show quite different line ratios, implying different excitation mechanisms. The fluxes for each component are extracted with custom apertures using the technique described in Chapter 1.4.2. The apertures are shown in Figures 4.6, 4.7, 4.8, and 4.9. We add a 15% systematic uncertainty to all the extracted line fluxes to account for systematic uncertainty in the relative flux calibration, telluric correction, and extinction correction. We list all the extracted fluxes in Tables 4.4 and 4.5, from which we calculate the H_2 rovibrational level populations for each component using the techniques described in Chapter 1.5.1. The physical constants needed to calculate the level populations from all of the rovibrational transitions observed can be found in Table A.1. We normalize all our level populations in both the low-velocity H_2 component and the higher velocity bullets to the column density of the low velocity component's $v = 5$, $J = 1$ state determined from the 5-3 O(3) transition. We did not normalize to the 4-2 O(3) transition as in Chapters 2 and 3, because telluric lines interfered with our measurement of 4-2 O(3) in Vy 2-2. The level populations for the low velocity components are reported in Table 4.7, and those for the bullets in Tables 4.8. 4.9, 4.10, and 4.11. Figures 4.6, 4.7, 4.8, and 4.9 show the excitation diagrams for all the extracted components.

The level populations for the low velocity H_2 in M 1-11, Vy 2-2, and Hen 2-459 (top panels in Figures 4.6, 4.7, 4.8, and 4.9) show the characteristic sawtooth pattern for UV excitation, with detected levels spanning excitation energies up to 50000 K and v =1–12.

As in Chapter 3.7.2, we use the 1-0 S(1)/2-1 S(1) flux ratio as a simple measure of the degree of collisional modification in a PDR. In our observations of M 1-11, this ratio is 2.0, which is close to 1.8 for the case of unmodified UV excitation. In our observations of Vy 2-2, Hen 2-459 (McD), and Hen 2-459 (DCT) this ratio has value of 10.0, 7.9, and 9.3 respectively, showing much more collisional modification of the low-velocity UV excited gas than in M 1-11. The same pattern is seen in the population of molecules in the $v = 1$ rotational ladder compared to $v > 1$ where the $v = 1$ states in M 1-11 are less collisionally excited and $v > 1$ states are less

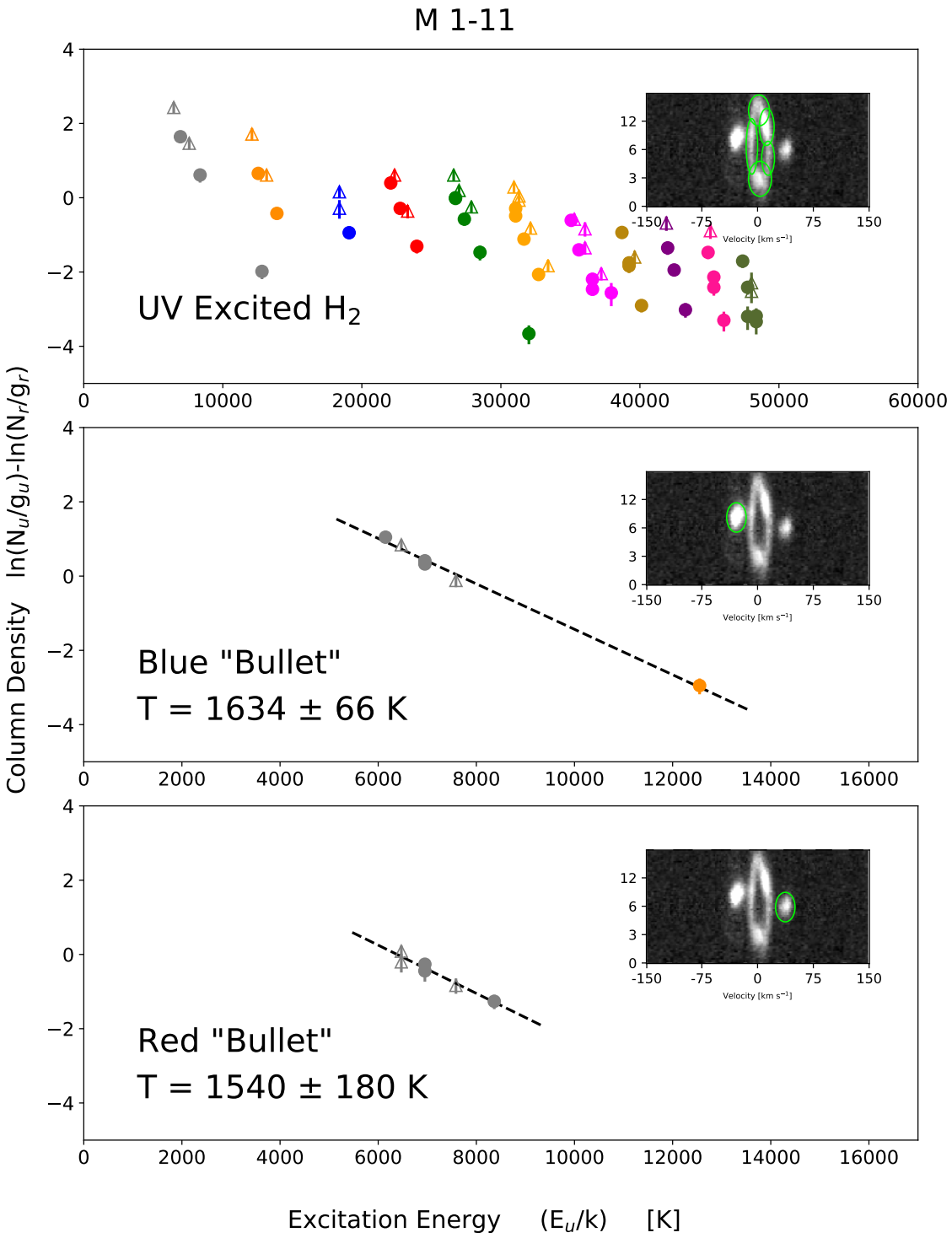

Figure 4.6: H_2 excitation diagrams for M1-11. The thumbnail PV diagrams show the 1-0 S(1) line and the aperture used to extract each H_2 component. The dashed lines show the least squares linear regression fits to the H_2 level populations in each of the thermal bullets for deriving their temperatures.

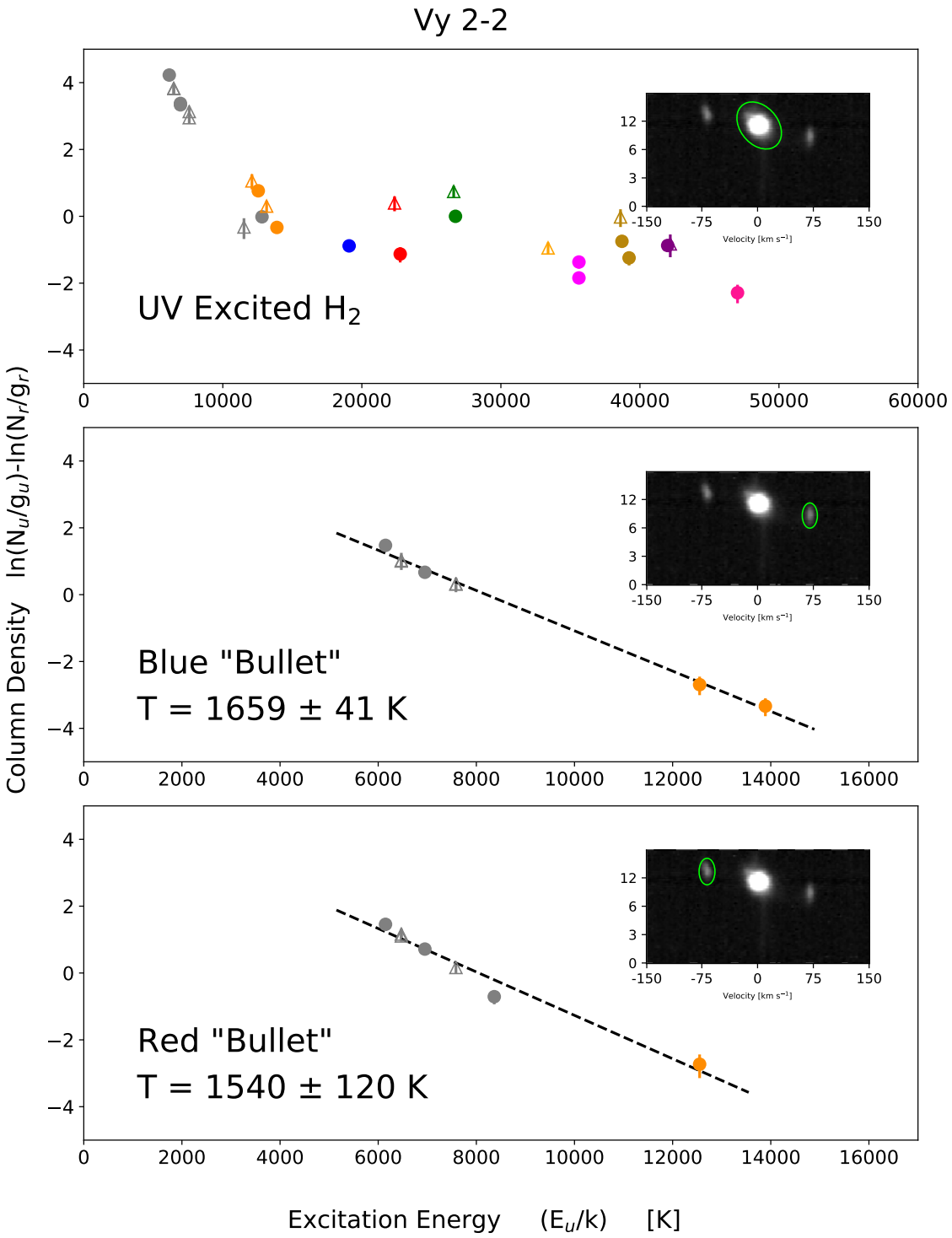

Figure 4.7: H_2 excitation diagrams for Vy 2-2. The thumbnail PV diagrams show the 1-0 S(1) line and the aperture used to extract each H_2 component. The dashed lines show the least squares linear regression fits to the H_2 level populations in each of the thermal bullets for deriving their temperatures.

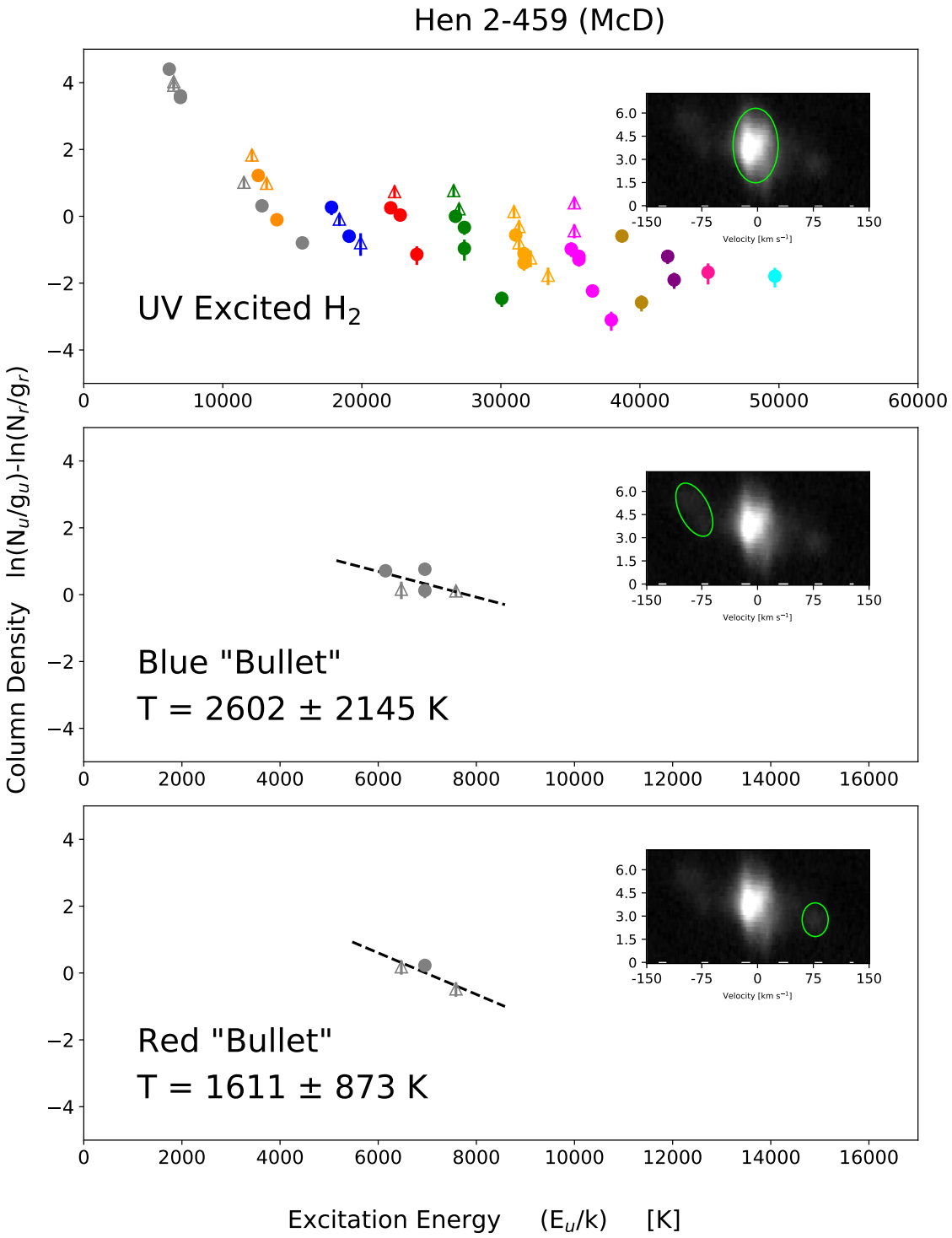

Figure 4.8: H_2 excitation diagrams for McD observations of Hen 2-459 which were observed with a slit PA of 45°. The thumbnail PV diagrams show the 1-0 S(1) line and the aperture used to extract each H_2 component. The dashed lines show the least squares linear regression fits to the H_2 level populations in each of the thermal bullets for deriving their temperatures.

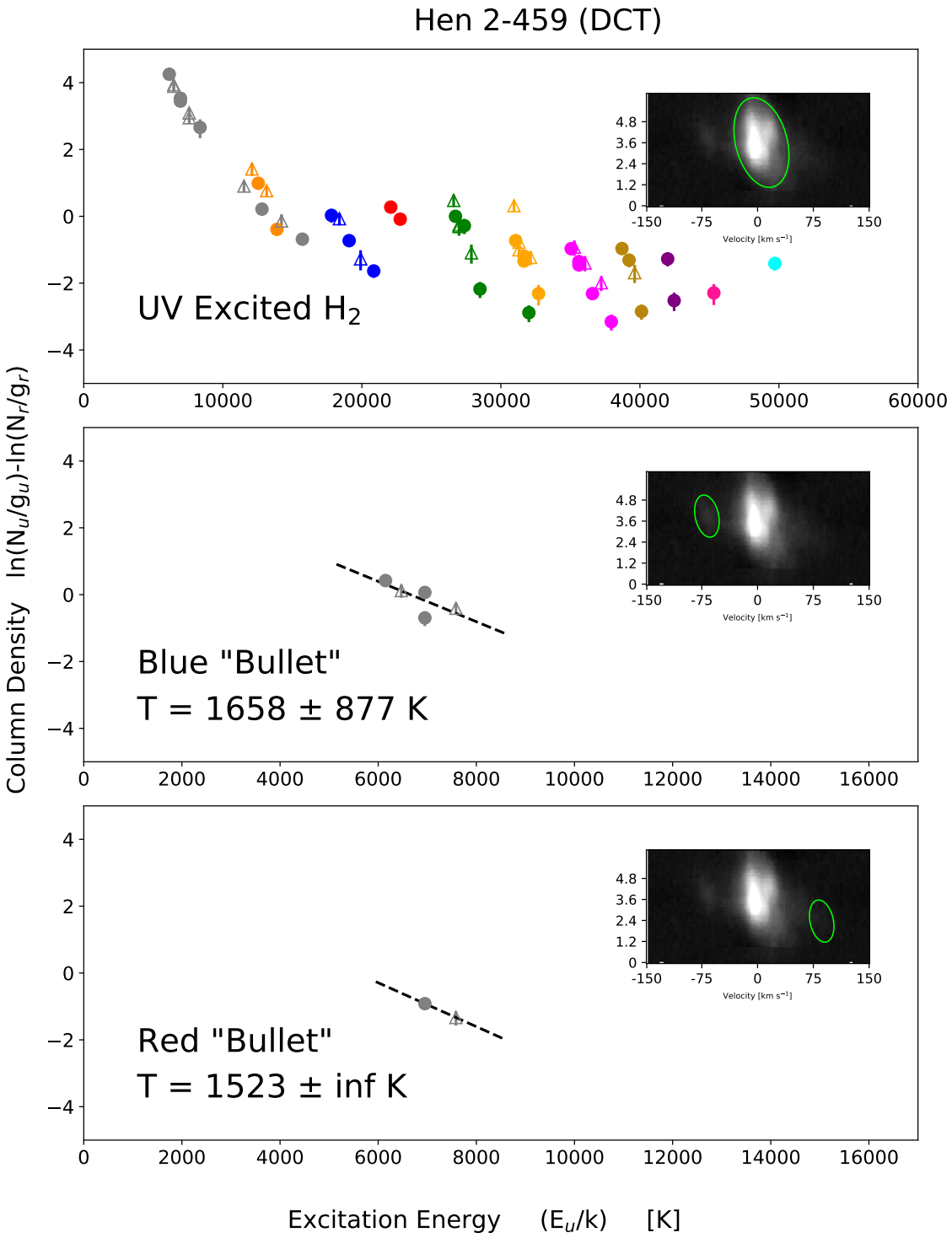

Figure 4.9: H_2 excitation diagrams for DCT observations of Hen 2-459 which were observed with a slit PA of 90°. The thumbnail PV diagrams show the 1-0 S(1) line and the aperture used to extract each H_2 component. The dashed lines show the least squares linear regression fits to the H_2 level populations in each of the thermal bullets for deriving their temperatures.

Table 4.4: Line Fluxes for Low Velocity UV Excited H_2 Component
(Normalized to H I Br γ)

Line ID	λ (μm)	v_u	J_u	M 1-11	Vy 2-2	Hen 2-459 (McD)	Hen 2-459 (DCT)
1-0 Q(1)	2.406592	1	1	–	$3.651 \pm 0.570 \times 10^{-2}$	$9.522 \pm 1.511 \times 10^{-2}$	$8.477 \pm 1.272 \times 10^{-2}$
1-0 Q(2)	2.413439	1	2	–	$9.614 \pm 1.448 \times 10^{-3}$	$2.308 \pm 0.348 \times 10^{-2}$	$2.314 \pm 0.348 \times 10^{-2}$
1-0 S(0)	2.223290	1	2	$1.100 \pm 0.165 \times 10^{-2}$	$8.621 \pm 1.295 \times 10^{-3}$	$2.324 \pm 0.349 \times 10^{-2}$	$2.197 \pm 0.330 \times 10^{-2}$
1-0 Q(3)	2.423730	1	3	–	$2.250 \pm 0.338 \times 10^{-2}$	$6.131 \pm 0.920 \times 10^{-2}$	$5.698 \pm 0.855 \times 10^{-2}$
1-0 S(1)	2.121834	1	3	$3.021 \pm 0.453 \times 10^{-2}$	$3.346 \pm 0.502 \times 10^{-2}$	$9.174 \pm 1.376 \times 10^{-2}$	$8.852 \pm 1.328 \times 10^{-2}$
1-0 Q(4)	2.437489	1	4	$7.227 \pm 1.107 \times 10^{-3}$	$7.478 \pm 1.154 \times 10^{-3}$	–	$1.407 \pm 0.213 \times 10^{-2}$
1-0 S(2)	2.033758	1	4	–	$1.120 \pm 0.168 \times 10^{-2}$	–	$2.928 \pm 0.439 \times 10^{-2}$
1-0 Q(5)	2.454752	1	5	$1.075 \pm 0.199 \times 10^{-2}$	–	–	–
1-0 S(3)	1.957559	1	5	–	–	–	$7.633 \pm 2.098 \times 10^{-2}$
1-0 S(6)	1.788050	1	8	–	$8.115 \pm 2.446 \times 10^{-4}$	$6.781 \pm 1.081 \times 10^{-3}$	$6.261 \pm 1.017 \times 10^{-3}$
1-0 S(7)	1.747955	1	9	$2.277 \pm 0.429 \times 10^{-3}$	$3.184 \pm 0.496 \times 10^{-3}$	$9.682 \pm 1.720 \times 10^{-3}$	$9.080 \pm 1.387 \times 10^{-3}$
1-0 S(8)	1.714738	1	10	–	–	–	$1.876 \pm 0.419 \times 10^{-3}$
1-0 S(9)	1.687761	1	11	–	–	$2.252 \pm 0.389 \times 10^{-3}$	$2.605 \pm 0.415 \times 10^{-3}$
2-1 S(0)	2.355605	2	2	$7.395 \pm 1.226 \times 10^{-3}$	$7.491 \pm 1.673 \times 10^{-4}$	$3.557 \pm 0.647 \times 10^{-3}$	$2.432 \pm 0.469 \times 10^{-3}$
2-1 S(1)	2.247716	2	3	$1.522 \pm 0.229 \times 10^{-2}$	$3.316 \pm 0.502 \times 10^{-3}$	$1.146 \pm 0.173 \times 10^{-2}$	$9.420 \pm 1.422 \times 10^{-3}$
2-1 S(2)	2.154216	2	4	$7.332 \pm 1.110 \times 10^{-3}$	$1.054 \pm 0.176 \times 10^{-3}$	$4.573 \pm 0.704 \times 10^{-3}$	$3.792 \pm 0.582 \times 10^{-3}$
2-1 S(3)	2.073482	2	5	$1.024 \pm 0.154 \times 10^{-2}$	$2.188 \pm 0.338 \times 10^{-3}$	$6.018 \pm 0.924 \times 10^{-3}$	$4.677 \pm 0.727 \times 10^{-3}$
2-1 S(4)	2.004109	2	6	–	$1.129 \pm 0.389 \times 10^{-3}$	–	–
3-1 O(5)	1.522033	3	3	–	–	$2.600 \pm 0.546 \times 10^{-3}$	$2.119 \pm 0.412 \times 10^{-3}$
3-1 O(6)	1.581171	3	4	$1.008 \pm 0.248 \times 10^{-3}$	–	–	–
3-2 S(2)	2.287045	3	4	$4.443 \pm 0.679 \times 10^{-3}$	–	$1.488 \pm 0.280 \times 10^{-3}$	$1.560 \pm 0.284 \times 10^{-3}$
3-2 S(3)	2.201399	3	5	$5.616 \pm 0.854 \times 10^{-3}$	$1.162 \pm 0.185 \times 10^{-3}$	$3.391 \pm 0.530 \times 10^{-3}$	$3.079 \pm 0.479 \times 10^{-3}$
3-2 S(4)	2.128015	3	6	–	–	$1.058 \pm 0.345 \times 10^{-3}$	$6.764 \pm 1.976 \times 10^{-4}$
3-2 S(5)	2.065584	3	7	–	–	–	$1.447 \pm 0.267 \times 10^{-3}$

Continued on next page...

Table 4.4 continued: Line Fluxes for Low Velocity UV Excited H_2 Component (Normalized to H I Br γ)

Line ID	λ (μm)	v_u	J_u	M 1-11	Vy 2-2	Hen 2-459 (McD)	Hen 2-459 (DCT)
4-2 O(3)	1.509865	4	1	$1.161 \pm 0.176 \times 10^{-2}$	–	$4.289 \pm 0.725 \times 10^{-3}$	$4.540 \pm 0.729 \times 10^{-3}$
4-2 O(4)	1.563515	4	2	$5.184 \pm 0.793 \times 10^{-3}$	$8.186 \pm 1.789 \times 10^{-4}$	$2.518 \pm 0.453 \times 10^{-3}$	–
4-2 O(5)	1.622299	4	3	$6.067 \pm 0.928 \times 10^{-3}$	$5.112 \pm 1.138 \times 10^{-4}$	$3.586 \pm 0.579 \times 10^{-3}$	$3.286 \pm 0.524 \times 10^{-3}$
4-2 O(6)	1.686462	4	4	$1.668 \pm 0.296 \times 10^{-3}$	–	–	–
4-2 O(7)	1.756281	4	5	$1.622 \pm 0.284 \times 10^{-3}$	–	$8.207 \pm 2.237 \times 10^{-4}$	–
4-2 Q(9)	1.498876	4	9	–	–	–	$9.417 \pm 3.179 \times 10^{-4}$
5-3 O(2)	1.560736	5	0	$4.529 \pm 0.699 \times 10^{-3}$	$1.010 \pm 0.179 \times 10^{-3}$	$2.271 \pm 0.407 \times 10^{-3}$	$1.754 \pm 0.315 \times 10^{-3}$
5-3 Q(1)	1.492933	5	1	$1.167 \pm 0.183 \times 10^{-2}$	–	–	–
5-3 O(3)	1.613520	5	1	$1.053 \pm 0.159 \times 10^{-2}$	$2.058 \pm 0.320 \times 10^{-3}$	$4.498 \pm 0.709 \times 10^{-3}$	$4.662 \pm 0.720 \times 10^{-3}$
5-3 Q(2)	1.497982	5	2	–	–	–	$1.604 \pm 0.446 \times 10^{-3}$
5-3 O(4)	1.671814	5	2	$4.723 \pm 0.724 \times 10^{-3}$	$2.437 \pm 0.846 \times 10^{-4}$	$2.074 \pm 0.372 \times 10^{-3}$	$1.263 \pm 0.241 \times 10^{-3}$
5-3 Q(3)	1.505588	5	3	$1.018 \pm 0.163 \times 10^{-2}$	–	$2.954 \pm 0.902 \times 10^{-3}$	$6.056 \pm 1.339 \times 10^{-3}$
5-3 O(5)	1.735889	5	3	–	–	$3.484 \pm 0.701 \times 10^{-3}$	–
5-3 Q(4)	1.515792	5	4	$5.815 \pm 0.905 \times 10^{-3}$	–	–	$1.104 \pm 0.305 \times 10^{-3}$
5-3 Q(5)	1.528648	5	5	$6.049 \pm 1.182 \times 10^{-3}$	–	–	$1.321 \pm 0.313 \times 10^{-3}$
5-3 Q(7)	1.562635	5	7	–	–	$1.226 \pm 0.278 \times 10^{-3}$	–
5-3 Q(9)	1.608398	5	9	$9.991 \pm 2.479 \times 10^{-4}$	–	–	$9.601 \pm 2.362 \times 10^{-4}$
6-4 O(2)	1.675032	6	0	$3.789 \pm 0.582 \times 10^{-3}$	–	$1.400 \pm 0.264 \times 10^{-3}$	$1.729 \pm 0.287 \times 10^{-3}$
6-4 Q(1)	1.601534	6	1	$9.985 \pm 1.505 \times 10^{-3}$	–	$3.257 \pm 0.529 \times 10^{-3}$	$2.856 \pm 0.456 \times 10^{-3}$
6-4 O(3)	1.732641	6	1	$7.576 \pm 1.155 \times 10^{-3}$	–	–	$2.182 \pm 0.746 \times 10^{-3}$
6-4 S(0)	1.536891	6	2	$4.786 \pm 0.739 \times 10^{-3}$	–	$8.840 \pm 2.725 \times 10^{-4}$	$7.431 \pm 2.124 \times 10^{-4}$
6-4 Q(2)	1.607390	6	2	$4.910 \pm 0.753 \times 10^{-3}$	$2.602 \pm 0.868 \times 10^{-4}$	$1.652 \pm 0.315 \times 10^{-3}$	$1.070 \pm 0.230 \times 10^{-3}$
6-4 S(1)	1.501560	6	3	–	–	$2.873 \pm 0.592 \times 10^{-3}$	$3.669 \pm 0.608 \times 10^{-3}$
6-4 Q(3)	1.616224	6	3	$6.645 \pm 1.006 \times 10^{-3}$	–	$2.829 \pm 0.461 \times 10^{-3}$	$2.347 \pm 0.381 \times 10^{-3}$
6-4 Q(4)	1.628094	6	4	$3.651 \pm 0.567 \times 10^{-3}$	–	$1.018 \pm 0.253 \times 10^{-3}$	$1.069 \pm 0.222 \times 10^{-3}$

Continued on next page...

Table 4.4 continued: Line Fluxes for Low Velocity UV Excited H_2 Component (Normalized to H I Br γ)

Line ID	λ (μm)	v_u	J_u	M 1-11	Vy 2-2	Hen 2-459 (McD)	Hen 2-459 (DCT)
6-4 O(7)	2.029684	6	5	–	–	–	$4.907 \pm 1.472 \times 10^{-4}$
6-4 Q(5)	1.643084	6	5	$3.685 \pm 0.570 \times 10^{-3}$	–	–	–
6-4 Q(6)	1.661304	6	6	$1.767 \pm 0.293 \times 10^{-3}$	$8.352 \pm 1.475 \times 10^{-4}$	$8.069 \pm 2.079 \times 10^{-4}$	–
7-5 Q(1)	1.728799	7	1	$7.254 \pm 1.117 \times 10^{-3}$	–	$2.140 \pm 0.454 \times 10^{-3}$	$2.242 \pm 0.385 \times 10^{-3}$
7-5 S(0)	1.658492	7	2	$2.483 \pm 0.412 \times 10^{-3}$	–	$1.230 \pm 0.251 \times 10^{-3}$	$7.771 \pm 1.744 \times 10^{-4}$
7-5 Q(2)	1.735762	7	2	–	–	$3.341 \pm 0.557 \times 10^{-3}$	–
7-5 S(1)	1.620548	7	3	$6.335 \pm 0.961 \times 10^{-3}$	$7.965 \pm 1.375 \times 10^{-4}$	$3.322 \pm 0.530 \times 10^{-3}$	$2.662 \pm 0.421 \times 10^{-3}$
7-5 O(5)	2.022053	7	3	–	$7.425 \pm 1.306 \times 10^{-4}$	$1.751 \pm 0.335 \times 10^{-3}$	$1.704 \pm 0.292 \times 10^{-3}$
7-5 Q(4)	1.760446	7	4	$2.118 \pm 0.359 \times 10^{-3}$	–	–	$8.943 \pm 1.991 \times 10^{-4}$
7-5 O(6)	2.109001	7	4	$2.019 \pm 0.381 \times 10^{-3}$	–	–	–
7-5 Q(5)	1.778390	7	5	$3.170 \pm 0.577 \times 10^{-3}$	–	–	–
7-5 S(3)	1.561510	7	5	$4.221 \pm 0.652 \times 10^{-3}$	–	$2.276 \pm 0.402 \times 10^{-3}$	$2.177 \pm 0.368 \times 10^{-3}$
7-5 S(4)	1.540006	7	6	$2.534 \pm 0.425 \times 10^{-3}$	–	–	$1.187 \pm 0.261 \times 10^{-3}$
7-5 O(9)	2.427661	7	7	$6.759 \pm 2.041 \times 10^{-4}$	–	–	–
7-5 S(5)	1.523623	7	7	–	–	$1.232 \pm 0.343 \times 10^{-3}$	$1.212 \pm 0.282 \times 10^{-3}$
8-6 O(2)	1.970799	8	0	–	$5.098 \pm 1.320 \times 10^{-4}$	–	–
8-6 O(3)	2.041830	8	1	$4.704 \pm 0.728 \times 10^{-3}$	$1.109 \pm 0.196 \times 10^{-3}$	$2.837 \pm 0.504 \times 10^{-3}$	$2.022 \pm 0.334 \times 10^{-3}$
8-6 O(5)	2.210763	8	3	$2.464 \pm 0.418 \times 10^{-3}$	–	–	–
8-6 S(1)	1.763952	8	3	$3.430 \pm 0.604 \times 10^{-3}$	$1.210 \pm 0.245 \times 10^{-3}$	–	$2.564 \pm 0.488 \times 10^{-3}$
8-6 S(2)	1.729672	8	4	$2.087 \pm 0.377 \times 10^{-3}$	–	–	$8.447 \pm 2.257 \times 10^{-4}$
8-6 O(6)	2.310167	8	4	$5.599 \pm 1.877 \times 10^{-4}$	–	–	–
8-6 S(3)	1.701803	8	5	$2.120 \pm 0.359 \times 10^{-3}$	–	$1.254 \pm 0.296 \times 10^{-3}$	$9.930 \pm 2.206 \times 10^{-4}$
9-7 O(2)	2.172715	9	0	$1.074 \pm 0.205 \times 10^{-3}$	–	–	–
9-7 O(3)	2.253724	9	1	$2.514 \pm 0.431 \times 10^{-3}$	$7.920 \pm 1.388 \times 10^{-4}$	$1.252 \pm 0.256 \times 10^{-3}$	$1.201 \pm 0.242 \times 10^{-3}$
9-7 Q(2)	2.084098	9	2	–	$3.014 \pm 0.988 \times 10^{-4}$	–	–

Continued on next page...

Table 4.4 continued: Line Fluxes for Low Velocity UV Excited H_2 Component (Normalized to H I Br γ)

Line ID	λ (μm)	v_u	J_u	M 1-11	Vy 2-2	Hen 2-459 (McD)	Hen 2-459 (DCT)
9-7 Q(3)	2.100664	9	3	$1.906 \pm 0.303 \times 10^{-3}$	–	$8.499 \pm 1.996 \times 10^{-4}$	$4.741 \pm 1.277 \times 10^{-4}$
9-7 Q(5)	2.151876	9	5	$8.797 \pm 1.690 \times 10^{-4}$	–	–	–
10-7 O(3)	1.548849	10	1	$2.400 \pm 0.396 \times 10^{-3}$	–	$8.371 \pm 2.546 \times 10^{-4}$	–
10-7 O(4)	1.595267	10	2	$1.574 \pm 0.314 \times 10^{-3}$	–	–	–
10-8 S(1)	2.176855	10	3	$1.037 \pm 0.186 \times 10^{-3}$	–	–	$3.924 \pm 1.188 \times 10^{-4}$
10-7 O(5)	1.648305	10	3	$9.913 \pm 1.998 \times 10^{-4}$	–	–	–
10-7 Q(5)	1.522674	10	5	$9.229 \pm 2.403 \times 10^{-4}$	–	–	–
10-7 Q(7)	1.584507	10	7	–	$6.014 \pm 1.628 \times 10^{-4}$	–	–
11-8 Q(1)	1.657102	11	1	$1.792 \pm 0.304 \times 10^{-3}$	–	–	–
11-8 S(1)	1.591504	11	3	$1.616 \pm 0.291 \times 10^{-3}$	–	–	–
11-8 Q(3)	1.687032	11	3	$5.930 \pm 1.813 \times 10^{-4}$	–	–	–
11-8 Q(4)	1.711844	11	4	$5.831 \pm 1.833 \times 10^{-4}$	–	–	–
11-8 S(2)	1.578830	11	4	$6.864 \pm 1.878 \times 10^{-4}$	–	–	–
11-8 S(3)	1.573164	11	5	$1.296 \pm 0.292 \times 10^{-3}$	–	–	–
11-8 Q(5)	1.744026	11	5	$6.930 \pm 2.015 \times 10^{-4}$	–	–	–
12-9 Q(3)	1.986307	12	3	–	–	$6.100 \pm 1.744 \times 10^{-4}$	$9.251 \pm 1.776 \times 10^{-4}$

Table 4.5: Line Fluxes for the H_2 Bullets (Normalized to H I Br γ)

Line ID	λ (μm)	v_u	J_u	M 1-11		Vy 2-2	
				Blue Bullet	Red Bullet	Blue Bullet	Red Bullet
1-0 Q(1)	2.406592	1	1	$7.780 \pm 1.172 \times 10^{-3}$	–	$2.332 \pm 0.388 \times 10^{-3}$	$2.289 \pm 0.349 \times 10^{-3}$
1-0 Q(2)	2.413439	1	2	–	$8.742 \pm 2.175 \times 10^{-4}$	$5.828 \pm 1.463 \times 10^{-4}$	$6.681 \pm 1.196 \times 10^{-4}$
1-0 S(0)	2.223290	1	2	$2.247 \pm 0.342 \times 10^{-3}$	$1.055 \pm 0.170 \times 10^{-3}$	$5.168 \pm 0.813 \times 10^{-4}$	$5.722 \pm 0.895 \times 10^{-4}$
1-0 Q(3)	2.423730	1	3	$5.682 \pm 0.862 \times 10^{-3}$	$2.633 \pm 0.665 \times 10^{-3}$	–	–
1-0 S(1)	2.121834	1	3	$8.822 \pm 1.325 \times 10^{-3}$	$4.490 \pm 0.676 \times 10^{-3}$	$2.231 \pm 0.336 \times 10^{-3}$	$2.337 \pm 0.352 \times 10^{-3}$
1-0 Q(4)	2.437489	1	4	$1.483 \pm 0.247 \times 10^{-3}$	$7.246 \pm 1.471 \times 10^{-4}$	$4.463 \pm 0.960 \times 10^{-4}$	–
1-0 S(2)	2.033758	1	4	–	–	$8.116 \pm 1.369 \times 10^{-4}$	$6.906 \pm 1.072 \times 10^{-4}$
1-0 Q(5)	2.454752	1	5	–	$1.648 \pm 0.313 \times 10^{-3}$	–	–
1-0 S(3)	1.957559	1	5	–	–	–	$1.162 \pm 0.237 \times 10^{-3}$
2-1 S(1)	2.247716	2	3	$4.150 \pm 0.869 \times 10^{-4}$	–	$1.047 \pm 0.283 \times 10^{-4}$	$1.009 \pm 0.342 \times 10^{-4}$
2-1 S(3)	2.073482	2	5	–	–	$1.088 \pm 0.284 \times 10^{-4}$	–
				Hen 2-459 (McD)		Hen 2-459 (DCT)	
				Blue Bullet	Red Bullet	Blue Bullet	Red Bullet
1-0 Q(1)	2.406592	1	1	$2.383 \pm 0.414 \times 10^{-3}$	–	$1.841 \pm 0.295 \times 10^{-3}$	–
1-0 S(0)	2.223290	1	2	$4.854 \pm 1.242 \times 10^{-4}$	$4.976 \pm 1.047 \times 10^{-4}$	$4.839 \pm 0.953 \times 10^{-4}$	–
1-0 Q(3)	2.423730	1	3	$1.986 \pm 0.408 \times 10^{-3}$	–	$9.065 \pm 1.970 \times 10^{-4}$	–
1-0 S(1)	2.121834	1	3	$5.343 \pm 0.807 \times 10^{-3}$	$3.134 \pm 0.475 \times 10^{-3}$	$2.764 \pm 0.418 \times 10^{-3}$	$1.035 \pm 0.162 \times 10^{-3}$
1-0 S(2)	2.033758	1	4	$1.433 \pm 0.238 \times 10^{-3}$	$7.967 \pm 1.674 \times 10^{-4}$	$8.837 \pm 1.517 \times 10^{-4}$	$3.505 \pm 0.756 \times 10^{-4}$

Table 4.6: Cloudy Model Details for the Low Velocity UV-excited H_2 Components

PN	$T^{\star}_{\rm eff}$ (K)	$L^{\star}/L_{\odot}$	Best-fit $\log_{10}(n_H)$ [cm^{-3}]	$\sum\left[\log_{10}(N_{\rm data}/N_{\rm model})\right]^2$
M 1-11	$31{,}830_e$	4710_a	4.5	3.15
Vy 2-2	$59{,}500_i$	6000_j	4.2	6.40
Hen 2-459 (McD)	$77{,}000_m$	23440_m	4.2	5.40
Hen 2-459 (DCT)	$77{,}000_m$	23440_m	4.1	6.97

collisionally de-excited than in Vy 2-2 and Hen 2-459.

To quantify the observed H_2 level populations in the low velocity UV-excited gas, we fit one-dimensional constant density Cloudy 13.03c (Ferland et al., 2013) models to the level populations. We set the central stars to be blackbodies with the effective temperatures and luminosities given in Table 4.1, enable the full treatments for H_2 (Shaw et al., 2005) and Fe II (Verner et al., 1999), and set the abundances and grain properties to Cloudy's default PN prescription. We vary the density from $n_H = 2.5 \times 10^3$–10^5 cm^{-3} to find the best fit. Each model is run until the H_2 column density reaches $N_{H_2} = 10^{21}$ cm^{-2} to ensure that we simulate the full emitting region of UV-excited H_2. We quantify the goodness-of-fit for each model using the χ^2 parameter of the data-to-model ratio logarithm $\sum\left[\log_{10}(N_{\rm data}/N_{\rm model})\right]^2$ (as we did for the Orion Bar in Chapter 2.4.1.2). We report our model details, best fit densities, and $\sum\left[\log_{10}(N_{\rm data}/N_{\rm model})\right]^2$ in Table 4.6, and the data-to-model ratios in Table 4.7. Figure 4.10 shows the models overlaid on excitation diagrams of the PNe, and Figure 4.11 shows data-to-model ratios.

The rovibrational level populations for the UV-excited H_2 are well fit by the model for M 1-11, but not as well fit by the models for Vy 2-2 and Hen 2-459. This is especially apparent for the $v = 1$ ladder, where the Vy 2-2 and Hen 2-459 models underpredict the level populations by about an order of magnitude. The densities derived from the best-fit models for the low velocity UV-excited component in each nebula are in the range $n_H = 1.26 \times 10^4$–3.16×10^4 cm^{-3}. These densities are also similar to the values derived from the [Fe II] and [Fe III] lines. The high-J lines in M 1-11 are also not well fit by the model, suggesting the low velocity UV excited H_2 component in M 1-11 is colder than the best-fit model. Conversely, the high level populations in $v = 1$ for Vy 2-2 and Hen 2-459 suggest that either the UV-excited gas is warmer than the model predictions or there is some shock-heated H_2, perhaps like

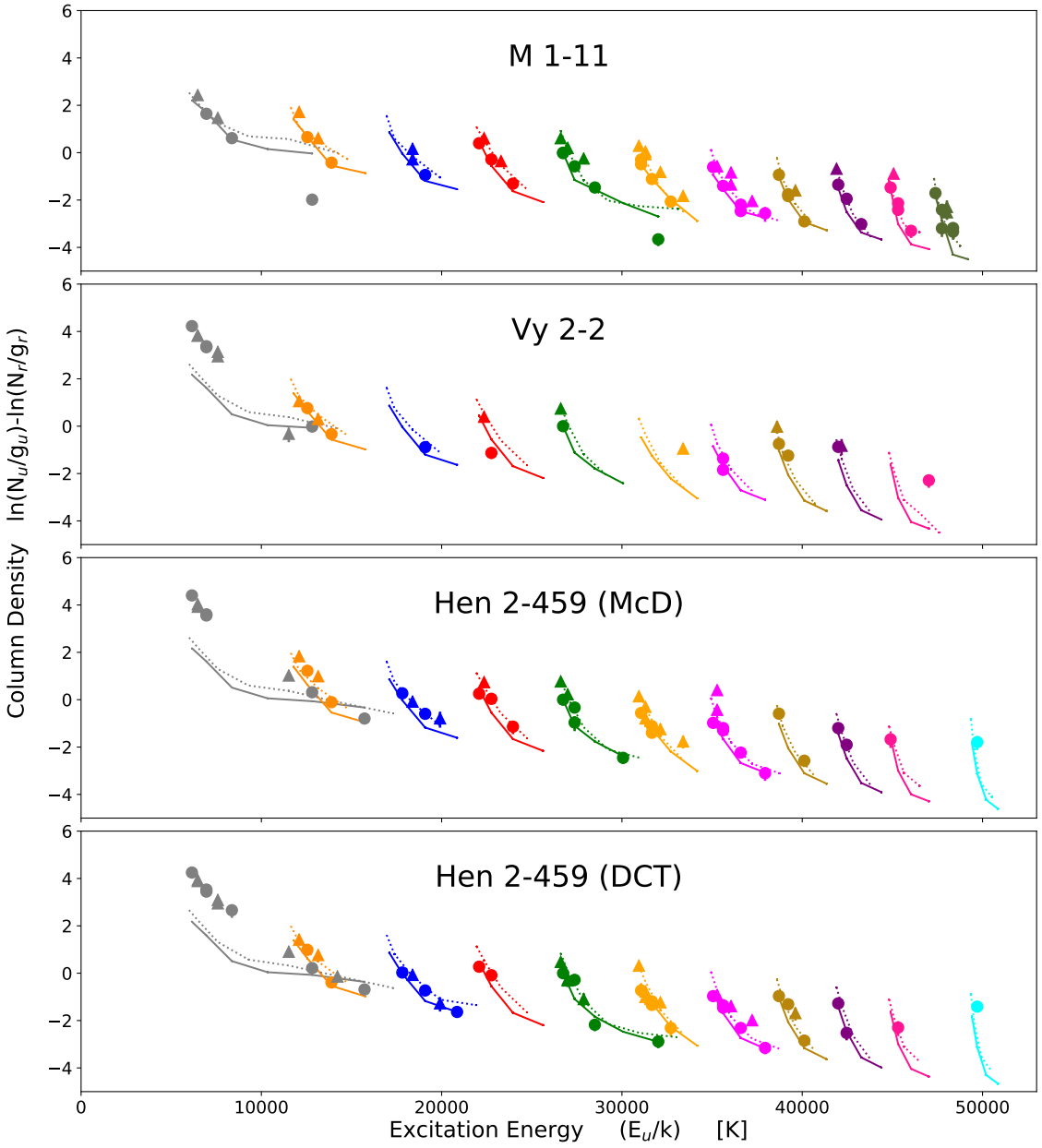

Figure 4.10: Excitation diagrams of the observed PNe with the Cloudy model fits overlaid as solid lines for the ortho levels and and dashed lines for the para levels.

the high velocity bullets but moving mainly perpendicular to the line of sight rather than radially so that it is not apparent in our observations.

The high velocity bullets in M 1-11 and Vy 2-2 show thermal H_2 level populations, with the characteristic monotonically decreasing trend in their excitation diagrams.

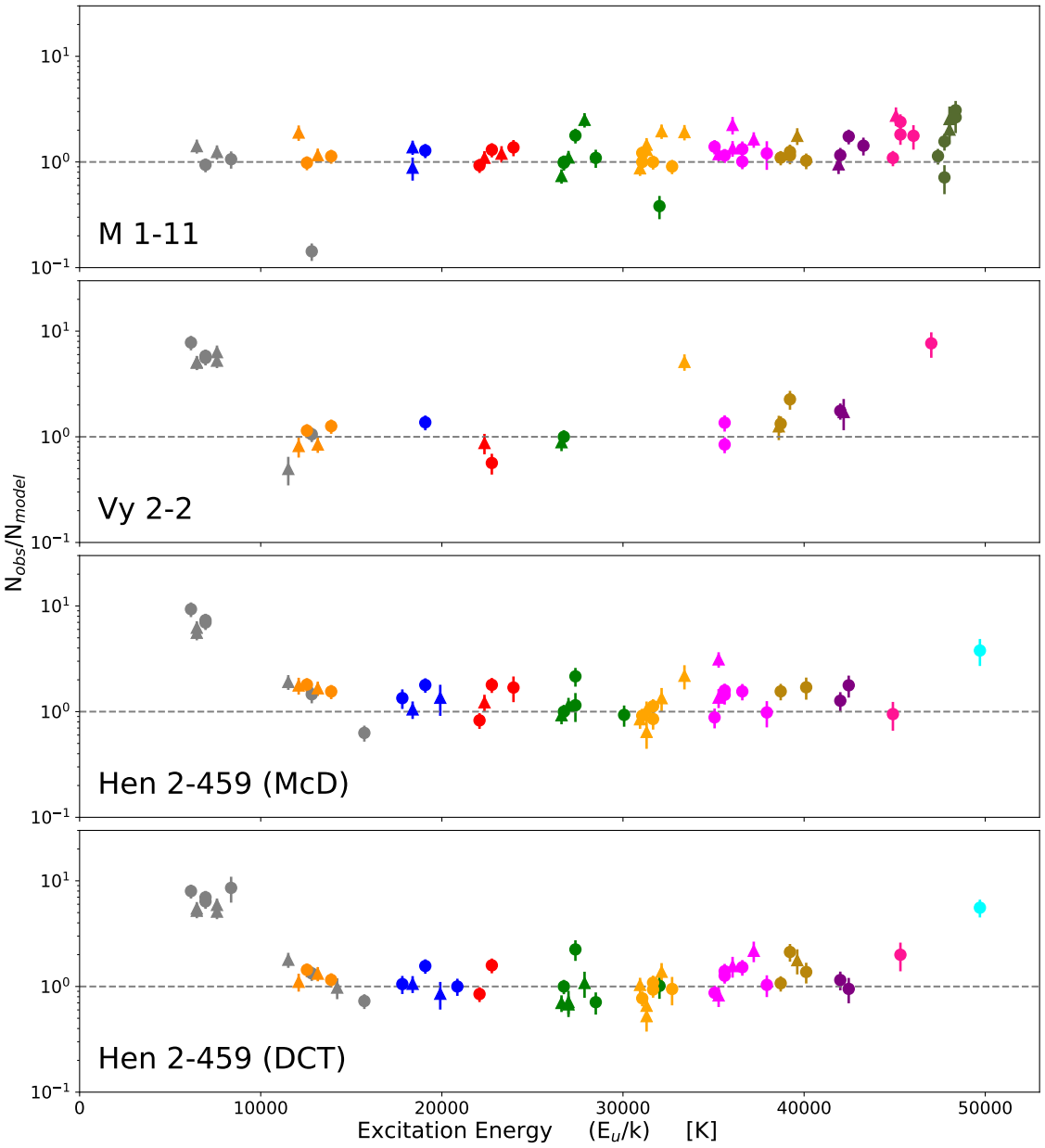

Figure 4.11: Semi-log plots of the ratios of the observed rovibrational level populations in our PNe data (N_{obs}) to the model predictions (N_{model}) shown in Figure 4.10. The horizontal dashed line represents a ratio of unity where the data and model are in perfect agreement. Deviations from unity show where the level populations are not exactly matched by the model predictions.

Table 4.7: H_2 column densities for low velocity UV excited components and comparison to Cloudy Models

H_2 Line ID	λ (μm)	v_u	J_u	M 1-11		Vy 2-2		Hen 2-459 (McD)		Hen 2-459 (DCT)	
				$\ln\left(\frac{N_u}{g_u}/\frac{N_r}{g_r}\right)$	N_u/N_m	$\ln\left(\frac{N_u}{g_u}/\frac{N_r}{g_r}\right)$	N_u/N_m	$\ln\left(\frac{N_u}{g_u}/\frac{N_r}{g_r}\right)$	N_u/N_m	$\ln\left(\frac{N_u}{g_u}/\frac{N_r}{g_r}\right)$	N_u/N_m
1-0 Q(1)	2.406592	1	1	–	–	$4.226^{+0.145}_{-0.170}$	7.80	$4.403^{+0.147}_{-0.173}$	9.33	$4.251^{+0.140}_{-0.163}$	7.99
1-0 Q(2)	2.413439	1	2	–	–	$3.830^{+0.140}_{-0.163}$	5.06	$3.924^{+0.140}_{-0.163}$	5.57	$3.891^{+0.140}_{-0.163}$	5.21
1-0 S(0)	2.223290	1	2	$2.432^{+0.140}_{-0.163}$	1.41	$3.821^{+0.140}_{-0.163}$	5.04	$4.031^{+0.140}_{-0.163}$	6.23	$3.939^{+0.140}_{-0.163}$	5.47
1-0 Q(3)	2.423730	1	3	–	–	$3.335^{+0.140}_{-0.163}$	5.57	$3.555^{+0.140}_{-0.163}$	6.97	$3.446^{+0.140}_{-0.163}$	6.39
1-0 S(1)	2.121834	1	3	$1.643^{+0.140}_{-0.163}$	0.94	$3.378^{+0.140}_{-0.163}$	5.82	$3.604^{+0.140}_{-0.163}$	7.34	$3.533^{+0.140}_{-0.163}$	6.97
1-0 Q(4)	2.437489	1	4	$1.468^{+0.143}_{-0.166}$	1.24	$3.134^{+0.144}_{-0.168}$	6.33	–	–	$2.949^{+0.141}_{-0.164}$	5.11
1-0 S(2)	2.033758	1	4	–	–	$2.950^{+0.140}_{-0.163}$	5.26	–	–	$3.094^{+0.140}_{-0.163}$	5.92
1-0 Q(5)	2.454752	1	5	$0.613^{+0.170}_{-0.205}$	1.06	–	–	–	–	–	–
1-0 S(3)	1.957559	1	5	–	–	–	–	–	–	$2.659^{+0.243}_{-0.321}$	8.57
1-0 S(6)	1.788050	1	8	–	–	$-0.321^{+0.263}_{-0.359}$	0.50	$1.020^{+0.148}_{-0.174}$	1.91	$0.905^{+0.150}_{-0.177}$	1.79
1-0 S(7)	1.747955	1	9	$-1.983^{+0.173}_{-0.209}$	0.14	$-0.015^{+0.145}_{-0.169}$	1.06	$0.315^{+0.164}_{-0.196}$	1.46	$0.215^{+0.142}_{-0.166}$	1.33
1-0 S(8)	1.714738	1	10	–	–	–	–	–	–	$-0.141^{+0.202}_{-0.253}$	0.98
1-0 S(9)	1.687761	1	11	–	–	–	–	$-0.795^{+0.159}_{-0.189}$	0.63	$-0.685^{+0.148}_{-0.174}$	0.73
2-1 S(0)	2.355605	2	2	$1.716^{+0.153}_{-0.181}$	1.90	$1.059^{+0.202}_{-0.253}$	0.82	$1.835^{+0.167}_{-0.201}$	1.77	$1.418^{+0.176}_{-0.214}$	1.11
2-1 S(1)	2.247716	2	3	$0.655^{+0.140}_{-0.163}$	0.98	$0.763^{+0.141}_{-0.164}$	1.14	$1.221^{+0.141}_{-0.164}$	1.80	$0.990^{+0.141}_{-0.164}$	1.44
2-1 S(2)	2.154216	2	4	$0.612^{+0.141}_{-0.164}$	1.16	$0.304^{+0.155}_{-0.183}$	0.85	$0.990^{+0.143}_{-0.167}$	1.66	$0.767^{+0.143}_{-0.167}$	1.32
2-1 S(3)	2.073482	2	5	$-0.422^{+0.140}_{-0.163}$	1.13	$-0.333^{+0.144}_{-0.168}$	1.26	$-0.103^{+0.143}_{-0.167}$	1.55	$-0.391^{+0.145}_{-0.169}$	1.15
2-1 S(4)	2.004109	2	6	–	–	$-0.062^{+0.296}_{-0.422}$	1.37	–	–	–	–
3-1 O(5)	1.522033	3	3	–	–	–	–	$0.270^{+0.190}_{-0.235}$	1.34	$0.029^{+0.178}_{-0.216}$	1.05
3-1 O(6)	1.581171	3	4	$-0.282^{+0.220}_{-0.282}$	0.88	–	–	–	–	–	–
3-2 S(2)	2.287045	3	4	$0.161^{+0.142}_{-0.166}$	1.38	–	–	$-0.083^{+0.172}_{-0.208}$	1.05	$-0.072^{+0.167}_{-0.201}$	1.06
3-2 S(3)	2.201399	3	5	$-0.942^{+0.142}_{-0.165}$	1.28	$-0.885^{+0.148}_{-0.174}$	1.37	$-0.596^{+0.145}_{-0.170}$	1.79	$-0.728^{+0.145}_{-0.169}$	1.56
3-2 S(4)	2.128015	3	6	–	–	–	–	$-0.789^{+0.282}_{-0.394}$	1.35	$-1.272^{+0.256}_{-0.346}$	0.85

Continued on next page...

Table 4.7 continued: H_2 column densities for low velocity UV excited components and comparison to Cloudy Models

H_2 Line ID	λ (μm)	v_u	J_u	M 1-11		Vy 2-2		Hen 2-459 (McD)		Hen 2-459 (DCT)	
				$\ln\left(\frac{N_u}{g_u}/\frac{N_r}{g_r}\right)$	N_u/N_m	$\ln\left(\frac{N_u}{g_u}/\frac{N_r}{g_r}\right)$	N_u/N_m	$\ln\left(\frac{N_u}{g_u}/\frac{N_r}{g_r}\right)$	N_u/N_m	$\ln\left(\frac{N_u}{g_u}/\frac{N_r}{g_r}\right)$	N_u/N_m
3-2 S(5)	2.065584	3	7	–	–	–	–	–	–	$-1.636^{+0.169}_{-0.204}$	1.00
4-2 O(3)	1.509865	4	1	$0.398^{+0.141}_{-0.164}$	0.93	–	–	$0.253^{+0.156}_{-0.185}$	0.83	$0.274^{+0.149}_{-0.175}$	0.85
4-2 O(4)	1.563515	4	2	$0.611^{+0.142}_{-0.166}$	1.10	$0.398^{+0.198}_{-0.247}$	0.87	$0.740^{+0.166}_{-0.198}$	1.22	–	–
4-2 O(5)	1.622299	4	3	$-0.287^{+0.142}_{-0.166}$	1.30	$-1.129^{+0.201}_{-0.252}$	0.57	$0.037^{+0.150}_{-0.176}$	1.79	$-0.086^{+0.148}_{-0.174}$	1.59
4-2 O(6)	1.686462	4	4	$-0.359^{+0.163}_{-0.195}$	1.20	–	–	–	–	–	–
4-2 O(7)	1.756281	4	5	$-1.308^{+0.161}_{-0.192}$	1.37	–	–	$-1.138^{+0.241}_{-0.318}$	1.69	–	–
4-2 Q(9)	1.498876	4	9	–	–	–	–	–	–	$-2.686^{+0.291}_{-0.412}$	inf
5-3 O(2)	1.560736	5	0	$0.610^{+0.144}_{-0.168}$	0.74	$0.742^{+0.163}_{-0.195}$	0.89	$0.771^{+0.165}_{-0.198}$	0.92	$0.477^{+0.165}_{-0.198}$	0.70
5-3 Q(1)	1.492933	5	1	$-0.019^{+0.145}_{-0.170}$	0.98	–	–	–	–	–	–
5-3 O(3)	1.613520	5	1	$0.000^{+0.140}_{-0.163}$	1.00	$0.000^{+0.145}_{-0.169}$	1.00	$0.000^{+0.146}_{-0.171}$	1.00	$0.000^{+0.144}_{-0.168}$	1.00
5-3 Q(2)	1.497982	5	2	–	–	–	–	–	–	$-0.256^{+0.246}_{-0.326}$	0.71
5-3 O(4)	1.671814	5	2	$0.198^{+0.143}_{-0.166}$	1.10	$-1.134^{+0.298}_{-0.426}$	0.29	$0.226^{+0.165}_{-0.198}$	1.15	$-0.306^{+0.175}_{-0.212}$	0.68
5-3 Q(3)	1.505588	5	3	$-0.577^{+0.148}_{-0.174}$	1.78	–	–	$-0.963^{+0.266}_{-0.364}$	1.15	$-0.281^{+0.200}_{-0.250}$	2.24
5-3 O(5)	1.735889	5	3	–	–	–	–	$-0.332^{+0.183}_{-0.224}$	2.16	–	–
5-3 Q(4)	1.515792	5	4	$-0.246^{+0.145}_{-0.169}$	2.51	–	–	–	–	$-1.092^{+0.244}_{-0.324}$	1.08
5-3 Q(5)	1.528648	5	5	$-1.470^{+0.178}_{-0.217}$	1.09	–	–	–	–	$-2.177^{+0.213}_{-0.271}$	0.71
5-3 Q(7)	1.562635	5	7	–	–	–	–	$-2.456^{+0.205}_{-0.258}$	0.93	–	–
5-3 Q(9)	1.608398	5	9	$-3.660^{+0.222}_{-0.285}$	0.38	–	–	–	–	$-2.885^{+0.220}_{-0.282}$	1.01
6-4 O(2)	1.675032	6	0	$0.289^{+0.143}_{-0.167}$	0.87	–	–	$0.144^{+0.173}_{-0.209}$	0.85	$0.319^{+0.154}_{-0.182}$	1.04
6-4 Q(1)	1.601534	6	1	$-0.291^{+0.140}_{-0.163}$	1.22	–	–	$-0.560^{+0.151}_{-0.177}$	0.92	$-0.728^{+0.148}_{-0.174}$	0.77
6-4 O(3)	1.732641	6	1	$-0.490^{+0.142}_{-0.165}$	1.00	–	–	–	–	$-0.920^{+0.294}_{-0.418}$	0.64
6-4 S(0)	1.536891	6	2	$0.047^{+0.144}_{-0.168}$	1.46	–	–	$-0.792^{+0.269}_{-0.369}$	0.64	$-1.001^{+0.251}_{-0.337}$	0.52
6-4 Q(2)	1.607390	6	2	$-0.066^{+0.143}_{-0.167}$	1.30	$-1.371^{+0.288}_{-0.406}$	0.36	$-0.304^{+0.174}_{-0.211}$	1.05	$-0.775^{+0.195}_{-0.242}$	0.66

Continued on next page...

Table 4.7 continued: H_2 column densities for low velocity UV excited components and comparison to Cloudy Models

H_2 Line ID	λ (μm)	v_u	J_u	M 1-11		Vy 2-2		Hen 2-459 (McD)		Hen 2-459 (DCT)	
				$\ln\left(\frac{N_u}{g_u}/\frac{N_r}{g_r}\right)$	N_u/N_m	$\ln\left(\frac{N_u}{g_u}/\frac{N_r}{g_r}\right)$	N_u/N_m	$\ln\left(\frac{N_u}{g_u}/\frac{N_r}{g_r}\right)$	N_u/N_m	$\ln\left(\frac{N_u}{g_u}/\frac{N_r}{g_r}\right)$	N_u/N_m
6-4 S(1)	1.501560	6	3	–	–	–	–	$-1.397^{+0.187}_{-0.231}$	0.85	$-1.188^{+0.153}_{-0.181}$	1.09
6-4 Q(3)	1.616224	6	3	$-1.113^{+0.141}_{-0.164}$	1.00	–	–	$-1.117^{+0.151}_{-0.178}$	1.13	$-1.339^{+0.150}_{-0.177}$	0.94
6-4 Q(4)	1.628094	6	4	$-0.817^{+0.144}_{-0.169}$	1.95	–	–	$-1.244^{+0.222}_{-0.285}$	1.34	$-1.230^{+0.189}_{-0.233}$	1.38
6-4 O(7)	2.029684	6	5	–	–	–	–	–	–	$-2.312^{+0.262}_{-0.357}$	0.95
6-4 Q(5)	1.643084	6	5	$-2.067^{+0.144}_{-0.168}$	0.91	–	–	–	–	–	–
6-4 Q(6)	1.661304	6	6	$-1.829^{+0.153}_{-0.181}$	1.92	$-0.946^{+0.163}_{-0.194}$	5.12	$-1.763^{+0.229}_{-0.298}$	2.19	–	–
7-5 Q(1)	1.728799	7	1	$-0.609^{+0.143}_{-0.167}$	1.39	–	–	$-0.979^{+0.192}_{-0.238}$	0.88	$-0.968^{+0.159}_{-0.189}$	0.87
7-5 S(0)	1.658492	7	2	$-0.578^{+0.154}_{-0.182}$	1.19	–	–	$-0.430^{+0.186}_{-0.228}$	1.36	$-0.925^{+0.203}_{-0.254}$	0.82
7-5 Q(2)	1.735762	7	2	–	–	–	–	$0.404^{+0.154}_{-0.182}$	3.13	–	–
7-5 S(1)	1.620548	7	3	$-1.403^{+0.141}_{-0.165}$	1.15	$-1.844^{+0.159}_{-0.189}$	0.84	$-1.198^{+0.148}_{-0.174}$	1.59	$-1.455^{+0.147}_{-0.172}$	1.26
7-5 O(5)	2.022053	7	3	–	–	$-1.368^{+0.162}_{-0.193}$	1.36	$-1.292^{+0.175}_{-0.213}$	1.44	$-1.355^{+0.158}_{-0.188}$	1.40
7-5 Q(4)	1.760446	7	4	$-1.347^{+0.156}_{-0.185}$	1.35	–	–	–	–	$-1.394^{+0.201}_{-0.252}$	1.56
7-5 O(6)	2.109001	7	4	$-0.837^{+0.173}_{-0.209}$	2.24	–	–	–	–	–	–
7-5 Q(5)	1.778390	7	5	$-2.195^{+0.167}_{-0.201}$	1.32	–	–	–	–	–	–
7-5 S(3)	1.561510	7	5	$-2.466^{+0.144}_{-0.168}$	1.01	–	–	$-2.233^{+0.163}_{-0.194}$	1.55	$-2.314^{+0.156}_{-0.185}$	1.52
7-5 S(4)	1.540006	7	6	$-2.044^{+0.155}_{-0.184}$	1.63	–	–	–	–	$-1.988^{+0.199}_{-0.249}$	2.18
7-5 O(9)	2.427661	7	7	$-2.560^{+0.264}_{-0.360}$	1.21	–	–	–	–	–	–
7-5 S(5)	1.523623	7	7	–	–	–	–	$-3.100^{+0.245}_{-0.326}$	0.98	$-3.153^{+0.209}_{-0.265}$	1.03
8-6 O(2)	1.970799	8	0	–	–	$-0.020^{+0.230}_{-0.300}$	1.26	–	–	–	–
8-6 O(3)	2.041830	8	1	$-0.935^{+0.144}_{-0.168}$	1.10	$-0.748^{+0.163}_{-0.194}$	1.33	$-0.591^{+0.163}_{-0.196}$	1.56	$-0.965^{+0.153}_{-0.181}$	1.07
8-6 O(5)	2.210763	8	3	$-1.754^{+0.157}_{-0.186}$	1.25	–	–	–	–	–	–
8-6 S(1)	1.763952	8	3	$-1.835^{+0.162}_{-0.194}$	1.15	$-1.244^{+0.184}_{-0.226}$	2.26	–	–	$-1.311^{+0.174}_{-0.211}$	2.12
8-6 S(2)	1.729672	8	4	$-1.597^{+0.166}_{-0.200}$	1.77	–	–	–	–	$-1.686^{+0.237}_{-0.311}$	1.77

Continued on next page...

Table 4.7 continued: H_2 column densities for low velocity UV excited components and comparison to Cloudy Models

H_2 Line ID	λ (μm)	v_u	J_u	M 1-11		Vy 2-2		Hen 2-459 (McD)		Hen 2-459 (DCT)	
				$\ln\left(\frac{N_u}{g_u}/\frac{N_r}{g_r}\right)$	N_u/N_m	$\ln\left(\frac{N_u}{g_u}/\frac{N_r}{g_r}\right)$	N_u/N_m	$\ln\left(\frac{N_u}{g_u}/\frac{N_r}{g_r}\right)$	N_u/N_m	$\ln\left(\frac{N_u}{g_u}/\frac{N_r}{g_r}\right)$	N_u/N_m
8-6 O(6)	2.310167	8	4	$-2.084^{+0.289}_{-0.408}$	1.08	–	–	–	–	–	–
8-6 S(3)	1.701803	8	5	$-2.903^{+0.156}_{-0.185}$	1.03	–	–	$-2.577^{+0.212}_{-0.269}$	1.70	$-2.846^{+0.201}_{-0.251}$	1.37
9-7 O(2)	2.172715	9	0	$-0.680^{+0.175}_{-0.212}$	0.95	–	–	–	–	–	–
9-7 O(3)	2.253724	9	1	$-1.351^{+0.158}_{-0.188}$	1.16	$-0.873^{+0.161}_{-0.193}$	1.76	$-1.198^{+0.186}_{-0.229}$	1.27	$-1.275^{+0.184}_{-0.225}$	1.15
9-7 Q(2)	2.084098	9	2	–	–	$-0.827^{+0.284}_{-0.397}$	1.72	–	–	–	–
9-7 Q(3)	2.100664	9	3	$-1.945^{+0.148}_{-0.173}$	1.74	–	–	$-1.902^{+0.211}_{-0.268}$	1.78	$-2.521^{+0.239}_{-0.314}$	0.95
9-7 Q(5)	2.151876	9	5	$-3.017^{+0.176}_{-0.213}$	1.43	–	–	–	–	–	–
10-7 O(3)	1.548849	10	1	$-1.472^{+0.153}_{-0.180}$	1.09	–	–	$-1.675^{+0.266}_{-0.363}$	0.95	–	–
10-7 O(4)	1.595267	10	2	$-0.886^{+0.182}_{-0.222}$	2.74	–	–	–	–	–	–
10-8 S(1)	2.176855	10	3	$-2.136^{+0.165}_{-0.197}$	2.40	–	–	–	–	$-2.293^{+0.265}_{-0.361}$	2.00
10-7 O(5)	1.648305	10	3	$-2.413^{+0.184}_{-0.225}$	1.82	–	–	–	–	–	–
10-7 Q(5)	1.522674	10	5	$-3.300^{+0.231}_{-0.302}$	1.77	–	–	–	–	–	–
10-7 Q(7)	1.584507	10	7	–	–	$-2.287^{+0.240}_{-0.316}$	7.67	–	–	–	–
11-8 Q(1)	1.657102	11	1	$-1.706^{+0.157}_{-0.186}$	1.14	–	–	–	–	–	–
11-8 S(1)	1.591504	11	3	$-2.411^{+0.166}_{-0.199}$	1.56	–	–	–	–	–	–
11-8 Q(3)	1.687032	11	3	$-3.195^{+0.267}_{-0.365}$	0.71	–	–	–	–	–	–
11-8 Q(4)	1.711844	11	4	$-2.289^{+0.273}_{-0.378}$	2.55	–	–	–	–	–	–
11-8 S(2)	1.578830	11	4	$-2.519^{+0.242}_{-0.320}$	2.02	–	–	–	–	–	–
11-8 S(3)	1.573164	11	5	$-3.181^{+0.203}_{-0.255}$	3.08	–	–	–	–	–	–
11-8 Q(5)	1.744026	11	5	$-3.336^{+0.255}_{-0.344}$	2.64	–	–	–	–	–	–
12-9 Q(3)	1.986307	12	3	–	–	–	–	$-1.791^{+0.251}_{-0.337}$	3.79	$-1.411^{+0.176}_{-0.213}$	5.57

Table 4.8: Column Densities and Ratio to Fitted Boltzmann Distribution for M 1-11 H_2 Thermal Bullets

H_2 Line ID	λ (μm)	v_u	J_u	Blue Bullet		Red Bullet	
				$\ln\left(\frac{N_u}{g_u}/\frac{N_r}{g_r}\right)$	N_u/N_m	$\ln\left(\frac{N_u}{g_u}/\frac{N_r}{g_r}\right)$	N_u/N_m
1-0 Q(1)	2.406592	1	1	$1.048^{+0.140}_{-0.163}$	1.13	–	–
1-0 Q(2)	2.413439	1	2	–	–	$-0.200^{+0.222}_{-0.286}$	0.87
1-0 S(0)	2.223290	1	2	$0.844^{+0.142}_{-0.165}$	1.12	$0.088^{+0.149}_{-0.176}$	1.15
1-0 Q(3)	2.423730	1	3	$0.326^{+0.141}_{-0.165}$	0.90	$-0.443^{+0.225}_{-0.291}$	0.93
1-0 S(1)	2.121834	1	3	$0.412^{+0.140}_{-0.163}$	0.98	$-0.263^{+0.140}_{-0.163}$	1.11
1-0 Q(4)	2.437489	1	4	$-0.116^{+0.154}_{-0.182}$	0.85	$-0.832^{+0.185}_{-0.227}$	0.95
1-0 Q(5)	2.454752	1	5	–	–	$-1.262^{+0.174}_{-0.211}$	1.02
2-1 S(1)	2.247716	2	3	$-2.948^{+0.190}_{-0.235}$	1.05	–	–

Table 4.9: Column Densities and Ratio to Fitted Boltzmann Distribution for Vy 2-2 H_2 Thermal Bullets

H_2 Line ID	λ (μm)	v_u	J_u	Blue Bullet		Red Bullet	
				$\ln\left(\frac{N_u}{g_u}/\frac{N_r}{g_r}\right)$	N_u/N_m	$\ln\left(\frac{N_u}{g_u}/\frac{N_r}{g_r}\right)$	N_u/N_m
1-0 Q(1)	2.406592	1	1	$1.476^{+0.154}_{-0.182}$	1.27	$1.457^{+0.142}_{-0.166}$	1.25
1-0 Q(2)	2.413439	1	2	$1.027^{+0.224}_{-0.289}$	0.98	$1.163^{+0.165}_{-0.197}$	1.15
1-0 S(0)	2.223290	1	2	$1.006^{+0.146}_{-0.171}$	0.96	$1.108^{+0.145}_{-0.170}$	1.09
1-0 S(1)	2.121834	1	3	$0.670^{+0.140}_{-0.163}$	0.92	$0.716^{+0.140}_{-0.163}$	1.00
1-0 Q(4)	2.437489	1	4	$0.316^{+0.195}_{-0.242}$	0.94	–	–
1-0 S(2)	2.033758	1	4	$0.326^{+0.156}_{-0.185}$	0.95	$0.165^{+0.144}_{-0.169}$	0.87
1-0 S(3)	1.957559	1	5	–	–	$-0.708^{+0.186}_{-0.228}$	0.60
2-1 S(1)	2.247716	2	3	$-2.692^{+0.239}_{-0.315}$	0.93	$-2.730^{+0.292}_{-0.415}$	1.21
2-1 S(3)	2.073482	2	5	$-3.334^{+0.232}_{-0.302}$	1.10	–	–

Table 4.10: Column Densities and Ratio to Fitted Boltzmann Distribution for Hen 2-459 (McD) H_2 Thermal Bullets

H_2 Line ID	λ (μm)	v_u	J_u	Blue Bullet		Red Bullet	
				$\ln\left(\frac{N_u}{g_u}/\frac{N_r}{g_r}\right)$	N_u/N_m	$\ln\left(\frac{N_u}{g_u}/\frac{N_r}{g_r}\right)$	N_u/N_m
1-0 Q(1)	2.406592	1	1	$0.715^{+0.160}_{-0.191}$	1.08	–	–
1-0 S(0)	2.223290	1	2	$0.162^{+0.228}_{-0.295}$	0.70	$0.187^{+0.191}_{-0.236}$	0.88
1-0 Q(3)	2.423730	1	3	$0.126^{+0.187}_{-0.230}$	0.82	–	–
1-0 S(1)	2.121834	1	3	$0.761^{+0.141}_{-0.164}$	1.54	$0.228^{+0.141}_{-0.164}$	1.24
1-0 S(2)	2.033758	1	4	$0.112^{+0.153}_{-0.181}$	1.03	$-0.475^{+0.191}_{-0.236}$	0.91

Table 4.11: Column Densities and Ratio to Fitted Boltzmann Distribution for Hen 2-459 (DCT) H_2 Thermal Bullets

H_2 Line ID	λ (μm)	v_u	J_u	Blue Bullet		Red Bullet	
				$\ln\left(\frac{N_u}{g_u}/\frac{N_r}{g_r}\right)$	N_u/N_m	$\ln\left(\frac{N_u}{g_u}/\frac{N_r}{g_r}\right)$	N_u/N_m
1-0 Q(1)	2.406592	1	1	$0.421^{+0.149}_{-0.175}$	1.12	–	–
1-0 S(0)	2.223290	1	2	$0.123^{+0.180}_{-0.219}$	1.01	–	–
1-0 Q(3)	2.423730	1	3	$-0.695^{+0.197}_{-0.245}$	0.60	–	–
1-0 S(1)	2.121834	1	3	$0.066^{+0.141}_{-0.164}$	1.27	$-0.916^{+0.145}_{-0.170}$	1.00
1-0 S(2)	2.033758	1	4	$-0.407^{+0.158}_{-0.188}$	1.16	$-1.332^{+0.195}_{-0.243}$	1.00

The case for thermal level populations for the bullets in Hen 2-459 is less clear due to the low S/N for this object, but we treat them as if they were thermal as is the case for M 1-11 and Vy 2-2. We fit single temperature Boltzmann distributions (Equation 1.6) to the level populations for each bullet, using linear least-squares regression. Figures 4.6, 4.7, 4.8, and 4.9 show the fits and Table 4.12 reports the best fit temperatures and uncertainties in the fits. These temperatures are well constrained for M1-11 and Vy 2-2, and range from T = 1472–1640. The inferred temperatures are less well constrained for Hen 2-459 due to low S/N and the fact that there are only a few usable lines, although the results are consistent with those for M1-11 and Vy 2-2.

4.8 Discussion of Results for the Individual PNe

4.8.1 M 1-11

Figures 4.2 and 4.4 and Table 4.2 reveal that M 1-11 has fainter [Fe II] and [Fe III] emission than Vy 2-2 and Hen 2-459. The [Fe II] and [Fe III] lines appear to arise only near the center of the nebula in PV space and follow the distribution of the ionized gas as seen in the H I, He I, [Kr III], and [Se IV] lines. We find that the UV-excited H_2 arises from a shell of radius $\sim 5-6''$ (in agreement with the observed spatial extent in Otsuka et al. 2013), and is expanding at $\sim$ 25 km s^{-1}. The excitation diagram (Figure 4.2) and model fits reveal level populations consistent with cold UV-excited gas. The H_2 bullets lie at projected velocities of $\sim \pm$50 km s^{-1}, with temperatures of $\sim$ 1,500 K.

Table 4.12: H_2 Bullet Fit Temperature

PN	Blue H_2 Bullet Temp. (K)	Red H_2 Bullet Temp. (K)
M 1-11	1634 ± 66	1540 ± 180
Vy 2-2	1659 ± 41	1540 ± 120
Hen 2-459 (McD)	2602 ± 2145	1611 ± 873
Hen 2-459 (DCT)	1658 ± 877	$1523 \pm inf$

4.8.2 Vy 2-2

Vy 2-2 is the easiest of these three nebulae to interpret. Figures 4.2 and 4.4 reveal [Fe II] and [Fe III] emission that appears to follow a bipolar structure that is an outflow where the velocity is linearly proportional to the position of the material's distance from the center (ie., a "Hubble" flow). The previous observations of this bipolar outflow in optical [N II] emission by Miranda & Solf (1991) corroborate our findings. Our observations of the [Fe II] and [Fe III] emission line up well in PV space with their observations of [N II]. The [Fe III] emission lies closer to the central star in PV space than the [Fe II] emission, implying that the outflow is being photoionized from within. The highest velocity ends of the [Fe II] emission and location of the thermal H_2 bullets are clearly coincident with the edge of the ionized zone traced by the H I recombination lines, showing where the outflow is shocking molecular gas.

4.8.3 Hen 2-459

Hen 2-459 is the least clear case, despite our having two observations taken with different PAs. The results from the two observations are similar. Unlike Vy 2-2, which shows a clear offset in PV space distribution between the H I, He I, and [Kr III] lines on one hand and the [Fe II] and [Fe III] lines on the other (Figures 4.2 and 4.4), Hen 2-459 shows a smaller offset. The H_2 emission in Hen 2-459 is also more extended and blobby than M 1-11 and Vy 2-2, filling the same region traced by the [Fe II] and [Fe III] lines. The low-velocity H_2 emission is clearly UV-excited, although it appears to be significantly heated compared to the Cloudy models, so it is possible that some shocked emission is mixed in. The excitation of the high velocity bullets is less clear for Hen 2-459 due to the low S/N in their emission compared to the bullets in M 1-11 and Vy 2-2. While the bullets in Hen 2-459 lie at high velocity

and we treat their H_2 level populations as thermal, we cannot rule out UV excitation for the bullets in the case of Hen 2-459. It is possible that instead of seeing shocked gas from a bipolar outflow, we are looking at UV-excited bubble walls in Hen 2-459. Deeper high spectral resolution observations of the H_2 lines in Hen 2-459 would help settle these issues.

4.9 Discussion and Interpretation

The thermal H_2 bullets appear to be symmetric and equidistant from the central stars in M 1-11, Vy 2-2 and Hen 2-459 and coincident with the ends of structures traced by the [Fe II] and [Fe III] lines, at least in Vy 2-2 and Hen 2-459. The bullets and ends of the [Fe II] and [Fe III] emission also appear coincident with the edge of the central photoionized zone traced by the H I recombination lines. The similarities among these three nebulae suggest that we should seek a unified model to explain what we are seeing. In this section, we discuss possible causes for these structures observed in PV space and the strengths and weaknesses of each case.

4.9.1 Extreme-UV Heating of H_2

As discussed throughout Chapters 1, 2, and 3, collisions in dense and/or warm gas can cause the H_2 rovibrational level populations to deviate from the unmodified UV-excited spectrum. In the most extreme cases (e.g., Bertoldi & Draine 1996; Störzer & Hollenbach 1998; Henney et al. 2007, the combination of a hard UV radiation field and low density gas can cause the ionization and dissociation fronts in a PDR to merge, exposing the H_2 to extreme-UV (EUV $>$ 13.6 eV) photons that rapidly heat the gas. In this hot gas, collisions dominate the excitation and de-excitation of the H_2 and the rovibrational level populations approach the thermal limit. For example, this is observed in high density molecular knots embedded within the ionized zone of the Helix nebula (Speck et al., 2002; Meixner et al., 2005; O'Dell et al., 2005; Matsuura et al., 2007; O'Dell et al., 2007; Aleman et al., 2011). Could the thermal H_2 bullets be similarly heated by EUV photons?

This scenario is unlikely for several reasons. The stars in M 1-11, Vy 2-2, and Hen 2-459 are cooler than those found in more evolved PNe such as the Helix, and the ratio of EUV/FUV photons they produce is much smaller. The thermal H_2 bullets

are not situated inside the ionized zone like the molecular knots in the Helix Nebula, but lie at the edge of the central ionized zone in PV space traced by the H I Br γ line (see Figures 4.2 and 4.3). The bullets are spatio-kinematically coincident with the edge of the the [Fe II] and [Fe III] emission, and this scenario provides no explanation for the distribution of [Fe II] and [Fe III] seen in Vy 2-2 or Hen 2-459. It also fails to explain the high velocities of the bullets.

4.9.2 Walls of a Bubble Blown by a Bipolar Outflow

Many PNe with bipolar morphologies show different spatial distributions for [Fe II] and H_2 emission, with the [Fe II] emission coming from inside the bipolar structure and the H_2 emission arising from the edges. A well studied example of this is the PN M 2-9. Near-IR imaging and spectra along the major axis of the bipolar structure in M 2-9 by Smith et al. (2005) reveal Fe and H_2 emission that bears a resemblance to what we observe in our three PN. The PN Hb 12 also shows a similar but more complicated structure, where [Fe II] and [Fe III] emission inside bubbles is surrounded by UV-excited H_2 in the bubble walls (Welch et al., 1999). The H_2 emission from the bubble walls is UV-excited in both M 2-9 (Hora & Latter, 1994) and Hb 12 (Dinerstein et al., 1988; Luhman & Rieke, 1996; Ramsay et al., 1993). In both of these PNe, the H_2 emission arises from the laterally expanding "walls" of the bipolar structure.

It is unlikely that the structures observed in M 1-11 and Vy 2-2 can be explained with this scenario. The H_2 bullets (at least in the case of M 1-11 and Vy 2-2) show thermal H_2 rovibrational level populations unlike the UV-excited level populations seen in M 2-9 and Hb 12. A fast moving bubble of UV-excited H_2 encompassing ionized gas traced by [Fe II] and [Fe III] could explain our observations of Hen 2-459. We are unable to rule out UV excitation for its bullets, and the H_2 emission extends throughout the same PV structure traced by the [Fe II] and [Fe III] lines, unlike Vy 2-2 where the H_2 and Fe emission are clearly differentiated.

4.9.3 The Major Axis of a Shocked Bipolar Outflow

In this scenario, a ballistic or jet-like bipolar outflow originates from the central star, passes through the ionized zone and/or evacuated cavity in the center of the nebula and collides with previously ejected cooler molecular gas. The ballistic outflow might

shock gas as it passes through the ionized zone so the spectrum will show strong collisionally excited ionic lines if the shock velocity is high enough. The line flux ratios observed in shocked gas deviates from what is expected for photoionized gas. For example, the collisionally excited Fe lines such as [Fe II] and [Fe III] are typically bright in shocks. In PNe these types of structures resemble at least some of what are typically referred to as low ionization structures (LIS, Gonçalves 2004; Gonçalves et al. 2009; Akras & Gonçalves 2016; also see FLIERs discussed by Balick et al. 1993). Material from the outflow itself could also become photoionized. When the fastest moving parts of the outflow collide with molecular gas, the H_2 becomes shock-heated.

It is likely in this scenario that the [Fe II] and [Fe III] arises from photoionized material either from the outflow itself or material in the ionized zone that was compressed by the outflow. This appears to be the case in our three PNe, where the Fe emission follows the structure expected for photoionized gas where [Fe III] emission arises closer to the central star in PV space than the [Fe II] emission.

We find this scenario to be the most likely cause of the structures we observe in our three PNe. It provides a unified explanation for nearly all our observations. The [Fe II] and [Fe III] lines in Vy 2-2 and Hen 2-459 show a nearly linear relation between position and velocity, indicative of a Hubble-like flow where the distance from the center of material within a ballistic outflow or jet is linearly proportional to its velocity. The location of the bullets are coincident with the edge of the ionized zone in each nebula. An outflow passing through the ionized zone or central evacuated cavity and colliding with molecular gas beyond it would certainly create shock-heated H_2 bullets just like the ones we have observed. M 1-11 lacks [Fe II] and [Fe III] emission that traces its outflow, so perhaps it is at a later stage in the outflow's evolution where the [Fe II] and [Fe III] emission has faded, its outflow consisted of ballistic knots that simply passed through the lower-density cavities without leaving behind entrained material to give off Fe emission, or it does not have an outflow at all and some other mechanism must be invoked to explain the observed high velocity thermal H_2 bullets.

4.10 Summary and Conclusions

We have presented high resolution near-IR IGRINS spectra for three PNe: M 1-11, Vy 2-2, and Hen 2-459, taken from a larger survey, that show interesting structures in their [Fe II], [Fe III], and H_2 emission. The high spectral resolution ($R \sim 45{,}000$) and large wavelength coverage (1.45–2.45 μm) of IGRINS makes it possible to spatio-kinematically resolve distinct structures within each nebula. Each PN shows similar features: a central ionized zone traced by H I, He I, [Kr III], and [Se IV] lines; and H_2 emission that consists of a low velocity UV-excited component and two high velocity "bullets" that appear to be shock excited. In Vy 2-2 and Hen 2-459, the thermal H_2 bullets appear to be coincident with the edge of a structure prominent in the [Fe II] and [Fe III] lines. The [Fe II] and [Fe III] emission traces a "Hubble" flow from the center of the nebula out to the H_2 bullets, which lie beyond the edge of the ionization zone traced by the H I lines. The [Fe II], [Fe III] and H_2 features are symmetric around and equidistant from the central star in both position and velocity.

We interpret these observations as in the following way:

1. The three PNe each have a central ionized zone seen in H I, He I, [Kr III], and [Se IV] lines with the ionization structure setting the extent of these emission lines in PV space. The central ionized zone is surrounded by slowly expanding molecular gas that exhibits characteristically UV-excited H_2 emission.

2. We suggest that that each nebula probably hosts a bipolar outflow within its central evacuated and/or ionized zone that is running into, compressing, and shock-exciting the molecular gas at the edge. For Vy 2-2 and Hen 2-459, the path of the outflow through the ionized zone is traced by [Fe II] and [Fe III] emission.

3. The shock-heated molecular gas at the edge of the ionized zone gives rise to the observed high velocity thermal H_2 bullets in each PN that are spatially and kinematically distinct from the slowly expanding UV-excited H_2.

Chapter Five: Summary and Conclusions

In this dissertation, we have undertaken a study of a variety of PDRs using the high spectral resolution near-IR spectrometer IGRINS to observe rovibrational transitions from excited H_2 within the PDRs. H_2 is the most abundant molecule in the universe but is normally hard to detect, except in regions where it is excited by UV radiation (ie. in PDRs) or heated by shocks. IGRINS, with its high spectral resolution, sensitivity, and large wavelength coverage, has proven to be an excellent instrument for this type of work, detecting well over 100 H_2 emission lines in some of the PDRs that we have observed. This H_2 emission arises at the dissociation front where FUV radiation is exciting H_2 molecules, and we have used the observed line ratios to probe the physical conditions within the observed PDRs. We have used Cloudy models (Ferland et al., 2013) to simulate and fit H_2 rovibrational level populations to the observed data and explore our understanding of the theoretical physics assumed in the models such as the H_2 collision rates or H_2 formation pumping.

In Chapter 2 we presented a deep near-IR spectrum of the bright Orion Bar PDR and, using a grid of constant density and constant temperature Cloudy models, found that its gas is quite warm with a temperature of $T = 625$ K and density on the moderately low side at $n_H = 5 \times 10^3$ cm^{-3}. The Orion Bar H_2 rovibrational level populations show a large degree of collisional modification, likely due to the Bar's warm temperature. In Chapter 3 we extended the type of analysis done for the Orion Bar in Chapter 2 to the Horsehead Nebula, IC 63, NGC 2023 and S 140, four other PDRs in regions of high-mass star formation. Some of these observations are quite deep, with over 200 H_2 lines observed in NGC 2023. By comparing these PDRs to Cloudy models and to each other, we found they all show some degree of collisional modification to their rovibrational level populations, but the H_2 in the Orion Bar still has rovibrational level populations that deviate the most from the case of unmodified UV excitation. We also found that Cloudy models consistently overpredict the level populations at high J in all the PDRs, suggesting that we should test different prescriptions in the models for H_2 formation pumping, which plays a significant role in populating the high J states. In Chapter 4 we presented near-IR spectra of three interesting planetary nebulae: M 1-11, Vy 2-2, and Hen 2-459. The

high spectral resolution of IGRINS has allowed us to kinematically resolve slowly expanding UV-excited H_2 (ie. PDR) from red- and blue-shifted high velocity shocked H_2 "bullets" in all three planetary nebulae. Vy 2-2 and Hen 2-459 also show [Fe II] and [Fe III] emission that likely traces a bipolar outflow that is colliding with molecular gas at the edge of each nebula's ionized zone, compressing, and shocking the H_2.

We have shown the extraordinary utility of using IGRINS observations of excited H_2 in PDRs around star forming regions and in planetary nebulae to reveal the physical conditions at the ionized/molecular gas interface. The advantages of high spectral resolution and large wavelength coverage have allowed us to observe an unprecedented number of H_2 rovibrational transitions arising from a large range of excitation energies. We have peered into the regions in the ISM that are affected by UV radiation from newly formed and recently deceased stars, and have helped test the limits of what we know about basic ISM physics. The data presented in this dissertation is just a fraction of PDR and planetary nebulae data that we have collected with IGRINS, so we will likely continue to exploit this rich dataset in future PDR studies using the tools, software, and techniques that we have built (e.g, such as fitting the data with large model grids) as part of this dissertation. Along with IGRINS, future ground-based and space-based infrared instruments will use the infrared emission from excited H_2 as a tool to probe and help refine our understanding of ISM physics.

Appendix A: H_2 Line Physical Constants

In Table A.1 we give the physical constants for each transition visible with IGRINS that are needed to calculate rovibrational level populations (column densities) from observed line fluxes using Equation 1.4. The constants given are: v_u is the upper quantum vibrational state of each transition, J_u is the upper quantum rotational state of each transition, ΔE_{ul} is the difference in energy between the states in units of inverse cm (cm^{-1}), and A_{ul} is the transition probability (s^{-1}) (we use the A_{ul} values from Wolniewicz et al. 1998, which are the same ones used by default in Cloudy). We show all transitions with wavelengths between $\lambda = 1.45$–2.45 μm and with upper states between $v_u = 1$–14 and $J_u = 1$–25.

Table A.1: Physical Constants for H_2 Lines

H_2 Line ID	λ (μm)	v_u	J_u	E_u/k (K)	$\log_{10}(A_{ul})$ [s^{-1}]	H_2 Line ID	λ (μm)	v_u	J_u	E_u/k (K)	$\log_{10}(A_{ul})$ [s^{-1}]
1-0 Q(1)	2.406592	1	1	6149	-6.37	7-5 S(3)	1.561510	7	5	36588	-5.86
1-0 Q(2)	2.413439	1	2	6471	-6.52	7-5 O(8)	2.310862	7	6	37220	-6.43
1-0 S(0)	2.223290	1	2	6471	-6.60	7-5 Q(6)	1.800283	7	6	37220	-6.06
1-0 Q(3)	2.423730	1	3	6951	-6.56	7-5 S(4)	1.540006	7	6	37220	-5.87
1-0 S(1)	2.121834	1	3	6951	-6.46	7-5 O(9)	2.427661	7	7	37941	-6.56
1-0 Q(4)	2.437489	1	4	7584	-6.58	7-5 Q(7)	1.826347	7	7	37941	-6.08
1-0 S(2)	2.033758	1	4	7584	-6.40	7-5 S(5)	1.523623	7	7	37941	-5.89
1-0 S(3)	1.957559	1	5	8365	-6.38	7-4 O(10)	1.459191	7	8	38743	-8.80
1-0 S(4)	1.891936	1	6	9286	-6.38	7-5 S(6)	1.512240	7	8	38743	-5.95
1-0 S(5)	1.835760	1	7	10341	-6.40	7-5 Q(8)	1.856868	7	8	38743	-6.10
1-0 S(6)	1.788050	1	8	11521	-6.45	7-4 O(11)	1.517790	7	9	39618	-10.60
1-0 S(7)	1.747955	1	9	12817	-6.53	7-5 S(7)	1.505784	7	9	39618	-6.02
1-0 S(8)	1.714738	1	10	14220	-6.63	7-5 Q(9)	1.892205	7	9	39618	-6.12
1-0 S(9)	1.687761	1	11	15721	-6.78	7-4 O(12)	1.582127	7	10	40559	-9.34
1-0 S(10)	1.666475	1	12	17311	-6.98	7-5 S(8)	1.504232	7	10	40559	-6.13
1-0 S(11)	1.650413	1	13	18979	-7.27	7-5 Q(10)	1.932812	7	10	40559	-6.15
1-0 S(12)	1.639178	1	14	20717	-7.78	7-5 Q(11)	1.979270	7	11	41558	-6.18
1-0 S(13)	1.632439	1	15	22516	-9.33	7-4 O(13)	1.653010	7	11	41558	-8.79
1-0 S(14)	1.629927	1	16	24367	-8.09	7-5 S(9)	1.507629	7	11	41558	-6.27
1-0 S(15)	1.631428	1	17	26263	-7.38	7-5 S(10)	1.516101	7	12	42605	-6.47
1-0 S(16)	1.636783	1	18	28194	-6.99	7-5 Q(12)	2.032316	7	12	42605	-6.22
1-0 S(17)	1.645885	1	19	30153	-6.72	7-4 O(14)	1.731471	7	12	42605	-8.55
1-0 S(18)	1.658679	1	20	32133	-6.52	7-4 O(15)	1.818843	7	13	43693	-8.45
1-0 S(19)	1.675165	1	21	34128	-6.36	7-5 Q(13)	2.092904	7	13	43693	-6.26
1-0 S(20)	1.695403	1	22	36130	-6.22	7-5 S(11)	1.529873	7	13	43693	-6.76
1-0 S(21)	1.719516	1	23	38133	-6.11	7-5 Q(14)	2.162278	7	14	44812	-6.31
1-0 S(22)	1.747702	1	24	40131	-6.02	7-4 O(16)	1.916876	7	14	44812	-8.43

Continued on next page...

Table A.1 continued: Physical Constants for H_2 Lines

H_2 Line ID	λ (μm)	v_u	J_u	E_u/k (K)	$\log_{10}(A_{ul})$ [s^{-1}]	H_2 Line ID	λ (μm)	v_u	J_u	E_u/k (K)	$\log_{10}(A_{ul})$ [s^{-1}]
2-1 S(0)	2.355605	2	2	12095	-6.43	7-5 S(12)	1.549304	7	14	44812	-7.23
2-1 S(1)	2.247716	2	3	12550	-6.30	7-5 Q(15)	2.242090	7	15	45954	-6.37
2-1 S(2)	2.154216	2	4	13150	-6.25	7-5 S(13)	1.574921	7	15	45954	-8.41
2-0 O(6)	1.486989	2	4	13150	-7.33	7-4 O(17)	2.027908	7	15	45954	-8.46
2-0 O(7)	1.546377	2	5	13890	-7.50	7-5 Q(16)	2.334583	7	16	47109	-6.44
2-1 S(3)	2.073482	2	5	13890	-6.24	7-5 S(14)	1.607489	7	16	47109	-7.82
2-1 S(4)	2.004109	2	6	14763	-6.25	7-4 Q(16)	1.467793	7	16	47109	-6.50
2-0 O(8)	1.610517	2	6	14763	-7.69	7-4 O(18)	2.155138	7	16	47109	-8.56
2-0 O(9)	1.679641	2	7	15763	-7.89	7-4 O(19)	2.303068	7	17	48267	-8.72
2-1 S(5)	1.944884	2	7	15763	-6.30	7-3 O(19)	1.458636	7	17	48267	-7.69
2-0 O(10)	1.754018	2	8	16880	-8.10	7-5 Q(17)	2.442876	7	17	48267	-6.53
2-1 S(6)	1.894755	2	8	16880	-6.37	7-5 S(15)	1.648108	7	17	48267	-7.02
2-0 O(11)	1.833970	2	9	18107	-8.33	7-4 Q(17)	1.529372	7	17	48267	-6.52
2-1 S(7)	1.852816	2	9	18107	-6.47	7-5 S(16)	1.698375	7	18	49417	-6.63
2-1 S(8)	1.818281	2	10	19434	-6.61	7-3 O(20)	1.549093	7	18	49417	-7.75
2-0 O(12)	1.919872	2	10	19434	-8.57	7-4 Q(18)	1.601375	7	18	49417	-6.55
2-1 S(9)	1.790479	2	11	20853	-6.82	7-5 S(17)	1.760678	7	19	50549	-6.37
2-0 O(13)	2.012175	2	11	20853	-8.83	7-3 O(21)	1.656032	7	19	50549	-7.83
2-0 O(14)	2.111414	2	12	22355	-9.12	7-4 Q(19)	1.686872	7	19	50549	-6.59
2-1 S(10)	1.768836	2	12	22355	-7.13	7-5 S(18)	1.838747	7	20	51647	-6.19
2-1 S(11)	1.752868	2	13	23930	-7.69	7-4 Q(20)	1.790597	7	20	51647	-6.65
2-0 O(15)	2.218234	2	13	23930	-9.43	7-3 O(22)	1.785608	7	20	51647	-7.95
2-0 O(16)	2.333406	2	14	25569	-9.77	8-6 Q(1)	1.882072	8	1	38708	-5.84
2-1 S(12)	1.742172	2	14	25569	-10.23	8-6 O(3)	2.041830	8	1	38708	-5.80
2-1 S(13)	1.736422	2	15	27265	-7.74	8-6 Q(2)	1.890613	8	2	38914	-5.99
2-0 Q(15)	1.464922	2	15	27265	-7.00	8-6 S(0)	1.804886	8	2	38914	-6.09
2-1 S(14)	1.735361	2	16	29008	-7.11	8-6 O(4)	2.121592	8	2	38914	-5.94
2-0 Q(16)	1.497965	2	16	29008	-7.01	8-6 O(5)	2.210763	8	3	39219	-6.05
2-1 S(15)	1.738801	2	17	30791	-6.74	8-6 Q(3)	1.903543	8	3	39219	-6.03
2-0 Q(17)	1.533947	2	17	30791	-7.03	8-6 S(1)	1.763952	8	3	39219	-5.97
2-1 S(16)	1.746619	2	18	32605	-6.48	8-6 S(2)	1.729672	8	4	39622	-5.93
2-0 Q(18)	1.573120	2	18	32605	-7.05	8-6 O(6)	2.310167	8	4	39622	-6.17
2-0 Q(19)	1.615796	2	19	34443	-7.07	8-6 Q(4)	1.921011	8	4	39622	-6.05
2-1 S(17)	1.758762	2	19	34443	-6.28	8-6 S(3)	1.701803	8	5	40116	-5.93
2-1 S(18)	1.775247	2	20	36298	-6.13	8-6 O(7)	2.420824	8	5	40116	-6.28
2-0 Q(20)	1.662355	2	20	36298	-7.09	8-6 Q(5)	1.943225	8	5	40116	-6.07
2-0 Q(21)	1.713266	2	21	38163	-7.12	8-6 Q(6)	1.970468	8	6	40695	-6.09
2-1 S(19)	1.796169	2	21	38163	-6.00	8-6 S(4)	1.680153	8	6	40695	-5.96
2-1 S(20)	1.821712	2	22	40031	-5.89	8-5 O(8)	1.483113	8	6	40695	-7.27
2-0 Q(22)	1.769116	2	22	40031	-7.15	8-5 O(9)	1.540361	8	7	41355	-7.54
2-0 Q(23)	1.830640	2	23	41896	-7.18	8-6 Q(7)	2.003105	8	7	41355	-6.12
2-1 S(21)	1.852166	2	23	41896	-5.81	8-6 S(5)	1.664584	8	7	41355	-6.01
2-0 Q(24)	1.898784	2	24	43750	-7.22	8-6 Q(8)	2.041614	8	8	42087	-6.15
2-1 S(22)	1.887955	2	24	43750	-5.73	8-6 S(6)	1.655023	8	8	42087	-6.09
3-1 O(4)	1.467714	3	2	17387	-6.54	8-5 O(10)	1.603657	8	8	42087	-7.83
3-1 O(5)	1.522033	3	3	17818	-6.70	8-5 O(11)	1.673817	8	9	42884	-8.17
3-2 S(1)	2.386471	3	3	17818	-6.29	8-6 Q(9)	2.086607	8	9	42884	-6.18

Continued on next page...

Table A.1 continued: Physical Constants for H_2 Lines

H_2 Line ID	λ (μm)	v_u	J_u	E_u/k (K)	$\log_{10}(A_{ul})$ [s^{-1}]	H_2 Line ID	λ (μm)	v_u	J_u	E_u/k (K)	$\log_{10}(A_{ul})$ [s^{-1}]
3-1 O(6)	1.581171	3	4	18386	-6.86	8-6 S(7)	1.651475	8	9	42884	-6.21
3-2 S(2)	2.287045	3	4	18386	-6.25	8-5 O(12)	1.751893	8	10	43738	-8.57
3-1 O(7)	1.645348	3	5	19086	-7.02	8-6 S(8)	1.654034	8	10	43738	-6.38
3-2 S(3)	2.201399	3	5	19086	-6.25	8-6 Q(10)	2.138877	8	10	43738	-6.22
3-2 S(4)	2.128015	3	6	19911	-6.28	8-5 O(13)	1.839252	8	11	44641	-9.04
3-1 O(8)	1.714816	3	6	19911	-7.19	8-6 Q(11)	2.199456	8	11	44641	-6.27
3-2 S(5)	2.065584	3	7	20856	-6.34	8-6 S(9)	1.662916	8	11	44641	-6.61
3-1 O(9)	1.789869	3	7	20856	-7.36	8-6 Q(12)	2.269699	8	12	45584	-6.32
3-1 O(10)	1.870854	3	8	21911	-7.54	8-5 O(14)	1.937698	8	12	45584	-9.60
3-2 S(6)	2.012979	3	8	21911	-6.44	8-6 S(10)	1.678483	8	12	45584	-6.98
3-2 S(7)	1.969231	3	9	23069	-6.59	8-5 O(15)	2.049656	8	13	46556	-10.21
3-1 O(11)	1.958185	3	9	23069	-7.73	8-6 S(11)	1.701301	8	13	46556	-7.67
3-2 S(8)	1.933509	3	10	24321	-6.80	8-5 Q(13)	1.477482	8	13	46556	-6.36
3-1 O(12)	2.052356	3	10	24321	-7.93	8-6 Q(13)	2.351422	8	13	46556	-6.39
3-2 S(9)	1.905107	3	11	25659	-7.14	8-6 Q(14)	2.447100	8	14	47550	-6.46
3-1 O(13)	2.153960	3	11	25659	-8.12	8-6 S(12)	1.732204	8	14	47550	-8.85
3-1 O(14)	2.263713	3	12	27073	-8.33	8-5 Q(14)	1.531891	8	14	47550	-6.38
3-1 Q(12)	1.473811	3	12	27073	-6.57	8-5 O(16)	2.178449	8	14	47550	-10.58
3-2 S(10)	1.883431	3	12	27073	-7.76	8-5 Q(15)	1.595375	8	15	48555	-6.41
3-2 S(11)	1.867989	3	13	28555	-9.59	8-5 O(17)	2.328781	8	15	48555	-10.35
3-1 Q(13)	1.502463	3	13	28555	-6.58	8-4 O(17)	1.483859	8	15	48555	-7.61
3-1 O(15)	2.382486	3	13	28555	-8.53	8-6 S(13)	1.772422	8	15	48555	-7.31
3-1 Q(14)	1.533983	3	14	30097	-6.59	8-5 Q(16)	1.670252	8	16	49560	-6.45
3-2 S(12)	1.858382	3	14	30097	-7.53	8-4 O(18)	1.576349	8	16	49560	-7.67
3-1 Q(15)	1.568584	3	15	31689	-6.61	8-6 S(14)	1.823762	8	16	49560	-6.79
3-2 S(13)	1.854303	3	15	31689	-6.96	8-6 S(15)	1.888964	8	17	50552	-6.49
3-2 S(14)	1.855530	3	16	33323	-6.62	8-4 O(19)	1.686182	8	17	50552	-7.77
3-1 Q(16)	1.606526	3	16	33323	-6.63	8-5 Q(17)	1.759925	8	17	50552	-6.50
3-0 O(18)	1.458563	3	16	33323	-8.40	8-6 S(16)	1.972355	8	18	51518	-6.29
3-2 S(15)	1.861924	3	17	34992	-6.37	8-4 O(20)	1.819912	8	18	51518	-7.90
3-1 Q(17)	1.648127	3	17	34992	-6.65	8-5 Q(18)	1.869674	8	18	51518	-6.57
3-0 O(19)	1.521936	3	17	34992	-8.43	9-7 Q(1)	2.073187	9	1	41997	-5.91
3-0 O(20)	1.590710	3	18	36688	-8.47	9-7 O(3)	2.253724	9	1	41997	-5.85
3-2 S(16)	1.873438	3	18	36688	-6.18	9-7 O(4)	2.345581	9	2	42185	-5.98
3-1 Q(18)	1.693780	3	18	36688	-6.67	9-7 S(0)	1.987350	9	2	42185	-6.18
3-2 S(17)	1.890118	3	19	38403	-6.03	9-7 Q(2)	2.084098	9	2	42185	-6.06
3-0 O(21)	1.665710	3	19	38403	-8.51	9-7 O(5)	2.449297	9	3	42462	-6.09
3-1 Q(19)	1.743969	3	19	38403	-6.70	9-7 Q(3)	2.100664	9	3	42462	-6.11
3-1 Q(20)	1.799303	3	20	40130	-6.73	9-6 O(5)	1.475519	9	3	42462	-6.42
3-2 S(18)	1.912116	3	20	40130	-5.91	9-7 S(1)	1.942958	9	3	42462	-6.08
3-0 O(22)	1.747975	3	20	40130	-8.56	9-6 O(6)	1.525166	9	4	42827	-6.59
3-2 S(19)	1.939710	3	21	41861	-5.81	9-7 S(2)	1.906608	9	4	42827	-6.06
3-1 Q(21)	1.860551	3	21	41861	-6.77	9-7 Q(4)	2.123137	9	4	42827	-6.13
3-0 O(23)	1.838831	3	21	41861	-8.63	9-6 O(7)	1.580697	9	5	43274	-6.77
3-0 O(24)	1.940001	3	22	43589	-8.70	9-7 S(3)	1.878039	9	5	43274	-6.08
3-1 Q(22)	1.928699	3	22	43589	-6.81	9-7 Q(5)	2.151876	9	5	43274	-6.16
3-2 S(20)	1.973329	3	22	43589	-5.72	9-7 Q(6)	2.187370	9	6	43798	-6.19

Continued on next page...

Table A.1 continued: Physical Constants for H_2 Lines

H_2 Line ID	λ (μm)	v_u	J_u	E_u/k (K)	$\log_{10}(A_{ul})$ [s^{-1}]	H_2 Line ID	λ (μm)	v_u	J_u	E_u/k (K)	$\log_{10}(A_{ul})$ [s^{-1}]
3-0 O(25)	2.053771	3	23	45308	-8.78	9-7 S(4)	1.857078	9	6	43798	-6.13
3-2 S(21)	2.013603	3	23	45308	-5.65	9-6 O(8)	1.642757	9	6	43798	-6.95
3-1 Q(23)	2.005038	3	23	45308	-6.85	9-7 Q(7)	2.230268	9	7	44392	-6.23
3-1 Q(24)	2.091288	3	24	47011	-6.90	9-6 O(9)	1.712184	9	7	44392	-7.13
3-0 O(26)	2.183243	3	24	47011	-8.88	9-7 S(5)	1.843656	9	7	44392	-6.23
3-2 S(22)	2.061432	3	24	47011	-5.60	9-7 Q(8)	2.281426	9	8	45049	-6.27
4-2 O(3)	1.509865	4	1	22079	-6.11	9-7 S(6)	1.837814	9	8	45049	-6.36
4-2 O(4)	1.563515	4	2	22352	-6.29	9-6 O(10)	1.790063	9	8	45049	-7.32
4-2 O(5)	1.622299	4	3	22759	-6.44	9-7 S(7)	1.839741	9	9	45762	-6.56
4-2 O(6)	1.686462	4	4	23295	-6.58	9-7 Q(9)	2.341977	9	9	45762	-6.32
4-3 S(2)	2.435457	4	4	23295	-6.32	9-6 Q(9)	1.472261	9	9	45762	-6.25
4-2 O(7)	1.756281	4	5	23955	-6.73	9-6 O(11)	1.877821	9	9	45762	-7.51
4-3 S(3)	2.344453	4	5	23955	-6.34	9-7 Q(10)	2.413431	9	10	46521	-6.38
4-2 O(8)	1.832080	4	6	24733	-6.88	9-7 S(8)	1.849804	9	10	46521	-6.86
4-3 S(4)	2.266764	4	6	24733	-6.39	9-6 O(12)	1.977355	9	10	46521	-7.70
4-2 O(9)	1.914244	4	7	25623	-7.03	9-6 Q(10)	1.513054	9	10	46521	-6.26
4-2 Q(7)	1.459195	4	7	25623	-6.30	9-7 S(9)	1.868609	9	11	47318	-7.38
4-3 S(5)	2.200974	4	7	25623	-6.49	9-6 O(13)	2.091224	9	11	47318	-7.86
4-2 O(10)	2.003229	4	8	26616	-7.19	9-6 Q(11)	1.560793	9	11	47318	-6.28
4-2 Q(8)	1.477736	4	8	26616	-6.31	9-6 Q(12)	1.616811	9	12	48143	-6.31
4-3 S(6)	2.145873	4	8	26616	-6.64	9-6 O(14)	2.222967	9	12	48143	-8.00
4-2 Q(9)	1.498876	4	9	27706	-6.32	9-7 S(10)	1.897090	9	12	48143	-9.05
4-2 O(11)	2.099586	4	9	27706	-7.36	9-7 S(11)	1.936651	9	13	48987	-7.67
4-3 S(7)	2.100426	4	9	27706	-6.86	9-5 O(15)	1.522515	9	13	48987	-7.73
4-2 O(12)	2.203981	4	10	28883	-7.52	9-6 Q(13)	1.682947	9	13	48987	-6.35
4-3 S(8)	2.063758	4	10	28883	-7.22	9-6 O(15)	2.377614	9	13	48987	-8.11
4-2 Q(10)	1.522734	4	10	28883	-6.33	9-7 S(12)	1.989403	9	14	49837	-6.99
4-2 Q(11)	1.549455	4	11	30139	-6.34	9-5 O(16)	1.618148	9	14	49837	-7.79
4-2 O(13)	2.317223	4	11	30139	-7.69	9-6 Q(14)	1.761818	9	14	49837	-6.40
4-3 S(9)	2.035135	4	11	30139	-7.95	9-6 Q(15)	1.857300	9	15	50682	-6.46
4-2 O(14)	2.440301	4	12	31465	-7.85	9-5 O(17)	1.732408	9	15	50682	-7.90
4-3 S(10)	2.013949	4	12	31465	-8.71	9-7 S(13)	2.058590	9	15	50682	-6.64
4-2 Q(12)	1.579217	4	12	31465	-6.36	9-6 Q(16)	1.975466	9	16	51506	-6.54
4-2 Q(13)	1.612237	4	13	32854	-6.37	9-6 S(14)	1.462896	9	16	51506	-8.19
4-3 S(11)	1.999717	4	13	32854	-7.38	9-5 O(18)	1.872469	9	16	51506	-8.06
4-2 Q(14)	1.648782	4	14	34296	-6.39	9-7 S(14)	2.149422	9	16	51506	-6.43
4-3 S(12)	1.992066	4	14	34296	-6.87	10-7 O(3)	1.548849	10	1	44903	-5.98
4-3 S(13)	1.990735	4	15	35783	-6.55	10-7 Q(1)	1.461391	10	1	44903	-5.95
4-1 O(17)	1.511318	4	15	35783	-8.00	10-8 Q(1)	2.322474	10	1	44903	-6.06
4-2 Q(15)	1.689178	4	15	35783	-6.41	10-7 Q(2)	1.469843	10	2	45070	-6.10
4-2 Q(16)	1.733831	4	16	37306	-6.44	10-7 O(4)	1.595267	10	2	45070	-6.14
4-3 S(14)	1.995574	4	16	37306	-6.31	10-8 Q(2)	2.337184	10	2	45070	-6.21
4-1 O(18)	1.578843	4	16	37306	-8.02	10-8 S(0)	2.225259	10	2	45070	-6.35
4-2 Q(17)	1.783242	4	17	38859	-6.47	10-8 Q(3)	2.359611	10	3	45317	-6.26
4-3 S(15)	2.006551	4	17	38859	-6.13	10-8 S(1)	2.176855	10	3	45317	-6.27
4-1 O(19)	1.652582	4	17	38859	-8.06	10-7 O(5)	1.648305	10	3	45317	-6.29
4-1 O(20)	1.733564	4	18	40433	-8.10	10-7 Q(3)	1.482704	10	3	45317	-6.13

Continued on next page...

Table A.1 continued: Physical Constants for H_2 Lines

H_2 Line ID	λ (μm)	v_u	J_u	E_u/k (K)	$\log_{10}(A_{ul})$ [s^{-1}]	H_2 Line ID	λ (μm)	v_u	J_u	E_u/k (K)	$\log_{10}(A_{ul})$ [s^{-1}]
4-2 Q(18)	1.838045	4	18	40433	-6.50	10-8 S(2)	2.138638	10	4	45641	-6.28
4-3 S(16)	2.023760	4	18	40433	-5.99	10-7 Q(4)	1.500204	10	4	45641	-6.15
4-3 S(17)	2.047446	4	19	42020	-5.87	10-7 O(6)	1.708625	10	4	45641	-6.44
4-1 O(21)	1.823103	4	19	42020	-8.16	10-8 Q(4)	2.390217	10	4	45641	-6.30
4-2 Q(19)	1.899043	4	19	42020	-6.54	10-8 Q(5)	2.429671	10	5	46037	-6.34
4-2 Q(20)	1.967271	4	20	43612	-6.58	10-8 S(3)	2.110354	10	5	46037	-6.34
4-1 O(22)	1.922912	4	20	43612	-8.23	10-7 Q(5)	1.522674	10	5	46037	-6.17
4-3 S(18)	2.078032	4	20	43612	-5.78	10-7 O(7)	1.777098	10	5	46037	-6.58
4-2 Q(21)	2.044087	4	21	45202	-6.62	10-7 O(8)	1.854869	10	6	46499	-6.73
4-3 S(19)	2.116170	4	21	45202	-5.70	10-8 S(4)	2.091920	10	6	46499	-6.45
4-1 O(23)	2.035262	4	21	45202	-8.31	10-7 Q(6)	1.550571	10	6	46499	-6.18
4-3 S(20)	2.162824	4	22	46782	-5.64	10-7 O(9)	1.943461	10	7	47021	-6.87
4-2 Q(22)	2.131310	4	22	46782	-6.68	10-8 S(5)	2.083446	10	7	47021	-6.62
4-1 O(24)	2.163241	4	22	46782	-8.42	10-7 Q(7)	1.584507	10	7	47021	-6.20
4-1 O(25)	2.311178	4	23	48343	-8.54	10-7 Q(8)	1.625307	10	8	47595	-6.23
4-3 S(21)	2.219392	4	23	48343	-5.60	10-8 S(6)	2.085280	10	8	47595	-6.87
4-2 Q(23)	2.231441	4	23	48343	-6.74	10-7 O(10)	2.044913	10	8	47595	-7.02
4-1 Q(24)	1.476104	4	24	49878	-7.24	10-7 Q(9)	1.674084	10	9	48213	-6.25
4-2 Q(24)	2.348044	4	24	49878	-6.82	10-7 O(11)	2.162010	10	9	48213	-7.16
4-0 O(26)	1.521331	4	24	49878	-8.95	10-8 S(7)	2.098075	10	9	48213	-7.31
4-3 S(22)	2.287933	4	24	49878	-5.57	10-6 O(12)	1.495605	10	10	48864	-8.46
4-2 S(22)	1.461167	4	24	49878	-6.43	10-7 O(12)	2.298631	10	10	48864	-7.29
5-3 Q(1)	1.492933	5	1	26735	-5.94	10-8 S(8)	2.122900	10	10	48864	-8.34
5-3 O(3)	1.613520	5	1	26735	-5.95	10-7 Q(10)	1.732359	10	10	48864	-6.29
5-3 Q(2)	1.497982	5	2	26992	-6.08	10-7 Q(11)	1.802258	10	11	49541	-6.34
5-3 O(4)	1.671814	5	2	26992	-6.12	10-8 S(9)	2.161417	10	11	49541	-8.09
5-3 Q(3)	1.505588	5	3	27374	-6.12	10-6 O(13)	1.580528	10	11	49541	-8.37
5-3 O(5)	1.735889	5	3	27374	-6.26	10-8 S(10)	2.216193	10	12	50231	-7.23
5-3 Q(4)	1.515792	5	4	27878	-6.13	10-7 Q(12)	1.886842	10	12	50231	-6.40
5-3 O(6)	1.806060	5	4	27878	-6.39	10-7 S(10)	1.487670	10	12	50231	-6.66
5-3 Q(5)	1.528648	5	5	28498	-6.14	10-6 O(14)	1.680903	10	12	50231	-8.39
5-3 O(7)	1.882689	5	5	28498	-6.53	10-8 S(11)	2.291260	10	13	50921	-6.83
5-3 O(8)	1.966206	5	6	29229	-6.67	10-7 Q(13)	1.990701	10	13	50921	-6.48
5-3 Q(6)	1.544232	5	6	29229	-6.16	10-7 S(11)	1.536694	10	13	50921	-7.07
5-4 S(4)	2.424758	5	6	29229	-6.59	10-6 O(15)	1.801860	10	13	50921	-8.50
5-4 S(5)	2.355478	5	7	30063	-6.74	10-7 Q(14)	2.121149	10	14	51595	-6.58
5-3 O(9)	2.057127	5	7	30063	-6.81	10-7 S(12)	1.600398	10	14	51595	-7.96
5-3 Q(7)	1.562635	5	7	30063	-6.17	10-6 O(16)	1.951559	10	14	51595	-8.76
5-4 S(6)	2.297937	5	8	30994	-6.97	10-8 S(12)	2.393251	10	14	51595	-6.61
5-3 O(10)	2.156073	5	8	30994	-6.95	11-8 O(3)	1.760924	11	1	47390	-5.95
5-3 Q(8)	1.583975	5	8	30994	-6.18	11-8 Q(1)	1.657102	11	1	47390	-5.97
5-3 O(11)	2.263803	5	9	32014	-7.10	11-8 O(4)	1.818283	11	2	47535	-6.11
5-3 Q(9)	1.608398	5	9	32014	-6.19	11-8 S(0)	1.611071	11	2	47535	-6.22
5-4 S(7)	2.251036	5	9	32014	-7.37	11-8 Q(2)	1.668935	11	2	47535	-6.12
5-3 O(12)	2.381246	5	10	33115	-7.24	11-8 S(1)	1.591504	11	3	47748	-6.10
5-3 Q(10)	1.636082	5	10	33115	-6.21	11-8 Q(3)	1.687032	11	3	47748	-6.17
5-4 S(8)	2.213858	5	10	33115	-8.28	11-8 O(5)	1.885081	11	3	47748	-6.24

Continued on next page...

Table A.1 continued: Physical Constants for H_2 Lines

H_2 Line ID	λ (μm)	v_u	J_u	E_u/k (K)	$\log_{10}(A_{ul})$ [s^{-1}]	H_2 Line ID	λ (μm)	v_u	J_u	E_u/k (K)	$\log_{10}(A_{ul})$ [s^{-1}]
5-4 S(9)	2.185653	5	11	34288	-8.26	11-8 O(6)	1.962552	11	4	48027	-6.36
5-3 Q(11)	1.667248	5	11	34288	-6.22	11-8 Q(4)	1.711844	11	4	48027	-6.19
5-4 S(10)	2.165825	5	12	35526	-7.28	11-8 S(2)	1.578830	11	4	48027	-6.06
5-3 Q(12)	1.702170	5	12	35526	-6.24	11-8 S(3)	1.573164	11	5	48365	-6.06
5-4 S(11)	2.153924	5	13	36818	-6.82	11-8 Q(5)	1.744026	11	5	48365	-6.22
5-3 Q(13)	1.741183	5	13	36818	-6.27	11-9 S(3)	2.437440	11	5	48365	-6.80
5-2 O(15)	1.506026	5	13	36818	-7.89	11-8 O(7)	2.052361	11	5	48365	-6.49
5-3 Q(14)	1.784708	5	14	38158	-6.29	11-9 S(4)	2.425958	11	6	48758	-7.03
5-2 O(16)	1.572415	5	14	38158	-7.88	11-8 S(4)	1.574790	11	6	48758	-6.10
5-4 S(12)	2.149645	5	14	38158	-6.52	11-8 Q(6)	1.784501	11	6	48758	-6.25
5-4 S(13)	2.152833	5	15	39537	-6.29	11-8 O(8)	2.156784	11	6	48758	-6.62
5-3 Q(15)	1.833267	5	15	39537	-6.32	11-8 O(9)	2.278963	11	7	49198	-6.75
5-2 O(17)	1.645053	5	15	39537	-7.89	11-9 S(5)	2.429052	11	7	49198	-7.43
5-3 Q(16)	1.887523	5	16	40946	-6.35	11-8 Q(7)	1.834557	11	7	49198	-6.28
5-4 S(14)	2.163489	5	16	40946	-6.12	11-8 S(5)	1.584201	11	7	49198	-6.17
5-2 O(18)	1.724966	5	16	40946	-7.92	11-7 O(9)	1.501941	11	7	49198	-7.83
5-3 Q(17)	1.948318	5	17	42377	-6.39	11-7 O(10)	1.578230	11	8	49676	-8.12
5-2 O(19)	1.813463	5	17	42377	-7.96	11-8 S(6)	1.602167	11	8	49676	-6.28
5-4 S(15)	2.181794	5	17	42377	-5.99	11-8 Q(8)	1.895995	11	8	49676	-6.33
5-4 S(16)	2.208143	5	18	43822	-5.88	11-8 O(10)	2.423341	11	8	49676	-6.89
5-3 Q(18)	2.016743	5	18	43822	-6.44	11-9 S(6)	2.447960	11	8	49676	-8.31
5-2 O(20)	1.912255	5	18	43822	-8.03	11-7 O(11)	1.668173	11	9	50183	-8.39
5-2 O(21)	2.023613	5	19	45273	-8.11	11-8 S(7)	1.629851	11	9	50183	-6.45
5-4 S(17)	2.243197	5	19	45273	-5.79	11-8 Q(9)	1.971382	11	9	50183	-6.39
5-3 Q(19)	2.094235	5	19	45273	-6.49	11-7 O(12)	1.775739	11	10	50708	-8.61
5-3 Q(20)	2.182723	5	20	46721	-6.55	11-8 Q(10)	2.064478	11	10	50708	-6.47
5-4 S(18)	2.287975	5	20	46721	-5.72	11-8 S(8)	1.669009	11	10	50708	-6.71
5-2 O(22)	2.150631	5	20	46721	-8.21	11-8 Q(11)	2.181044	11	11	51238	-6.57
5-4 S(19)	2.344000	5	21	48158	-5.68	11-8 S(9)	1.722349	11	11	51238	-7.13
5-2 O(23)	2.297646	5	21	48158	-8.34	11-7 O(13)	1.906976	11	11	51238	-8.72
5-3 S(19)	1.474949	5	21	48158	-6.69	11-7 Q(11)	1.486320	11	11	51238	-6.54
5-3 Q(21)	2.284873	5	21	48158	-6.62	11-8 Q(12)	2.330510	11	12	51757	-6.72
5-4 S(20)	2.413553	5	22	49573	-5.64	11-7 O(14)	2.071716	11	12	51757	-8.71
5-2 Q(22)	1.507850	5	22	49573	-6.92	11-7 Q(12)	1.572096	11	12	51757	-6.60
5-3 Q(22)	2.404497	5	22	49573	-6.70	11-8 S(10)	1.794264	11	12	51757	-8.03
5-3 S(20)	1.523555	5	22	49573	-6.43	12-9 Q(1)	1.940134	12	1	49413	-6.11
5-1 O(24)	1.523762	5	22	49573	-8.33	12-9 O(3)	2.069971	12	1	49413	-6.05
5-3 S(21)	1.581770	5	23	50957	-6.24	12-8 O(4)	1.451849	12	2	49532	-6.43
5-1 O(25)	1.627845	5	23	50957	-8.40	12-9 O(4)	2.146015	12	2	49532	-6.19
5-2 Q(23)	1.587881	5	23	50957	-6.95	12-9 Q(2)	1.958298	12	2	49532	-6.27
6-4 Q(1)	1.601534	6	1	31063	-5.85	12-9 S(0)	1.886018	12	2	49532	-6.39
6-4 O(3)	1.732641	6	1	31063	-5.85	12-9 S(1)	1.866448	12	3	49706	-6.30
6-4 S(0)	1.536891	6	2	31303	-6.08	12-9 Q(3)	1.986307	12	3	49706	-6.32
6-4 Q(2)	1.607390	6	2	31303	-6.00	12-9 O(5)	2.237053	12	3	49706	-6.31
6-4 O(4)	1.796524	6	2	31303	-6.01	12-8 O(5)	1.500226	12	3	49706	-6.60
6-4 S(1)	1.501560	6	3	31661	-5.94	12-9 O(6)	2.345724	12	4	49932	-6.43
6-4 Q(3)	1.616224	6	3	31661	-6.04	12-9 S(2)	1.857168	12	4	49932	-6.30

Continued on next page...

Table A.1 continued: Physical Constants for H_2 Lines

H_2 Line ID	λ (μm)	v_u	J_u	E_u/k (K)	$\log_{10}(A_{ul})$ [s^{-1}]	H_2 Line ID	λ (μm)	v_u	J_u	E_u/k (K)	$\log_{10}(A_{ul})$ [s^{-1}]
6-4 O(5)	1.867037	6	3	31661	-6.14	12-8 O(6)	1.557732	12	4	49932	-6.76
6-4 S(2)	1.471213	6	4	32132	-5.88	12-9 Q(4)	2.025166	12	4	49932	-6.37
6-4 Q(4)	1.628094	6	4	32132	-6.06	12-8 O(7)	1.625986	12	5	50204	-6.93
6-4 O(6)	1.944593	6	4	32132	-6.27	12-9 Q(5)	2.076394	12	5	50204	-6.42
6-4 O(7)	2.029684	6	5	32711	-6.39	12-9 S(3)	1.858617	12	5	50204	-6.36
6-4 Q(5)	1.643084	6	5	32711	-6.07	12-9 S(4)	1.871662	12	6	50514	-6.47
6-4 Q(6)	1.661304	6	6	33394	-6.08	12-8 O(8)	1.707273	12	6	50514	-7.09
6-4 O(8)	2.122901	6	6	33394	-6.52	12-9 Q(6)	2.142220	12	6	50514	-6.48
6-4 O(9)	2.224960	6	7	34172	-6.65	12-8 Q(6)	1.465294	12	6	50514	-6.43
6-4 Q(7)	1.682897	6	7	34172	-6.10	12-8 Q(7)	1.514357	12	7	50856	-6.46
6-4 Q(8)	1.708041	6	8	35040	-6.11	12-9 Q(7)	2.225938	12	7	50856	-6.55
6-4 O(10)	2.336740	6	8	35040	-6.79	12-9 S(5)	1.897754	12	7	50856	-6.64
6-5 S(7)	2.427962	6	9	35989	-8.94	12-8 O(9)	1.804886	12	7	50856	-7.25
6-4 Q(9)	1.736958	6	9	35989	-6.13	12-8 Q(8)	1.575802	12	8	51218	-6.50
6-4 Q(10)	1.769930	6	10	37012	-6.15	12-9 S(6)	1.939211	12	8	51218	-6.92
6-5 S(8)	2.391064	6	10	37012	-7.97	12-9 Q(8)	2.332531	12	8	51218	-6.66
6-5 S(9)	2.364392	6	11	38100	-7.20	12-8 O(10)	1.923729	12	8	51218	-7.40
6-4 Q(11)	1.807304	6	11	38100	-6.17	12-9 S(7)	1.999793	12	9	51587	-7.39
6-3 O(13)	1.507469	6	11	38100	-8.14	12-8 Q(9)	1.653290	12	9	51587	-6.57
6-5 S(10)	2.347404	6	12	39244	-6.79	12-8 O(11)	2.071475	12	9	51587	-7.55
6-3 O(14)	1.572809	6	12	39244	-8.04	12-8 O(12)	2.261125	12	10	51947	-7.69
6-4 Q(12)	1.849515	6	12	39244	-6.20	12-8 Q(10)	1.752852	12	10	51947	-6.67
6-5 S(11)	2.339748	6	13	40438	-6.51	12-9 S(8)	2.085967	12	10	51947	-8.54
6-4 Q(13)	1.897114	6	13	40438	-6.23	12-8 S(8)	1.459273	12	10	51947	-6.65
6-3 O(15)	1.644503	6	13	40438	-7.99	12-7 O(12)	1.540214	12	10	51947	-9.09
6-5 S(12)	2.341277	6	14	41671	-6.30	13-9 Q(1)	1.614808	13	1	50907	-6.25
6-3 O(16)	1.723573	6	14	41671	-7.98	13-9 O(3)	1.703755	13	1	50907	-6.24
6-4 Q(14)	1.950795	6	14	41671	-6.26	13-10 Q(1)	2.396138	13	1	50907	-6.47
6-5 S(13)	2.352064	6	15	42936	-6.14	13-9 S(0)	1.582542	13	2	50995	-6.50
6-4 Q(15)	2.011451	6	15	42936	-6.31	13-9 Q(2)	1.633121	13	2	50995	-6.41
6-3 O(17)	1.811336	6	15	42936	-8.00	13-9 O(4)	1.761627	13	2	50995	-6.41
6-4 Q(16)	2.080239	6	16	44223	-6.35	13-10 Q(2)	2.428341	13	2	50995	-6.65
6-3 O(18)	1.909513	6	16	44223	-8.04	13-10 S(0)	2.329592	13	2	50995	-6.82
6-5 S(14)	2.372440	6	16	44223	-6.02	13-10 S(1)	2.313551	13	3	51122	-6.79
6-3 O(19)	2.020396	6	17	45524	-8.11	13-9 O(5)	1.833496	13	3	51122	-6.55
6-4 S(15)	1.476947	6	17	45524	-8.91	13-9 S(1)	1.576873	13	3	51122	-6.39
6-4 Q(17)	2.158692	6	17	45524	-6.41	13-9 Q(3)	1.661581	13	3	51122	-6.46
6-5 S(15)	2.403055	6	17	45524	-5.92	13-9 Q(4)	1.701533	13	4	51283	-6.51
6-3 O(20)	2.147109	6	18	46831	-8.22	13-9 S(2)	1.581345	13	4	51283	-6.38
6-4 S(16)	1.510677	6	18	46831	-7.35	13-9 O(6)	1.922241	13	4	51283	-6.69
6-5 S(16)	2.444978	6	18	46831	-5.84	13-10 S(2)	2.315607	13	4	51283	-6.88
6-4 Q(18)	2.248875	6	18	46831	-6.47	13-9 O(7)	2.032186	13	5	51472	-6.84
6-3 O(21)	2.294044	6	19	48132	-8.36	13-9 Q(5)	1.755092	13	5	51472	-6.57
6-4 Q(19)	2.353653	6	19	48132	-6.55	13-9 S(3)	1.596931	13	5	51472	-6.42
6-4 S(17)	1.551516	6	19	48132	-6.82	13-10 S(3)	2.337554	13	5	51472	-7.08
6-3 Q(19)	1.478765	6	19	48132	-6.68	13-9 S(4)	1.625343	13	6	51679	-6.53
6-3 Q(20)	1.548649	6	20	49420	-6.70	13-9 O(8)	2.170039	13	6	51679	-7.00

Continued on next page...

Table A.1 continued: Physical Constants for H_2 Lines

H_2 Line ID	λ (μm)	v_u	J_u	E_u/k (K)	$\log_{10}(A_{ul})$ [s^{-1}]	H_2 Line ID	λ (μm)	v_u	J_u	E_u/k (K)	$\log_{10}(A_{ul})$ [s^{-1}]
6-2 O(22)	1.532425	6	20	49420	-7.97	13-9 Q(6)	1.825564	13	6	51679	-6.65
6-4 S(18)	1.600900	6	20	49420	-6.50	13-8 O(8)	1.499925	13	6	51679	-7.74
6-2 O(23)	1.637549	6	21	50682	-8.04	13-10 S(4)	2.382768	13	6	51679	-7.41
6-4 S(19)	1.660959	6	21	50682	-6.28	13-9 O(9)	2.346884	13	7	51892	-7.20
6-3 Q(21)	1.631050	6	21	50682	-6.74	13-9 Q(7)	1.918373	13	7	51892	-6.77
6-3 Q(22)	1.730302	6	22	51905	-6.78	13-9 S(5)	1.669547	13	7	51892	-6.72
6-2 O(24)	1.764464	6	22	51905	-8.14	13-8 O(9)	1.597246	13	7	51892	-7.97
6-4 S(20)	1.734986	6	22	51905	-6.12	14-10 O(3)	2.225420	14	1	51782	-6.62
7-5 O(3)	1.872635	7	1	35057	-5.80	14-9 Q(1)	1.470400	14	1	51782	-6.64
7-5 Q(1)	1.728799	7	1	35057	-5.82	14-10 Q(1)	2.091366	14	1	51782	-6.70
7-5 S(0)	1.658492	7	2	35281	-6.06	14-9 O(3)	1.543789	14	1	51782	-6.67
7-5 Q(2)	1.735762	7	2	35281	-5.97	14-10 O(4)	2.325065	14	2	51829	-6.79
7-5 O(4)	1.943455	7	2	35281	-5.95	14-10 Q(2)	2.128487	14	2	51829	-6.91
7-5 Q(3)	1.746280	7	3	35613	-6.01	14-10 S(0)	2.052236	14	2	51829	-7.05
7-5 S(1)	1.620548	7	3	35613	-5.93	14-9 Q(2)	1.491784	14	2	51829	-6.83
7-5 O(5)	2.022053	7	3	35613	-6.07	14-9 O(4)	1.598285	14	2	51829	-6.87
7-5 S(2)	1.588294	7	4	36051	-5.88	14-9 Q(3)	1.525561	14	3	51894	-6.93
7-5 Q(4)	1.760446	7	4	36051	-6.03	14-9 S(1)	1.453855	14	3	51894	-6.83
7-5 O(6)	2.109001	7	4	36051	-6.19	14-9 O(5)	1.669264	14	3	51894	-7.08
7-5 O(7)	2.204989	7	5	36588	-6.31	14-10 S(1)	2.058053	14	3	51894	-7.06
7-5 Q(5)	1.778390	7	5	36588	-6.05	14-10 Q(3)	2.187738	14	3	51894	-7.04

Bibliography

Abergel, A., Teyssier, D., Bernard, J. P., et al. 2003, A&A, 410, 577

Akras, S., & Gonçalves, D. R. 2016, MNRAS, 455, 930

Aleman, I., Zijlstra, A. A., Matsuura, M., Gruenwald, R., & Kimura, R. K. 2011, MNRAS, 416, 790

Allers, K. N., Jaffe, D. T., Lacy, J. H., Draine, B. T., & Richter, M. J. 2005, ApJ, 630, 368

Andree-Labsch, S., Ossenkopf-Okada, V., & Röllig, M. 2017, A&A, 598, A2

Bailey, J. A. 1998, in Proc. SPIE, Vol. 3355, Optical Astronomical Instrumentation, ed. S. D'Odorico, 932–939

Balick, B., & Frank, A. 2002, ARA&A, 40, 439

Balick, B., Rugers, M., Terzian, Y., & Chengalur, J. N. 1993, ApJ, 411, 778

Barlow, M. J., & Méndez, R. H. 2007, Planetary Nebulae in our Galaxy and Beyond (IAU S234)

Batrla, W., & Wilson, T. L. 2003, A&A, 408, 231

Bautista, M. A., Fivet, V., Ballance, C., et al. 2015, ApJ, 808, 174

Bertoldi, F., & Draine, B. T. 1996, ApJ, 458, 222

Black, J. H., & Dalgarno, A. 1976, ApJ, 203, 132

Black, J. H., & van Dishoeck, E. F. 1987, ApJ, 322, 412

Blanco Cárdenas, M. W., Käufl, H. U., Guerrero, M. A., Miranda, L. F., & Seifahrt, A. 2014, A&A, 566, A133

Brittain, S. D., Najita, J. R., & Carr, J. S. 2015, Astrophysics and Space Science, 357

Burton, M. G. 1992, Australian Journal of Physics, 45, 463

Burton, M. G., Geballe, T. R., Brand, P. W. J. L., & Moorhouse, A. 1990a, ApJ, 352, 625

Burton, M. G., Hollenbach, D. J., & Tielens, A. G. G. M. 1990b, ApJ, 365, 620

Burton, M. G., Howe, J. E., Geballe, T. R., & Brand, P. W. J. L. 1998, PASA, 15, 194

Caballero, J. A. 2008, MNRAS, 383, 750

Cahn, J. H., Kaler, J. B., & Stanghellini, L. 1992, A&AS, 94, 399

Cazetta, J. O., & Maciel, W. J. 2000, Rev. Mexicana Astron. Astrofis., 36, 3

Christianto, H., & Seaquist, E. R. 1998, AJ, 115, 2466

Compiègne, M., Abergel, A., Verstraete, L., & Habart, E. 2008, A&A, 491, 797

Corradi, R. L. M., Manchado, A., & Soker, N., eds. 2007, Asymmetrical planetary nebulae IV: proceedings of an international conference held on La Palma, Canary Islands, Spain, 18-22 June 2007 (I.A.C. electronic publication)

Dabrowski, I. 1984, Canadian Journal of Physics, 62, 1639
Danby, G., Flower, D. R., Valiron, P., Schilke, P., & Walmsley, C. M. 1988, MNRAS, 235, 229
Davis, C. J., Smith, M. D., Stern, L., Kerr, T. H., & Chiar, J. E. 2003a, MNRAS, 344, 262
Davis, C. J., Whelan, E., Ray, T. P., & Chrysostomou, A. 2003b, A&A, 397, 693
Davis, C. J., Froebrich, D., Stanke, T., et al. 2009, A&A, 496, 153
De Marco, O. 2009, PASP, 121, 316
De Marco, O. 2014, in Asymmetrical Planetary Nebulae VI Conference, 122
Dinerstein, H. L., Lester, D. F., Carr, J. S., & Harvey, P. M. 1988, ApJ, 327, L27
Draine, B. T., & Bertoldi, F. 1996, ApJ, 468, 269
Ferland, G. J., Henney, W. J., O'Dell, C. R., et al. 2012, ApJ, 757, 79
Ferland, G. J., Porter, R. L., van Hoof, P. A. M., et al. 2013, RMxAA, 49, 137
Field, D., Gerin, M., Leach, S., et al. 1994, A&A, 286, 909
Field, D., Lemaire, J. L., Pineau des Forets, G., et al. 1998, A&A, 333, 280
Field, G. B., Somerville, W. B., & Dressler, K. 1966, ARA&A, 4, 207
Fleming, B., France, K., Lupu, R. E., & McCandliss, S. R. 2010, ApJ, 725, 159
France, K., Andersson, B.-G., McCandliss, S. R., & Feldman, P. D. 2005, ApJ, 628, 750
Frank, A., Balick, B., Icke, V., & Mellema, G. 1993, ApJ, 404, L25
Frew, D. J., Parker, Q. A., & Bojičić, I. S. 2016, MNRAS, 455, 1459
Galli, D., & Palla, F. 1998, A&A, 335, 403
García-Segura, G., Langer, N., Różyczka, M., & Franco, J. 1999, ApJ, 517, 767
Gatley, I., & Kaifu, N. 1987, in IAU Symposium, Vol. 120, Astrochemistry, ed. M. S. Vardya & S. P. Tarafdar, 153–166
Gatley, I., Hasegawa, T., Suzuki, H., et al. 1987, ApJ, 318, L73
Genzel, R., & Stutzki, J. 1989, ARA&A, 27, 41
Girard, P., Köppen, J., & Acker, A. 2007, A&A, 463, 265
Gnerucci, A., Marconi, A., Capetti, A., Axon, D. J., & Robinson, A. 2013, A&A, 549, A139
Goicoechea, J. R., Joblin, C., Contursi, A., et al. 2011, A&A, 530, L16
Goicoechea, J. R., Pety, J., Cuadrado, S., et al. 2016, Nature, 537, 207
Gonçalves, D. R. 2004, in Astronomical Society of the Pacific Conference Series, Vol. 313, Asymmetrical Planetary Nebulae III: Winds, Structure and the Thunderbird, ed. M. Meixner, J. H. Kastner, B. Balick, & N. Soker, 216
Gonçalves, D. R., Mampaso, A., Corradi, R. L. M., & Quireza, C. 2009, MNRAS, 398, 2166
Gould, R. J., & Salpeter, E. E. 1963, ApJ, 138, 393
Gullikson, K., Dodson-Robinson, S., & Kraus, A. 2014, AJ, 148, 53
Habart, E., Abergel, A., Boulanger, F., et al. 2011, A&A, 527, A122

Habart, E., Abergel, A., Walmsley, C. M., Teyssier, D., & Pety, J. 2005, A&A, 437, 177
Habart, E., Boulanger, F., Verstraete, L., Walmsley, C. M., & Pineau des Forêts, G. 2004, A&A, 414, 531
Hajduk, M., van Hoof, P. A. M., & Zijlstra, A. A. 2015, A&A, 573, A65
Harpaz, A., & Soker, N., eds. 1995, Asymmetrical planetary nebulae : University of Haifa at Oranim conference, Vol. 11
Hasegawa, T., Gatley, I., Garden, R. P., et al. 1987, ApJ, 318, L77
Hayashi, M., Hasegawa, T., Gatley, I., Garden, R., & Kaifu, N. 1985, MNRAS, 215, 31P
Henney, W. J., Williams, R. J. R., Ferland, G. J., Shaw, G., & O'Dell, C. R. 2007, ApJ, 671, L137
Herczeg, G. J., Dong, S., Shappee, B. J., et al. 2016, ApJ, 831, 133
Hippelein, H. H., & Müench, G. 1989, A&A, 213, 323
Hirota, T., Ando, K., Bushimata, T., et al. 2008, PASJ, 60, 961
Hollenbach, D., & Salpeter, E. E. 1971, ApJ, 163, 155
Hollenbach, D. J., & Tielens, A. G. G. M. 1997, ARA&A, 35, 179
—. 1999, Reviews of Modern Physics, 71, 173
Hora, J. L., & Latter, W. B. 1994, ApJ, 437, 281
Hora, J. L., Latter, W. B., & Deutsch, L. K. 1999, ApJS, 124, 195
Howe, J. E., Jaffe, D. T., & Geballe, T. R. 1990, in BAAS, Vol. 22, Bulletin of the American Astronomical Society, 1328
Hurwitz, M. 1998, ApJ, 500, L67
Jaffe, D. T., Mar, D. J., Warren, D., & Segura, P. R. 2006, in Society of Photo-Optical Instrumentation Engineers (SPIE) Conference Series, Vol. 6269, Society of Photo-Optical Instrumentation Engineers (SPIE) Conference Series
Johansson, S., Zethson, T., Hartman, H., et al. 2000, A&A, 361, 977
Jones, D., & Boffin, H. M. J. 2017, Nature Astronomy, 1, 0117 EP
Kaplan, K. F., Dinerstein, H. L., Oh, H., et al. 2017, The Astrophysical Journal, 838, 152
Kastner, J. H., Soker, N., & Rappaport, S., eds. 2000, Astronomical Society of the Pacific Conference Series, Vol. 199, Asymmetrical Planetary Nebulae II: From Origins to Microstructures
Komasa, J., Piszczatowski, K., Łach, G., et al. 2011, Journal of Chemical Theory and Computation, 7, 3105
Kondratyeva, L. N. 2005, Astronomical and Astrophysical Transactions, 24, 291
Koo, B.-C., Raymond, J. C., & Kim, H.-J. 2016, Journal of Korean Astronomical Society, 49, 109
Kwok, S. 2000, The Origin and Evolution of Planetary Nebulae

—. 2010, PASA, 27, 174
Kwok, S., Purton, C. R., & Fitzgerald, P. M. 1978, ApJ, 219, L125
Le, H. A. N., Pak, S., Kaplan, K. F., et al. 2016, ArXiv e-prints, arXiv:1609.01818
Le Bourlot, J. 1991, A&A, 242, 235
Le Bourlot, J. 2000, in ESA Special Publication, Vol. 456, ISO Beyond the Peaks: The 2nd ISO Workshop on Analytical Spectroscopy, ed. A. Salama, M. F. Kessler, K. Leech, & B. Schulz, 309
Le Bourlot, J., Le Petit, F., Pinto, C., Roueff, E., & Roy, F. 2012, A&A, 541, A76
Lee, J.-J. 2015, plp: Version 2.0, doi:10.5281/zenodo.18579
Lee, S., Yuk, I.-S., Lee, H., et al. 2010, in Society of Photo-Optical Instrumentation Engineers (SPIE) Conference Series, Vol. 7735, Society of Photo-Optical Instrumentation Engineers (SPIE) Conference Series
Leuenhagen, U., & Hamann, W.-R. 1998, A&A, 330, 265
Likkel, L., Dinerstein, H. L., Lester, D. F., Kindt, A., & Bartig, K. 2006, AJ, 131, 1515
Lique, F. 2015, MNRAS, 453, 810
Lis, D. C., & Schilke, P. 2003, ApJ, 597, L145
Luhman, K. L., Engelbracht, C. W., & Luhman, M. L. 1998, ApJ, 499, 799
Luhman, K. L., & Rieke, G. H. 1996, ApJ, 461, 298
Luhman, M. L., Luhman, K. L., Benedict, T., Jaffe, D. T., & Fischer, J. 1997, ApJ, 480, L133
Lumsden, S. L., Puxley, P. J., & Hoare, M. G. 2001, MNRAS, 328, 419
Luridiana, V., Morisset, C., & Shaw, R. A. 2015, A&A, 573, A42
Mace, G., Kim, H., Jaffe, D. T., et al. 2016, in Proc. SPIE, Vol. 9908, Ground-based and Airborne Instrumentation for Astronomy VI, 99080C
Manchado, A., Guerrero, M. A., Stanghellini, L., & Serra-Ricart, M. 1996, The IAC morphological catalog of northern Galactic planetary nebulae
Marconi, A., Testi, L., Natta, A., & Walmsley, C. M. 1998, A&A, 330, 696
Martin, P. G., & Whittet, D. C. B. 1990, ApJ, 357, 113
Martini, P., Sellgren, K., & DePoy, D. L. 1999, ApJ, 526, 772
Matsuura, M., Speck, A. K., Smith, M. D., et al. 2007, MNRAS, 382, 1447
Meixner, M., Kastner, J. H., Balick, B., & Soker, N., eds. 2004, Astronomical Society of the Pacific Conference Series, Vol. 313, Asymmetrical planetary nebulae III : proceedings of a meeting held at Mt. Rainier, Washington, 28 July-1 August 2003
Meixner, M., McCullough, P., Hartman, J., Son, M., & Speck, A. 2005, AJ, 130, 1784
Meixner, M., & Tielens, A. G. G. M. 1993, ApJ, 405, 216
Miranda, L. F., & Solf, J. 1991, A&A, 252, 331

Nagy, Z., Van der Tak, F. F. S., Ossenkopf, V., et al. 2013, A&A, 550, A96
Nisini, B., Caratti o Garatti, A., Giannini, T., & Lorenzetti, D. 2002, A&A, 393, 1035
O'Dell, C. R. 2001, PASP, 113, 29
O'Dell, C. R., Henney, W. J., Abel, N. P., Ferland, G. J., & Arthur, S. J. 2009, AJ, 137, 367
O'Dell, C. R., Henney, W. J., & Ferland, G. J. 2005, AJ, 130, 172
—. 2007, AJ, 133, 2343
Oh, H., Pyo, T.-S., Yuk, I.-S., et al. 2016a, ApJ, 817, 148
Oh, H., Pyo, T.-S., Kaplan, K., et al. 2016b, ApJ, 833, 275
Otsuka, M., Kemper, F., Cami, J., Peeters, E., & Bernard-Salas, J. 2014, MNRAS, 437, 2577
Otsuka, M., Kemper, F., Hyung, S., et al. 2013, ApJ, 764, 77
Panagia, N. 1973, AJ, 78, 929
Parise, B., Leurini, S., Schilke, P., et al. 2009, A&A, 508, 737
Park, C., Jaffe, D. T., Yuk, I.-S., et al. 2014, Proc. SPIE, 9147, 1
Parker, Q. A., Acker, A., Frew, D. J., et al. 2006, MNRAS, 373, 79
Parmar, P. S., Lacy, J. H., & Achtermann, J. M. 1991, ApJ, 372, L25
Peimbert, M. 1990, Reports on Progress in Physics, 53, 1559
Pellegrini, E. W., Baldwin, J. A., Ferland, G. J., Shaw, G., & Heathcote, S. 2009, ApJ, 693, 285
Pellegrini, E. W., Baldwin, J. A., Brogan, C. L., et al. 2007, ApJ, 658, 1119
Perryman, M. A. C., Lindegren, L., Kovalevsky, J., et al. 1997, A&A, 323, L49
Pesenti, N., Dougados, C., Cabrit, S., et al. 2003, A&A, 410, 155
Phillips, J. P., & Ramos-Larios, G. 2005, MNRAS, 364, 849
Porter, J. M., Oudmaijer, R. D., & Baines, D. 2005, in Astronomical Society of the Pacific Conference Series, Vol. 337, The Nature and Evolution of Disks Around Hot Stars, ed. R. Ignace & K. G. Gayley, 299
Pyo, T.-S., Hayashi, M., Kobayashi, N., et al. 2002, ApJ, 570, 724
Quinet, P., Le Dourneuf, M., & Zeippen, C. J. 1996, A&AS, 120, 361
Quireza, C., Rocha-Pinto, H. J., & Maciel, W. J. 2007, A&A, 475, 217
Ramsay, S. K., Chrysostomou, A., Geballe, T. R., Brand, P. W. J. L., & Mountain, M. 1993, MNRAS, 263, 695
Rieke, G. H., & Lebofsky, M. J. 1985, ApJ, 288, 618
Rosenthal, D., Bertoldi, F., & Drapatz, S. 2000, A&A, 356, 705
Sabin, L., Zijlstra, A. A., & Greaves, J. S. 2007, MNRAS, 376, 378
Sahai, R., Morris, M., Sánchez Contreras, C., & Claussen, M. 2007, AJ, 134, 2200

Sahai, R., Morris, M. R., & Villar, G. G. 2011, AJ, 141, 134
Sahai, R., & Trauger, J. T. 1998, AJ, 116, 1357
Salgado, F., Berné, O., Adams, J. D., et al. 2016, ApJ, 830, 118
Schlafly, E. F., Green, G., Finkbeiner, D. P., et al. 2014, ApJ, 786, 29
Sellgren, K. 1986, ApJ, 305, 399
Shaw, G., Ferland, G. J., Abel, N. P., Stancil, P. C., & van Hoof, P. A. M. 2005, ApJ, 624, 794
Shaw, G., Ferland, G. J., Henney, W. J., et al. 2009, ApJ, 701, 677
Sheffer, Y., Wolfire, M. G., Hollenbach, D. J., Kaufman, M. J., & Cordier, M. 2011, ApJ, 741, 45
Shenavrin, V. I., Taranova, O. G., & Nadzhip, A. E. 2011, Astronomy Reports, 55, 31
Shull, J. M., & Beckwith, S. 1982, ARA&A, 20, 163
Sigut, T. A. A., & Jones, C. E. 2007, ApJ, 668, 481
Simon, R., Stutzki, J., Sternberg, A., & Winnewisser, G. 1997, A&A, 327, L9
Skrutskie, M. F., Cutri, R. M., Stiening, R., et al. 2006, AJ, 131, 1163
Smith, N., Balick, B., & Gehrz, R. D. 2005, AJ, 130, 853
Soker, N. 2016, MNRAS, 455, 1584
Speck, A. K., Meixner, M., Fong, D., et al. 2002, AJ, 123, 346
Sterling, N. C., Dinerstein, H. L., Kaplan, K. F., & Bautista, M. A. 2016, ApJ, 819, L9
Sternberg, A. 1988, ApJ, 332, 400
—. 1989, ApJ, 347, 863
Sternberg, A., & Dalgarno, A. 1989, ApJ, 338, 197
Sternberg, A., & Neufeld, D. A. 1999, ApJ, 516, 371
Storey, P. J., & Hummer, D. G. 1995, MNRAS, 272, 41
Störzer, H., & Hollenbach, D. 1998, ApJ, 495, 853
Sugar, J., & Corliss, C. 1985, Atomic energy levels of the iron-period elements: Potassium through Nickel
Takahashi, J., & Uehara, H. 2001, ApJ, 561, 843
Takami, M., Bailey, J., Chrysostomou, A., Tamura, M., & Terada, H. 2004, in IAU Symposium, Vol. 221, Star Formation at High Angular Resolution, ed. M. G. Burton, R. Jayawardhana, & T. L. Bourke, 417
Takami, M., Usuda, T., Sugai, H., et al. 2000, ApJ, 529, 268
Takami, M., Chrysostomou, A., Ray, T. P., et al. 2006, ApJ, 641, 357
Takayanagi, K., Sakimoto, K., & Onda, K. 1987, ApJ, 318, L81
Tanaka, M., Hasegawa, T., Hayashi, S. S., Brand, P. W. J. L., & Gatley, I. 1989, ApJ, 336, 207

Tauber, J. A., Tielens, A. G. G. M., Meixner, M., & Goldsmith, P. F. 1994, ApJ, 422, 136
Thi, W.-F., van Dishoeck, E. F., Bell, T., Viti, S., & Black, J. 2009, MNRAS, 400, 622
Tielens, A. G. G. M., & Hollenbach, D. 1985, ApJ, 291, 722
Tielens, A. G. G. M., Meixner, M. M., van der Werf, P. P., et al. 1993, Science, 262, 86
Timmermann, R., Bertoldi, F., Wright, C. M., et al. 1996, A&A, 315, L281
Tylenda, R., Acker, A., & Stenholm, B. 1993, A&AS, 102, 595
Tylenda, R., Acker, A., Stenholm, B., & Koeppen, J. 1992, A&AS, 95, 337
Vacca, W. D., Cushing, M. C., & Rayner, J. T. 2003, PASP, 115, 389
van Dokkum, P. G. 2001, PASP, 113, 1420
van Leeuwen, F. 2007, A&A, 474, 653
van Regemorter, H. 1962, ApJ, 136, 906
Verner, E. M., Verner, D. A., Korista, K. T., et al. 1999, ApJS, 120, 101
Vickers, S. B., Frew, D. J., Parker, Q. A., & Bojičić, I. S. 2015, Monthly Notices of the Royal Astronomical Society, 447, 1673
Walmsley, C. M., Natta, A., Oliva, E., & Testi, L. 2000, A&A, 364, 301
Warren, Jr., W. H., & Hesser, J. E. 1977, ApJS, 34, 115
Weilbacher, P. M., Monreal-Ibero, A., Kollatschny, W., et al. 2015, A&A, 582, A114
Welch, C. A., Frank, A., Pipher, J. L., Forrest, W. J., & Woodward, C. E. 1999, ApJ, 522, L69
Witt, A. N., Stecher, T. P., Boroson, T. A., & Bohlin, R. C. 1989, ApJ, 336, L21
Wolniewicz, L., Simbotin, I., & Dalgarno, A. 1998, ApJS, 115, 293
Wrathmall, S. A., Gusdorf, A., & Flower, D. R. 2007, MNRAS, 382, 133
Wyrowski, F., Schilke, P., Hofner, P., & Walmsley, C. M. 1997, ApJ, 487, L171
Young Owl, R. C., Meixner, M. M., Wolfire, M., Tielens, A. G. G. M., & Tauber, J. 2000, ApJ, 540, 886
Yuk, I.-S., Jaffe, D. T., Barnes, S., et al. 2010, in Society of Photo-Optical Instrumentation Engineers (SPIE) Conference Series, Vol. 7735, Society of Photo-Optical Instrumentation Engineers (SPIE) Conference Series
Zhang, H. 1996, A&AS, 119, 523
Zijlstra, A. A., Lykou, F., McDonald, I., & Lagadec, E., eds. 2011, Asymmetric Planetary Nebulae 5
Zuckerman, B. 1973, ApJ, 183, 863